ulm university universität

uulm

Dynamics of ultracold Fermi gases in the vicinity of the BEC-BCS crossover

Dissertation

zur Erlangung des Doktorgrades Dr. rer. nat.

der

Fakultät für Naturwissenschaften

der

Universität Ulm

vorgelegt von

Daniel Kai Hoffmann

aus Nürnberg

2020

Dekan der Fakultät für Naturwissenschaften: Prof. Dr. Thomas Bernhardt

Erstgutachter/Betreuer: Prof. Dr. Johannes Hecker Denschlag

Zweitgutachter: Prof. Dr. Alexander Kubanek

Tag der mündlichen Prüfung: 15.09.2020

Die in dieser Dissertation beschriebenen Arbeiten wurden an der

Universität Ulm

Institut für Quantenmaterie

Albert-Einstein-Allee 45

89081 Ulm

durchgeführt.

„Whatever nature has in store for mankind, unpleasant as it may be, men must accept, for ignorance is never better than knowledge."

Enrico Fermi

Abstract

Dynamics play an important role in physics. From classical mechanics, astrophysics, hydrodynamics to quantum physics, the dynamics of physical systems have crucial impact on our understanding of nature. For simple configurations such as in the two-body problem the dynamics can be calculated analytically. However, things get more complicated once the number of contributors in a system increases such as in few- or many-body systems. One way to study such an ensemble is to use a model system where decisive parameters can be controlled. In this thesis I make use of an ultracold cloud of fermionic ^{6}Li atoms close to zero temperature to study dynamics of few- and many-body systems. Two experimental studies to this topic are presented.

In the first study, I produced a gas of di-atomic molecules (dimers), consisting of two ^{6}Li atoms in different states, to study the reaction kinetics of the four-body process of a dimer-dimer collision. At temperatures close to absolute zero the internal and external degrees of freedom of the dimers can be well controlled. This allowed us to investigate the kinetics of a single-channel reaction. To resolve the dynamics of the process we heated a gas of molecules and tracked the state of the system as a function of time. We determined the reaction-rate constant of the process for various thermal energies which allowed us to verify the Arrhenius law for molecule-molecule reactions in the ultracold regime. Additionally, we provided first insight into the dependence of this four-body process on the particle interaction.

In the second experimental work, I focused on the thermodynamical properties of the ultracold gas. Cooling the gas of ^{6}Li atoms close to zero temperature the gas undergoes a phase transition and superfluidity is established. To study the dynamics in such a gas, we used a local perturbation to produce sound waves. Depending on the excitation scheme we either excited first sound, i.e. a pressure wave, known from classical mechanics, or second sound, i.e. an entropy wave. In the study we focused on second sound and determined the second sound speed as a function of the particle interaction. We found agreement of our results with both - a numerical and an analytical description of the interaction strength dependence of the second sound speed.

Besides the experimental work, a theoretical proposal for a novel imaging technique for a 2D ultracold gas in an optical lattice is presented. The scheme is based on a holographic approach and enables the detection of individual particles with only a few hundred scattered photons per atom.

v

Zusammenfassung

Dynamiken spielen eine wichtige Rolle in der Physik. Von der klassischen Mechanik, über die Astrophysik, der Hydrodynamik bis zur Quantenphysik, die Dynamik in physikalischen Systemen hat einen entscheidenden Einfluss auf unser Verständnis von der Natur. Für einfache Anordnungen, wie im Zweikörperproblem, kann die Dynamik analytisch beschrieben werden. Erhöht man jedoch die Anzahl der Körper im System bis hin zu Vielteilchensystemen, so wird die Beschreibung kompliziert. Eine Möglichkeit sich einem solchen Ensemble zu nähern besteht darin, Modellsysteme, in denen entscheidenden Parameter kontrolliert werden können, zu studieren. In dieser Arbeit verwende ich ein ultrakaltes Gas von ^{6}Li Atomen nahe dem absoluten Nullpunkt um die Dynamik in Prozessen zwischen einigen wenigen Teilchen als auch in Vielteilchensystemen zu untersuchen. In diesem Rahmen werden zwei experimentelle Studien vorgestellt.

In der ersten Studie wird ein Gas aus zweiatomigen Lithiummolekülen, wobei sich die einzelnen Atome in unterschiedlichen Zuständen befinden, genutzt um die Reaktionskinetik des Vierkörperprozesses einer Molekül-Molekül-Kollision zu untersuchen. Bei Temperaturen nahe dem absoluten Nullpunkt können sowohl interne als auch externe Freiheitsgrade der Moleküle kontrolliert werden. Dies ermöglichte es uns die Reaktionskinetik eines einzelnen Reaktionskanals zu untersuchen. Um die Dynamik des Prozesses zu studieren heizten wir das ultrakalte Gas auf und beobachteten die Zustandsänderung des Systems. Wir ermittelten den Reaktionsratenkoeffizient für verschiedene thermische Energien. Dies ermöglichte es uns das Arrhenius Gesetz für Molekül-Molekül-Kollisionen im ultrakalten Regime zu verifizieren. Darüber hinaus konnten wir erste Einblicke zur Wechselwirkungsabhängigkeit dieses Vierkörperprozesses liefern.

In der zweiten experimentellen Studie befasse ich mich mit den thermodynamischen Eigenschaften der verwendeten ultrakalten Atome. Wird ein Gas von ^{6}Li Atomen auf Temperaturen nahe dem absoluten Nullpunkt gekühlt, so durchläuft das Gas einen Phasenübergang in einen suprafluiden Zustand. Um die Dynamik in einem solchen Gas zu untersuchen nutzten wir eine lokale Störung um Schallwellen zu erzeugen. Abhängig vom Anregungsschema konnte hauptsächlich erster Schall, eine Druckwelle wie sie aus der klassischem Mechanik bekannt ist, oder zweiter Schall, eine Entropiewelle, angeregt werden. Im Speziellen ermittelten wir die Geschwindigkeit des zweiten Schalls als Funktion der Teilchenwechselwirkung. Dabei fanden wir eine Übereinstimmung unserer Resultate sowohl mit einer numerischen als auch einer analytischen Beschreibung.

Neben den experimentellen Studien wird in dieser Arbeit eine neuartige Abbildungstechnik für ein 2D Gas ultrakaler Atome in einem optischen Gitter auf theoretischer Ebene beschrieben. Das Schema basiert auf einem holografischen Ansatz und ermöglicht die Detektion einzelner Atome, wobei nur wenigen hundert Photonen pro Atom gestreut werden müssen.

Contents

1 Introduction

The dynamics of physical systems have been studied over many centuries. This includes classical phenomena as the movement of planets. In the simplest case a system consists of two objects, where the dynamics are well understood and can be discussed analytically in the framework of the two-body problem. However, adding more complexity to the system, e.g. adding additional bodies, the analytic calculations start to fail and the description of the system gets more and more complicated. This is even increased when we consider more complex bodies with additional internal structure. For instance, this is of relevance for small objects as atoms, especially when we are looking at collision processes. Particularly, when atoms form larger complexes as molecules, the complexity of collisions can quickly become complicated when it comes to dynamics.

Ultracold chemistry

A collision of two objects, involving at least one molecule, can either be elastic or inelastic/reactive. While an elastic collision is simply described by kinematics, a reactive collision is more complex and leads to a change in the composition of the system. Reactive collisions can have a multitude of reaction channels even when the molecule consist of only two atoms. The number of possible reaction channels is highly depending on the available collision energy. Therefore, it can be very difficult to study fundamental collisions with control over the available reaction channels at room temperature.

In the past decades experiments with molecular beams emerged, providing a controllable setting to study and isolate basic reactions (see [1, 2]). In these experiments molecular beams, at temperatures of only a few Kelvin, are brought to collision inside a vacuum chamber. This way, the investigated process can be isolated from background collisions and the possible reaction channels can be restricted by controlling the collision energy. The latter is typically done in two ways. First, the gases are produced at low temperatures, setting the scale of the collision energies. Second, the collision angle of the beams is tuned to adjust the relative momentum of the colliding particles. Although the work on molecular beams is a remarkable step in the control of reactive collisions, individual channels and especially individual quantum states cannot be fully isolated at the collision energies of these experiments.

One way to reduce the number of possible reaction channels is to cool the atoms to even lower temperatures, where the number of reaction paths are further reduced.

This has been achieved with the realization of ultracold quantum gas experiments in the past decades. In the experiments, atomic gases are cooled close to absolute zero temperature and are confined in magnetic or optical traps inside a vacuum chamber. In recent years a multitude of experimental tools have been developed to allow an unprecedented control over both, the external and internal parameters of the trapped atoms. This makes ultracold atoms highly suited to study all kinds of fundamental collisions [3, 4].

One crucial parameter in this context is the scattering length a which describes the particle interaction at ultracold temperatures. In experiments with cold atoms the scattering length a can be tuned by means of a magnetic Feshbach resonance [5]. This way a can be set to positive values (effectively repulsive interaction), infinity on the resonance, and negative values (effectively attractive interaction).

Tuning the particle interaction by means of the Feshbach resonance di-atomic molecules, called dimers in the following, can be produced in the ultracold regime [6–15]. However, this is only one way to produce ultracold molecules. In the field of ultracold quantum gases other options for the production of molecules and studies to chemical reactions emerged. For instance ultracold molecules can be produced by means of photoassociation, where a photon transfers two unbound atoms to an excited molecular state [16–18]. Tuning the photon energy the produced excited state can be controlled. Another way to study molecular physics in the ultracold regime is to investigate three-body recombination processes. A reactive collision of three atoms leads to a bound state, where the products carry away the release energy. Studies to the process enable to investigate the product state of the produced molecule [5, 8, 19–21]. A similar direction of research addresses three-body collisions in the framework of Efimov physics. The Efimov effect is characterized by an infinite number of trimer states that can be found for three identical bosons or three distinguishable fermions in the close vicinity of a two-body resonance [22]. The exceptional control over the atoms in ultracold quantum gas experiments enabled a first experimental realization of such a trimer state more than one decade ago [23–28]. An alternative approach to study cold molecules uses the direct cooling of molecules via Stark or magnetic decelerators. In this field of research, a bunch of molecules is slowed in an inhomogenoeus electric or magnetic field [29, 30]. Such experiments allow studies on even more complex molecules with decent control over the contributors.

The variety of the different approaches to study cold molecules shows that the topic has drawn broad interest in the community. However, although major steps have been made to study chemical reactions on the most fundamental level, not all processes could be studied in detail. Even in collisions at temperatures of a few μK not all reaction channels can be isolated easily making it hard to investigate chemical reactions on a state-to-state level. In the collision of ultracold dimers relaxation processes are possible which can lead to losses of the trapped reaction products. This makes especially the analysis of the reaction dynamics complicated

[31–39].

One system suitable to study a single isolated reaction channel is an ultracold cloud of fermionic ^{6}Li atoms close to a magnetic Feshbach resonance. In this work, we make use of such a gas. We produced weakly bound dimers to study reactive molecule-molecule collisions and its dynamics [40]. For the weakly bound dimers, consisting of two fermionic atoms, a relaxation process and accompanying losses are absent. Due to the low binding energy the fermionic character of the contributing atoms is still present. Therefore, in our case the Pauli exclusion principle, which states that two Fermions cannot occupy the same quantum state inside the same quantum system [41], leads to a suppression of relaxation processes in the collisions of the dimers.

With this, we were able to study the isolated process of a dimer dissociation for a single quantum state. We determined the rate coefficient for various collision energies to verify the well known Arrhenius law which connects the dissociation rate constant with the binding energy of the dimers and the thermal energy of the gas. Besides this, we performed experiments for various interaction strengths in which we found agreement with an a^4 scaling of the reaction rate constant. As predicted in few-body theory, the reaction rate constant is connected to the scattering length via an universal constant. However, with our measurements we found that the value is by a factor of ten larger as in the theoretical prediction [42–44]. This indicates two things. First, additional effort is needed to get a deeper understanding of this type of four-body process on the theoretical side. Second, this discrepancy shows how complex a few-body collision can be, even with a small number of contributors.

Second sound

Leaving the field of few-body collisions and adding additional contributors to the system, the dynamics, as mentioned above, gets complicated in its full microscopic description. To discuss the behavior of such a systems, many-body theory is used with which the collective behavior of the system, including interactions and quantum effects, can be described. Close to absolute zero we find remarkable features for many-body systems. For instance, in gases or liquids superfluidity has to be mentioned.

Superfluidity was discovered first by P. Kapitza, J. F. Allen and D. Misener in liquid Helium II [45, 46] in the late 1930s. The superfluid Helium showed the remarkable feature of friction less flow, characteristic for a liquid or gas in the superfluid state. Shortly after the first experiments L. Landau and L. Tisza presented a two-fluid model to describe the system [47–51]. In the model the fluid consists of a normal and a superfluid part within a hydrodynamic description. It successfully explained phenomena detected in experiments with the Helium II and predicted that two types of wave phenomena should be observable in such a system. The first sound, which is a pressure wave known from classical fluid mechanics, and second sound, an

entropy wave describing how thermal energy propagates in the superfluid. A few years after its prediction second sound was detected in superfluid Helium II by V. Peshkov [52]. In the following decades second sound could only be studied in liquids. However, recently second sound was measured in a different type of superfluid system, namely an ultracold quantum gas [53].

Besides repeating the measurements done in Helium before, ultracold gases can be used to extend the studies on second sound to improve our basic understanding of superfluidity. This includes second sound experiments in two-dimensional systems, which could not be investigated in liquid Helium [54–56]. Additionally, in cold quantum gases the particle interaction is tunable and second sound can be studied for different types of many-body systems easily.

However, so far the experimental work on second sound in three dimensional ultracold gases is limited to one study in which second sound was measured for resonant particle interaction [53]. In my thesis, we extended the work to the regimes of repulsive and attractive interactions using the ultracold Fermi gas of ^{6}Li atoms. In the regime of repulsive interaction (BEC regime) bosonic dimers can form, which can undergo a phase transition to a molecular Bose Einstein condensate (mBEC) [9, 57, 58]. For attractive interaction (BCS regime) and below the critical temperature Cooper pairing sets in and superfluidity is established [59, 60].

Analogue to the work in ref. [53] we applied a local perturbation on a confined ultracold gas to determine the speed of second sound. Performing experiments for various magnetic fields, i.e. particle interactions, allowed us to determine the speed of second sound in the crossover between the BEC and the BCS regime [61].

The speed of second sound is a valuable quantity since it gives access to the superfluid density of the cloud. For the weak attractive, weak repulsive, and resonant interaction the connection between sound speed and superfluid density is known [53, 62]. In the crossover the link between the two quantities is missing. Therefore, our results, presented in this thesis, can be used as benchmark data to develop this connection theoretically. This knowledge is required for a complete understanding of the thermodynamical state of the gas in the crossover.

Detection of ultracold atoms in an optical lattice

In the past decades the work on ultracold atoms in optical lattice led to a multitude of experimental studies in the framework of many-body physics with remarkable success. Besides experiments related to quantum optics and quantum information processing, optical lattices are ideally suited to study aspects of condensed-matter physics on a fundamental level (see e.g. [63–65]). Especially, for the studies on solid-state like systems major achievements have been made. One prominent example is the production of a Mott insulating state with both, bosonic and fermionic atoms [63, 66–68]. An ensemble of cold atoms in this state is characterized by a fixed number of atoms per lattice site which is an ideal starting point to address

fundamental questions of condensed matter physics. For such studies it is beneficial if the atomic distribution can be directly accessed on a single-site single-atom level. Many efforts have been made to achieve such a detection technique [69–75]. However, on the way to its realization it has turned out that this type of detection is technically challenging, particularly for the detection of light elements as lithium. To detect individual particles via fluorescence imaging a few thousand photons have to be scattered by a single atom typically. The photon scattering heats the atoms which can lead to a de-localization of the atoms in the lattice or to atom losses. To suppress this effect in most experiments a deep optical lattice and a simultaneous cooling of the atoms has to be used during fluorescence detection which complicates the process from a technical point of view [72, 75]. Therefore, it is convenient to study alternative approaches for the detection of particles in an optical lattice.

One alternative to a direct detection of cold atoms is phase-contrast imaging. Several groups used the phase modulation a weak off-resonant beam experiences when it is propagating through an atomic cloud to measure the particle distribution [76–79]. The information on the atomic distribution is imprinted on the phase of the detection beam and can be reconstructed.

In the work presented here, we proposed a similar approach based on off-axis holography. In off-axes holography, a beam illuminates the imaged object and is scattered [80]. The scattered light is superimposed with a reference wave in the image plane/ hologram plane under an angle. Using a readout wave an observer can obtain the information stored in the hologram. Here, we essentially propose a similar scheme for cold atoms in the lattice [81]. A laser beam illuminating the atoms in a lattice is scattered coherently and carries the information on the lattice occupancy. The beam is collimated by a high resolution lens and guided to a detector where the scattered light is superimposed with a reference beam under an angle. The produced interferogram can be used to reconstruct the information on the lattice occupancy. We show that even under the influence of noise the scheme is robust and reliable and requires only a few hundred scattered photons per atom.

Outline

This thesis is organized as follows.

In the second chapter, I give a brief introduction to the most relevant theoretical concepts used in this thesis. First, I introduce the statistical properties of Fermi gases in harmonic traps. Then, I concentrate on a few principles of scattering theory and introduce the properties of ^{6}Li in high magnetic fields. Thereafter, I give an overview of a few fundamentals of magnetic Feshbach resonances and molecule formation close to such a resonance. This is followed by the theoretical description of sound propagation in a partially superfluid Fermi gas in terms of a hydrodynamic approach.

In the third chapter the technical realization of the experimental apparatus, which has been set up in the course of this thesis, is presented. This includes the vacuum system, the control unit, coil systems, laser sources, imaging and projection optics. In this context technical limitations and challenges are addressed.

In the fourth chapter, I introduce the experimental steps required to produce a degenerate quantum gas. This includes standard cooling methods as laser cooling, molasses cooling as well as evaporative cooling. An extended description of particle trapping in terms of a magneto optical trap, optical dipole traps, and an optical lattice is given. Additionally, first steps towards ultracold atoms in optical lattices and two-dimensional gases are shown.

In the fifth chapter our experimental work on the chemical reaction dynamics in ultracold molecule-molecule collisions is reported. A sample of ultracold Feshbach molecules in a single quantum state is produced and is shifted out of thermal equilibrium. The dissociation of the dimers is observed and its dependence on particle interaction and thermal energy is discussed.

In the sixth chapter, I present our study on sound excitation in a superfluid Fermi gas. Starting from the BEC side of the broad Feshbach resonance I describe a systematic study of second-sound propagation in a strongly interacting Fermi gas across the BEC-BCS crossover. Furthermore, an extensive study of the coupling of a local perturbation to first and second sound modes is given. The experimental work is strongly supported by the theoretical work done in the group of Ludwig Mathey [82].

In the seventh chapter, the holographic imaging approach is introduced. Besides the numerical simulation of the detection scheme, we discuss an analytic description of the method. We are able to demonstrate that the scheme provides a high detection fidelity although only a few hundred photons are scattered per atom during imaging.

In the eighth chapter, an outlook on possible future experiments and suggestions for the extension of ongoing work is presented.

2 Ultracold gases - theory overview

The work presented in this thesis is based on the production and manipulation of interacting fermionic atoms in the ultracold regime. The thermodynamical properties of ultracold atoms and gases are determined by particle statistics, phase space densities, trapping geometries and the particle interaction. Therefore, the following chapter is devoted to give a brief overview of significant properties of interacting Fermi gases including the fundamentals of particle statistics and scattering theory. In this context, I will introduce theoretical aspects relevant for this thesis. The information is taken from several textbooks, reviews, and research articles.

2.1 Particle statistics and distribution functions

All experiments presented in this thesis start with an atomic beam of ^{6}Li atoms at a temperature of $673\,\mathrm{K}$. Subsequently, the atoms are cooled to temperatures on the order of one millikelvin in a first stage using laser cooling and are confined in a trap as a cold atomic cloud. This is still far away from the ultracold regime and the gas can be treated in a classical approach. The ensemble has a low phase space density, obeys the Maxwell-Boltzmann statistics, and follows the distribution function f_{MB}[1] which reads

$$f_{\mathrm{MB}} = e^{-(E_{\mathrm{kin}}+V-\mu)/k_{\mathrm{B}}T}. \tag{2.1}$$

Here, E_{kin} is the kinetic energy, V the external trapping potential, and μ the chemical potential, k_{B} is the Boltzmann constant, and T is the temperature.
The phase space density is given by $n\lambda_{\mathrm{dB}}^3$, where $\lambda_{\mathrm{dB}} = \hbar\sqrt{(2\pi)/(mk_{\mathrm{B}}T)}$ is the thermal de Broglie wavelength, and n is the atomic density.
In our experiments we use harmonic traps typically. Therefore, the external potential is expressed by

$$V(\mathbf{r}) = \sum_{i=1}^{3} \frac{1}{2} m\omega_i^2 x_i^2. \tag{2.2}$$

Here ω_i are the trapping frequencies and x_i are the displacements from the trap center. The index i denotes the spatial coordinate in the Cartesian coordinate system.

---

[1]See ref. [83] and textbooks like [84, 85]

To calculate the spatial density distribution of a thermal cloud in such a trap, we have to integrate the phase-space distribution of eq. (2.1) in the momentum space (for more details see [86])

$$n(\mathbf{r}) = \int \int \int \frac{f_{\mathrm{MB}}}{h^3} \, \mathrm{d}^3 \mathbf{p} = n_0 \sum_{i=1}^{3} e^{\frac{-m\omega_i^2 r_i^2 \beta}{2}}. \tag{2.3}$$

Here n_0 is the peak density and $\beta = (k_{\mathrm{B}}T)^{-1}$. The factor $(2\pi\hbar)^3$ is the phase space cell.

If we cool the gas further down, i.e. close to absolute zero temperature, the phase space density of the gas approaches $\lambda_{\mathrm{dB}}^3 n \approx 1$ and quantum statistics starts to dominate the thermodynamical properties of the gas. Depending on external parameters we find fermionic lithium and/or diatomic bosonic molecules of two ^{6}Li atoms in the trapped gas (see also sec. 2.5). These two particle classes are distinguished by the symmetry of their wave function and the spin. Fermions have an anti-symmetric wave function, half integer spin and obey the Pauli principle [41]. Bosons have a symmetric wave function (see eq. (2.4)), full integer spin, and have no restrictions concerning state occupation. The properties of the two classes can be easily visualized looking at the two particle wave function

$$|\Psi_{\mathrm{F}}, \Psi_{\mathrm{F}}'\rangle = -|\Psi_{\mathrm{F}}', \Psi_{\mathrm{F}}\rangle \qquad\qquad |\Psi_{\mathrm{B}}, \Psi_{\mathrm{B}}'\rangle = |\Psi_{\mathrm{B}}', \Psi_{\mathrm{B}}\rangle. \tag{2.4}$$

Here $\Psi_{\mathrm{i}}^{(')}$ are the wave functions and their complex conjugates for two indistinguishable particles and the index F (B) marks fermions (bosons), respectively. The wave function symmetry of fermions leads to a sign change for a particle exchange in a two particle wave function, while it does not for bosons. This difference leads to a diversity in the particle statistics. Fermions follow the Fermi-Dirac distribution f_{FD}, while bosons obey Bose-Einstein statistics f_{BE}.

$$f_{\mathrm{FD}} = \frac{1}{e^{(E_{\mathrm{kin}}+V-\mu)/k_{\mathrm{B}}T} + 1} \qquad\qquad f_{\mathrm{BE}} = \frac{1}{e^{(E_{\mathrm{kin}}+V-\mu)/k_{\mathrm{B}}T} - 1} \tag{2.5}$$

Analog to the thermal gas, we can compute valuable quantities for a non-interacting Bose and Fermi gas from the distribution functions. This includes the spatial density distribution and the total particle number. Especially the density distribution is a central quantity, since all experimental results gained within this thesis are exclusively derived from the density distribution. To obtain the density distribution we again integrate the phase space distribution in the momentum space [60, 86] which gives

$$n_{\mathrm{F}}(\mathbf{r}) = -\lambda_{\mathrm{dB}}^{-3} \mathrm{Li}_{3/2}\left(-e^{(\mu-V(\mathbf{r}))/k_{\mathrm{B}}T}\right) \quad n_{\mathrm{B}}(\mathbf{r}) = \lambda_{\mathrm{dB}}^{-3} \mathrm{Li}_{3/2}\left(e^{(\mu-V(\mathbf{r}))/k_{\mathrm{B}}T}\right). \tag{2.6}$$

Here, Li_l is the l-th order polylogarithm[2] and $n_{\text{F(B)}}$ is the fermionic (bosonic) density distribution.

From the density distribution useful expressions for both particle classes in a harmonic confinement will be derived in the following (see also ref. [86]).

Fermions

The first quantity to be derived for a non-interacting Fermi gas is the total particle number in a harmonic confinement. To do so, we integrate the density distribution of eq. (2.6) in the position space

$$N = \int n_{\text{F}} \text{d}V = - \left(\frac{k_{\text{B}}T}{\hbar \bar{\omega}} \right)^3 \text{Li}_3 \left(-e^{\beta \mu} \right). \tag{2.7}$$

Here, $\bar{\omega} = (\omega_x \omega_y \omega_z)^{1/3}$ is the geometrical mean value of the trapping frequencies, and N is the atom number. The relation between the chemical potential and the particle number holds for $T > 0$.

In our experiments the gas is cooled from temperatures of a few hundred Kelvin to close to zero[3]. Therefore, it is convenient to discuss a few limiting cases for a gas of fermions in a harmonic confinement.

Initially, the pre-cooled gas[4] follows the Maxwell Boltzmann distribution and the particle density is given by eq. (2.3). Reducing the temperature the Fermi gas enters the regime of quantum degeneracy, where the density distribution smoothly changes from the classical to the $T \to 0$ distribution. To quantify the degree of quantum degeneracy the ratio of the absolute temperature and the Fermi temperature T/T_F is essential. The smaller the ratio the larger the degree of quantum degeneracy and the larger the influence of Fermi statistics in the system. The Fermi temperature T_F for a harmonic confinement is given by

$$T_{\text{F}} = \frac{E_{\text{F}}}{k_{\text{B}}} = \frac{\hbar}{k_{\text{B}}} \left(\omega_x \omega_y \omega_z \right)^{1/3} \left(6N \right)^{1/3}, \tag{2.8}$$

where E_{F} is the Fermi energy. E_{F} is a central quantity since it sets the energy scale of the system. It is given by the energy to which the particles fill up the three-dimensional harmonic trap at $T = 0$. Another important quantity related to the Fermi energy is the peak angular Fermi wavenumber k_{F} (trap center) which sets the scale of the momentum in the gas.

---

[2]$\text{Li}_l(z) = \Gamma(l)^{-1} \int_0^\infty \text{d}y \, y^{l-1}/(e^y/z - 1)$ is the l-th order polylogarithm for $l \neq 0$ and $\Gamma(l)$ is the Gamma function.

[3]In our case the typical temperatures range from about one microkelvin to a few tens of nanokelvin.

[4]Typical temperatures at this stage range from about a millikelvin to a few microkelvin.

$$k_{\mathrm{F}} = \frac{\sqrt{2mE_{\mathrm{F}}}}{\hbar} \tag{2.9}$$

Since the thermodynamical properties of the gas are strongly depending on the degree of degeneracy, we will discuss a few notable cases:

- $T/T_{\mathrm{F}} \gg 1$: classical gas, $n_{\mathrm{F}}(\mathbf{r})$ follows a Gaussian density distribution, the chemical potential[5] $\mu < 0$

- $T/T_{\mathrm{F}} \approx 0.6$: crossover from thermal to degenerate quantum gas, $n_{\mathrm{F}}(\mathbf{r})$ starts to deviate from a Gaussian distribution and approaches the $T = 0$ distribution, the chemical potential $\mu \approx 0$ (see fig.2.1 d))

- $T/T_{\mathrm{F}} \ll 1$: degenerate Fermi gas, $n_{\mathrm{F}}(\mathbf{r})$ is close to the $T = 0$ density distribution, the chemical potential $\mu \approx E_{\mathrm{F}}$

- $T/T_{\mathrm{F}} = 0$: degenerate Fermi gas, $n_{\mathrm{F}}(\mathbf{r})$ is given by eq. (2.10), the chemical potential $\mu = E_{\mathrm{F}}$

As described above, the density distribution of the cloud smoothly transforms from a thermal to the $T = 0$ density distribution. At zero temperature the density distribution is given by

$$n_{\mathrm{F}}(\mathbf{r}) = \frac{8N}{\pi^2 R_{\mathrm{F}x} R_{\mathrm{F}y} R_{\mathrm{F}z}} \left[\max \left(1 - \sum_{i=1}^{3} \frac{x_i^2}{R_{\mathrm{F}i}^2}, 0 \right) \right]^{3/2} \tag{2.10}$$

with the Thomas-Fermi radius $R_{\mathrm{F}i} = \sqrt{\frac{2E_{\mathrm{F}}}{m\omega_i^2}}$. The transition from high to zero temperature regime is visualized by the density distributions in fig. 2.1 a)-c).
A widely used description of the trapped Fermi sgas is done in the framework of the so called local density approximation (LDA). Within the LDA a trapped gas is seen as a cluster of individual 3D homogeneous gas segments. Therefore, it is useful to have a look on relevant quantities for such a uniform Fermi gas. In this case $k_{\mathrm{F,u}}$ reads

$$k_{\mathrm{F,u}} = \left(6\pi^2 n \right)^{1/3}. \tag{2.11}$$

The local Fermi temperature is given by

$$T_{\mathrm{F,u}} = \frac{\hbar^2}{2mk_{\mathrm{B}}} \left(6\pi^2 n \right)^{2/3}. \tag{2.12}$$

---

[5]Please note, that the energy scale is set by E_F. The chemical potential has to be compared to the Fermi energy.
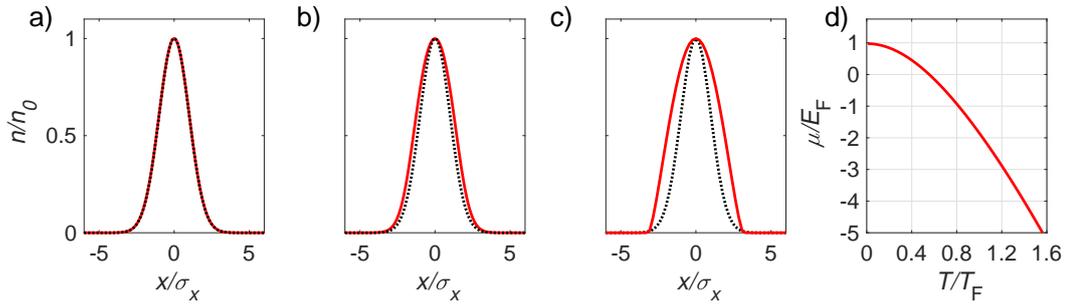
Figure 2.1: Three dimensional density distribution of a Fermi gas (red solid line) at a) $T = 1.5T_F$, b) $T = 0.4T_F$ and c) $T = 0$. In each case the density distribution for $y = z = 0$ is shown. For comparison in a) and b) a corresponding thermal distribution with width σ_x is drawn (dashed black lines). For c) the density distribution is compared to a thermal distribution at $T = 0.1T_F$ (dashed black line). For temperatures below T_F the density distribution deviates from a Gaussian distribution. d) Shows the chemical potential μ as a function of T/T_F. The chemical potential has a sign change at about $T/T_F \approx 0.6$ and approaches E_F for $T \to 0$.

Within the LDA the local density of the gas $n(\mathbf{r})$, in combination with the global temperature, gives the thermodynamical state of the cloud including quantities like the local degree of degeneracy of the gas T/T_F.

Bosons

With the two component interacting Fermi gas we are able to produce Feshbach molecules/dimers of two fermions with opposite spin state in the vicinity of a magnetic Feshbach resonance (see sec. 2.3). The dimers show Bose-statistics in the so called deep BEC regime. There, the dimer-dimer interaction is small and therefore will be neglected in the following (weakly interacting case). In the next section I will summarize a few properties of such a gas in a harmonic trap[6].

For high temperatures, the bosonic gas follows eq. (2.3) and the total particle number is given by

$$N_{th} = \left(\frac{k_B T}{\hbar \bar{\omega}}\right)^3 \text{Li}_3 \left(e^{\beta \mu}\right). \tag{2.13}$$

Reducing the temperature $T \to 0$, the bosonic nature of the dimers becomes visible. Considering weak repulsive interaction, as in some of our experiments (see sec. 2.3), the gas can Bose condense for temperatures below the critical temperature T_C, where

---

[6]For a more detailed description of trapped bosonic gases see textbooks like [85] or the review article [86].

$$T_C = 0.94 \, \hbar \bar{\omega} N^{1/3}. \tag{2.14}$$

Below this critical temperature the ground state of a harmonically trapped molecular gas is occupied macroscopically. As for standard BECs the number of condensed molecules N_C in a gas of N bosons is given by

$$N_C = N \left(1 - (T/T_C)^3 \right). \tag{2.15}$$

The transition to this state causes significant changes in the density distribution. A BEC of repulsively interacting particles in the deep BEC regime can be described with the time-independent Gross-Pitaevskii equation

$$\mu \, \psi(\mathbf{r}) = \left(-\frac{\hbar^2}{2m} \nabla^2 + V(\mathbf{r}) + g \, |\psi(\mathbf{r})|^2 \right) \psi(\mathbf{r}). \tag{2.16}$$

$g = 4\pi\hbar^2 a_{dd}/m$ is the coupling constant, a_{dd} is the scattering length (see sec. 2.3 for details) and the density is given by $n = |\psi|^2$. Here, the particle interaction is included in the framework of mean field theory, where particle interaction is mediated by the contact potential $g\delta(\mathbf{r}-\mathbf{r}')$. In this case $\mathbf{r}$ and $\mathbf{r}'$ are the coordinates of two colliding particles.

Considering expectation values, it can be shown that the kinetic term can be neglected in the Gross-Pitaevskii equation. This is known as the Thomas Fermi approximation (for further details see [43, 84, 86]).

For interacting particles the density distribution of the condensed part n_C is given by

$$n_C = \frac{15 N_C}{8\pi R_{\mathrm{B}x} R_{\mathrm{B}y} R_{\mathrm{B}z}} \max \left(1 - \sum_{i=1}^{3} \frac{x_i^2}{R_{\mathrm{B}i}^2}, 0 \right). \tag{2.17}$$

Here, $R_{\mathrm{B}i} = \sqrt{\frac{2\mu_{\mathrm{B}}}{M\omega_i^2}}$ are the Thomas Fermi radii for the spatial directions $i = x, y, z$, $M = 2m$ is the mass of the bosonic dimers and μ is the chemical potential. Within this approximation the chemical potential is given by

$$\mu = \frac{1}{2}\hbar\bar{\omega} \left(\frac{15 N_C a_{dd}}{\bar{d}} \right)^{2/5}. \tag{2.18}$$

Here $\bar{d} = (d_x d_y d_z)^{1/3} = \sqrt{\hbar/(M\bar{\omega})}$ is the geometric mean of the harmonic oscillator lengths, which are given by $d_i = \sqrt{\hbar/(M\omega_i)}$ with $i = \{x, y, z\}$. Using the chemical potential we can compute the Thomas Fermi radii

$$R_{\mathrm{B}i} = d_i \sqrt{\frac{\bar{\omega}}{\omega_i}} \left(\frac{15 N_C a_{dd}}{\bar{d}} \right)^{1/5}. \tag{2.19}$$

For a cloud at $0 < T < T_C$ we find a bimodal distribution with a condensed core following eq. (2.17) and a thermal wing at the edges which follows eq. (2.3).

For comparison, a non-interacting condensate in a harmonic trap would follow a Gaussian distribution, where the variance is given by the harmonic oscillator length. This directly shows how crucial particle interaction is in such a gas is. In the following section I will briefly discuss the impact of particle interaction on ultracold gases.

2.2 Elastic particle scattering

Particle interaction plays a crucial role for the thermodynamical state of an ultra-cold gas. In an interacting gas, the particles undergo a variety of collisional events. As a starting point for a further description I will shortly summarize a few aspects of scattering theory following refs. [85, 87, 88].

I start the discussion considering the elastic collision of two distinguishable particles in relative coordinates. The center-of-mass motion of the two objects is given by a plane wave $\psi_{in} \propto e^{i\mathbf{kr}}$. The center-of-mass and the relative motion both obey the Schrödinger equation. For colliding particles the wave function ψ is a superposition of an incoming plane wave, in the case of large interatomic separation, and an outgoing spherical wave

$$\psi \propto e^{ikz} + f(\theta,k)\frac{e^{ikr}}{r}.$$ (2.20)

Here, we consider a collision along the z-direction. f is the scattering amplitude, k is the angular wave number and θ is the collision angle. For spherical symmetric interaction, we can obtain the scattering amplitude via partial wave expansion

$$f(\theta,k) = \frac{1}{2ik}\sum_{l=0}^{\infty}(2l+1)\left(e^{2i\delta_l(k)} - 1\right)P_l(\cos\theta).$$ (2.21)

Here, l is the partial wave index equivalent to the quantum number of the orbital angular momentum, $\delta_l(k)$ are the phase shifts of the outgoing waves and P_l are Legendre polynomials.

The scattering amplitude can now be connected to the scattering cross section σ via

$$\frac{d\sigma(k)}{d\Omega} = |f(\theta,k)|^2,$$ (2.22)

with the solid angle Ω. With this, the scattering cross section can be computed in the partial wave expansion, which yields

$$\sigma(k) = \frac{4\pi}{k^2} \sum_{l=0}^{\infty} (2l+1)\sin^2 \delta_l(k). \tag{2.23}$$

In the case of small collision energies, which are given for ultracold collisions, centrifugal barriers cannot be overcome. Therefore, for $k \to 0$ s-wave collisions with $l = 0$ are contributing to the scattering amplitude solely and we get

$$f(k) = -\frac{a}{1+ika}. \tag{2.24}$$

using eq. (2.21). Here, a is the s-wave scattering length

$$a = \lim_{k \ll 1/r_0} -\frac{\tan(\delta_0)}{k} \tag{2.25}$$

and r_0 is the range of the interaction potential. Inserting eq. (2.24) in eq. (2.22) we obtain a cross section of

$$\sigma(k) = \frac{4\pi a^2}{1+k^2 a^2}. \tag{2.26}$$

For $ka \ll 1$, which is the case in the BEC regime (see sec. 2.5) of the Feshbach resonance and low temperatures of a few microkelvin, we get

$$\sigma(k) = 4\pi a^2 \tag{2.27}$$

for two distinguishable particles. For a collision of two identical bosons, the scattering amplitudes of the particles add up and the scattering cross section reads

$$\sigma(k)_{id,B} = 8\pi a^2. \tag{2.28}$$

For identical fermions the s-wave scattering cross section cancels, i.e. $\sigma(k)_{id,F} = 0$, in agreement with the Pauli principle. The collision of two identical fermions is limited to partial waves with odd numbers exclusively. However, close to quantum degeneracy collisions with $l > 0$ are absent and a gas of fermions in a single state is essentially non-interacting due to the centrifugal barrier. This limitation can be overcome in collisions between atoms in different internal states, which is the case in a mixture of fermions in two different spin states. In such a gas s-wave collisions are possible.

Therefore, in our experiments we use a balanced gas of ^{6}Li-atoms, i.e. an incoherent 50:50 mixture of lithium atoms in the lowest two hyperfine states. The particle interaction for fermions in opposite spin states can be tuned by means of a magnetic Feshbach resonance. A few basic concepts of such resonances in two particle collisions will be introduced in the next section.

2.3 Feshbach resonances and the special case of ^{6}Li

In recent years magnetic Feshbach resonances have turned out to be an ideal tool to tune the particle interaction in two-body collisions in the ultracold regime. In the experiments presented in this thesis we make use of this tool as well. Therefore, I will give a brief summary on the magnetic Feshbach resonances using a few basic concepts. The description used here is based on [5, 85, 89].

At a Feshbach resonance the collision of two particles with a collision energy E can be described in the framework of a two-channel model. To do so, we consider two molecular potential curves (see fig. 2.2). The first one describes the collision of free particles for large internuclear distances R which is denoted by V_{bg} and refereed to as the open or entrance channel. The second channel is the so called closed channel, which describes a state addressed within the Feshbach association. Here, the potential curve V_c for two neutral atoms is given by the van der Waals potential with $V_c \propto R^{-6}$. For a finite coupling between these two channels a resonance of continuum and bound states can be found. There, the asymptote of the open channel (for small E) approaches a bound state E_c in the closed channel.

In the case of a magnetic Feshbach resonance the energy offset between the two channels is tuned by an offset magnetic field. This is possible since the magnetic moments of the particles in the two channels typically differ by a value $\delta\mu$.

From a collisional point of view the magnetic field influences an appearing phase shift (see previous section) of the atomic wave function at the s-wave collision. This effect is quantified by the s-wave scattering length a. According to ref. [90] the magnetic field B and the s-wave scattering length a are connected via

$$a = a_{bg}\left(1 - \frac{\Delta}{B - B_0}\right). \tag{2.29}$$

Here, a_{bg} is the background scattering length, Δ is the width and B_0 the position of the resonance. The width is given by the zero crossing of the scattering length with respect to the magnetic field. The sign of the scattering length indicates if an interaction is attractive ($a < 0$) or repulsive ($a > 0$). Additionally, the statistical properties of the gas change with the sign of the scattering length. The regime with $a > 0$ is called the BEC side of the resonance, where, in the case of ^{6}Li, bosonic dimers of two atoms in opposite spin states can be produced. This is in contrast to $a < 0$, the so called BCS[7] side, where Cooper pairs[8] can be produced.

We use this feature in the experiments to produce bosonic molecules of two atoms in the most weakly bound state of the relevant molecular potential (Feshbach mol-

---

[7]BCS: Bardeen-Cooper-Schrieffer

[8]This is only fully true in the deep BCS regime of $a \to 0^-$. Close to resonance the pairing mechanism is more complicated (see sec. 2.5).

a)

b)
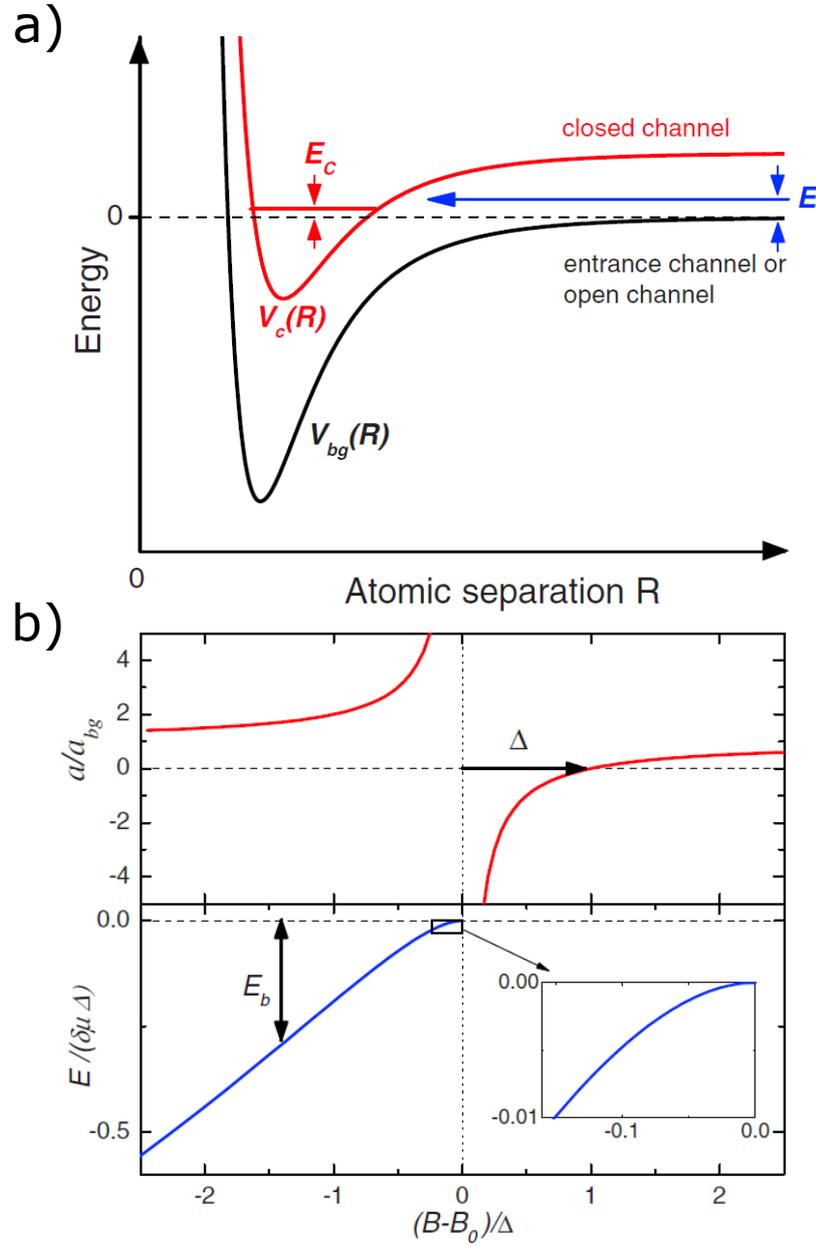
Figure 2.2: Two channel description of a magnetic Feshbach resonance. a) Entrance/open and closed channel V_{bg} and V_c respectively, as a function of the internuclear distance R. The collision energy of two particles is close to the asymptote of the open channel in the case of ultracold collisions ($E \approx 0$). If the asymptote and a bound state with energy E_c approach each other, the colliding particles can be transferred into a bound state within the closed channel, in case of non-vanishing coupling of the channels. b) The relative energy of the two channels and the scattering length can be tuned via an offset magnetic field (see [90]). The upper curve shows the s-wave scattering length a as a function of B in the vicinity of the resonance at B_0 (see eq. (2.29)). The lower graph shows the universal connection of the binding energy E_b with the B-field (see eq. (2.30)). Picture taken from [5].
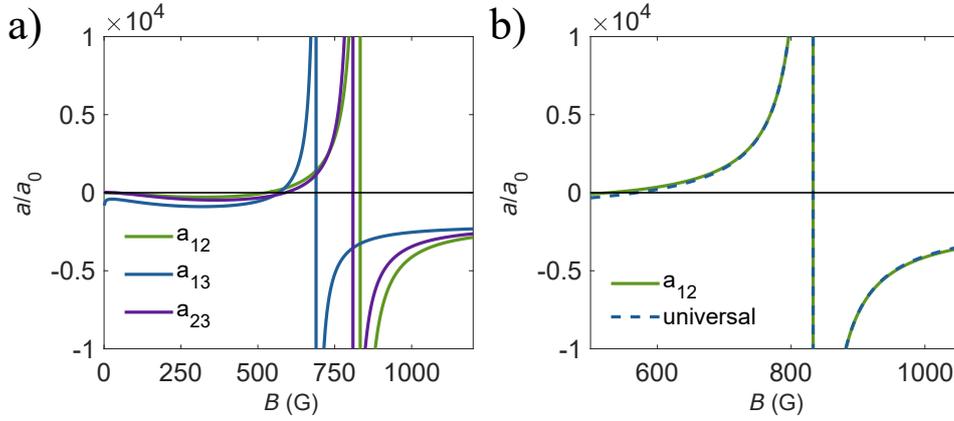
Figure 2.3: Feshbach resonance of ^{6}Li. At high magnetic field the two lowest hyperfine states split into six states marked by the indices 1 to 6 as given in fig. 2.4 (see also sec. 2.4). a) Scattering length as a function of the B-field for the s-wave collision of particles in the $|1\rangle$ and $|2\rangle$ (index 12), the $|2\rangle$ and $|3\rangle$ (index 23), and the $|1\rangle$ and $|3\rangle$ (index 13) states (data taken from ref. [91]). b) Scattering length to the $|12\rangle$ collision in the vicinity of the broad Feshbach resonance (data taken from ref. [91]). For comparison the universal relation of eq. (2.29) is shown. It deviates from the measured values for $|B - B_0| \gtrsim \Delta B$.

ecule). The binding energy of a Feshbach dimer shows a strong magnetic field dependence and can be approximated by the universal relation

$$E_b = -\frac{\hbar^2}{2\mu a^2} \tag{2.30}$$

in the vicinity of the resonance. Here, the reduced mass $\mu = m_1 m_2/(m_1 + m_2)$, with m_i being the masses of the colliding particles, is introduced. In our case it reads $\mu = m_2$, since $m_1 = m_2 = m$.

Specifically, we use the broad magnetic Feshbach resonance of ^{6}Li (see fig. 2.3) located at $B_0 = 832.2\,$G, with $\Delta = -262.3\,$G and $a_{bg} = -1582 a_0$ for particles in the states $|1\rangle$ and $|2\rangle$ [91]. Here, a_0 is the Bohr radius.

On the deeper BEC side of the resonance, where $a \rightarrow^+ 0$, the binding energy starts to deviate from eq. (2.30). Introducing corrections for the potential of the closed channel the binding energy can be computed using [92, 93]

$$E_b = -\frac{\hbar^2}{m(a - \bar{a})^2}\left(1 + 2.92\frac{\bar{a}}{a - \bar{a}} - 0.95\frac{\bar{a}^2}{(a - \bar{a})^2}\right). \tag{2.31}$$

Here $\bar{a} = 29.9 a_0$ is the characteristic length scale of the van der Waals potential. It is important to note that the binding energy is only related to the bound states

in the two-body picture. This implies that the binding energy of two atoms drops to zero at the resonance and particles are in continuum states (neglecting trapping potentials) for $a < 0$. This is true for the association of diatomic molecules, e.g. produced using a magnetic field ramp across the resonance (see e.g. [5]).

However, in the case of fermionic atoms and for $T \ll T_F$ a Fermi gas shows a non-vanishing binding energy for $a < 0$ (see [94]). The appearance of bound states close and above the Feshbach resonance ($B \approx B_0$ and $B > B_0$) is a consequence of many-body effects. This includes preformed pairs close to resonance for $T > T_C$, as well as Cooper pairing which occurs below T_C in the BCS regime.

2.4 Lithium at high magnetic field

Most of the experiments reported in this thesis are performed using strongly inter-acting ^{6}Li atoms. The lithium atoms are prepared in the two lowest hyperfine states of the electronic ground state. This state is doubly degenerate (with $F = 1/2$) and splits to the $|1\rangle = |2^2\mathrm{S}, m_F = -1/2\rangle$ and $|2\rangle = |2^2\mathrm{S}, m_F = 1/2\rangle$ in the presence of an external magnetic field.

To achieve strong particle interaction the external B-field is tuned to the broad magnetic Feshbach resonance at 832.2 G. For ^{6}Li, which has a small nuclear charge, magnetic fields $B \gtrsim 100$ G have notable influence on the coupling of electronic and nuclear spins. At such fields pure hyperfine coupling does not describe the behavior of the lithium atoms properly anymore, such that F is no longer a good quantum number and the states are defined by the total electronic angular momentum quantum number J and the nuclear spin quantum number I. This regime is called the Back-Goudsmit regime or the Paschen-Back regime of the hyperfine states. The term scheme of the electronic ground state sublevels in this regime can be computed using the Breit-Rabi formula [95, 96], valid for $J = 1/2$

$$E_{\mathrm{F=I\pm1/2}} = -\frac{\Delta E_0}{4(I+1/2)} + m_\mathrm{F} g_\mathrm{I} \mu_\mathrm{I} B \pm \Delta E_0/2 \left(1 + \frac{4m_\mathrm{F}}{2I+1}x + x^2\right)^{1/2}. \quad (2.32)$$

Here $\Delta E_0 = 228.2$ MHz $\times h$ is the hyperfine splitting (HFS) at $B = 0$, m_F is the projection on the quantization axis, g_I (g_J) is the g-factor of the nucleus (spin-orbit coupling), μ_B is the Bohr magneton and $x = (g_\mathrm{J}\mu_\mathrm{B} - g_\mathrm{I}\mu_\mathrm{I})/\Delta E_0$. ^{6}Li has $I = 1$ which leads to a sixfold splitting of the $2^2\mathrm{S}_{1/2}$ state (see fig. 2.4).

For small $B \ll 100$ G the atoms are in the Zeeman regime, and the energy splitting of the hyperfine states increases almost linearly with the magnetic field. At larger B-field, the Back-Goudsmit regime is entered, where the nucleus and the atomic shell decouple. At fields close to the Feshbach resonance $|2\rangle$ becomes a high field and $|4\rangle$ a low field seeking state, respectively. In our case, the particles are loaded
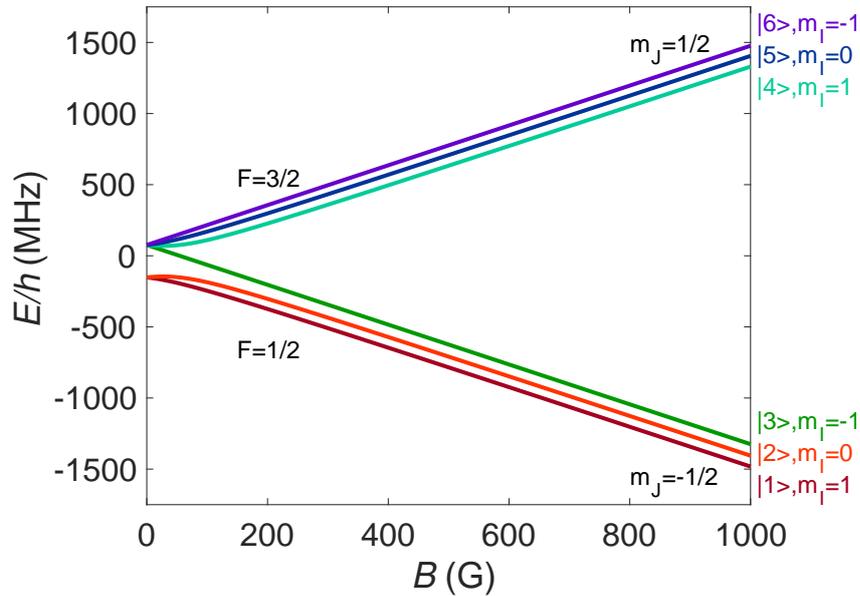
Figure 2.4: Term scheme of the $2^2S_{1/2}$ states from zero to high magnetic field. We find a sixfold splitting of the electronic ground state labelled from bottom to top by $|1\rangle - |6\rangle$.

to the $|1\rangle, |2\rangle$ states, which means that all particles are high field seekers. This simplifies the particle trapping especially when offset magnetic fields are present. Experimentally, we use this property to produce a trapping potential in two spatial directions for the particles using a bias magnetic field[9].

2.5 Phase diagram in the vicinity of the Feshbach resonance

In our experiments we prepare a gas of lithium atoms in the two lowest hyperfine states. By tuning the particle interaction by means of the broad magnetic Feshbach resonance we find different phases. For strong repulsive interaction and low temperatures Feshbach molecules form, while for strong attractive interaction below a critical temperature Cooper pairs are produced.

The phase diagram of such a gas is illustrated in fig. 2.5. The temperature axis in the diagram is given in units of the Fermi temperature T/T_{F}, which scales the thermal energy to the natural energy scale of the Fermi gas $E_F = k_B T_F$. On the horizontal axis the particle interaction is drawn. It is given by $(k_{\mathrm{F}}a)^{-1}$, where the scattering length is scaled by the particle density or interparticle distance[10]. For

---

[9]According to Wing's theorem a local field maximum in free space is not possible [97].

[10]According to eq. (2.11) $k_f \propto n^{1/3}$ and therefore linearly depending on the interparticle distance

simplicity, I will discuss the different regions of the phase diagram separately in the following.

From the BEC limit to the crossover $(1 \lesssim (k_\mathrm{F}a)^{-1} < \infty)$

The description starts on the deep BEC side or BEC limit, where $(k_\mathrm{F}a)^{-1} \gg 1$. In this regime diatomic molecules form by exothermic three-body collisions. In the three-body process two of the colliding particles (in opposite spin states) form a molecule, while the third particle assures energy and momentum conservation. In our case, either most weakly [100] $|\mathrm{X}^1\Sigma_g^+, v = 38\rangle$ or more deeply bound dimers (*here:* $|\mathrm{X}^1\Sigma_g^+, v < 38\rangle$) can be produced. Here, v is the vibrational quantum number of the molecular potential. However, only for the most weakly bound molecules the released energy is small enough that the associated molecules remain trapped. The molecule fraction in the gas is highly temperature dependent (see refs. [98, 99]). The range where dimers can be found is sketched in fig. 2.5. For this, the temperature for a molecule contribution of 50% is drawn (see e.g. [86, 101]).
The Feshbach dimers can interact via elastic scattering with both, unbound atoms and other dimers. The collision is characterized by the atom-dimer a_{ad} and the dimer-dimer scattering length a_{dd} for a large internuclear distance, respectively [42, 43, 102, 103]

$$a_{ad} = 1.18a \qquad\qquad a_{dd} = 0.6a. \qquad (2.33)$$

Besides elastic scattering, a gas of Feshbach dimers can undergo inelastic collisions. Since the dimers are produced in the most weakly bound state, a collision of a dimer with a free atom or another dimer can cause a decay to a deeper bound state. In the case of ^{6}Li, such a relaxation features release energies on the order of a few Kelvin. This energy is orders of magnitude larger than the typical trap depth in our (or typical atomic) experiments and therefore inelastic collisions lead to particle losses. The rate constants of such a relaxation are given by [42, 43, 104]

$$\Gamma_{ad} = C\frac{\hbar r_\mathrm{e}}{m}\left(\frac{a}{r_\mathrm{e}}\right)^{-3.33} \qquad\qquad \Gamma_{dd} = C\frac{\hbar r_\mathrm{e}}{m}\left(\frac{a}{r_\mathrm{e}}\right)^{-2.55} \qquad (2.34)$$

with a non-universal constant C which specifically depends on the properties of the species, and the characteristic range of the potential r_e. For ^{6}Li the constant is $C \approx 10^{-15}$ [88]. Equation (2.34) shows that a gas of dimers in the BEC regime has only limited stability. This complicates the production of long-lived dimers especially at high phase space densities. At low temperatures, such as $T \ll T_F$, the molecule contribution in the gas approaches unity[11] and the molecule density

---

[11]Molecule contribution: $2M/N$, where M is the number of molecules and N is the total number of atoms in both spin states. The factor 2 accounts for the two particles forming the dimer.
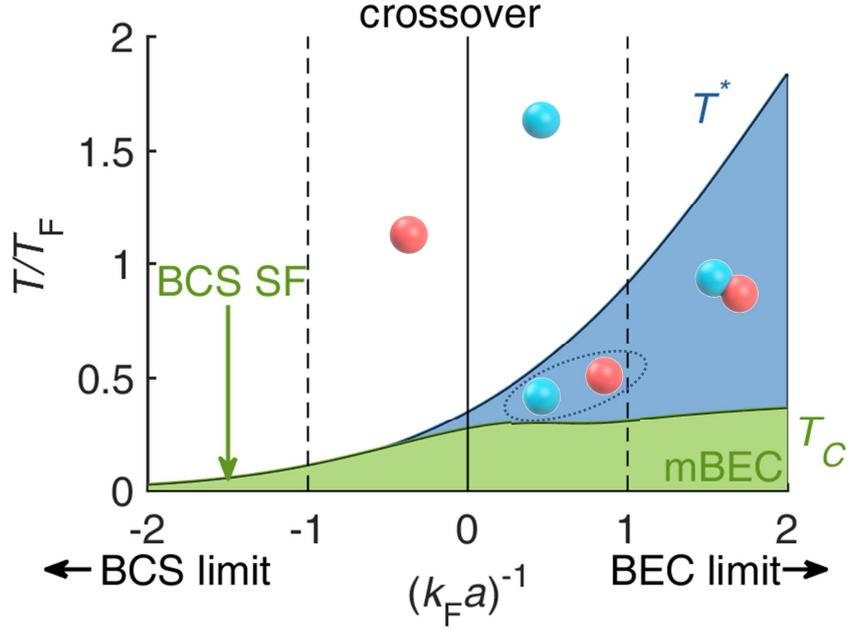
Figure 2.5: Sketch of the phase diagram of a two component gas of ^{6}Li atoms in the vicinity of a Feshbach resonance. The temperature is given in units of the Fermi temperature. The horizontal axis is the reciprocal value of the dimensionless quantity $k_F a$, defining the particle interaction. $(k_F a)^{-1} > 0$ corresponds to the BEC side of the resonance. T^* (blue curve) marks the temperature where 50% of all possible dimers are formed on the BEC side (see also refs. [98, 99]), while T^* approaches the critical temperature T_C (green curve) on the BCS side. Close to resonance T^* interpolates between the regimes. Close to unitarity $((k_F a)^{-1} = 0)$ the thermodynamics of the gas change and pairs are no longer pure two-body objects. The gas is strongly influenced by the fermionic nature of the particles and many body effects contribute to the pairing mechanism. $(k_F a)^{-1} < 0$ represents the BCS side. There, pairing is mainly a many body phenomenon. In the limiting case of $(k_F a)^{-1} \ll -1$ the pairs are Cooper pairs.

increases. The loss rate scales with the molecule density squared such that the particle losses in a harmonically confined gas above T_C scale as

$$\dot{M} = -(4\pi)^{-3/2}\Gamma_{dd}\frac{M^2}{\sigma_x\sigma_y\sigma_z}. \tag{2.35}$$

Here, σ_i are the widths (standard deviations) of the thermal cloud in the three spatial directions.

However, approaching the crossover regime $(k_F a)^{-1} \approx 1$ the dimers are more weakly bound such that the fermionic nature of the particle plays a role. With this, the Pauli exclusion principle leads to a suppression of relaxation collisions [40]. Close to the crossover the lifetime of the gas is on the order of 10s or more, which allows us to cool the gas to temperatures $T < T_C$ and to produce a molecular BEC (mBEC).

The crossover and unitarity $(-1 < (k_F a)^{-1} < 1)$

Approaching the crossover regime from the BEC side, the character of the gas changes. The gas smoothly converts from an ensemble of bosonic dimers for temperatures below T_C to a Fermi liquid on the BCS side. In the crossover, properties of both regimes can be found in the gas. Specifically, on the BCS side the singlet contribution of a pair is non-vanishing [105] which is typically the case for diatomic molecules on the BEC side. Equally, the Tan's contact, which is a measure for short range correlations, does not drop to zero at resonance as well [106]. This is in contrast to the BCS type of pairing where particles with opposite momentum are correlated.

On the other side, a Fermi liquid behavior of the gas can be found on the BEC side as well. This has been investigated with photoemission spectroscopy (PES) from which the dispersion relation of the ensemble can be obtained [106]. A Fermi liquid typically shows a sharp quadratic dispersion (quasiparticle dispersion), while a Bose gas shows an incoherent spectrum. Using PES measurements indications for a quasiparticle dispersion can be found on the BEC side of the resonance showing the Fermi character of the gas even for $a > 0$.

This implies how non-trivial the state of the gas in the intermediate regime is. To describe the properties several studies have been performed to describe the phases of the gas. A special focus lies on the resonance where the scattering length diverges and the gas shows universal behavior. To characterize the thermodynamical state of the gas on the resonance the equation of state has been measured [107, 108].

However, so far a full description of the gas in the crossover is absent. To add valuable information to the phase diagram, we have performed pair fraction measurements in the crossover regime to map out the thermal/chemical equilibrium of the gas in this intermediate regime (for more details see appendix A.2 or [99]). In

this framework we were able to show that a classical statistics description of the atom-molecule equilibrium holds for the BEC regime and describes our data even in the vicinity of the resonance (BEC side) with reasonable accuracy.

From the crossover to the BCS regime $(-\infty < (k_\mathrm{F}a)^{-1} \lesssim -1)$

In the BCS regime Fermi statistics dominate and the normal state of the gas can be well described within the Fermi liquid theory [106]. Additionally, the Fermi gas character has crucial consequences for the pairing mechanism. In this regime pairing appears only below the critical temperature $T < T_C$, where Cooper pairs establish [85, 86, 103] and the gas can be described within BCS theory. The pairs consist of two fermions in the $|1\rangle$ and $|2\rangle$ state and have opposite momentum. In this state the gas shows an excitation gap Δ (see e.g. ref. [86]) which reads

$$\Delta \approx \frac{8}{e^2} e^{-\pi/2k_\mathrm{F}|a|}. \tag{2.36}$$

The superfluid transition temperature can be computed using upper gap equation and the number equation as in BCS theory[12]. With this the superfluid transition temperature reads,

$$T_C \approx \frac{1.93}{k_\mathrm{B}\pi} E_\mathrm{F} \exp\left(\frac{\pi}{2k_\mathrm{F}|a|}\right). \tag{2.37}$$

However, the pairs do not exclusively show the attributes of many-body pairing. As mentioned in previous subsection even for $1/(k_F a) < -1$ the pairs show a non-vanishing closed channel contribution [105, 109] similar as for diatomic molecules in the BEC regime.

2.6 Sound excitation in a partially superfluid gas in the vicinity of a Feshbach resonance

In the previous section I have introduced the phase diagram of a two component Fermi gas in the vicinity of a broad magnetic Feshbach resonance. Within the description, it has been mentioned that a superfluid phase can be found throughout the resonance for $T < T_C$.
The superfluid phase in the vicinity of the broad Feshbach resonance is exceptional since two different types of superfluids can be found across the resonance. We find a BEC of molecules for non-resonant repulsive interaction on one side and a BCS type superfluid in the BCS regime on the other side. Especially, the intermediate regime is of interest since the gas undergoes a crossover from one type to the other.

---

[12]For more information on BCS type pairing in ultracold Fermi gases see e.g. [86, 94].

To shed additional light on this regime, we study the superfluidity in this regime within this work.

One way to do this is to perform excitation experiments. The response of the gas on the perturbation gives deeper insight into the thermodynamics of the system. In the past years a multitude of studies on the excitation of superfluid gases have been performed using different types of excitation protocols. This includes studies on vortex excitation [60], laser stirring [110], Bragg spectroscopy [111–114], and experiments on second sound [53].

Especially, sound experiments are also in the focus of this work (see also sec. 2.5). One reason for this is the fact that second sound, an entropy wave, gives access to the local superfluid density of the gas. Within this thesis a study on sound propagation has been carried out in order to investigate the superfluid phase of a Fermi gas across the Feshbach resonance.

In our experiment we use a local perturbation to excite first and second sound modes. First sound is the well known pressure wave, which propagates at constant entropy, while second sound is an entropy wave propagating at constant pressure. Measuring the two sound modes enables us in principle to reconstruct the local superfluid density of a partially superfluid gas in a harmonic trap.

In the following lines I will summarize a few basic thermodynamic equations relevant to calculate the sound velocities. The full description can be found e.g. in ref. [85]. The theoretical description to the second sound can be done using Landau's two-fluid model (the following summary is based on refs. [82, 85, 115]). In the two fluid model we assume that the gas consists of a super- and normal-fluid part. Under this assumption classical thermodynamical relations for the two components can be derived. For this, I will consider a frictionless flow and the absence of an external potential.

In this context, the first relevant equation is the continuity relation

$$\frac{\partial \rho}{\partial t} + \nabla \mathbf{j} = 0, \tag{2.38}$$

where $\rho = \rho_\mathrm{s} + \rho_\mathrm{n}$ is the mass density, $\mathbf{j} = n_\mathrm{s}\mathbf{v}_\mathrm{s} + n_\mathrm{n}\mathbf{v}_\mathrm{n}$ the particle current density, and n_i and v_i with $i = \{\mathrm{s},\mathrm{n}\}$ are the densities and velocities in the superfluid and normal fluid part, respectively. The second relevant quantity is the particle current density which is connected to the pressure p via

$$\frac{\partial \mathbf{j}}{\partial t} = -\nabla p. \tag{2.39}$$

From equations (2.38) and (2.39) a wave equation can be obtained

$$\frac{\partial^2 \rho}{\partial^2 t} - \nabla^2 p = 0. \tag{2.40}$$

Another important eq. is the equation of motion for the superfluid part. For an

absent external potential, and neglecting non-linear contributions the superfluid velocity is given by the chemical potential μ via

$$\frac{m\partial \mathbf{v_s}}{\partial t} = -\nabla \mu \tag{2.41}$$

with the particle mass m.

This very generic description of the gas (including Maxwell relations) is sufficient to calculate the sound velocity in the two component gas for small perturbations. There, the variations in the density $\delta\rho$, pressure δp, temperature δT, and entropy δs are small and resulting modulations propagate as plane waves $e^{i(\mathbf{kr}-\omega t)}$. Using

$$c_T^2 = \left(\frac{\partial p}{\partial \rho}\right)_T, \quad c_2^2 = \frac{\rho_s}{\rho_n}\frac{s^2 T}{c_V}, \quad c_V = T\left(\frac{\partial s}{\partial T}\right)_\rho, \quad c_3^2 = \left(\frac{\partial s}{\partial \rho}\right)_T^2 \frac{\rho^2 T}{c_V} \tag{2.42}$$

the sound speeds is calculated. Here, c_V is the heat capacity per unit mass, $s = S/(Nm)$ is the entropy per particle, where the total entropy is S, and N is the particle number. The sound speeds reads,

$$u_{1/2}^2 = \frac{1}{2}\left(c_T^2 + c_2^2 + c_3^2\right) \pm \left[\frac{1}{4}\left(c_T^2 + c_2^2 + c_3^2\right)^2 - c_T^2 c_2^2\right]^{1/2}. \tag{2.43}$$

Here u_1 is the speed of the first and u_2 the speed of the second sound, respectively. However, this description uses rather abstract thermodynamical relations. Since we focus on the crossover from the BEC to the BCS regime in the experiments, it is convenient to evaluate eq. 2.43 in the limiting cases. In the following, I will summarize the results of corresponding calculations. A detailed description of the sound speeds in the BEC, BCS, and unitary regimes are presented in sec. 6 (see also ref. [82]).

For a BEC close to zero temperature and with $k_B T \ll gn$, the sound speeds are given by[13]

$$u_1 = \sqrt{\frac{g\rho}{m^2}}, \qquad u_2 = \sqrt{\frac{g\rho_s}{3m^2}}. \tag{2.44}$$

Equation (2.44) shows that both sound modes are only depending on the local densities (ρ_s and ρ_n), which makes sound excitation measurements ideal to investigate the state of the gas and its thermodynamical properties. For a better handling equation (2.44) can be written in Fermi gas related quantities

---

[13]Please note that the description presented in the following lines is only valid for a homogeneous gas.

$$u_1 = v_F \sqrt{\frac{k_F a}{10\pi}}, \qquad\qquad u_2 = v_F \sqrt{\frac{k_F a}{30\pi}}. \qquad\qquad (2.45)$$

Here, the Fermi velocity $v_F = \hbar k_F / m$ is used.

In the BCS regime, we combine hydrodynamics and the BCS theory, which gives

$$u_1 = \frac{v_F}{\sqrt{3}} \sqrt{1 + \frac{2k_F a}{\pi} + \frac{88 - 16\ln(2)}{15\pi^2}(k_F a)^2}. \quad u_2 = \frac{\sqrt{3}}{2}\frac{k_B T}{E_F} v_F \qquad (2.46)$$

Especially the result for the second sound velocity is remarkable, since it scales with the temperature of the gas and drops to zero for $T \to 0$. This is in contrast to the BEC limit, where the speed of second sound (for fixed particle numbers) has its maximum for $T \to 0$.

At unitarity the speeds of sound can be estimated using quantum Monte Carlo calculations for the first sound and considering BCS theory for the second sound. Using such an approach the second sound is given by the result of (2.46) and the first sound reads [82]

$$u_1 \approx 0.37\, v_F. \qquad\qquad (2.47)$$

3 Experimental setup

In order to investigate degenerate fermionic quantum gases and many-body physics in optical lattices we started to set up a new experiment in the course of my thesis. We decided to build an apparatus with ^{6}Li [116, 117]. The chosen species provides a broad magnetic Feshbach resonance [91, 118] which makes the particle interaction easy to control. Moreover, the chosen species facilitates extensive studies on both, long-lived bosonic Feshbach dimers [8, 13, 14] and degenerate Fermi gases [94, 119–121]. Our assembly follows the setups in Innsbruck and Heidelberg (see refs. [116, 117]) which have proven to be reliable, robust, and simple in the basic conception [88]. In the following chapter I will introduce the setup in Ulm and will describe the main components of our experiment.

More and detailed information on implemented devices can also be found in several master's theses [122–126] and in the PhD thesis of Thomas Paintner (under preparation).

3.1 Vacuum system

In general, experiments with degenerate quantum gases are performed in ultra high vacuum (UHV). This is needed to enable cooling and trapping of atoms which are prerequisites to reach the ultracold regime. Without the isolation from ambient environmental conditions a pre-cooled trapped gas would be unstable due to collisions with room temperature ambient gas. At UHV the lifetime of an ultracold gas can be easily extended to minutes, which is enough to perform experiments in the regime of quantum degeneracy. In fig. 3.1 our realization of such an UHV system is illustrated.

The setup has two main parts: the oven-chamber and the experimental chamber. The oven-chamber (marked by the red text) consists of the oven loaded with enriched[1] ^{6}Li, a titanium sublimation pump (TiSub) inside a cylindrical chamber and an ion getter pump (IGP) with a pump volume of $40\,\mathrm{l/s}$ (Agilent VacIon Plus 40). In the oven-chamber we reach a background pressure of $p_{oven} = 7.0 \times 10^{-10}\,\mathrm{mbar}$ (measured via the current at the IGP) which is too high for sufficient lifetimes of cooled and trapped atoms. Therefore, the initial trapping of the pre-cooled particles is done in the experimental chamber where the background pressure is roughly two to three orders of magnitude lower as in the oven-chamber (blue text in fig. 3.1).

---

[1]Here, the enriched lithium consists of 95 atomic percent ^{6}Li and about 5 atomic percent ^{7}Li.

a)

b)
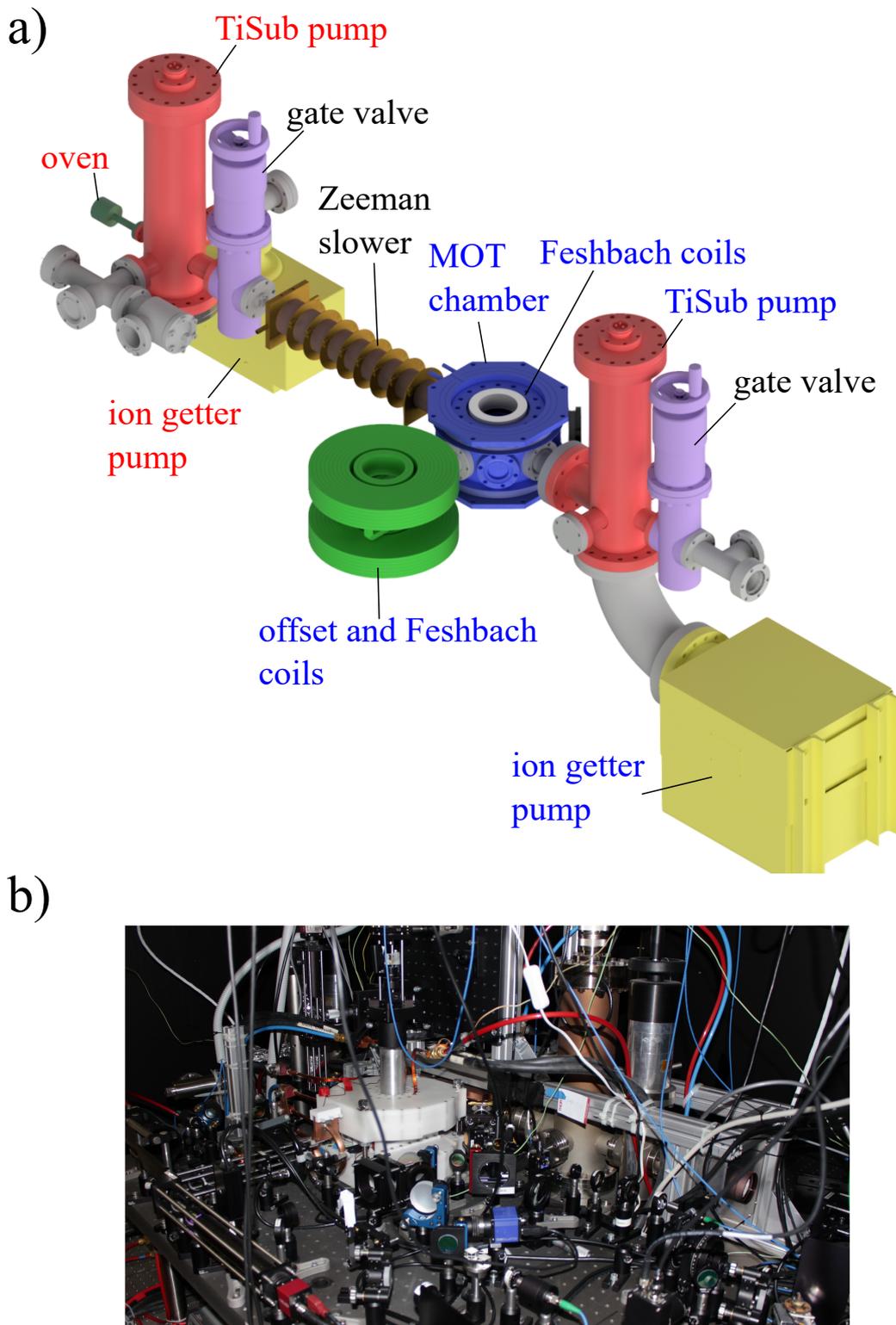
Figure 3.1: Experimental setup. a) Drawing of the setup. The system consists
of two parts, the oven-chamber (red text color) and the experimental
chamber (blue text color). The two parts are connected by a differential
pumping tube (enclosed by the Zeeman slower). Detailed descriptions
of the sub-parts can be found in the text. b) Photography of the real
system. The perspective matches the perspective of the drawing in a).
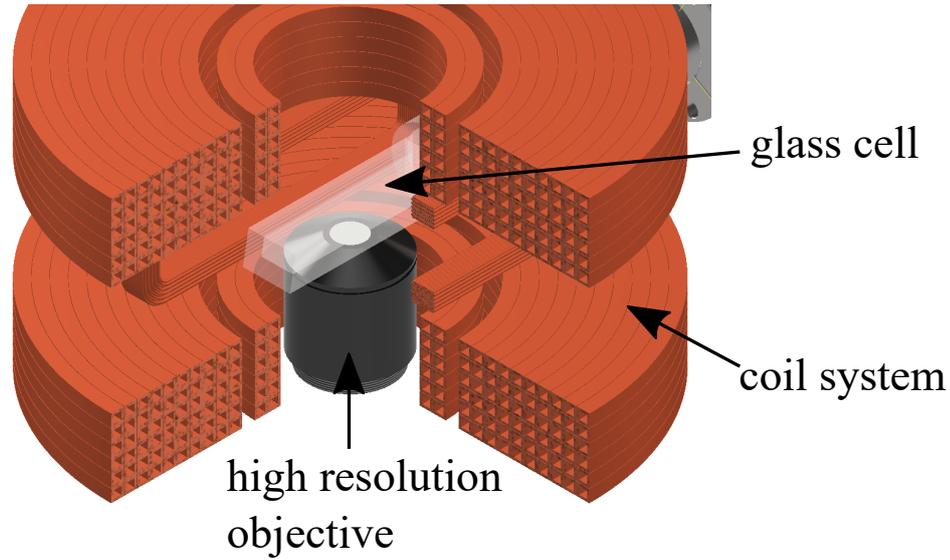
Figure 3.2: Glass cell and coil system. Three quarter section view of the coil system around the glass cell (for details see sec. 3.4). A high resolution objective is placed about 1 mm below the glass cell.

The experimental chamber is connected via a gate valve and a differential pumping tube (enclosed by the Zeeman slower in fig. 3.1) to the oven-chamber. This type of connection has two advantages. First, the valve enables us to open the oven-chamber without venting the experimental chamber, e.g. in order to refill the oven with lithium. Second, the differential pumping tube provides a pressure gradient of up to three orders of magnitude between experimental and oven-chamber. This way the experimental chamber can be pumped to $p_{exp} \approx 10^{-12}$ mbar using a continuously activated IGP with a pump volume of 150 l/s (Agilent VacIon Plus 150). This configuration facilitates lifetimes on the order of minutes for trapped atoms.

The experimental chamber consists of the MOT chamber, which is a spherical octagon from Kimball physics (MCF600-SphOct-F2C8) with view ports from Torr Scientific (VPZ38QWAR-LN), a glass cell of Hellma Analytics attached to the octagon (see fig. 3.2), a TiSub pump in a cylindrical chamber, and an IGP. In the running experiment the atoms are pre-cooled in the Zeeman slower and are trapped in the MOT chamber. For experiments, the atoms are transported to the glass cell subsequently (see fig. 3.2). The glass cell is used as a science chamber and provides excellent optical access. With this, we were able to implement a high-resolution imaging system outside the vacuum (see sec. 3.7). For the control of the scattering length a (particle interaction) and to produce field gradients, the glass cell is surrounded by a set of magnetic field coils, such as the Feshbach coils and several offset coils (coil parameters can be found in section 3.4).

3.2 Control system

Our experiment is designed to provide continuous operation and a centralized control of all experimental devices. To do so, we implemented an ADwin-Pro-II of Jäger Messtechnik (ADwin) as the main control unit of the setup. It consists of a $19''$ rack with a 300 MHz TigerSharc ADSP-TS101S (T11) main processor and multiple slide-modules. Alongside, storing and managing of experimental sequences the control unit allows us to send digital and analog signals to external devices (see fig. 3.3) using the additional modules. The latter include four analog output cards (Pro II-AOut-8/16-B), two digital output cards (DIO-32), an external co-processor card (Pro II-DIO-32-TiCo) with a 32-Bit digital output and two multi-input-output cards[2] (MIO, Pro II-MIO-4).

To control the experiment remotely, sequences are programmed on an external PC using a NI LabVIEW based User-Interface. Once an experimental sequence is programmed as an array of commands and execution times, the input is transferred to the ADwin unit. Within an experimental cycle (run) the main processor of the control unit distributes the commands to the slide-modules which send the demanded signals at the demanded time. This includes analog set values (e.g. current control of power supplies), trigger signals (e.g. camera triggers) and the control of external devices via a bus system (e.g. direct-digital-synthesizers). The time resolution in the sequence lists is limited to $10\,\mu$s and is mainly given by the main processor-clock.

The additional MIO cards include a co-processor and are implemented to act as digital PID (proportional-integral-differential) controllers for the intensity stabilization of laser sources and the current control of coils. These cards convert the analog process values via ADC[3], calculates the controller output on the MIO processor and sends the signals to the device using a DAC. One MIO card includes four individual channels (here: four PID controllers) evaluated serially using multiplexing. The latter limits the control speed to 40 kHz.

Due to the large number of connections of the control system to external devices, the implementation of a centralized control unit can lead to ground loops disturbing the system. To avoid this, we make use of opto-couplers or inductive coupling.

3.3 Laser systems for cooling and MOT

The laser sources providing the light for laser cooling and magnetooptical trapping have to fulfill a few requirements. The emitted light has to be single longitudinal mode, has to be stabilized close to the cooling transition of ^{6}Li (here: *D*2-Line) and has to provide enough laser power for a homogeneous restoring force for the

---

[2]Multi-input-output cards provide both - digital or analog signals.

[3]DAC: digital-to-analog converter, ADC: analog-to-digital converter
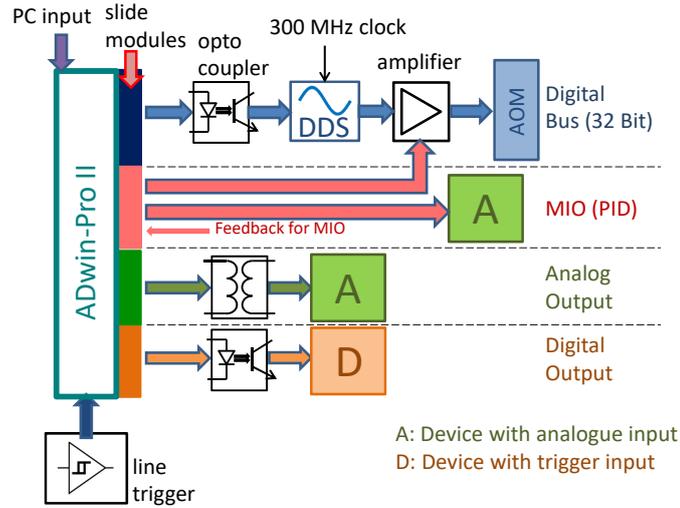
Figure 3.3: Control system of the lithium experiment. The heart of the control unit is the ADwin-Pro II and its slide modules. Experimental sequences are programmed on an external PC and sent to the ADwin. The commands are distributed to the modules which send the signals to external devices. The isolation of the ADwin and the external devices avoids ground loops. The starting point of individual experimental runs is synchronized to the mains supply via a line trigger.

particles within the cooling and trapping schemes. In this context, the laser power is limiting the efficiency of the laser cooling. During laser cooling a single atom has to scatter a few ten thousand photons during propagation from the oven to the steel chamber to be captured in a MOT. For sufficient MOT trapping/cooling the cooling beam intensity has to be large compared to the saturation intensity I_{sat} of the cooling transition[4].

To fulfill upper requirements we have chosen grating stabilized diode lasers of Toptica Photonics (DL pro) amplified by tapered amplifiers (TA pro, BoosTA) as light sources. The grating stabilized lasers provide single mode operation, narrow short-term linewidths $< 200\,\mathrm{kHz}$ and can be tuned by means of the grating angle, diode current and diode temperature. To stabilize the light sources with respect to optical transitions we use a master laser system as a frequency reference.

The master laser is a grating stabilized diode laser which is frequency locked to the crossover peak (see fig. 3.4) of the $|2^2\mathrm{S}_{1/2}, F = 1/2\rangle \rightarrow |2^2\mathrm{P}_{3/2}\rangle$ and $|2^2\mathrm{S}_{1/2}, F = 3/2\rangle \rightarrow |2^2\mathrm{P}_{3/2}\rangle$ transitions using frequency modulation (FM) saturation spectroscopy (see fig. 3.5 (red path) or [122, 124]). All other laser sources are stabilized with respect to the master laser frequency using beat note stabilization of the mode-locked lasers (BNL) (see [122]). This includes the MOT light source

---

[4]In our case we use the D2 line of $^6\mathrm{Li}$ with a saturation intensity of $I_{sat} = 2.54\,\mathrm{mW/cm}^2$.
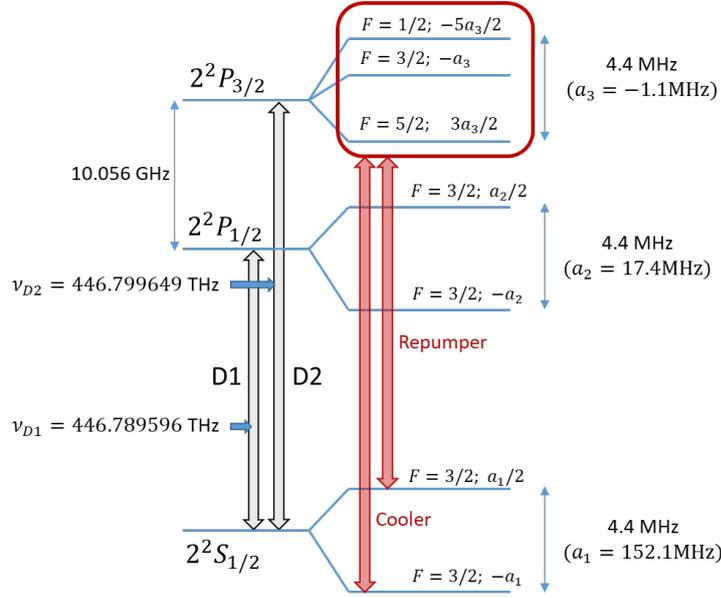
Figure 3.4: ^{6}Li term scheme (relative distances are not to scale). The transition frequencies are taken from [127]. All other values are taken from [95]. Please note that the hyperfine splitting of the $2^{2}\mathrm{P}_{3/2}$ state is not resolved in the laser cooling since it is smaller than the natural linewidth of $\gamma = 2\pi \times 5.87\,\mathrm{MHz}$. The a_{i} denote hyperfine constants.

and an additional grating stabilized diode laser used for particle imaging.

To produce the required laser power for the laser cooling and the magnetooptical trapping (green path in fig. 3.5), the diode laser beam in the TApro ($\approx 35\,\mathrm{mW}$) is guided to a tapered amplifier leading to an output power of $500\,\mathrm{mW}$. For laser and MOT cooling, the light of the TApro is split into two paths to produce light resonant with the $|2^{2}\mathrm{S}_{1/2}, F = 1/2\rangle \rightarrow |2^{2}\mathrm{P}_{3/2}\rangle$ (cooler) and $|2^{2}\mathrm{S}_{1/2}, F = 3/2\rangle \rightarrow |2^{2}\mathrm{P}_{3/2}\rangle$ (repumper) transitions. This is needed to avoid de-pumping of one of the two ground states and is therefore essential to assure a closed cooling cycle. Since the branching ratio of the two transitions is unity, the beam power is distributed equally.

The two beams are overlaid and guided to three single mode polarization maintaining (PM) fibers to transport the light to the vacuum system and to a second TA used to post-amplify the light for laser cooling. The laser cooling light is frequency shifted by an acousto-optical-modulator (AOM) and coupled to a PM fiber, subsequently.

The separate imaging laser is used for absorption and fluorescence detection[5]. The BNL provides an offset stabilization of up to $\approx 1.5\,\mathrm{GHz}$, limited by the built-in

---

[5]The light is again transported to the vauum setup by a PM fiber.
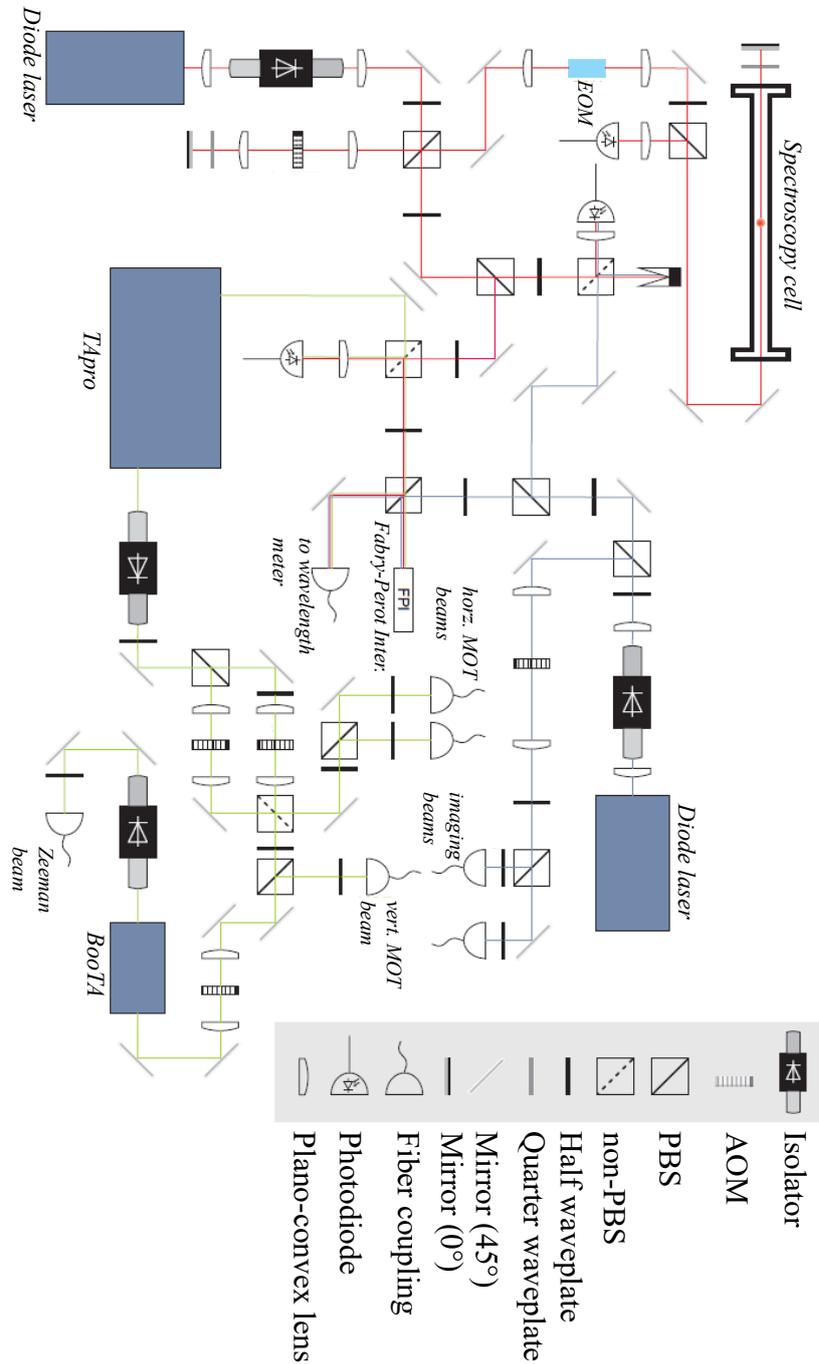
Figure 3.5: Laser cooling setup (adapted from [122, 124] and used with permission from the authors). The master laser (red path) is stabilized via FM saturation spectroscopy (see text). For laser cooling and MOT we use two tapered amplifiers (green path). The seed laser is frequency stabilized with respect to the master laser using the beat note stabilization of the mode-locked lasers (BNL) (see [122]). For imaging of ultracold clouds a separate laser source is set up (blue path), which is stabilized via BNL to the atomic transitions.

locking electronics. This way, frequency shifts of the optical transitions of a few hundred MHz can be compensated. This is necessary for particle detection at high magnetic field where the optical transitions are shifted.

3.4 Coil systems

Our setup includes a multitude of individual coils and coil systems. These are used to produce magnetic fields for the MOT or to tune the scattering length/particle interaction by means of a magnetic Feshbach resonance. This section is devoted to give an overview over all implemented coil systems. Detailed information about the coil properties can be found in several Master's theses [123–126].

Following the timeline of a typical experimental run, we start this overview with the Zeeman slower coils (ZSC) relevant for the initial laser cooling [84, 128]. The Zeeman slower coil system consists of nine individual coils (see fig. 3.6) with decreasing winding number [123, 124]. In operation the coil configuration produces a magnetic field of

$$B_{\mathrm{ZS}} \approx B_0 \sqrt{1 - \frac{y}{L_{\mathrm{ZS}}}}. \tag{3.1}$$

Here, the atomic beam propagates along the y axis, $y = 0$ is the position of the first coil where the magnetic field is $B_0 \approx 850\,\mathrm{G}$ and $L_{\mathrm{ZS}} = 47\,\mathrm{cm}$ is the length of the coil system. In combination with a counterpropagating laser cooling beam, the Zeeman slower provides an almost constant deceleration of $a_{de} \approx 8.4 \times 10^5\,\mathrm{m/s^2}$ for atoms travelling through the ZSC. The pre-cooled particles are trapped in the MOT (see e.g. [84] for more information) subsequently, where σ^- polarized light is combined with a magnetic quadrupole field produced by a pair of coils (MOTC) in Anti-Helmholtz (AH) configuration. There, the beams and the magnetic field produce a restoring force in both, the position and momentum space. The force is given by

$$F_{\mathrm{MOT}} = -\alpha v - \frac{\alpha\beta}{k} x_i. \tag{3.2}$$

Here, $\alpha = 4\hbar k^2 \frac{I}{I_{sat}} \frac{2\Delta/\Gamma}{\left(1 + (2\Delta/\Gamma)^2\right)^2}$, $\beta = \frac{g\mu_B}{\hbar} \frac{\mathrm{d}B}{\mathrm{d}x_i}$ is the damping coefficient, k is the angular wavenumber of the light, I is the beam intensity, I_{sat} is the saturation intensity of the cooling transition, Δ is the detuning from the cooling transition, Γ is the natural linewidth of the transition, $g = g_J \simeq 1$ is the g-factor, μ_B is the Bohr magneton, and v is the velocity [84].

For further cooling the atoms are loaded from the MOT into an optical dipole trap (see sec. 3.5). To do so, the trap centers are overlaid by moving the MOT with respect to the dipole trap by using the offset coils (MOTG) (see fig. 3.6).
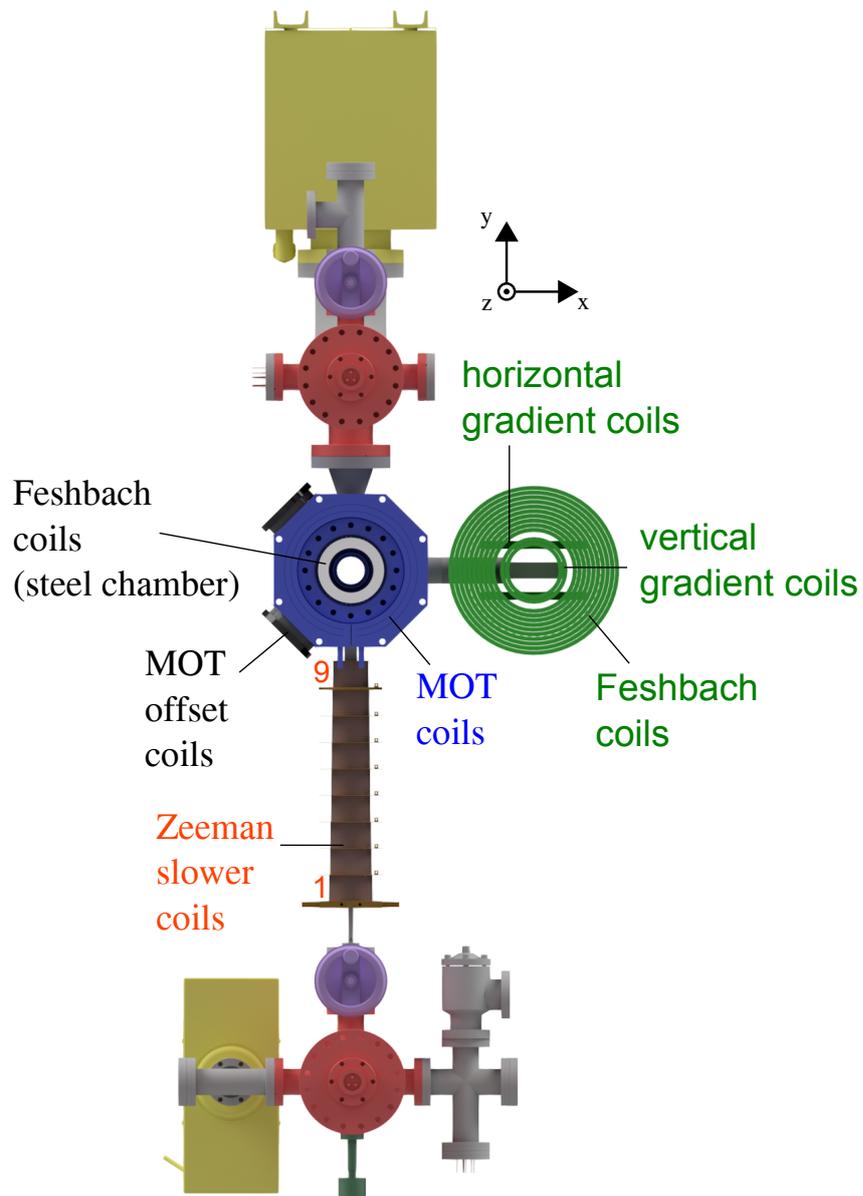
Figure 3.6: Top view presentation of the vacuum system to display all coil systems. The Zeeman slower coil system consists of nine individual coils. Coil one to eight are driven by one power supply and coil nine is driven independently. The MOT coil system includes additional offset coils, used to shift the zero crossing of the magnetic field. The Feshbach coils produce bias magnetic fields used to tune the particle interaction. **The coordinate system defined in the figure is used throughout this thesis**.

In the dipole trap evaporative cooling is applied[6]. The efficiency of evaporative cooling is highly depending on the particle interaction. A strong particle interaction leads to a fast thermalization in the residual gas after an evaporation step and yields a favorable particle loss to cooling-rate-ratio. To tune the particle interaction we use a broad magnetic Feshbach resonance [91] at about 832 G. This requires a stabilized offset magnetic field, which we produce with water cooled hollow wire coils (FBC=Feshbach coils) in Helmholtz configuration (HH) both, at the steel chamber and at the glass cell [125, 126]. The hollow wires at the steel chamber, with an inner (core) cross section of $2.4 \times 2.4 \, \text{mm}^2$, enable high power operation at constant currents of up to 200 A and a low steady state temperature of $< 70°$C.

However, most of our experiments are performed in the glass cell and therefore evaporative cooling is done there. Therefore, we use a similar coil system placed around the glass cell. Here, we use hollow wire coils with an inner (core) cross section of $4 \times 4 \, \text{mm}^2$. Due to the increased inner diameter the cooling capacity is higher as for the coils at the steel chamber. With this we reach a steady state temperature of about $\approx 30°$C for a current of 200 A.

In addition to the FBC we placed another two pairs of coils around the glass cell. The vertical and the horizontal gradient coils VGC and HGC, respectively (see fig. 3.6).

These coils serve several purposes. First, in the experiment we superimpose the fields of the FBC and the VGC, both driven in HH configuration, to control the field curvature of the produced magnetic field. A finite field curvature leads to a magnetic confinement for the high field seeking particles[7]. For particles inside the dipole trap, the field curvature dominates the trapping in the axial direction and defines the corresponding frequency (see sec. 4.5).

Second, driving the two VGCs with different currents allows us to shift the field maximum in the glass cell along the gravitational direction (here: z-direction). This way, the field gradient in z-direction can be adjusted to levitate the particles.

Third, the VGC and HGC coils can be used to produce non-static field gradients in the setup, using a step function switching of the coils. With this, well defined momenta for the high field seeking particles can be generated.

In table 3.1 I summarize the properties of all available coil systems. This includes coil resistances, operation currents, and the produced fields or field gradients. To control the coil currents in our setup we use the main control unit of our experiment, the ADwin. Figure 3.7 shows the control schemes used here. Except for the FBC, the coil currents are controlled by an analog control signal from the ADwin unit sent to the power supply. The FBC current is actively stabilized by means of an external digital PID controller. The control loop consists of a current transducer

---

[6]For an overview on optical dipole traps see [129]. More information on evaporative cooling of gases in the cold/ultracold regime can be found in [130].

[7]In our experiments the particles are prepared in high field seeking states.
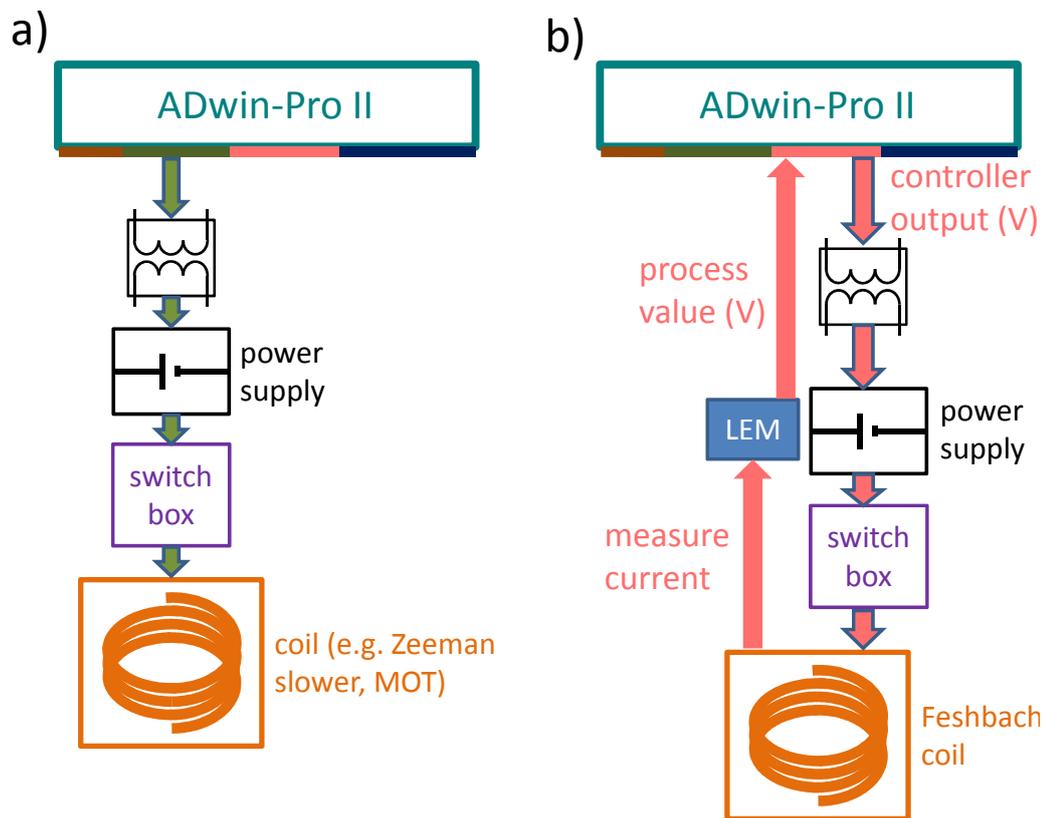
Figure 3.7: Control scheme for coils. a) To set the coil currents of the Zeeman slower, MOT, MOT gradient, vertical gradient and horizontal gradient coils, the power supplies are controlled via analog signals from the ADwin. To switch off the current flow in the coils an additional switch box is placed between power supply and coils. b) The current of the FBC is actively controlled (PID-controller) using the MIO card and an external current transducer of the company LEM.

Table 3.1: Coil systems. Resistances R at room temperature (22°C), operation currents I_{op}, and produced magnetic fields B (field gradients B/I).

Coils	Ref.	Configuration	$R\,(\Omega)$	$I_{op}\,(A)$	HH & single coils: $B/I\,(G/A)$ AH: $\Delta B/I\Delta x_i\,(G/(A\,cm))$
ZS (coils 1-8)	[123, 124]	stack of coils	11.65 ± 0.05	6	≈ 50 to 92
ZS (coil 9)	[123, 124]	single coil	0.74 ± 0.02	5.55	≈ 41.4
MOTC	[126]	AH	2.20 ± 0.02 (both)	15	(2.47 ± 0.02) (z-axis)
					(1.27 ± 0.02) (y-axis)
MOTG	[126]	single coil	0.55 ± 0.02 (both)	3	≈ 1.1
FBC (steal chamber)	[125]	HH	0.04 ± 0.02 (both)	100 to 200	≈ 5.15
FBC (glass cell)	[126]	HH	0.03 ± 0.02 (both)	80 to 120	5.79
VGC (upper & lower)	[126]	HH	0.004 ± 0.001	252 & 154	1.13
HGC (glass cell)	[126]	HH	1.00 ± 0.02	4	6.04

(LEM[8]), the ADwin (MIO card) and the power supply. With the LEM the coil current is measured, a process value (voltage) generated and sent to the MIO card of the ADwin. On the ADwin a digital controller is realized which calculates a controller output transferred to the power supply subsequently. This way the magnetic field can be stabilized to fields $\lesssim 1\,G$. This value was determined by performing radiofrequency (RF) spectroscopy on the $|1\rangle \rightarrow |2\rangle$ transition at high magnetic field. Since the natural linewidth of the transition is $\Delta\nu_{RF} \ll 1\,kHz$ any broadening of the line can be attributed to a field jitter.

3.5 Optical dipole trap and transport to glass cell

As mentioned in the previous section after pre-cooling of the atoms in the MOT the particles are transported to a single beam optical dipole trap for further cooling. The trap is given by a focused laser beam, far red detuned from the D1, D2 transitions of ^{6}Li. The electric field of the beam produces a position dependent ac Stark shift for the ground state atoms. For large and negative detuning Δ this leads to an attractive potential [129] given by

$$U_d(\mathbf{r}) = -\frac{\pi c^2 \Gamma}{2\omega_0^3}\left(\frac{2}{\Delta_2} + \frac{1}{\Delta_1}\right)I(\mathbf{r}). \tag{3.3}$$

Here, $\Delta_{1,2} = \omega - \omega_{1,2} < 0$ where ω is the frequency of the trap laser, $\omega_{1,2}$ are the transition frequencies, $I(\mathbf{r}) = I_0\exp(-2r^2/w(x)^2)\frac{w_0^2}{w(x)^2}$ is the intensity of the laser beam along the propagation direction (x-axis), r is the radial coordinate (here: $r = \sqrt{z^2 + y^2}$), $w(x)$ is the beam waist, $I_0 = 2P/\pi w_0^2$ is the peak intensity, and P is the beam power. Using a Taylor expansion at the intensity maximum the optical trap can be approximated by a harmonic confinement with cylindrical symmetry

---

[8]Current transducer from the company Liaisons Electroniques-Mécaniques.

$$U_d \approx \frac{1}{2}m\omega_r^2 r^2 + \frac{1}{2}m\omega_{ax}^2 x^2. \tag{3.4}$$

The radial and axial trapping frequencies are given by $\omega_r = \sqrt{4U_d(0)/(mw_0^2)}$ and $\omega_{ax} = \sqrt{2U_{d,0}/(mx_R^2)}$, respectively. Here $x_R = w_0^2 \pi / \lambda$ is the Rayleigh length and λ is the wavelength of the light.

In our case, the optical trap is generated by a 1064 nm laser beam obtained from a ytterbium fiber laser (IPG YLR-200-LP-AC). The laser has a maximum output power of 220 W, a M^2-factor of about 1.04, a beam divergence of 0.29 mrad, and an output beam diameter (doubled waist $2w_0$) of 5.2 mm.

As depicted in the sketch shown in fig. 3.8 the free space beam is guided through beam shaping optics and a pair of orthogonally aligned acousto-optical modulators (Crystal Technologiy AOM 3080-199) with an active aperture diameter of 2.5 mm. The intensity of the first diffraction order of both AOMs (marked by (1,1) in fig. 3.8) is stabilized and used for the trap. For intensity stabilization we combine an intensity measurement using an amplified photo diode (Thorlabs PDA 100A-EC) and a digital controller realized on the MIO card of the ADwin. The controller produces an output signal that regulates the diffraction efficiencies of the AOMs tuning the RF powers of the driving signals for the AOMs (see fig. 3.9). The stabilized beam is guided to a beam expander and alignment optics, subsequently (see upper part in fig. 3.8). The beam expander allows us to tune the beam size of the collimated beam. Adjusting the beam sizes enables us to tune the beam waist at the position of the atoms which defines the volume of the optical trap. We increase the beam diameter by a factor of eight such that the waist at the focus is set to $w_0 \approx 38 \, \mu\text{m}$.

In an experimental run the trap center is initially located at the center of the steel chamber to load the particles from the MOT to the dipole trap. However, for further cooling we transport the gas to the glass cell. This is done by an optical/mechanical transport of the particles. For this we shift the focus of the dipole beam from the steel to the science chamber (glass cell). To do so, we use a configuration of three $f = 300$mm lenses and an air bearing translation stage as illustrated in fig. 3.8. For the transport one lens, placed on the stage (Nelson Air Corp. ATLAS-101-400-HD), is moved over a distance of 27 cm with sub-micron precision (see ref. [126]). Shifting the lens from position one to position two moves the focus of the dipole beam from the MOT chamber to the glass cell. We use a simple trajectory for the transport which includes an acceleration period (almost linear increase in the velocity), followed by a passage with no acceleration. Finally, a deceleration step to zero velocity terminates the transport. The forces acting on the particles during the acceleration/deceleration phase are smaller than the restoring force of the dipole trap. With this, the trap provides a loss-free transport of the atoms (see
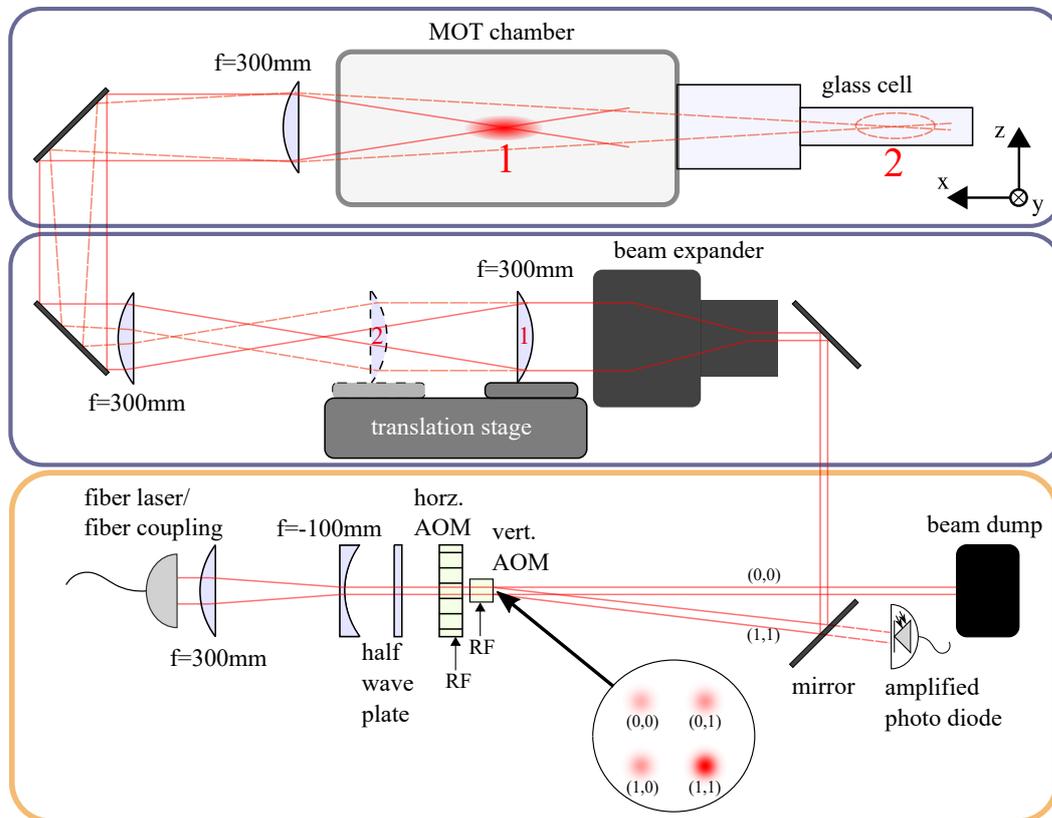
Figure 3.8: Dipole trap beam path. Lower box: The light of the ytterbium fiber
laser is outcoupled and shaped before it is guided to two AOMs. The
first order diffraction of both AOMs (here marked as (1,1)) is used as
the trap beam and is intensity stabilized (see text). Middle box: The
(1,1) order is transferred to a beam expander and a translation stage.
Upper box: The beam is guided via a periscope to the steel chamber
where the beam is focused to the center of the MOT. This way, both
traps are overlapped which allows a transfer of the particles from MOT
to dipole trap. In the optical/mechanical transport the focus of the beam
is moved from position 1 to 2 by shifting a lens on the translation stage.
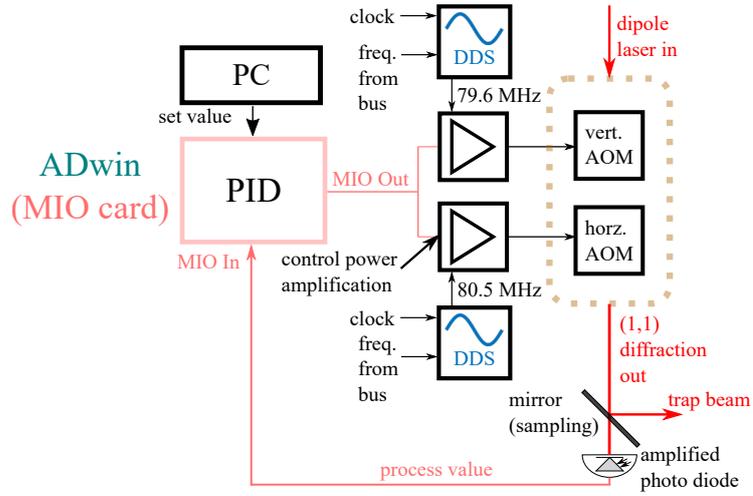
Figure 3.9: Intensity stabilization of the dipole trap beam. The intensity of the (1,1) diffraction order is measured with an amplified photodiode. The signal is sent to the MIO card, where a digital PID controller is realized. The controller output sets the diffraction efficiencies via the power of the RF signals driving the AOMs.

also [126]). The overall transport duration is 750 ms.

3.6 RF/MW antennas

Our experimental setup includes two RF and one microwave (MW) antenna which we use to transfer particles to desired states at high magnetic field. The three antennas have different tasks within an experimental cycle. In the following I will introduce the different emitters and assign the experimental purposes of the antennas.

Balanced distribution of particles in the states $|1\rangle$ and $|2\rangle$

Most of our experiments are performed with a balanced distribution (50/50 distribution) of particles in the states $|1\rangle$ and $|2\rangle$. To assure a balanced incoherent distribution of the particles in the two states, we make use of a strong radiofrequency pulse within our experimental sequence.

For this purpose a magnetic loop antenna has been built and placed in the close vicinity of the glass cell (for more information see ref. [126]). It consists of a single hollow copper loop with an inductance of $L = 0.238\,\mu H$ and a resistance of $R = 25\,m\Omega$. It is terminated by a copper plate capacitor with $C = 20\,pF$ (see fig. 3.10 a) and b)). The antenna has a bandwidth of 740 kHz and a resonance frequency
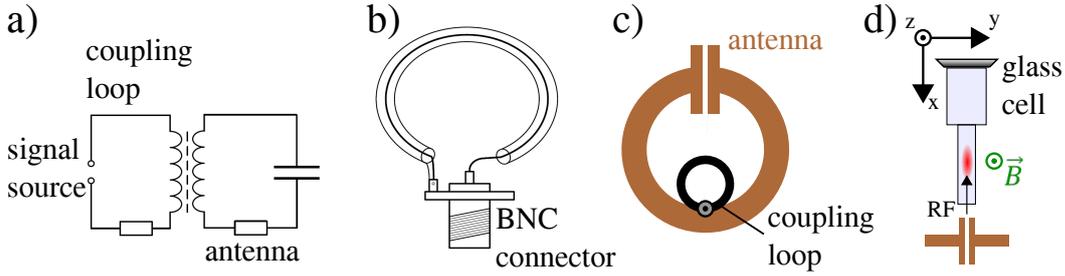
Figure 3.10: RF antenna. a) Inductive coupling of the inner loop and the antenna. b) Coupling loop. The signal is coupled via the BNC connector to the coaxial cable. a) and b) are taken from [126] (used with permission from the author). c) Sketch of coupling loop and antenna. d) Position of the antenna near the glass cell (top view). The polarization of the RF signal is oriented along the x-axis, perpendicular to the quantization axis given by the offset magnetic field.

of $\nu_{RF} = 76.2\,\mathrm{MHz}$ which matches the transition of the hyperfine states at $B = 780\,\mathrm{G}$, where evaporative cooling is performed typically. To drive the antenna we use a DDS and an amplifier to produce a radiofrequency signal at the desired frequency with a power of $P \approx 1\,\mathrm{W}$. This signal is transferred to a BNC loop (see fig. 3.10 c)) which couples inductively to the antenna. The antenna is aligned to the glass cell, such that its linearly polarized RF signal is oriented perpendicular to the quantization axis (z-axis) defined by the offset magnetic field (see fig. 3.10 d)). By this, the emission is σ polarized with respect to the quantization axis, to match the selection rules for a $|1\rangle = |m_I = 1\rangle$ to $|2\rangle = |m_I = 0\rangle$ transition.

Please note that an identical loop antenna is also placed at the steel chamber in close vicinity of the MOT coils. Since all of our experiments, including spin preparation, are performed in the glass cell the antenna is not operated in the experiments introduced in the following. However, if future studies are performed in the steel chamber this antenna might be used.

Pairing measurements

In our experiments a gas of Feshbach molecules of particles in the states $|1\rangle$ and $|2\rangle$ can be produced. The binding energy and number of dimers can be measured by RF spectroscopy [91, 118, 131]. RF spectroscopy is performed by counting the number of atoms in state $|2\rangle$ (see also energy level diagram in sec. 2.4) as a function of the frequency of a previous RF pulse. For this, the frequency of the pulse is tuned close to the $|2\rangle \rightarrow |3\rangle$ transition of ^{6}Li at high magnetic field[9].

[9]Most experiments are performed in the field range of 700 to 900 G.
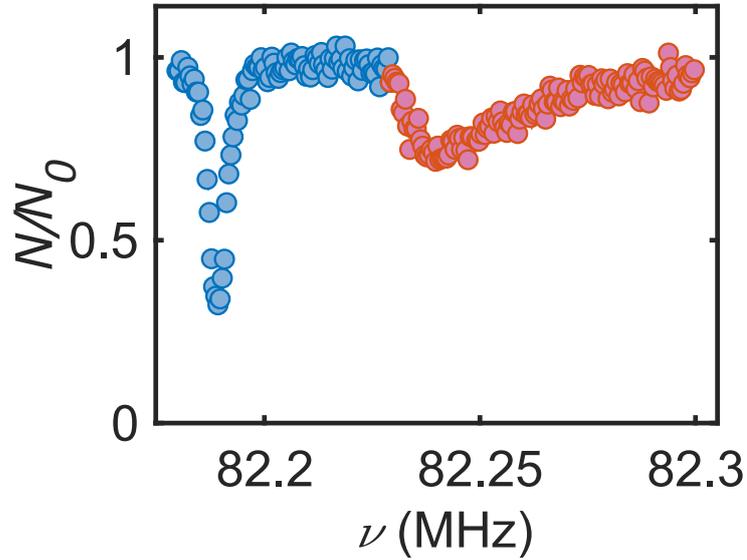
Figure 3.11: RF molecule spectroscopy. RF spectroscopy on the $|2\rangle \rightarrow |3\rangle$ transition on a mixed gas of dimers and free atoms at $B = 755\,\mathrm{G}$. For $\nu \approx 82.198\,\mathrm{MHz}$ the unbound atoms are transferred to the $|3\rangle$ state such that the number of particles in $|2\rangle$ N reduces (blue circles). The transition for atoms in $|2\rangle$ which are bound to dimers (red circles) is shifted from the RF transition of unbound atoms by the binding energy.

However, since the $|2\rangle \rightarrow |3\rangle$ transition is about $6\,\mathrm{MHz}$ blue detuned from the $|1\rangle \rightarrow |2\rangle$ transition and since the bandwidth of the loop antenna is small, the previously introduced antenna cannot be used here. Therefore, our setup includes an additional antenna adjusted to match the $|2\rangle \rightarrow |3\rangle$ transition in the given field range. This antenna is identical to the one for the $|1\rangle \rightarrow |2\rangle$ transition except for a different resonance frequency.

Performing RF spectroscopy with this additional antenna, we are able to identify two distinct features (see fig. 3.11). First, we find the resonance of the $|2\rangle \rightarrow |3\rangle$ transition. Second, we find an additional dip corresponding to atoms in state $|2\rangle$ which are bound to dimers additionally. This dip is blue detuned from the $|2\rangle$ to $|3\rangle$ transition where the offset is the binding energy. Using the full spectrum we get information on the molecule number in principle. However, to extract the molecule number from the spectroscopic data is quite challenging, since initial and final state effects have to be included in advanced calculations [131]. Therefore, this type of methodology has not been used in the studies presented in this work. An alternative approach for the molecule number measurement is presented in sec. 3.10.
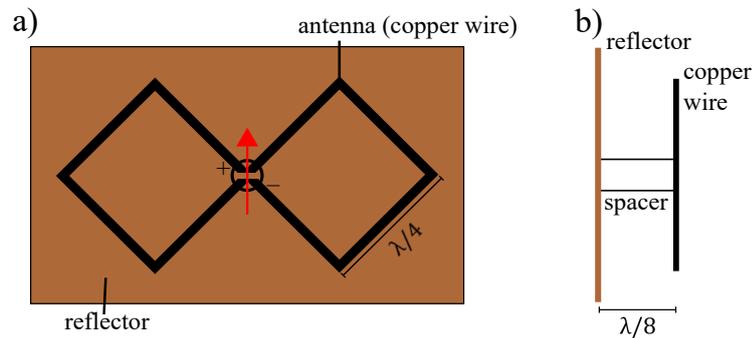
Figure 3.12: Bi-quad antenna. a) Top view of the antenna. The copper wires (black lines) are folded to match the desired frequency. The direction of the E-field emission is given by the red arrow. b) Side view of the antenna. The MW signal is coupled to the antenna via a BNC connector (not shown).

MW antenna

In future experiments spin-selective measurements of individual particles in a flat 2D optical lattice will be performed. To do so, the particles in one spin state will be removed prior to the particle detection. For this, we have constructed a bi-quad antenna (see fig. 3.12) which allows us to transfer particles to un-confined states before the atoms are imaged.

The antenna provides a linearly polarized MW signal aligned perpendicularly to the quantization axis (see e.g. [132]). This way, atoms prepared in a high field seeking state, such as state $|2\rangle$, can be transferred to a low field seeking state, such as state $|5\rangle$. Atoms in the latter state experience a repulsive potential at high magnetic field[10]. With this repelling force the atoms are removed from the trap, enabling a selective detection of the remaining atoms in $|1\rangle$. For an experiment at 780 G the required frequency for the transition lies at 2.2 GHz.

3.7 Imaging systems

To obtain information about the processed atomic gases we use fluorescence or absorption imaging[11]. Therefore, we have prepared a multitude of imaging systems in our setup.

At the steel chamber I have implemented a low resolution absorption (SC AI) and a low resolution fluorescence imaging system [124] (SC FI) to observe atoms in a MOT. Both detection systems consist of an objective lens, a tube lens and a CCD

---

[10] Similar as in runaway evaporative cooling in magnetic traps, see textbooks like [84].

[11] see textbooks like [84, 85].

Table 3.2: Overview of imaging systems. Upper: Lens systems. To specify the imaging systems the working distance (WD) and the numerical aperture (NA) are given. In the case of a single lens as an objective or as a tube lens, the focal length is given instead of the WD. The resolution is given for the imaging wavelength of 671 nm. Lower: Cameras of the imaging configurations.

	SC AI	SC FI	GC LR	GC HR
Objective				
Lens	EO 2X M Plan APO	Plano-convex lens	Achromat	custom objective (ASE)
NA	0.055	0.025	0.084	0.61
WD/ focal length (mm)	34	450	150	8.2
Tube lens				
Lens	Achromat	Plano-convex lens	Achromat	custom tube lens (ASE)
WD/ focal length (mm)	200	500	500	250
Camera				
(EM)CCD camera	AVT: Stingray F-145B	AVT: Guppy F-038B NIR	AVT: Stingray F-145B	Andor iXon 897
Pixelsize	$6.45 \times 6.45\,\mu m^2$	$8.4 \times 9.8\,\mu m^2$	$6.45 \times 6.45\,\mu m^2$	$16 \times 16\,\mu m^2$
Pixels	1388×1038	768×492	1388×1038	512×512
System				
Magnification	2	1.1	3.33	43

camera. The absorption imaging is aligned along the z-axis of the setup and is placed on the upper view port of the MOT chamber (imaging system properties are summarized in table 3.2) as depicted in fig. 3.13. The fluorescence imaging system is aligned along the x-axis and is placed at the end facet of the glass cell.

At the glass cell two imaging systems are available. A low and a high resolution detection setup. The low resolution system (GC LR) is oriented along the y-axis of the setup, consists of a two-lens imaging system and a CCD camera. It is used for absorption imaging at high magnetic field, where we drive the $|1\rangle$ ant the $|2\rangle$ to $|2^2P_{3/2}, m_J = -3/2\rangle$ transition, respectively. According to the selection rules σ polarized light is required to drive the imaging transition. We use a beam with a linear polarization aligned along the x-axis, which is perpendicular to the quantization axis (the configuration is also shown in fig. 3.14 c)).

The high resolution system uses a customized objective and a customized tube lens of ASE Optics as well as an electron multiplying CCD camera (EMCCD) from Andor. It is aligned along the z-axis of the setup and located below the glass cell (see fig. 3.14 a) and d))

The high NA objective has two applications. First, it is used to project optical lattices or an excitation beam on the atoms. Second, the particles, especially at experiments in the lattice, can be detected (see sec. 3.9).

Our experiment is designed such that the projected optical lattice has a lattice constant of about 1.2 µm. This sets the requirements for the imaging resolution. To provide single-atom single-site imaging the resolution of our objective at the de-

a)

glass cell

GC LR

z

y

x

GC HR

b)

SC AI

z

x

y

steel
chamber

glass cell

SC FI
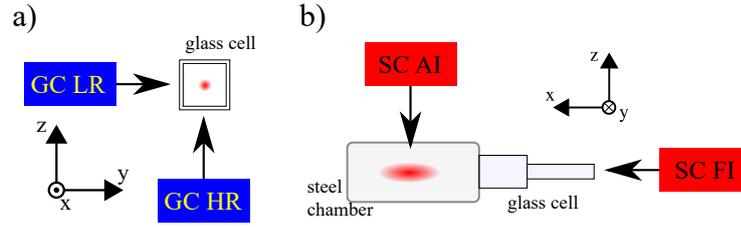
Figure 3.13: Positions of the imaging systems. In this figure the glass cell low reso-
lution imaging system (GC LR), the glass cell high resolution imaging
system (GC HR), the steel chamber absorption imaging system (SC
AI) and the steel chamber fluorescence imaging system (SC FI) are
shown. The working directions of the individual setups are given by
the black arrows. The red cloud illustrates the position of the atoms.
a) Positions of the imaging systems around the glass cell. A more de-
tailed picture can be found in fig. 3.14 c). b) Positions of the imaging
systems around the steel chamber.

tection wavelength has to be smaller or at least comparable to the lattice constant.
The resolution of an imaging setup can be characterized by the response of the
system to a point emitter, the so called point spread function (PSF) (see e.g. [133,
134]). Imaging a point emitter with a lens-based imaging system leads to an Airy
pattern in the detection plane which reads

$$I(r) = I(0) \left(\frac{2J_1(\pi r)}{\pi r} \right)^2. \tag{3.5}$$

Here, I is the intensity of the light, J_1 is the Bessel function of first kind, and
$r = \sqrt{x^2 + y^2}$ is the radial coordinate in the image plane centered at the intensity
maximum of the pattern.

According to the Rayleigh criterion the resolution of an imaging system is given
by the minimal distance of two point emitters in the object plane that can be re-
solved. By definition, this is given when the maximum of the Airy pattern from the
first emitter coincides with the first minimum of the Airy pattern from the second
emitter in the image plane. Under this assumption the resolution can be calculated
from eq. (3.5) and reads

$$D = 0.61 \frac{\lambda}{NA}. \tag{3.6}$$

In our case we find $D = 0.67 \, \mu m$, which is sufficient for the detection of particles
inside a lattice with a $1.2 \, \mu m$ spacing. To test the performance of our imaging sys-
tem and to compare it with the calculation, I measured the PSF of the system. To
do so, I imaged an illuminated pinhole with a diameter of $0.2 \, \mu m$, which is suffi-
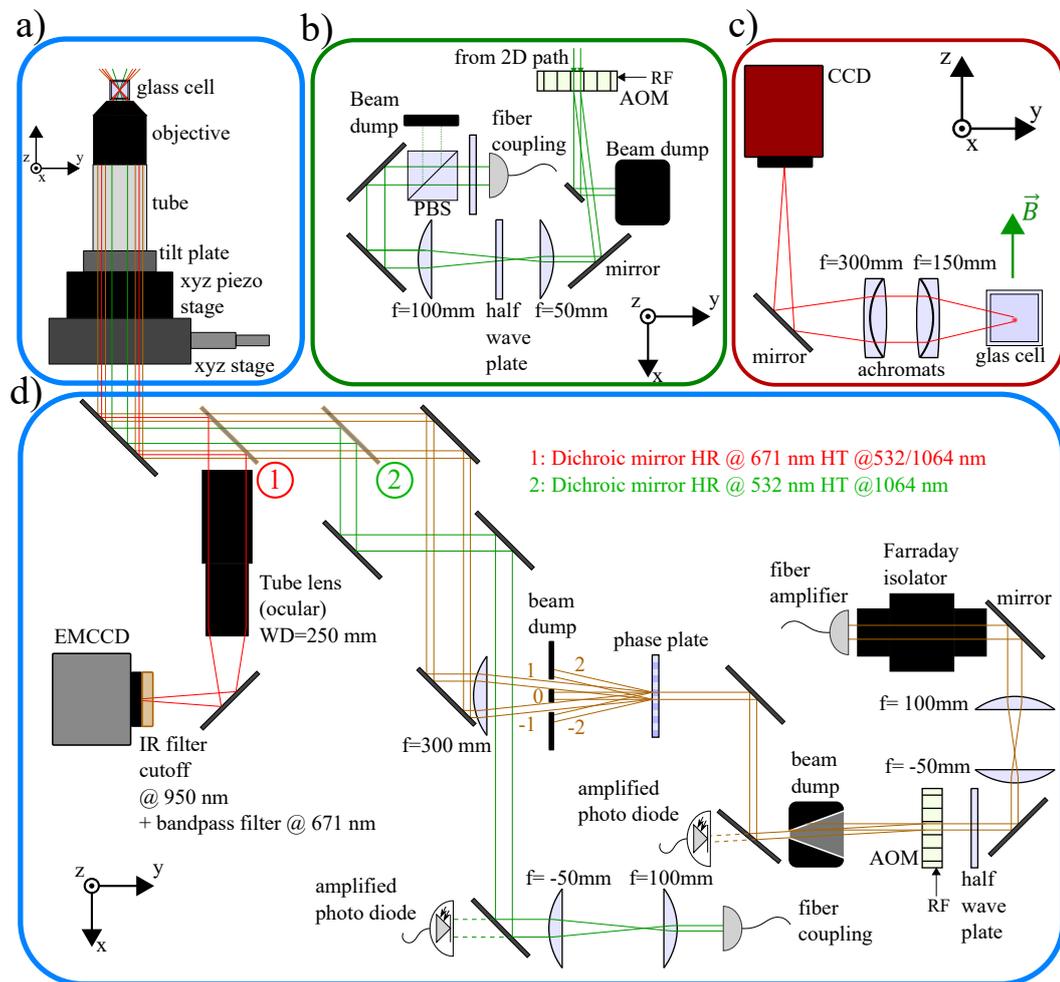
Figure 3.14: Panel of the imaging/projection setups. a) High NA objective below the glass cell including the positioning system and beam paths for the imaging (red lines), the excitation beam (green lines), and the lattice projection beam (orange lines). b) Intensity stabilization and beam path of the excitation beam. The light source is depicted in fig. 3.16. c) Low resolution absorption imaging system at the glass cell. d) Projection and imaging beam paths. The light, collected by the high NA objective (red path in a) and d)) is guided to an EMCCD camera. The IR and bandpass filter cuts off stray light. The excitation beam shown in b) is guided to the objective (green path) via a dichroic mirror (2). The lattice beam (brown path) is guided over a second dichroic mirror (1) to the objective.

ciently smaller than the expected imaging resolution of the system. The measured intensity distribution is shown in fig. 3.15 a).

From a fit to the intensity distribution using eq. (3.5) we obtain a peak to valley distance of $D_M \approx 0.7\,\mu m$, which is in good agreement with the calculation.

Two other crucial parameters for an imaging or projecting system are the depth of field/focus (DOF) and the field of view (FOV). The FOV is the size of the area in the object plane that can be imaged sharply. The DOF is the range around the focus of an imaging system, in which the object can be imaged sharply.

For the objective used here, the supplier specified a FOV of $150 \times 150\,\mu m^2$. This I have confirmed with another test (not shown here), where I imaged an array of illuminated pinholes over the full operation range. The image showed no significant aberrations.

Finally, I have investigated the DOF. Using wave optics the DOF for the objective reads [135]

$$\text{DOF} = 0.5\frac{n\lambda}{NA^2}, \tag{3.7}$$

where n is the index of refraction. In this case we obtain a $\text{DOF} = 0.9\,\mu m$. To confirm this value, I have measured the DOF of the imaging system. For this, I have imaged a point emitter for various objective displacements from the object plane. To determine changes in the intensity distribution with respect to the displacement z the width of the inner peak of the Airy pattern is determined. For simplicity, I fit a Gaussian distribution[12] to the inner peak with $I = I_0\exp(-2x^2/w^2)$ for each individual z. The result is shown in fig. 3.15 b). We find that the intensity pattern is almost constant for about one micron displacement, which is in good agreement with the predicted DOF.

3.8 2D confinement setup

To perform experiments in a two-dimensional gas, we load the pre-cooled atoms into a 2D trap. For this, we use the 2D confinement scheme introduced in ref. [136].

A Hermite-Gaussian TEM$_{01}$ beam at a wavelength of $\lambda_{2D} = 532\,nm$, which is blue detuned from the cooling transition, produces a repulsive double peak potential (see fig. 3.17) for the atoms (in our case: along z-direction). In the trapping scheme, the particles are strongly confined between these two peaks (confinement in one axis) and are unconfined in the other directions. To close the trap a weak harmonic confinement is added in the other two-directions, resulting in a highly anisotropic trap. This type of confinement leads to a pancake shaped cloud in the experiment and allows us to freeze out one degree of freedom (see also sec. A.1).

---

[12]x denotes the x-axis in the image plane.
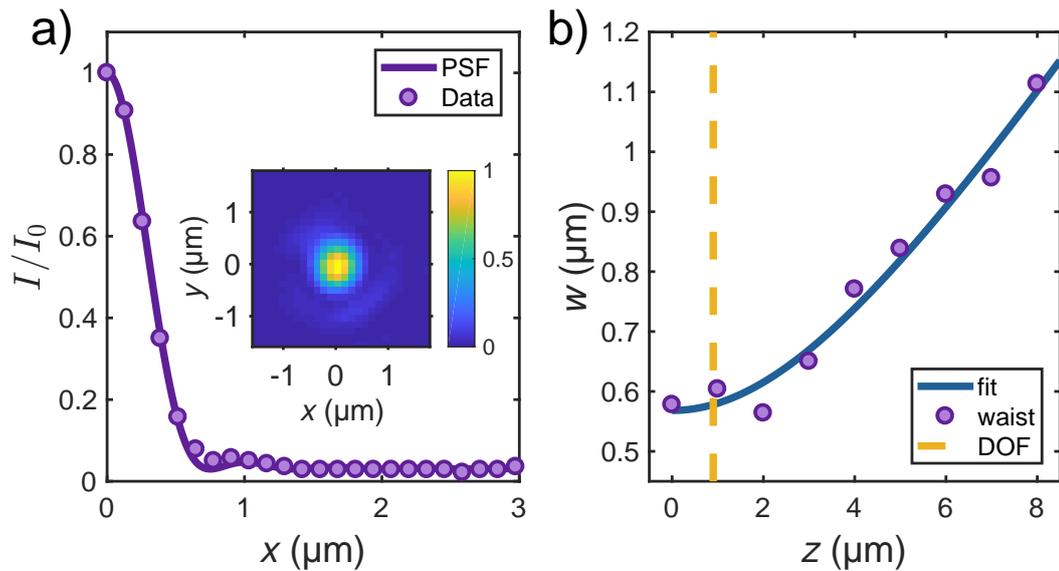
Figure 3.15: Point spread function and depth of field of the high resolution imaging system. a) PSF of the imaging system. The inset shows a false color representation of an imaged pinhole. The pinhole has a diameter sufficiently smaller than the expected resolution and can be considered as a point source for the objective. The plot shows a cut through the false color image (circles) for $y = 0$ and a fit to the data based on eq. (3.5). I_0 is the peak intensity. b) DOF of the system. The focus of the objective is moved from the object plane by z and the width w is measured. For this, the inner peak of the detected Airy pattern is approximated by a Gaussian distribution. As a guide to the eye, a parabola fit is applied to the data. For comparison the result of the predicted DOF (see text) is shown as the dashed line.
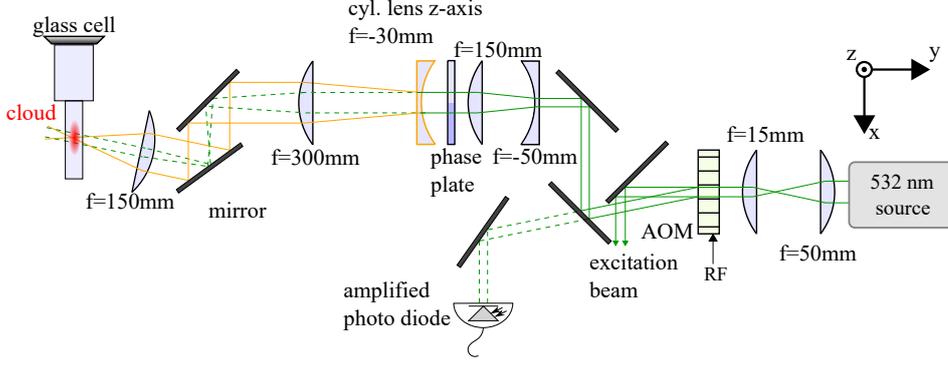
Figure 3.16: 2D confinement setup. A solid state laser source is used to provide 532 nm light at a power of up to 4 W. The intensity of the beam is stabilized using an AOM with the scheme of sec. 3.5. The first order diffraction is used for the two-dimensional confinement, while the zeroth order is used for excitation experiments (see sec. 3.9). To generate the TEM$_{01}$ like beam, we use a π phase plate. Further beam shaping leads to the required intensity distribution at the position of the atoms. To avoid unwanted reflections at the glass cell the beam delivery is adjusted with a small angle with respect to the y-axis (for a better visibility a larger angle is drawn).

In the following lines I will introduce the potential produced by the Hermite-Gaussian beam and present a few experimental details of our implementation to this trap.

The potential produced by the Hermite-Gaussian beam is given by

$$U(x,z) = -\frac{P\hbar\Gamma}{W_z^3 W_x \pi I_{sat}} \left(\frac{1}{\omega_{2D} - \omega_0} + \frac{1}{\omega_{2D} + \omega_0} \right) z^2 e^{-\frac{2z^2}{W_z^2} - \frac{2x^2}{W_x^2}} \qquad (3.8)$$

with W_l the waist for the direction l, ω_0 the atomic transition frequency, ω_{2D} the frequency of the TEM$_{01}$ beam, and P the beam power.

In the z-axis and close to $z = 0$ the potential is approximately harmonic with a frequency of $\omega_z = \sqrt{4eU_0/(mW_z^2)}$, where U_0 is the potential at the center, and $e = \exp(1)$. In the other two directions the beam produces a repulsive potential. This anti-trapping potential is harmonic in the vicinity of the trap center and the frequencies [136] read $\omega_x = \frac{i}{\sqrt{2W_z}\pi W_x} \left(\frac{\hbar^2 eU_0}{m^3} \right)^{1/4}$ and $\omega_y = \sqrt{\frac{3}{2}} i \frac{\lambda_{2D}}{2\pi^2 W_z^{5/2}} \left(\frac{\hbar^2 eU_0}{m^3} \right)^{1/4}$, respectively. Here, i is the imaginary number.

Our implementation of the trap is illustrated in fig. 3.16. We use a solid state laser (Laser Quantum Opus 532) with a maximum output power of $P = 4$ W and a beam diameter of 1.85 mm. The beam is shaped by two lenses and guided to an AOM, where the beam is intensity stabilized using a similar scheme as the one

introduced in sec. 3.5. Subsequently, the beam is guided to a phase-plate. One half of the plate leads to a phase shift of π with respect to the other half (for further information see [137]). This phase shift changes the intensity distribution from the Gaussian ground mode to a double peak intensity pattern, comparable to a TEM_{01} beam.

To produce a high aspect ratio W_x/W_z, required to produce a highly anisotropic cloud, subsequent beam shaping is performed. The beam is expanded in the z-axis selectively, using a concave cylindrical lens (see orange path in fig. 3.16). A subsequent lens collimates the beam in the z-axis again, while it focuses the beam in the x-axis (green path). In combination with the final $f = 150\,\text{mm}$ plano-convex lens, the beam is collimated along the x-axis, while it is focused on the atoms in the z-direction. This produces the desired highly anisotropic potential with $W_z = (9 \pm 1.5)\,\mu\text{m}$ and $W_x \approx (240 \pm 5)\,\mu\text{m}$ at the position of the atoms.

Since the beam is guided through multiple optics and is finally focused to the center of the un-coated glass cell, we lose about 45% of the initial beam power in this setup due to unwanted absorption and reflection. This limits the achievable trapping frequency to $\omega_z \approx 2\pi \times 11.3\,\text{kHz}$. The anti-trapping potential for the x- and y-axis at maximum beam power is given by $\omega_x = 2\pi i \times 18\,\text{Hz}$ and $\omega_y = 2\pi i \times 8\,\text{Hz}$, respectively.

In fig. 3.17 the potential is shown for the given parameters. Fig. 3.17 b) shows a cut through the potential at $x = 0$. At the center of the trap the potential is harmonic, in good approximation.

3.9 Lattice projection and excitation beam

Besides imaging, the high NA objective has a second function in our experiment. Namely, the projection of optical potentials on the cold atomic clouds.

For projection, the objective has to be positioned such that the laser beams are focused on the atomic cloud inside the glass cell. The objective is placed on a mechanical three axis stage[13], a second three axis piezoelectric stage and a tilt plate (see fig. 3.14 a)).

The mechanical stage is used for coarse positioning and can be adjusted using three micrometer screws. The piezoelectric stage[14] is used for fine tuning and provides sub-micron resolution. To tune the orientation/angle of the objective with respect to the optical table we use a tilt plate (Newport M-TTN80).

---

[13]Home-built stage, produced at the Wissenschaftliche Werkstatt (University of Ulm). The design is taken from the groups of Tilman Pfau (University of Stuttgart) and Fedor Jelezko (Institute for Quantum Optics, University of Ulm).

[14]Piezosystem Jena: TRITOR 102 SG, driver and controller: NV 40/3CLE.
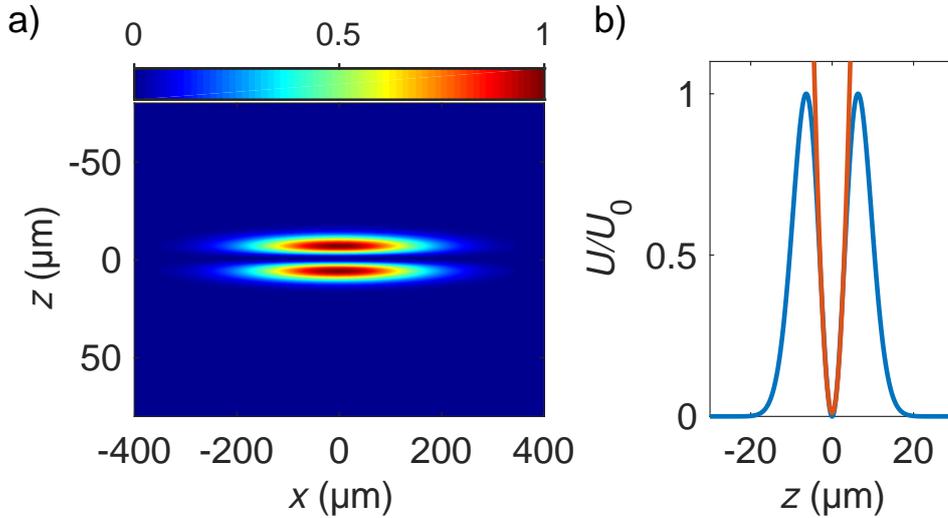
Figure 3.17: Calculated potential produced by a TEM$_{01}$ beam. a) False color image of the potential U/U_0 (normalized to the potential maximum as given in the text). For the calculation the experimental parameters presented in the text are used. b) Potential at $x = 0$ (blue line). An expansion to second order close to $z = 0$ shows that the potential is harmonic in good approximation (see orange curve).

Once the correct position is found, the objective is used to project multiple potentials on the trapped atoms. I will focus on the individual beam paths in the following, starting with the excitation beam (see fig. 3.14 b),d)).

Excitation beam

In the sound excitation experiments presented in sec. 6, we modulate the confining potential to generate a local perturbation. We make use of a laser beam blue detuned to the D2-line of ^{6}Li, which is aligned perpendicular to the dipole trap beam along the z-direction. The excitation beam is focused to the trap center (for details of the potential see sec. 6.7). For the excitation we use a portion of the light of the Opus laser introduced in sec. 3.8. Specifically, the zeroth order diffraction of the AOM in the 2D confinement setup is extracted and guided to a separate intensity stabilization[15] (see fig. 3.14 b),d). With a PM fiber the light is transported to the beam projection setup shown in fig. 3.14 d). There the beam (green path) is shaped and guided to the objective via a dichroic mirror (high reflectivity at 532 nm, and high transmission at 1064 nm). The beam is focused via the objective to a waist of 31.4 μm at the position of the atoms and produces a local repulsive potential (see sec. 4.5). The Rayleigh length of the beam $z_R = 5.8$ mm is large compared to the

---

[15]The stabilization scheme follows the one introduced in sec. 3.5.

typical size of a cloud of a few tens of microns. Therefore, the produced potential can be considered as cylindrical along the z-direction.

Lattice projection

To produce optical lattices, we use the phase hologram projection technique introduced in [70, 138]. A laser beam illuminates a periodically etched phase plate and is diffracted (see fig. 3.14 d) (brown path)). After Fourier filtering the beam is guided to the objective and is focused on the atoms located at the center of the glass cell in order to provide the desired potential.

In the setup we use a home-built grating stabilized diode laser at $\lambda_L = 1064\,\text{nm}$ combined with a fiber amplifier (Nufern NUA-1064-PB-0050-D0) which has a maximum output power of $50\,\text{W}$ as the laser source. The beam (see fig. 3.14 d) (brown path)) is outcoupled from the fiber and guided to an AOM where intensity stabilization is carried out[16]. Subsequently, the beam is directed to the phase plate. In our case the phase plate[17] is made of fused silica which has an index of refraction of $n = 1.4496$. The plate has a triangular pattern with edge lengths of $l = 90\,\mu\text{m}$ (see fig. 3.18 a) and b)). One of the two triangular sub-lattices is etched such that it has a depth of $d = \lambda_L/(2(n-1)) = 1.19\,\mu\text{m}$ and produces a local π phase shift. Illuminating the phase plate with the lattice beam leads to a diffraction pattern.

In the setup the diffracted light is filtered (zeroth, second and higher diffraction orders are blocked). The remaining first order diffraction is collimated and transported to the objective via a dichroic mirror. The high NA objective Fourier transforms the light field to a honeycomb pattern in the focal plane. Since the frequency of the lattice beam is red detuned from the optical transitions of ^6Li the light field produces an attractive honeycomb lattice for the particles (see fig. 3.18 c)). The potential well depth of the lattice is determined by the intensity of the beam (see also sec. 3.5). In contrast, the trapping frequency of a single well is depending on the spatial intensity gradient additionally. The larger the spatial intensity gradient, the larger the trapping frequency (see e.g. also [129]).

3.10 Detection of pairs

In some of our experiments we investigate fundamental chemical processes in a gas of interacting ^6Li atoms. To do so, we have to obtain the number of dimers and free atoms selectively. The difficulty in particle counting is to distinguish between the two species. In the vicinity of the broad Feshbach resonance pairs are very

---

[16]The stabilization scheme is similar as the one introduced in sec. 3.5.

[17]Phase plates have been produced in collaboration with the Institut für elektronische Bauelemente und Schaltungen and the Institut für Optoelektronik (both University of Ulm).
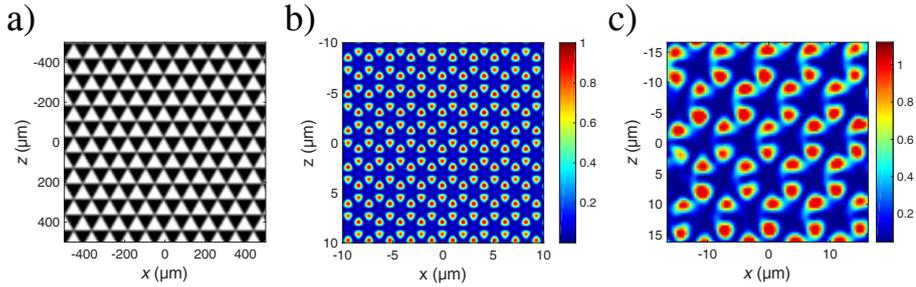
Figure 3.18: Lattice projection. a) Drawing of a binary phase plate of triangles with edge lengths of about 90 μm. b) Simulated intensity pattern of a projected honeycomb lattice as it will be used in future projects (lattice constant of about one micron). c) Projected lattice in the experiment (larger lattice constant as in future experiments). The projected pattern is imaged with a high NA aspheric lens arranged in a confocal configuration with the objective. The lattice has a constant of ≈ 3.3 μm. Small irregularities in the intensity pattern might be due to misalignment of the beam in the projection path.

loosely bound, such that they absorb light stabilized to the imaging transition of the unbound atoms (see also [86]). Excited molecules can decay to unbound atoms after scattering a first photon. This complicates to discriminate between pairs and unbound atoms. To separate the different particles from each other, we make use of two different techniques. These are the magnetic field ramp technique (for more information see appendix A.2) and the optical transfer method (see sec. 5.7 and [105]). In this section I will focus on the setup for the optical transfer method.

In this scheme the number of molecules and free atoms in one spin state are determined in a two-step process. In a first experiment, the total number of atoms in the gas is determined via absorption imaging. As mentioned above, this is possible since unbound atoms and atoms bound to dimers both are on resonance with light stabilized to the atomic transition in the close vicinity of the Feshbach resonance[18]. In a second experiment, with an identical sample/cloud, the weakly bound molecules are removed prior to absorption imaging using an optical excitation beam resonant with the pairs/molecules. The molecules, initially prepared in the $|X^1\Sigma_g^+, v = 38\rangle$ state, are transferred to $|A^1\Sigma_u^+, v' = 68\rangle$ from which the dimers either dissociate to highly excited unbound atoms, which quickly leave the trap, or decay to deeper bound states invisible for the particle detection. Performing absorption imaging

---

[18]Our experiments are typically done at magnetic fields of $B > 700$ G, where both, unbound atoms and atoms bound to dimers are on resonance with the detection light. Typically, we image the atoms in state $|1\rangle$ or $|2\rangle$. Our experiments are done with a balanced distribution of particles in the two spin states. Therefore, the detection of particles in one of the spin states gives us the total particle number.
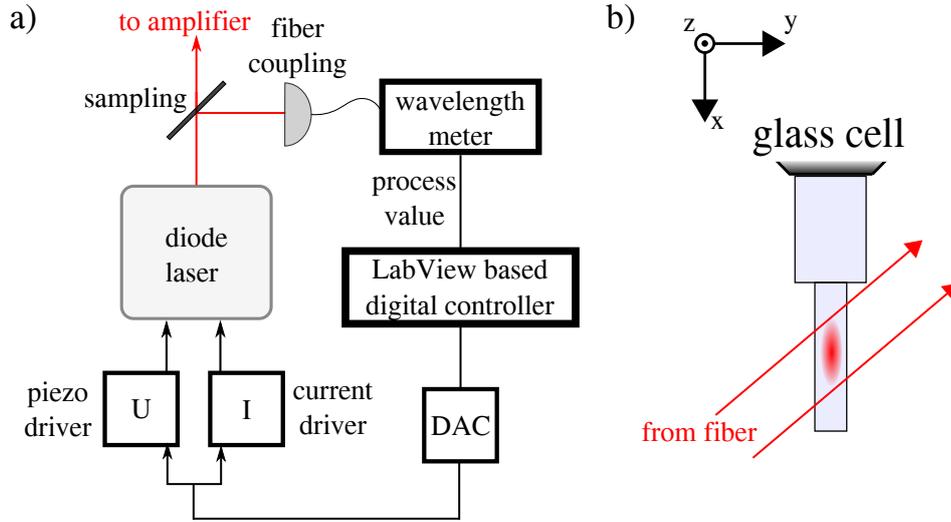
Figure 3.19: Setup for the molecule excitation scheme. a) Frequency stabilization. The wavelength is measured using a wavelength meter. The information is transferred to a LabVIEW based digital controller on a separate PC which controls the diode current and the laser grating orientation of the home-built laser in order to adjust the wavelength. b) Alignment of the molecule purification beam at the glass cell.

after the excitation pulse gives the number of free atoms.

To perform the optical excitation scheme we have set up a separate home-built grating stabilized diode laser locked to the $|X^1\Sigma_g^+, v = 38\rangle - |A^1\Sigma_u^+, v' = 68\rangle$ molecular transition with a transition frequency of $\nu \approx 445.28762\,\mathrm{THz}$ at 780 G. To lock the laser to the molecular transition, we use a wavelength meter based locking scheme (see fig. 3.19 a)). The laser frequency is measured with a wavelength meter (High-Finesse WS7) which is transferred to a LabVIEW based digital controller. The controller is connected via a DAC to the driver of a piezoelectric element, which tunes the tilt of the grating, and to the current controller of the diode in order to tune the laser frequency (feed forward). The frequency stabilization is limited by the readout resolution of the wavelength meter of $\approx 1\,\mathrm{MHz}$ and the readout speed which is about[19] one second.

The light is amplified using a tapered amplifier (Toptica BoosTA), and finally transported to the glass cell via a PM fiber. At the glass cell the beam has a waist of 1.1 mm, provides peak intensities of $500\,\mathrm{mW/cm^2}$ and is aligned to the atomic cloud (see fig. 3.19 b)).

---

[19]In our case the fiber is connected via a fiber splitter to the wavelength meter.

4 Experimental steps

This chapter is devoted to summarize the experimental steps needed to produce a degenerate quantum gas in our setup. Additionally, experimental protocols to the studies, presented in this thesis, are introduced.

4.1 Laser cooling

To reach quantum degeneracy we use several steps of cooling and trapping. In this section I will give a brief overview of the first cooling step used in this setup, the laser cooling.

The starting point of all the experiments is the lithium oven (see fig. 4.1). It is source of the lithium atoms and is filled with solid enriched ^{6}Li. At room temperature the vapor pressure inside the oven is $p_{sol,vap} \approx 10^{-20}$ mbar [95], which is too low for a sufficient particle flux in the atomic beam. Therefore, the oven is heated to a temperature of 658.15 K which is above the melting point of lithium $T_m = 453.65$ K. At this temperature the vapor pressure is fifteen orders of magnitude larger than at room temperature. The particle flux of the extracted atoms is large enough that subsequent cooling leads to a loading rate of about 2×10^8 atoms per second in the magnetooptical trap.

In the setup, the atoms are extracted via a nozzle from the oven leading to an atomic beam. It is collimated by an aperture, located in the beam path, and propagates towards the MOT chamber (see simplified sketch in fig. 4.1) inside a Zeeman slower. There, the atoms are cooled via laser cooling with a laser beam stabilized close to the D2-Line of lithium (see ref. [128] or [85, 123, 124]).

At laser cooling the particles are decelerated to velocities catchable with a MOT (typically a few mK). To reach the required velocities, the initial particle momentum has to be reduced by roughly ten thousand photon momenta. Therefore, the atoms have to undergo a multitude of absorption/emission events during laser cooling for which closed cooling cycles are required (see also energy level diagram in fig. 3.4). In our case we use the D2 transition of ^{6}Li for cooling. To avoid optical de-pumping of one of the electronic ground states within the cooling process we use two overlapped beams, resonant with the two relevant transitions $|2^2\text{S}_{1/2}, F = 1/2\rangle \rightarrow |2^2\text{P}_{3/2}\rangle$ and $|2^2\text{S}_{1/2}, F = 3/2\rangle \rightarrow |2^2\text{P}_{3/2}\rangle$.
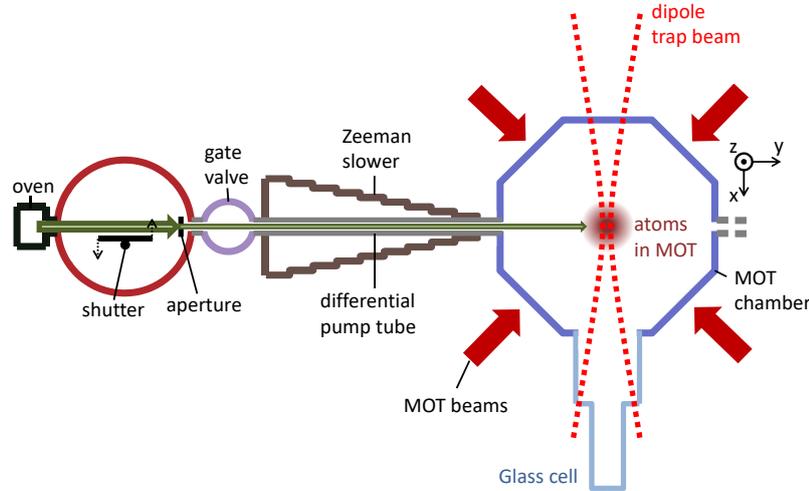
Figure 4.1: Simplified sketch of the vacuum setup (top view). The atoms leave the oven via a nozzle and are cooled on the way to the MOT chamber. Subsequently, the particles are trapped in the MOT from which they can be loaded to a dipole trap.

4.2 MOT

The pre-cooled atoms enter the MOT chamber with velocities on the order of a few ten meter per second (see also fig. 4.2). The atoms reach the MOT formed by a quadrupole field (see sec. 3.4) and six laser beams adjusted to intersect at the zero crossing of the magnetic field. The combination of the σ^- polarized red detuned[1] beams and the magnetic field (see fig. 4.2 b)) lead to a restoring force in both, the position and momentum space.

Using the MOT the atoms can be cooled down to the Doppler limit at which cooling and radiative decay induced heating matches (for more information see e.g. [85]). For the D2-Line of ^{6}Li, with a natural linewidth of $\gamma = 2\pi \times 5.87\,\text{MHz}$, the Doppler limit is $T_D = \hbar\gamma/2k_B \approx 141\,\mu\text{K}$. This value can not be reached in the case of ^{6}Li since the hyperfine states of the electronically excited state $2^2\text{P}_{3/2}$, which has a splitting of 4.4 MHz, can not be resolved (see also fig. 3.4). In our experiment, loading the MOT for a time of 4 s, about 10^9 (see fig. 4.2 a)) atoms can be captured. At this stage the gas has a temperature of $\approx 0.7\,\text{mK}$.

However, the phase space density (see e.g. [85]) of the captured gas is too low to provide an efficient transfer to the optical dipole trap. Therefore, we perform a compression of the MOT (cMOT) subsequently. In this step the detuning of the beam is reduced. This way, the restoring force inside the trap increases while the

---

[1]Red detuned to the D2 line.
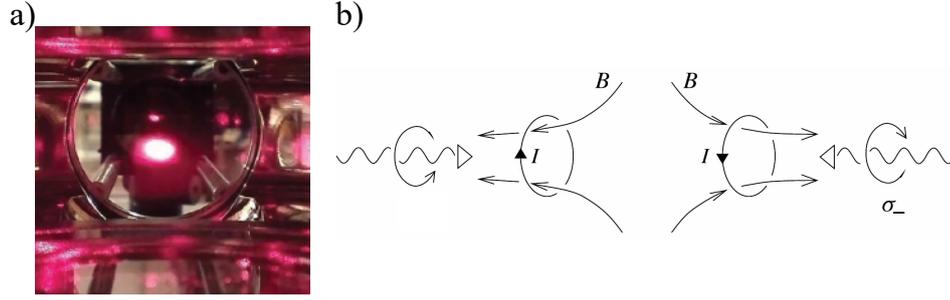
Figure 4.2: The lithium MOT. a) Photography of 10^9 lithium atoms at a temperature of $T_{MOT} \approx 0.7$ mK trapped in a MOT. b) Principle of the MOT taken from [85]. A quadrupole field combined with red detuned σ^- polarized beams forms the MOT.

trap size reduces. As a consequence, about half of the particles are lost and the temperature lowers to a value of $T_{cMOT} \approx 250$ μK. With this, we increase the phase space density of the cloud. It typically reads

$$\rho = n \times \lambda_{dB}^3 = n \times (h^2/(2\pi m k_B T))^{3/2} = 2.3 \times 10^{-5} \quad (4.1)$$

at the trap center. After the compression the gas is loaded to an optical dipole trap by overlapping MOT and dipole beam. During transfer about 1% of the atoms are loaded to the dipole trap, which is sufficient for the following steps.

4.3 Evaporative cooling in the presence of a bias magnetic field

After the cooling in the MOT the atoms are loaded to the optical dipole trap. For this purpose the dipole beam power is ramped up while the cooling beam intensity, as well as the quadrupole field, are ramped to zero simultaneously. After the transfer, the atoms are transported from the MOT chamber to the glass cell. The focus of the single beam optical dipole trap is shifted by moving a lens on an airbearing translation stage (for technical details see sec. 3.5 or [126]). Once the particles are moved to the glass cell, we ramp up the Feshbach and vertical gradient coils to produce a bias magnetic field.

The offset field has three consequences. First, it leads to a splitting of the hyperfine states to $|2^2S_{1/2}, F = 1/2, m_F = \pm\frac{1}{2}\rangle$ which enables us to produce a two-component Fermi gas (see sec. 4.4) favourable for efficient evaporative cooling [59, 139, 140]. Second, the bias magnetic field allows us to tune the particle interaction of atoms in these two spin states by means of a broad magnetic Feshbach resonance located at $B_0 = 832.2$ G [91]. Third, the field curvature produces an additional har-

monic confinement for the particles which essentially defines the confinement of the high field seeking particles in the x-axis (weakly confined axis of the dipole trap, see also fig. 4.1).

For evaporative cooling we tune to a magnetic field of 780 G, where a strong repulsive particle interaction with a scattering length of $6400a_0$ is present [88]. Evaporative cooling in a two-component strongly interacting Fermi gas has the advantage that a fast thermalization rate is provided. In our case, and at low temperatures, the energy is re-distributed during thermalization via s-wave collisions between atoms in the two states $|1\rangle$ and $|2\rangle$.

During evaporation, we lower the dipole trap depth from about 3.5 mK to below 1 µK within 6 s. Using this, the gas reaches quantum degeneracy with a the phase space density $\rho > 1$.

After evaporative cooling the magnetic offset field can be tuned to change the particle interaction as well as the chemical/thermodynamical state of the gas. For our gas there are two distinctive limits/regimes connected via the crossover (see sec. 2.5). For $(k_F a)^{-1} \gg 1$ the gas is in the BEC limit, where particles in opposite spin states can form dimers. For $(k_F a)^{-1} \ll -1$ we approach the BCS regime, where the Fermi character of the gas dominates and Cooper pairs form for $T < T_C$. The impact of the particle interaction becomes evident for $T < T_C$ in time-of-flight (TOF) experiments, where the momentum distribution can be obtained from the particle distribution.

Figure 4.3 shows the density distributions of clouds in the BEC and BCS regime at temperatures below T_C and after a TOF. The gas on the BEC side shows the expected bimodal distribution (see fig. 4.3 a), b)). It has a condensed core at the center showing a parabolic particle distribution and a thermal wing at the edges with a Gaussian particle distribution. In contrast, on the BCS side the gas smoothly approaches the $T = 0$ Fermi gas distribution for $T < T_C$ (see fig. 4.3 c), d)).

4.4 RF coupling

To control the distribution of ^{6}Li atoms over the states $|1\rangle$ and $|2\rangle$ at high magnetic field, or to measure the binding energy of Feshbach molecules, we make use RF transitions driven via the magnetic loop antennas introduced in sec. 3.6.

To drive the $|1\rangle \rightarrow |2\rangle$ transition in order to produce a balanced distribution of the particles we use an RF pulse at a frequency of $\nu \approx 76.198$ MHz which is resonant with the energy splitting at 780 G where evaporative cooling is performed typically (see also fig. 4.4 a)). The pulse has a power of ≈ 2 W and a duration of 150 ms. This allows us to produce an incoherent mixture of particles in the states $|1\rangle$ and $|2\rangle$. Figure 4.4 b) shows RF spectroscopy data on the $|1\rangle \rightarrow |2\rangle$ transition at 780 G. In the experiments the pulse is applied prior to the final evaporation step such that
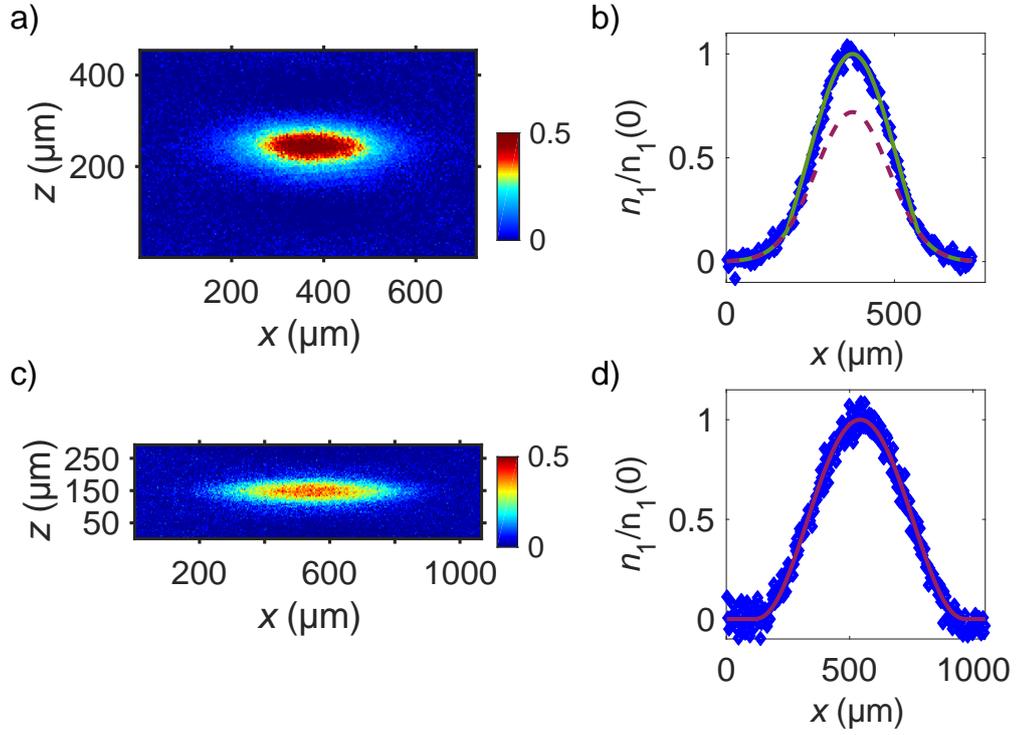
Figure 4.3: False color image of a mBEC and a degenerate Fermi gas after time-of-flight t_{TOF}. The color coding in the false color images indicates the number of particles per pixel along the line of sight. a) Partly condensed mBEC. The gas shows the characteristic bimodal distribution with a condensed core and a thermal wing. Here, the TOF is $t = 1.7\,\text{ms}$ and the magnetic field is $B = 726\,\text{G}$. b) Doubly integrated density profile using the data of a) (blue diamonds). As a guide to the eye a bimodal fit is applied (green line). For comparison a Gaussian fit is applied to the wings (red dashed line). c) Degenerate Fermi gas at $860\,\text{G}$ after TOF $t_{\text{TOF}} = 0.7\,\text{ms}$. d) Doubly integrated density profile using the data of c) (blue diamonds). The gas almost takes the form of a $T = 0$ Fermi gas (red line).

a balanced two-component Fermi gas is produced, supporting an efficient evaporation process.

Working with a balanced distribution has two advantages. First, the symmetry in the state occupation simplifies assumptions on the particle distribution of the trapped gas. Second, evaporative cooling is more efficient since thermalization via s-wave collisions are enhanced in a balanced distribution.

Besides the preparation of the two-component gas, we use RF spectroscopy on the $|2\rangle \rightarrow |3\rangle$ transition to determine the binding energy of the dimers (as reported in [91, 94]). Fig. 4.4 c) shows the spectrum of a measurement at 755 G. Here, we measured the number of particles N in $|2\rangle$ after a RF pulse with a frequency of ν (N_0 is the baseline of the spectrum). We find a resonance at $\nu \approx 82.198$ MHz, where unbound atoms are transferred from $|2\rangle$ to $|3\rangle$. For atoms bound to dimers this transition is shifted by the binding energy (see fig. 4.4 c) red circles), where the RF signal drives a bound-to-free transition and leads to a broad resonance with a large tail to higher frequencies. The large tail can be explained with the final state of the unbound atoms. The particles transferred to $|3\rangle$ can occupy a variety of external/trap states (see [91]). From the spectrum shown in fig. 4.4 c) we obtain a binding energy of $E_b \approx 40.5$ kHz $\times h$, which is consistent with the values reported in ref. [91].

4.5 Trapping potentials in the glass cell

This section is devoted to give a brief overview of the potentials used in our experiments. The experiment is constructed to provide several well controlled potentials which can be used to control/tune the motional states of the ultracold particles. Additional potentials can be easily included which makes this assembly an ideal testbed for almost arbitrary configurations.

The starting point for all studies performed in the glass cell is an ultracold cloud confined by the optical dipole trap and the field curvature of the Feshbach and the vertical gradient coils (see fig. 4.5). The magnetic field curvature produces an almost harmonic confinement in the x-y-plane with a trapping frequency of $\omega_x = 2\pi \times 21$ Hz. The single beam dipole trap produced by a focused TEM$_{00}$ laser beam with a minimal waist of $w = 38\,\mu$m and a Rayleigh length of $z_R = 4.3$ mm, generates a cylinder symmetric confinement along the x-axis (see fig. 4.5 a)).

Due to the large Rayleigh length, the confinement of the dipole trap in the x-direction is weak compared to the magnetic confinement and can be neglected in good approximation. In contrast, in the other two directions the dipole trap dominates the potential of the magnetic field curvature which leads to a cylinder symmetric trap where the radius is given by $r^2 = y^2 + z^2$. This confinement can be considered to be harmonic at the center $r \approx 0$, with a tunable trapping frequency

a)

b)

c)
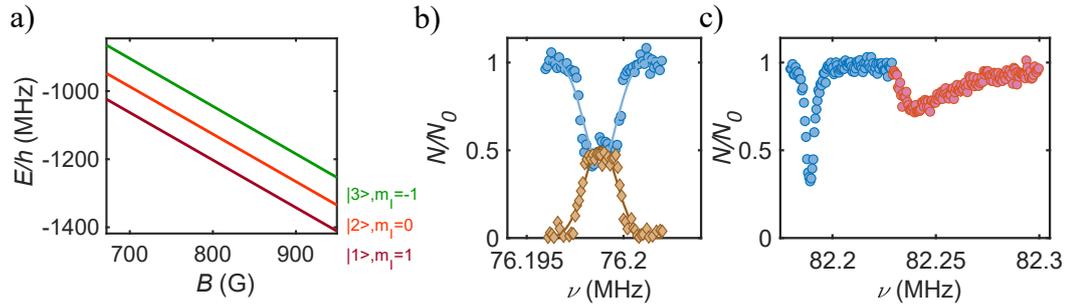
Figure 4.4: RF spectroscopy. a) Energy splitting of the lowest hyperfine states in a magnetic field range of 670 G to 950 G. b) Spectroscopy on the $|1\rangle \to |2\rangle$ transition at 780 G. All particles are loaded into $|1\rangle$ (blue circles), initially. N/N_0 gives the number of atoms in $|1\rangle$ with respect to the total number of atoms in the gas. Once the resonance is reached at $\nu_0 = (76.198 \pm 0.001)$ MHz atoms are transferred from $|1\rangle$ to $|2\rangle$ and N reduces. To determine the resonance position a Gaussian (dip) fit is used (straight line). The line is broadened by magnetic field instabilities given by the finite resolution of the magnetic field control of roughly 1 G. For comparison a measurement to the $|2\rangle$ occupancy (brown circles) is shown. c) RF spectroscopy on the $|2\rangle \to |3\rangle$ transition on a mixed gas of dimers and free atoms at $B = 755$ G. For $\nu \approx 82.198$ MHz the unbound atoms are transferred to $|3\rangle$ such that the number of particles in $|2\rangle$ reduces (blue circles). Here, N_0 is the baseline of the spectrum. The RF transition for atoms in $|2\rangle$, and bound to dimers, is shifted from the RF transition $|2\rangle \to |3\rangle$ by the binding energy (red circles).
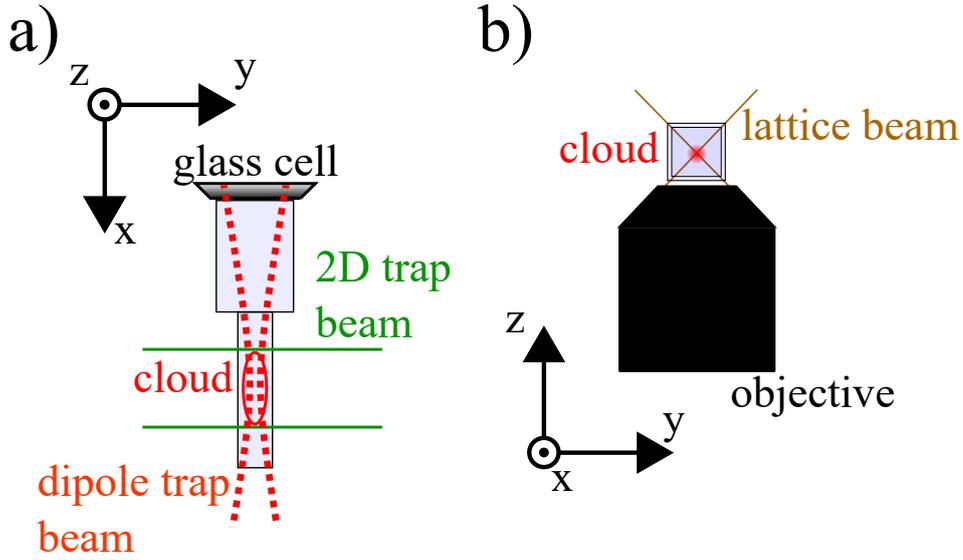
Figure 4.5: Sketch of the trapping beams at the glass cell. a) Top view of the glass cell including the dipole trap beam and the beam for the 2D confinement. b) Side view of the glass cell. The objective, located below the glass cell, projects the lattice onto the cloud. Please note that the offset (Feshbach) magnetic field is oriented along the z-direction.

ω_r ranging from a few hundred Hz to a few ten kHz. Considering magnetic and optical confinement, the particles experience the following potential

$$U = \frac{1}{2}m\omega_x^2 x^2 + \frac{1}{2}m\omega_r^2 r^2. \tag{4.2}$$

2D confinement

In order to perform experiments in two-dimensional gases, an additional 2D confinement (see fig. 4.5 a)) is added. This is done using the repulsive potential produced by the TEM_{01} beam introduced in sec. 3.8. In our case, we superimpose the potential created by this additional beam with the previously introduced trap. Figure 4.6 a) shows the corresponding potential. In the illustration the gravity, which causes a tilt in the potential along the z-axis, is neglected. At the trap center the particles experience a harmonic confinement in x-direction given by the field curvature of the offset magnetic field, in y-direction by the dipole trap beam, and by the TEM_{01} beam in the z-direction. For $z > 0$ the particles experience the anti-trapping potential of the TEM_{01} beam (see fig. 4.6 b)) leading to an anharmonicity of the trap. Therefore, only in the close vicinity of the trap center the confinement can be considered to be harmonic in good approximation.
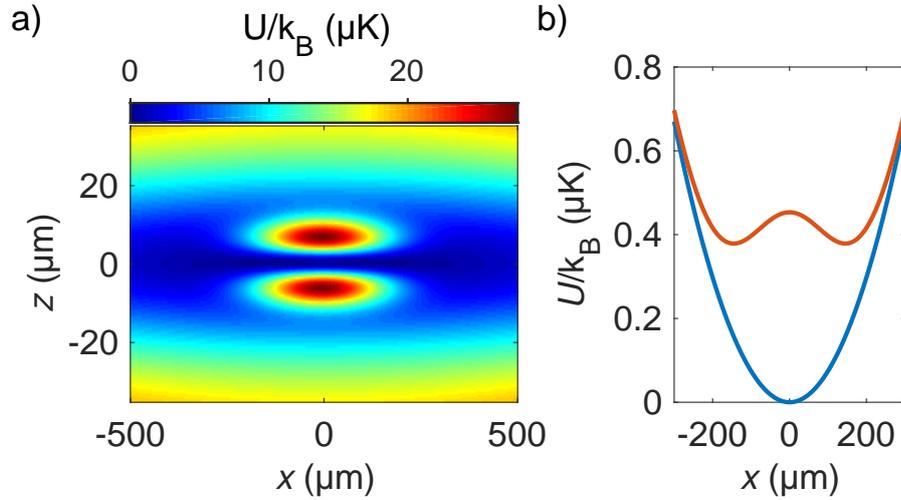
Figure 4.6: Potential for the 2D confinement. a) False color image of the potential at the center of the glass cell $y = 0$ (dipole beam power 0.8 W, power of 2D confinement beam ≈ 2 W). The color coding indicates the potential energy U. b) Potential at $z = 0$ ($z = 0.5\,\mu$m) blue (red) straight line, respectively. The attractive confinement is given by the field curvature of the coils. For $z = 0.5\,\mu$m the gas experiences the anti-trapping potential of the TEM_{01} beam.

Optical lattices

Besides experiments in two dimensions, our setup is constructed to provide studies of cold atoms in optical lattices. We can superimpose the lattice beams with the other traps to produce an additional periodic potential (see sec. 3.9). In general, to calculate the intensity pattern of the projected beam, Fourier optics are used to obtain the intensity distribution at the focus of the high NA objective. However, at this point it is instructive to simplify the projected pattern. In the following, we consider the lattice to be produced by a cluster of individual dipole traps/dimples added to the previously introduced traps. Close to the focus of the projecting system this assumption holds in good approximation. Figure 4.7 a) shows the potential for a single well. The dimensions of the dimple shown here are limited by the resolution of the objective of 1.1 μm at the projection wavelength of $\lambda_{Lat} = 1064$ nm. In future experiments we expect to have small lattices with about 50 wells and will use a laser power of 0.5 W per well. The corresponding trapping frequencies for such a potential are $\omega_{x,y} = 2\pi \times 1.04$MHz and $\omega_z = 2\pi \times 250$kHz.

The trapping frequencies in x- and y-direction as well as the trap depth is much larger as in standard dipole traps used for neutral atoms. However, for single-site single-atom imaging of light particles as lithium (see also chapter 7) this is favorable [74, 75]. Deep lattices have the advantage that tunnelling is suppressed
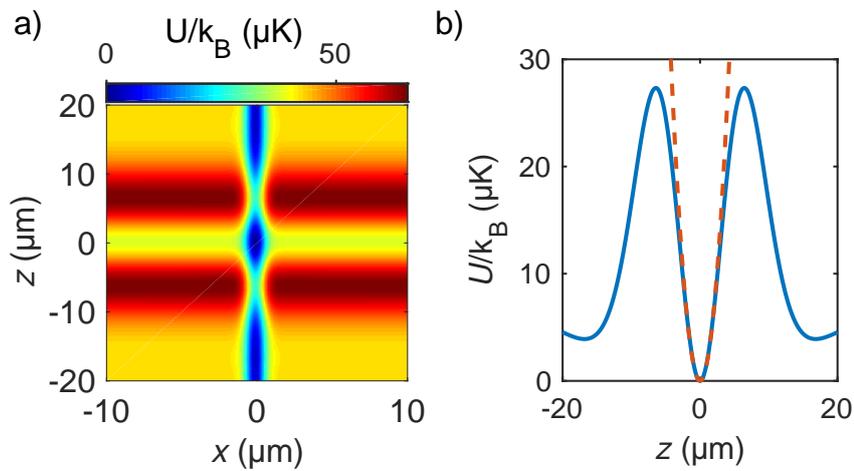
Figure 4.7: Lattice projection. a) The 2D trap, the dipole trap, and the magnetic field confinement are superimposed with a single beam dipole trap representing a single well of a projected lattice. The color coding gives the potential energy U. Here, I assume that the dimple is produced by a beam with a power of $1\,\mathrm{mW}$ and a waist of $1.1\,\mu\mathrm{m}$. Please note, that gravity is not included in the calculation, since it is small compared to the other contributors and can be neglected. b) Shows the potential of a) at $x = 0$. At the trap center the potential (blue line) is almost harmonic. The red dashed line shows a parabolic fit to the trap center.

and Raman sideband cooling can be applied, using state of the art laser sources.

4.6 Quasi 2D gases

With the trapping potentials introduced in the previous section, we are able to produce a quasi 2D quantum gas. For this, a pre-cooled gas is transferred to the 2D confinement produced by the dipole trap, the magnetic trap and the TEM_{01} beam trap. This is done adiabatically ramping up the intensity of the TEM_{01} beam within $300\,ms$ to a full power of $\approx 2\,W$. After the loading process the confinement is defined by the single beam dipole trap in the y-direction, the field curvature of the FBC and VGC in the x-direction and by the TEM_{01} beam in the z-direction.

To be kinematically two-dimensional, the gas has to fulfil several requirements (see sec. A.1). In such a trap the number of Fermions in the lowest transversal state (z-axis) with $n_z = 0$ is limited by the in-plane trapping frequencies ω_x, ω_y and is called critical particle number $N_{crit} = \omega_z^2/2\omega_x\omega_y$ [141]. This quantity can be measured. Figure 4.8 shows an experiment performed to determine the critical particle number experimentally at $900\,G$ (here $(k_F a)^{-1} < -1$) for $\omega_z = 2\pi \times 7.5\,kHz$, $\omega_x = 2\pi \times 21\,Hz$ and $\omega_y = 2\pi \times 65\,Hz$ (analog experiment as in ref. [141]). There, the expansion of a cloud released from the trap is measured as a function of the number of particles loaded to the trap. In our experiment, the particle number is tuned using a magnetic field gradient along the z-axis during sample preparation. The field gradient produces an additional force in negative z-direction, which removes particles from the trap selectively (similar to the technique used in [142]). Performing TOF experiments on clouds with varying initial particle number, we find that the expansion of the gas, given by the cloud size σ_z, is almost constant for $N < N_{crit} \approx 2.0 \times 10^4$ which is in good agreement with a calculated critical particle number of $N'_{crit} = 2.06 \times 10^4$ for a non-interacting 2D gas.

Below the critical particle number all atoms are in the motional ground state in the z-direction which leads to a particle number independent expansion of the cloud. For $N > N_{crit}$ σ_z increases almost linearly for larger particle numbers where higher transversal states are occupied. Please note, that in principle the critical particle number is scattering-length dependent. The redistribution of energies in collisions can excite higher transversal states as observed in ref. [143]. However, for $(k_F a)^{-1} < -1$, which is the case in our experiment, the influence of the interaction is small and the critical particle number can be directly obtained by measuring $\sigma_z(N)$ in a TOF experiment.

Our result indicates that a quasi 2D gas can be produced in our setup which is a prerequisite for future studies in two dimensional systems.
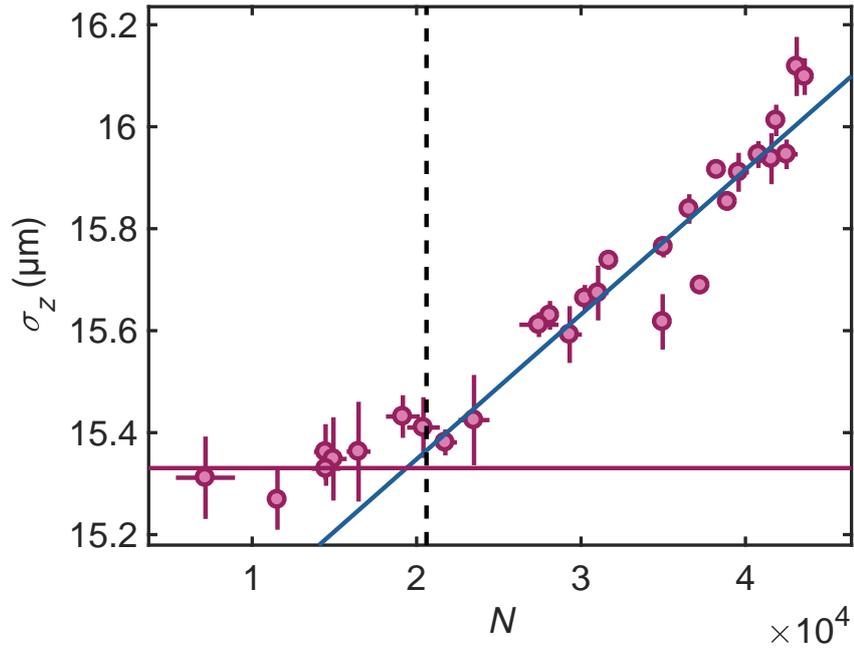
Figure 4.8: Time of flight (TOF) experiment on a quasi 2D Fermi gas. A degenerate Fermi gas at 900 G is loaded into the 2D confinement and released from the trap subsequently. We measure the cloud expansion after a time of flight of t_{TOF} in the z-direction $\sigma_z(t_{TOF})$ for various initial particle numbers N. Here, N is the number of particles per spin state. Increasing N we cross N_{crit}. For $N < N_{crit}$ all particles are in the transversal ground state where σ_z is constant. The red line gives the mean value for $N < N_{crit}$. For $N > N_{crit}$ atoms occupy states with $n_z > 0$ and σ_z increases with the particle number. The blue line is a linear fit to the data for $N > N_{crit}$, used as a guide to the eye. For comparison the calculated critical particle number $N'_{crit} = 2.06 \times 10^4$ is shown (black dashed line).

4.7 Optical lattice

To perform experiments in an optical lattice, we load the cooled gas from the 2D trap into the lattice. This is done by ramping up the optical lattice within 300 ms to the desired trap depth. Once particles populate the lattice, the initial confinement can be ramped down such that the particles are trapped by the projected lattice, solely.

Figure 4.10 shows the particle distribution for a first experiment in an optical lattice where about 300 atoms are loaded into a lattice with a weak in plane confinement of a few hundred Hz. The particles have enough thermal energy to delocalize over the lattice. The lattice constant $d \approx 2.4\,\mu$m in the experiment presented here is approximately a factor of two larger than in future experiments.

Most of the future experiments will address the physics in a honeycomb potential at half filling, where each lattice site is occupied by a single atom. To prepare this configuration the lattice sites have to be emptied down to a single particle per well, occupying the motional ground state, prior to subsequent experiments. This can be done applying a magnetic field gradient along the z-direction (see also ref. [142]). The field gradient produces a tilted harmonic potential, where the particles can tunnel through the lowered barrier to unconfined states. Similar as in evaporative cooling this way the number of atoms can be reduced to the desired state occupancy.

To investigate the dynamics or the equilibrium states of such an ensemble, single particle detection is desired. However, the detection of individual atoms in a flat optical lattice is complicated. The direct fluorescence imaging of the atomic distribution requires a large number of scattered photons per particle for a sufficient detection fidelity. A large number of scattered photons heats the atoms, which complicates to localize particles on a singe lattice site during detection.

In the following lines I will estimate requirements for a sufficient single-atom detection in our case. Our imaging system basically consists of a high resolution objective with $NA = 0.61$, a tube lens, and an EMCCD camera with a pixel size of 16 μm and a quantum efficiency of 90% (see fig. 4.9a)). Another important boundary condition is the transmission loss of the detection system which is roughly 40% in our case.

To calculate the intensity distribution on the camera we have to consider that individual atoms in the lattice act as localized point sources. During detection this leads to an array of airy disks on the camera (see fig. 4.9b)). To get the requirements for the signal strength or number of scattered photons in a detection process, I calculated the intensity distribution for a partially occupied lattice with 36 sites in the detection plane (see fig. 4.9e)). To be as realistic as possible, I added shot and readout noise to the intensity distribution (see fig. 4.9c)). The shot noise is caused by photon statistics, while readout noise is caused by the electronics of the camera. For the readout noise I considered a Gaussian distributed noise with a standard

a)

objective

iXon

atom

tube lens

b)

y

x

c)

0   0.5   1

y (µm)

-5

0

5

-5   0   5

x (µm)

d)

occurence

1000

500

0

0   0.5   1

normalized amplitudes

e)

0   0.5   1

y (µm)

-5

0

5

-5   0   5

x (µm)
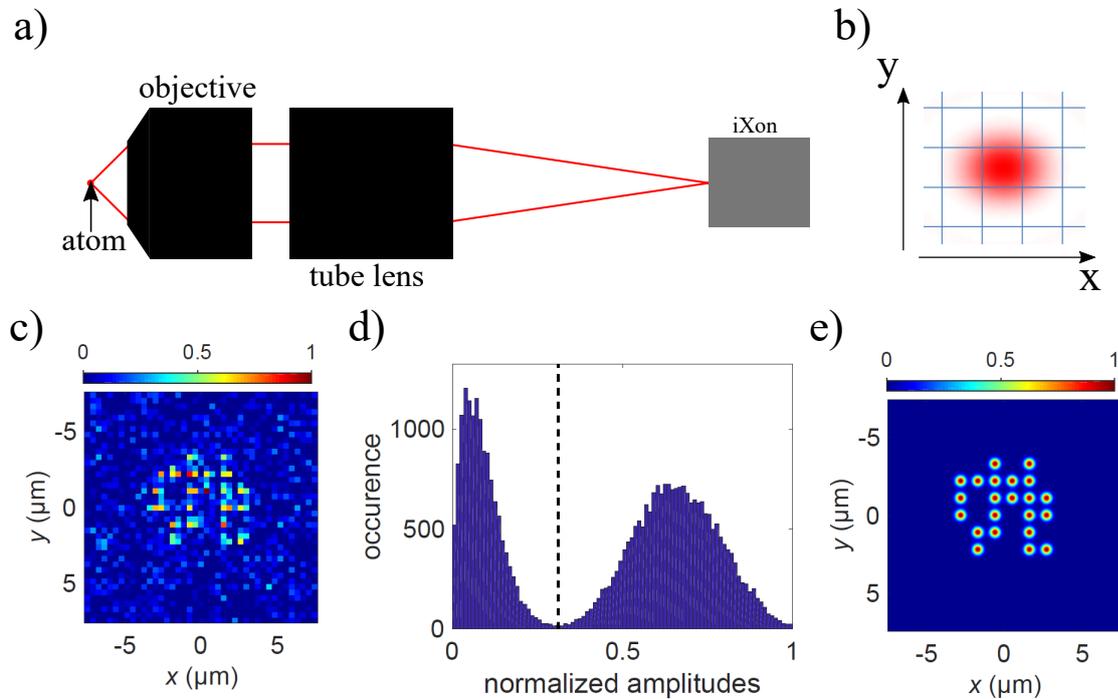
Figure 4.9: Simulation of a single-site single-atom detection. a) Setup for the flu-
orescence detection with the high NA objective, the tube lens, and the
EMCCD camera (see also sec. 3.7). b) During fluorescence detection
an individual atom acts as a point-like light source. This leads to an
airy disk on the detector for each emitter/atom. With the given resolu-
tion, the light of a single atom mainly distributes over nine pixels. c)
Calculated intensity distribution for a direct fluorescence detection of a
small partially occupied lattice with 36 sites. In the calculation I have
considered 1700 scattered photons per atom and added shot and read-
out noise. With the given photon number a detection fidelity >99% can
be reached applying Gaussian fits on each lattice site. d) Amplitude
distribution obtained from Gaussian fits applied on 1000 calculated in-
tensity distributions. To discriminate between empty and occupied sites
a threshold rule is defined (dashed line) which set to 0.4 for the normal-
ized amplitudes obtained from the fits. e) Simulation of a fluorescence
image with smaller pixel size and without noise for comparison.

.

deviation of 3 counts, which is a typical value for high performance cameras (see also sec. 7).

To determine the impact of the signal strength on the image quality I have to define a fidelity for the detection. Here, it is given by the percentage of successfully reconstructed occupied (unoccupied) lattice sites. To determine the lattice occupancy in the calculation, I have performed a Gaussian 2D fit on every lattice site. From the amplitude distribution of the Gaussians for 1000 individual simulations a threshold law (see fig. 4.9d)) for occupied lattice sites is defined and is used to determine the fidelity. From the calculation I find that the fidelity reaches values $> 99\%$ for about 1700 scattered photons per atoms, which is sufficient for single-atom detection in such a lattice experiment.

However, as mentioned above, using such a large number of scattered photons comes at a price. Each scattering event heats the trapped particles. A large number of scattered photons can cause excitations to higher lying external states (bands/trap states). The tunnelling rate between neighbouring lattice sites for high lying bands is increased and particles tend to delocalize during detection which complicates the single-atom single-site detection.

However, recently the detection of fermions in such a lattice has been reported [74, 75, 144]. To avoid the delocalization or losses the groups performed imaging in a deep optical lattice with trapping frequencies on the order of $\omega > 1\,\mathrm{MHz}$ in all spatial directions and additional Raman sideband cooling. Especially, the deep optical lattice has two major advantages. First, the excitation of the particles to higher lying trap/well states is suppressed. Second, the large state separation enables Raman sideband cooling with high selectivity.

In our experiment, it is planned to implement the reported scheme in future work. However, up to now our setup does not provide the required laser beam power for a pinning lattice as in the recent work. Nevertheless, the first steps towards single-site single-atom detection have been made by implementing lattice projection and by setting up the light source for the sideband cooling technique (see [145]). A next step would be to set up a laser source to provide the power for a sufficiently deep pinning lattice.
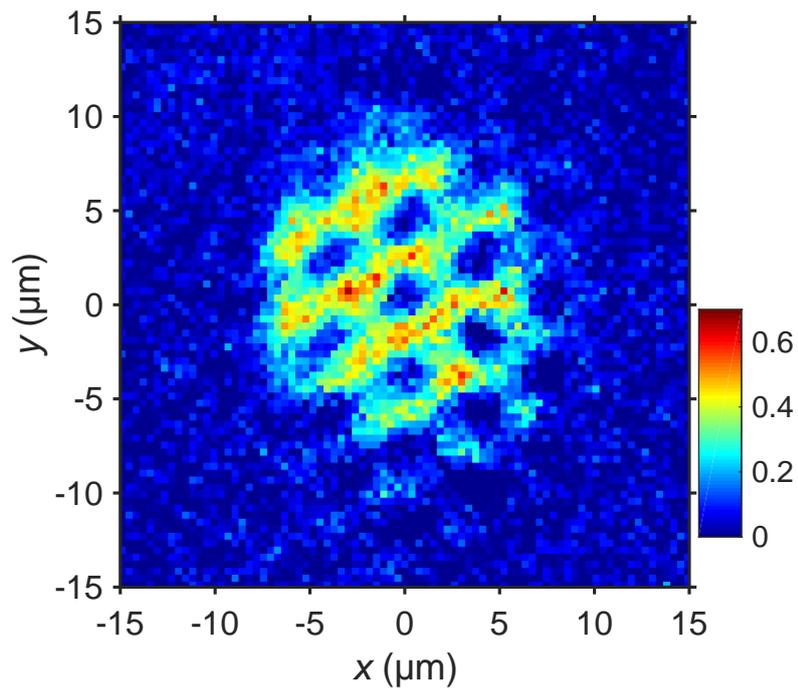
Figure 4.10: Particles in an optical lattice (The false color image gives the number of particles per pixel along the line of sight). We use the high NA detection system for absorption imaging (see also sec. 3.7 and sec. 3.9). The lattice has a size of about 30 wells. The total number of atoms is ≈ 300 and the lattice constant is $d \approx 2.4\,\mu$m. A single pixel corresponds to $0.37\,\mu$m in the object plane.

5 Reaction kinetics in ultracold molecule-molecule collisions

The content of the sections 5.1 to 5.6.3 has been published in Nature Communications. The material is taken from:

Hoffmann, D. K., Paintner, T., Limmer, W., Petrov, D. S., and Hecker Denschlag, J., *Reaction kinetics in ultracold molecule-molecule collisions*, Nat. Commun. **9**, 5244 (2018), DOI: https://doi.org/10.1038/s41467-018-07576-1.

Remarks: The authors acknowledge the publication in Nature Communications. The content can also be found on arXiv: 1805.08128. Please note that the format of the (journal) article was modified in order to fit the style and layout of the thesis. Hence a consecutive numbering of figures and references for the whole thesis was applied as well.

5.1 Abstract

Studying chemical reactions on a state-to-state level tests and improves our fundamental understanding of chemical processes. For such investigations it is convenient to make use of ultracold atomic and molecular reactants as they can be prepared in well defined internal and external quantum states.

Here, we investigate a single-channel reaction of two Li_2-Feshbach molecules where one of the molecules dissociates into two atoms $2AB \Rightarrow AB + A + B$. The process is a prototype for a class of four-body collisions where two reactants produce three product particles. We measure the collisional dissociation rate constant of this process as a function of collision energy/ temperature and scattering length. We confirm an Arrhenius-law dependence on the collision energy, an a^4 power-law dependence on the scattering length a and determine a universal four body reaction constant.

5.2 Introduction

The field of ultracold chemistry has been demonstrating an increasing level of control over internal and external states of atomic and molecular reactants [3, 4, 17, 146]. However, even cold reactions have in general many possible final product states [32, 33, 35, 36, 38, 147–152] and reaction channels are therefore hard to track individually [39]. Nevertheless, reactions do exist where essentially only a single reaction channel is participating, such as atom-Feshbach molecule exchange reactions in Bose-Bose [153] and Bose-Fermi [154] mixtures, and three-body recombination A+A+B→AB+A in a Fermi-Fermi mixture [8]. Especially for reactions involving identical Fermions the Pauli exclusion principle can lead to a particularly strong single-channel character and can also ensure a high collisional stability of AB molecules. By contrast, for a reaction A+B+D→AB+D, where A, B, and D are distinguishable atoms, the Pauli exclusion principle does not play a direct role. In the limit of zero-range interactions the A-A-B and A-B-D systems belong to different universality classes, denoted non-Efimovian and Efimovian, respectively. Efimov physics and a broad range of associated phenomena have recently been studied to a great extent [24, 28]. Here, we report on the first observation and characterization of the ultracold non-Efimovian reaction AB+AB→A+B+AB (break-up) and its inverse A+B+AB→AB+AB (three-body recombination). Besides being intrinsically four-body, these reactions also exhibit two- and three-body aspects. A peculiarity is that although the molecule AB is distinguishable from the atoms A and B, similar as for particle D, the large size of the weakly-bound AB molecule prevents, however, the system from being Efimovian. A simple dimensional analysis then suggests [155] that at low energies the recombination rate constant reads $R_2 = C\hbar a^4/m$, where a is the AB scattering length, m is the atom

mass, and C is a *universal* number.

In our experiments we measure R_2 and the break-up rate constant C_2 using a gas of ^{6}Li atoms in the lowest two hyperfine states denoted by A and B and weakly-bound AB dimers. By driving the mixture out of chemical equilibrium we observe the subsequent reaction dynamics. Our measurements confirm the detailed-balance relation between these two constants [98] R_2 and C_2 and, in particular, the Arrhenius law for the break-up reaction. We confirm this a^4-dependence of R_2 and provide the first experimental estimate for $C \approx 470$. Our results are important for the stability problem of a pure atomic mixture, an issue proved to be relevant for the controversial issue of itinerant ferromagnetism (see, for example ref. [156, 157]). Due to the different threshold laws and the large value of C, the reaction A+B+AB→AB+AB may be faster than A+A+B→AB+A, as soon as there is a sizeable seed of bound AB molecules in the system [98].

5.3 Results

5.3.1 Experimental scheme

The initial atomic and molecular sample is prepared from an ultracold gas of $N_{\text{tot}} = 2.6 \times 10^5$ fermionic ^{6}Li atoms which consists of a balanced mixture of the two lowest hyperfine states $|m_F = \pm 1/2 >$ of the electronic ground state. In the vicinity of the Feshbach resonance at $B_0 = 832.2\,$G (see ref. [91]) exothermic three-body recombination can convert pairs of $|-1/2 >, |+1/2 >$ atoms into weakly-bound Feshbach molecules with the same well defined internal quantum state. The process is reversible and a Feshbach molecule can dissociate again into the unbound $|-1/2 >, |+1/2 >$ atoms via an inelastic, endothermic collision with another molecule or atom. At thermal equilibrium balance of the back and forth reactions is established. This balance is a function of the particle densities, temperature, molecular binding energy, and scattering length, all of which can be controlled in our setup via confinement, evaporative cooling, and by choosing a magnetic offset field $B < B_0$. Our trap is a combination of a magnetic trap and an optical dipole trap and is cigar shaped. The trap has a depth of $U_0 = 21\,\mu\text{K} \times k_{\text{B}}$, corresponding to a radial (axial) trapping frequency of $\omega_{\text{r}} = 2\pi \times 0.99\text{kHz}$ ($\omega_{\text{ax}} = 2\pi \times 21\text{Hz}$), respectively. We use evaporative cooling to set the temperature to approximately 1.2 to 1.3 μK. At this temperature 80% to 90% of all atoms are bound in Feshbach molecules within the B-field range of 705 G to 723 G of our experiments, corresponding to a binding energy E_{b} between 6 and 10 μK × k_{B} (see Methods). We note that at these settings where $T \geq T_{\text{F}}$ (T_{F} is the Fermi temperature) and $E_{\text{b}} > k_{\text{B}}T_{\text{F}}$, quantum degeneracy only plays a negligible role for the reaction kinetics.

In our first experiment we suddenly raise the temperature of the gas using an excitation pulse of parametric heating. This shifts the gas out of thermal equilibrium
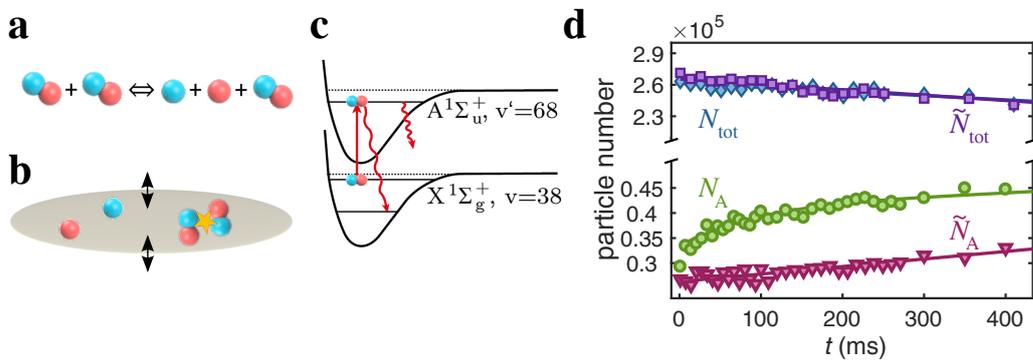
Figure 5.1: Molecule dissociation dynamics. **a** Detailed balance of collisional dissociation and association of dimers. **b** A parametric heating pulse triggers the reaction dynamics. **c** As part of the detection scheme, the Feshbach molecules which have a large admixture of the $X^1\Sigma_g^+, v = 38$ state are optically pumped to undetected atomic or molecular states via the intermediate level $A^1\Sigma_u^+, v' = 68$. **d** Measurement of dissociation dynamics at 709 G. Lower part: Circle (triangle) symbols show the number of unbound atoms N_A ($\tilde{N}_A$) for variable holding time t with (without) initial parametric heating pulse. Upper part: Diamond (square) symbols show the total particle number N_{tot} ($\tilde{N}_{\text{tot}}$) with (without) parametric heating pulse.

and the gas responds by collisionally dissociating a part of its molecules, (see fig. 5.1a). For this, we modulate the dipole trap depth (see fig. 5.1b) with frequency $\omega_{\text{heat}} \approx 1.7\omega_{\text{r}}$ and amplitude $\Delta U = 0.21 U_0$ during a period $t_{\text{p}} = 20\,\text{ms}$. After the excitation atoms and dimers thermalize on a time scale of a few milliseconds via elastic collisions, whereas the chemical equilibrium requires a much longer time of $150\,\text{ms}$.

5.3.2 Dynamics

To investigate these dynamics we measure how the number of molecules N_{M} and the number of unbound atoms N_{A} change as a function of time. We measure N_{A} by using standard absorption imaging. However, prior to the imaging we first remove all Feshbach molecules from the gas. For this, a resonant laser pulse transfers the molecules to an electronically excited molecular state $A^1\Sigma_{\text{u}}^+, v' = 68$ which subsequently decays with in a few ns to undetected atomic or molecular states [99, 105] (see fig. 5.1c), see Methods. The laser pulse has a duration of $0.5\,\text{ms}$ which is short compared to the reaction dynamics. In order to determine N_{M} we measure in a second run the total number of atoms $N_{\text{tot}} = 2N_{\text{M}} + N_{\text{A}}$, whether they are bound or unbound, and subtract N_{A}. For this we use again absorption imaging. The Feshbach molecules are so weakly bound that the imaging laser resonantly dissociates them quickly into two cold atoms which are subsequently detected via absorption imaging [86].

Figure 5.1d shows the measurements of N_{A} and N_{tot} as a function of holding time after the heating pulse. While the total number of atoms N_{tot} is essentially constant apart from some slow background losses, the atom number N_{A} exhibits a 30% increase in about 100ms which is the dissociation response of Li_2 molecules to the thermal pulse. Besides this, N_{A} also exhibits a slow, steady increase which we attribute to a background heating of the gas, e.g. due to spontaneous photon scattering of the dipole trap light (see Supplementary Note 1[1]). As shown by $\tilde{N}_{\text{A}}$ in fig. 5.1d) this background heating is also present in the absence of the initial heating pulse. Similarly, the slow decay of N_{tot} is also present without the heating pulse (see $\tilde{N}_{\text{tot}}$ in fig. 5.1d). It can be completely explained by inelastic collisions between molecules as previously investigated in ref. [104].

In principle, collisional dissociation in our experiment can be driven either by atom-molecule collisions or by molecule-molecule collisions. We only consider molecule-molecule dissociation since its rate is about two orders of magnitude larger in our experiments than for atom-molecule dissociation with its known rate constant of [98] $C_1 \approx 10^{-13}\text{cm}^3\,\text{s}^{-1}$ and given the fact that the mean density of atoms is a factor of ten smaller than for the dimers. In a simple physical picture, the suppression of the atom-dimer dissociation is due to the Pauli principle act-

---

[1]See also sec. 5.6.1

ing on the outgoing channel, which involves two identical fermionic atoms [158, 159]. In the molecule-molecule collisional dissociation, the molecules can either dissociate into four unbound atoms, $2AB \Rightarrow 2A + 2B$, or into two unbound atoms, $2AB \Rightarrow AB + A + B$. However, since in our experiments the molecular binding energy E_b is typically by a factor of 5 larger than the thermal energy $k_B T$, the dissociation into four atoms comes at an additional sizeable energy cost and is therefore comparatively suppressed by an Arrhenius factor of $\exp(-E_b/k_B T) \approx 7 \times 10^{-3}$, see also [98]. Therefore, to first order, we only need to consider dissociation into two atoms. The evolution of the density n_A of unbound atoms is then given by the rate equation,

$$\dot{n}_A = 2 C_2 \, n_M^2 - R_2 \, n_A^2 \, n_M / 2 \tag{5.1}$$

Here, n_M is the molecule density and C_2 (R_2) are the rate constants of molecule dissociation (association). A spatial integration of eq. 5.1 gives the rate equation for the number of unbound atoms,

$$\dot{N}_A = (4\pi^{3/2})^{-1} \frac{C_2}{\sigma_r^2 \sigma_{ax}} N_M^2 - 2^{-7} (2\pi^2)^{-3/2} \frac{R_2}{\sigma_r^4 \sigma_{ax}^2} N_A^2 N_M \tag{5.2}$$

where we assume a Boltzmann distribution in a harmonic trap. Here, $\sigma_{r(ax)} = \sqrt{k_B T / 2m\omega_{r(ax)}^2}$ denote the radial (axial) cloud width of the molecular gas and m is the mass of ^{6}Li. Furthermore, in eq. 5.2 we have used the fact that the cloud size for the unbound atoms is $\sigma_{r(ax),A} = \sqrt{2}\sigma_{r(ax)}$. By fitting eq. 5.2 to the data of fig. 5.1d we can determine the rate coefficients to be $C_2 = (2.0 \pm 0.6) \times 10^{-12}\,\mathrm{cm}^3\,\mathrm{s}^{-1}$ and $R_2 = (4.1 \pm 1.2) \times 10^{-22}\,\mathrm{cm}^6\,\mathrm{s}^{-1}$. For the fit we use the measured widths $\sigma_{r(ax)}$ which turn out to be fairly constant during the holding time t (a more detailed discussion will be given below).

5.3.3 Temperature dependence

Next, we investigate how the reaction rates depend on temperature. For this, it is convenient to study the atom molecule system in a state of near equilibrium, where $\dot{N}_A \approx 0$, i.e. $\dot{N}_A$ is much smaller than the individual collisional dissociation/association rates of eq. 5.2. We can then set $\frac{C_2}{R_2} = 2^{-5}(2\pi)^{-3/2} \frac{1}{\sigma_r^2 \sigma_{ax}} \frac{N_A^2}{N_M}$. Thus, a change in the ratio C_2/R_2 due to a variation in temperature, can be experimentally observed in terms of a change of particles numbers and widths. Figure 5.2a shows such measurements at $B = 723\,\mathrm{G}$ ($\dot{N}_A$ was always at least a factor of ten smaller than the collisional dissociation/association rates). Within the small temperature range between 1 and $3\,\mu\mathrm{K}$, the rate constant ratio $\frac{C_2}{R_2}$ increases by more than two orders of magnitude. This result can be compared to a prediction based on statisti-
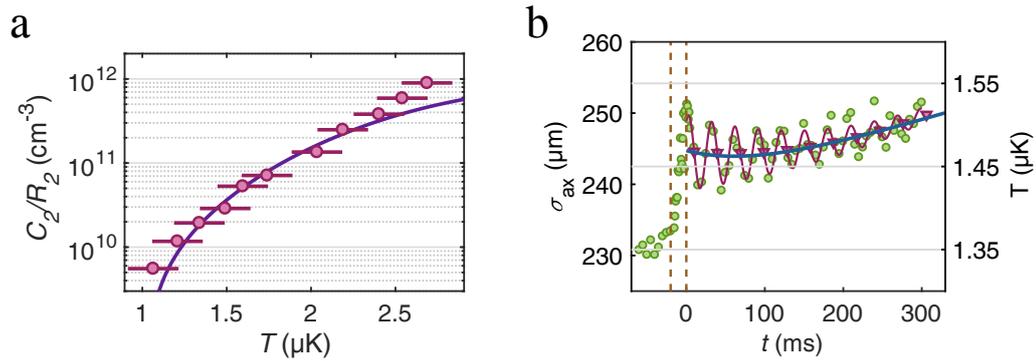
Figure 5.2: Temperature dependence of the equilibrium state and temperature evolution. **a** The ratio C_2/R_2 (circles) is plotted as a function of temperature T at $B = 723$G. The errorbars denote the s.d. in the thermometry. The continuous line is a calculation without any free parameters (see text passage to Temperature dependence). **b** Measured evolution of the axial cloud size σ_{ax} (green circles) at $B = 705$G after injecting a heat pulse during -20 ms$< t < 0$ ms (vertical dashed lines). The heat pulse abruptly increases the temperature T and size $\sigma_{ax} \propto \sqrt{T}$. In addition it excites small collective breathing mode oscillations, see red line as a guide to the eye. The red triangles mark the evolution of σ_{ax} when averaged over one oscillation period. This evolution is well described by a model calculation (blue line) as described in Supplementary Note 1 and Supplementary Fig. 1^2. The temperature scale applies to the non-oscillatory part of the data.

cal mechanics [98],

$$\frac{C_2}{R_2} = h^{-3}(\pi m k_{\mathrm{B}} T)^{3/2} \mathrm{e}^{-E_{\mathrm{b}}/k_{\mathrm{B}} T} \tag{5.3}$$

which is shown in Fig. 5.2a as a continuous line with no adjustable parameters. The agreement between experiment and theory is quite good. The strong increase of $\frac{C_2}{R_2}$ with temperature is dominated by the Arrhenius law exponential $\mathrm{e}^{-E_{\mathrm{b}}/k_{\mathrm{B}} T}$ which comes into play for the endothermic dissociation (C_2) but is absent for the exothermic recombination process (R_2).

The strong temperature dependence of the rate constants potentially has a strong influence on the reaction dynamics of our atom/ molecule system, as the chemical reactions change the temperature of the gas. To quantify this influence, we take a closer look at the temperature evolution in our experiment by tracking the cloud size $\sigma_{\mathrm{ax}} \propto \sqrt{T}$, see fig. 5.2b. Initially the system is in thermal equilibrium and the molecular cloud has an axial cloud size of about $\sigma_{\mathrm{ax}} = 230\,\mu\mathrm{m}$ which corresponds to a temperature of $T \approx 1.3\,\mu\mathrm{K}$ (see Supplementary Note 2 and Supplementary Fig. 2[3]). The heating pulse, which starts at $t = -20\,\mathrm{ms}$ and ends at $t = 0$, deposits thermal energy in the system. Due to the fast elastic collisions of dimers and atoms the thermal energy deposition results in a fast increase of the cloud size of about 6% which corresponds to a temperature increase of $\Delta T \approx 0.15\,\mu\mathrm{K}$. In addition, the modulation of the dipole trap during the heating pulse excites unwanted breathing mode oscillations in the cloud with a small amplitude of two percent. The mean cloud size which is obtained by averaging over one oscillation (red circles in fig. 5.2b) is almost constant within the first 150 ms after the heating pulse. This might be at first surprising since one might expect the endothermic dissociation to considerably lower the temperature again. However, since the initial atom number is quite small, only a small amount of molecules need to break up to significantly increase the recombination rate $\propto N_{\mathrm{A}}^2$ and thus to reach a new balance. Therefore only a small amount of the injected heat is consumed for the dissociation, corresponding to a small amount of cooling. Moreover, this residual cooling is almost canceled by the background heating. As a consequence the remaining temperature variation is less than 1%. For later times, $t > 150\,\mathrm{ms}$, when the reaction triggered by the heating pulse has already stopped, the background heating leads to monotonically increasing mean cloud size. From our results in fig. 2a we conclude that a temperature variation of 1% leads to C_2/R_2 variations of at most a few percent, which is negligible with respect to our current measurement accuracy.

In view of these complex dynamics we have set up a system of coupled differential equations that describe in a more complete fashion the various reaction/loss processes at varying temperatures (see Supplementary Note 1[4]). The solid curve in fig. 5.2b is a result of these calculations which in general show very good agreement

---

[3]sec. 5.6.2

[4]sec. 5.6.1
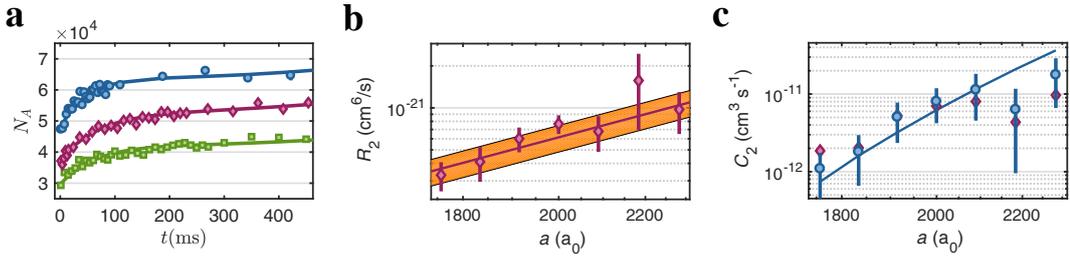
Figure 5.3: Dependence of the reaction rate constants on the scattering
length. **a** Reaction dynamics for three scattering lengths of $a =
(1760, 1920, 2000)a_0$ (green squares, red diamonds and blue circles),
corresponding to the magnetic fields $B = (705, 711, 714)\,\text{G}$, respec-
tively. The continuous lines are fits based on eq. 5.2 from which R_2
and C_2 can be extracted. **b** The measured association rate constant R_2
as a function of a (red diamonds). R_2 roughly follows the universal re-
lation $R_2 = C\hbar a^4/m$, with $C = 470$ obtained from a fit to the data (red
continuous line). The majority of the data can be found in a band (or-
ange area) around the fit curve. The band is bounded by $370 < C < 570$.
c The dissociation rate constant C_2 (red diamonds) as a function of a.
The temperatures between the individual measurements varied by about
15%. To compensate the influence of the temperature we use eq. 5.4
to rescale C_2 to values corresponding to $T = 1.5\,\mu\text{K}$ (blue circles). The
error bars correspond to temperature uncertainties and the 95% confi-
dence bounds determined by fits as in **a**. The blue continuous line is the
theoretical prediction of eq. 5.4 for a universal constant of $C = 470$.

with our measurements.

5.3.4 Interaction strength dependence

Finally, we investigate the influence of the interaction strength between the par-
ticles on the reaction dynamics. For this, we tune the scattering lengths with the
help of the magnetic B-field. We note that the dimer-dimer scattering length a_{dd}
is given by $a_{\text{dd}} = 0.6a$, where a is the scattering length for atom-atom collisions
[42]. Figure 5.3a shows three measurements for $a = (1760, 1920, 2000)\,a_0$. For
technical reasons, we start with three different N_A at $t = 0$. However, this has neg-
ligible influence on the dynamics of the dissociation, which we have checked with
a numerical calculation. Already from the data shown in fig. 5.3a it is obvious
that the dissociation rates strongly increase with the scattering length. From fits to
these and additional measurements we extract $R_2(a)$ and $C_2(a)$ for various scatter-
ing lengths and plot the results on a double logarithmic scale in fig. 5.3b, c (red
diamonds).

The association (three-body recombination) process characterized by the rate constant R_2 has been extensively discussed for various Efimovian systems [25–27], where it depends on the three-body parameter, and for non-Efimovian Fermi-Fermi mixtures, where it is suppressed in the low-energy limit [158, 159]. By contrast, here we are dealing with a non-Efimovian system of three distinguishable particles, for which a simple dimensional analysis [155] predicts the low-energy threshold law $R_2 = C\hbar a^4/m$, where C is a universal constant. In fig. 5.3b this a^4 scaling behavior is plotted for $C = 470$, obtained from a fit to our data. Our results show quite good agreement with the expected power law dependence within the error bars. Figure 5.3c shows C_2 for various a (red diamonds). These data are still raw in the sense that each measurement is taken at a slightly different temperature which increases with the scattering length (see Supplementary Note 3[5]). In order to compensate this temperature change we use eq. 5.3 to rescale the measured C_2 rate constants to values corresponding to a constant temperature $T = 1.5\,\mu\mathrm{K}$ (see blue circles in fig. 5.3b). The resulting rate constant C_2 increases by more than one order of magnitude in the tuning range and agrees reasonably with the theoretical prediction (without any free parameter),

$$C_2 = C\,\frac{(\pi m k_\mathrm{B})^{1/2}\,k_\mathrm{B}}{2h^2}\,T^{3/2}\,a^4\,e^{-\frac{E_\mathrm{b}(a)}{k_\mathrm{B}T}}, \qquad (5.4)$$

which is obtained by inserting $R_2 = C\hbar a^4/m$ into eq. 5.3 and using again $C = 470$. As far as we know there is no direct theoretical prediction for this number. D'Incao and co-workers [44] calculated dimer-dimer elastic and inelastic scattering properties in a wide range of collision energies. For the energy interval relevant here, these calculations indicate $30 \lesssim C \lesssim 100$ which is also consistent with our own numerical estimates based on [42, 43]. The large discrepancy between the theoretical and experimental value needs to be investigated in future studies. It may be due to an atom dimer attraction in the p-wave channel (see supplemental material of ref. [160]), which is difficult to take into account theoretically within our current approach.

5.4 Discussion

In conclusion, we have investigated the collisional dissociation of ultracold molecules in a single reaction channel which is characterized by the precisely defined quantum states of the involved atoms and molecules. Using a heating pulse we shift an atom/ molecule mixture which is initially in detailed balance out of equilibrium and measure the evolution of the system until it reaches a new equilibrium. This allows us to determine reaction rate constants, in particular for the collisional

---

[5]sec. 5.6.3

dissociation of two molecules. Furthermore, we find a strong temperature dependence of this rate which is consistent with the well known Arrhenius equation. In addition, we find agreement of the association (dissociation) rate constant with a scaling behavior of a^4 ($a^4 e^{-E_\text{b}/k_\text{B}T}$), respectively. From our data we estimate the universal constant $C \approx 470$, which is in discrepancy with the theoretical prediction. For the future, we plan to extend the current work to study the dynamics of chemical reactions in a regime, where Fermi and Bose statistics play an important role.

5.5 Methods

5.5.1 Preparation of the atomic and molecular quantum gas

To prepare our sample of ultracold atoms and molecules, we initially trap 10^9
^{6}Li atoms in a magneto-optical trap, where the atoms are cooled to a temperature of $700\,\mu$K. The particles are transferred to an optical dipole trap of a focused 1070nm laser beam with an efficiency of 1%. To generate a balanced distribution (50%/50%) of atoms in the $|m_F = \pm 1/2 >$ spin states we apply a resonant 100ms radio frequency pulse. Initially the optical trap has a depth of $4\,$mK $\times k_B$ and is subsequently ramped down within 6s to $1.3\,\mu$K $\times k_B$ to perform forced evaporative cooling. This is carried out at a magnetic field of 780G and during this process Feshbach molecules form via three-body recombination. To suppress particle loss in the experiments and to assure harmonicity of the trapping potential, the trap depth is ramped up again to $U_0 = 21\,\mu$K $\times k_B$ after evaporation. We then ramp the B-field in a linear and adiabatic fashion to the specific value at which the experiment will be carried out, within the range of 705G to 723G. After a holding time of 100ms the gas has a temperature of approximately 1.2 to $1.3\,\mu$K and is in chemical equilibrium, with 80% to 90% of all atoms being bound in Feshbach molecules. The binding energy of the molecules can be determined from [93] $E_\mathrm{b} = \frac{\hbar^2}{m(a-\bar{a})^2}\left(1 + 2.92\frac{\bar{a}}{a-\bar{a}} - 0.95\frac{\bar{a}^2}{(a-\bar{a})^2}\right)$ using $\bar{a} = 29.9a_0$, which yields values between 6 and $10\,\mu$K $\times k_B$ in our B-field range. The scattering length a as a function of the B-field is taken from ref. [91]. It can be approximated with $a = a_\mathrm{bg}\left(1 - \frac{\Delta B}{B-B_0}\right)$, where $\Delta B = -263.3$G is the width of the resonance and $a_\mathrm{bg} = -1582\,a_0$ is the background scattering length.

5.5.2 Removing of Feshbach molecules

To optically pump the Feshbach molecules into undetected states, we use a 673nm laser with a peak intensity of $I_0 = 500$mW cm^{-2} which excites all Feshbach molecules to the $\mathrm{A}^1\Sigma_u^+, v' = 68$ state [105] (see fig. 1c) within 500μs. The excited molecular state decays within a few ns either into two unbound atoms which quickly leave the trap or into deeply bound Li$_2$ molecules which are invisible for our detection.
Besides molecule excitation, the pulse leads to photoassociation of unbound atoms. This reduces the number of free atoms and leads to an overestimation of the molecule number. However, in our parameter range and for our free atom densities the resulting error for the free atom number is below one percent and can be neglected (see also [99]).

5.6 Supplementary Information

5.6.1 Supplementary Note 1: Modelling of the reaction dynamics

We perform model calculations to describe in more detail the measured dynamics of the atom/ molecule system, triggered by the initial heat pulse. For this, we integrate the following coupled system of rate equations for the atom number N_A, the molecule number N_M and the temperature T,

$$\dot{N}_A = C_2\,a_1\frac{N_M^2}{\sigma_r^2\,\sigma_{ax}} - R_2\,a_2\frac{N_M N_A^2}{\sigma_r^4\sigma_{ax}^2} \tag{5.5}$$

$$\dot{N}_M = -\frac{\dot{N}_A}{2} - C_{DD}\,a_1\frac{N_M^2}{2\,\sigma_r^2\,\sigma_{ax}} \tag{5.6}$$

$$\dot{T} = -\frac{E_b}{6k_B\,(N_A+N_M)}\dot{N}_A + C_H \tag{5.7}$$

where $a_1 = (4\pi^{3/2})^{-1}$ and $a_2 = 2^{-7}(2\pi^2)^{-3/2}$ are numerical constants. Equation (5.5) is identical to eq. (2) in the main text. The first term in eq. (5.6) corresponds to the conversion between molecules and unbound atoms, while the second term accounts for molecule losses in inelastic dimer-dimer collisions with rate constant of $C_{DD} = 2.3 \times 10^{-13}\,\mathrm{cm^3 s^{-1}}$, which is extracted from the previous measurement of ref. [104]. Equation (5.7) has two contributions. The first one accounts for cooling due to endothermic dissociation and heating due to exothermic recombination reactions. The second contribution corresponds to background heating of the gas caused, e.g., by off-resonant scattering of the dipole-trap light. Equations (5.5) and (5.6) are coupled via the cloud sizes $\sigma_{r(ax)} = \sqrt{k_B T / m_M \omega_{r(ax)}^2}$ to the temperature equation (5.7).

The results of a corresponding calculation at $709\,\mathrm{G}$ are shown in Supplementary Fig. 5.4 and are in very good agreement with the experimental data. The values of the parameters C_2 and R_2 are the same as in the main text. $C_H = (3.0 \pm 1.0) \times 10^{-7}\,\mathrm{s^{-1}}$ is mainly determined by the long-time evolution of the cloud size (see Supplementary Fig. 5.4d,e).

The total particle number in Supplementary Fig. 5.4c) exhibits the losses caused by the inelastic dimer-dimer collisions and agrees well with the experimental measurements. The temperature in Supplementary Fig. 5.4d) first decreases slightly due to endothermic dissociation after the heat pulse and then increases again due to the dipole-laser induced photodissociation. Supplementary fig. 5.4e shows the calculated cloud width σ_{ax} as determined by the temperature T. It agrees well with the measurements (green circles) if we average over the small-amplitude collective oscillations which have been excited by the initial heat pulse.
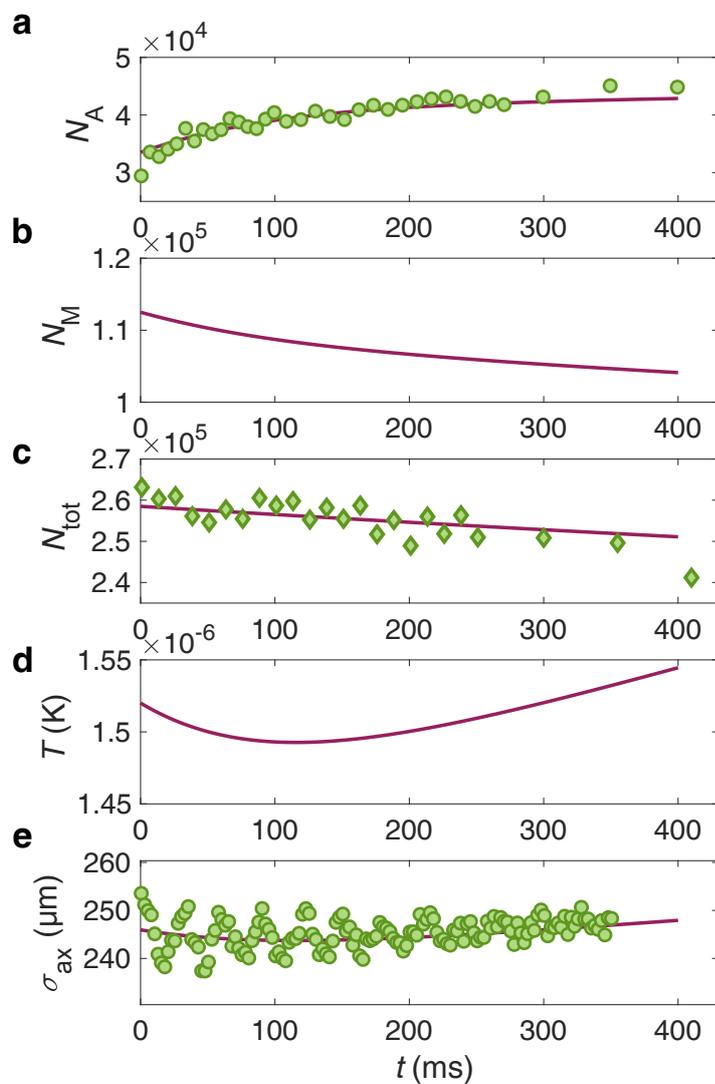
Figure 5.4: Model calculation for the evolution of the atom/ molecule system. Results from the coupled differential equations (5.5-5.7) (continuous lines). Plot symbols show experimental data for 709 G. For details see text of Supplementary Note 1.

5.6.2 Supplementary Note 2: Thermometry

Within the parameter range of our experiments the molecular and atomic density distributions are each well described by that of a non-interacting thermal gas located in a harmonic trap. The axial sizes of the molecular and atomic clouds are given by $\sigma_{\mathrm{ax}} = \sqrt{k_{\mathrm{B}}T/m\omega_{\mathrm{ax}}^2}$ and $\sigma_{\mathrm{ax,A}} = \sqrt{2}\sigma_{\mathrm{ax}}$, respectively. Because the axial trapping frequency ω_{ax} is precisely known for our setup, we can determine the temperature T by measuring the molecular or atomic cloud size. These cloud sizes are extracted from images of the mixed atom/ molecule clouds after careful analysis, for which we also determine the atom fraction $N_{\mathrm{A}}/N_{\mathrm{tot}}$ of the cloud. Supplementary Figure 5.5 shows a calculated typical example for the 1D density distributions (where the transverse directions have been integrated out) for atoms n_{A}, molecules n_{M} and both $n_{\mathrm{tot}} = 2n_{\mathrm{M}} + n_{\mathrm{A}}$.

5.6.3 Supplementary Note 3: Rescaling the measured C_2 to a constant temperature

Supplementary table 5.1 is the list of temperatures at which the C_2 measurements in fig. 5.2 are taken. The statistical uncertainty of the temperatures is around $\Delta T = 0.08\,\mu\mathrm{K}$.

Table 5.1: Temperatures and scattering lengths of the measurements in fig. 5.2.

a (a_0)	1760	1830	1920	2000	2090	2180	2280
T (μK)	1.60	1.52	1.51	1.47	1.42	1.41	1.35

The temperatures increase with decreasing scattering length a. This temperature change is a result of the way we prepare the sample. In particular, the magnetic field ramp to the target field takes place within a $21\,\mu\mathrm{K} \times k_{\mathrm{B}}$ deep trap which prevents further evaporative cooling. With decreasing a, the binding energy of the dimers increases and therefore for a given temperature the equilibrium molecule fraction increases. The corresponding molecular association, however, heats the sample.
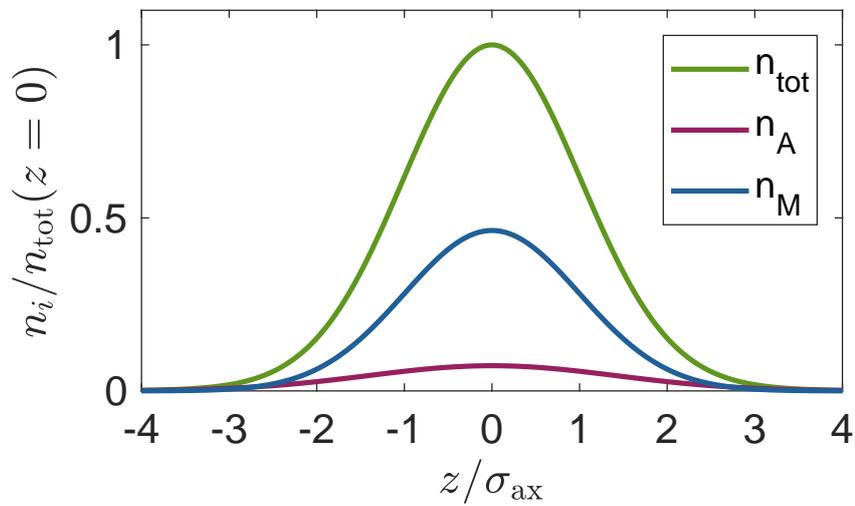
Figure 5.5: Calculated 1D density distribution for a thermal cloud of atoms and molecules. In a harmonic potential non-interacting atoms and molecules exhibit a Gaussian density distributions n_A and n_M, respectively, of which the widths differ by a factor or $\sqrt{2}$. The total density distribution is the sum $n_{tot} = 2n_M + n_A$. Here, the atom fraction N_A/N_{tot} is 0.6.

5.7 Additional information to the molecule detection technique

In this section I present additional information to the molecule detection technique described in this chapter so far (not included in the paper, i.e. sections 5.1 to 5.6.3).

The key technique used in the experiments presented in this chapter, is the molecule detection technique. It allows us to determine the number of dimers and unbound atoms in an ensemble of ultracold ^{6}Li atoms. In the case of strongly interacting ^{6}Li atoms, this information can not be accessed directly via absorption imaging since both species (unbound fermions and bosonic dimers) are detected simultaneously. This is due to the fact that the binding energy of the dimers is small compared to the width of the transition in the investigated magnetic field range (here: $(700 - 726)$ G).

Therefore, spin selective absorption imaging in the vicinity of the Feshbach resonance, e.g. measuring the number of atoms in $|1\rangle$, gives the total number of particles in $|1\rangle$ whether they are bound or not. To determine the number of free atoms and molecules in a given configuration, we perform two experimental runs as described in sec. 5.3.1. In the first experimental run the total number of atoms is determined via absorption imaging. In a second experiment, with an identical cloud, molecules are optically excited prior to the detection. From the excited state the dimers decay either to deeper bound vibrational states of the electronic ground state, invisible for the detection system, or dissociate to unbound atoms which quickly leave the trap. A subsequent detection of the remaining particles in the $|1\rangle$ state yield the number of unbound atoms.

To make use of this scheme, the frequency of the laser has to be adjusted to the molecular transition (see refs. [100, 105]). To determine the position of the excitation frequency, we performed spectroscopy on the molecular gas. In fig. 5.6 a) spectroscopy data for a measurement at a magnetic field of $B = 650$ G is shown. In the experiment we find the resonance to be located at $v_0 = 445.287245$ THz which we identify as the $X^1\Sigma_g^+, v = 38 \rightarrow A^1\Sigma_u^+, v' = 68$ transition. Here, for simplicity a Gaussian fit is used to determine the resonance position which is reasonable since we observe power broadening and a broadening due to magnetic field fluctuations.

For the identification of the molecular transition we performed extended spectroscopy in the frequency range of 444 THz to 446 THz. We compared the detected transition frequencies with the results of coupled channel calculations (see fig. 5.6 b)) provided by Eberhard Tiemann (University of Hannover) [161].

It is important to note that the molecular transitions shift with the magnetic field similar as the bare atomic transition. This is due to the fact that the dimers have a large triplet contribution [162]. For 700 G $< B < 900$ G the $X^1\Sigma_g^+, v = 38 \rightarrow A^1\Sigma_u^+, v' = 68$ transition tunes with $\Delta v / \Delta B \approx 2.7$ MHz/G.
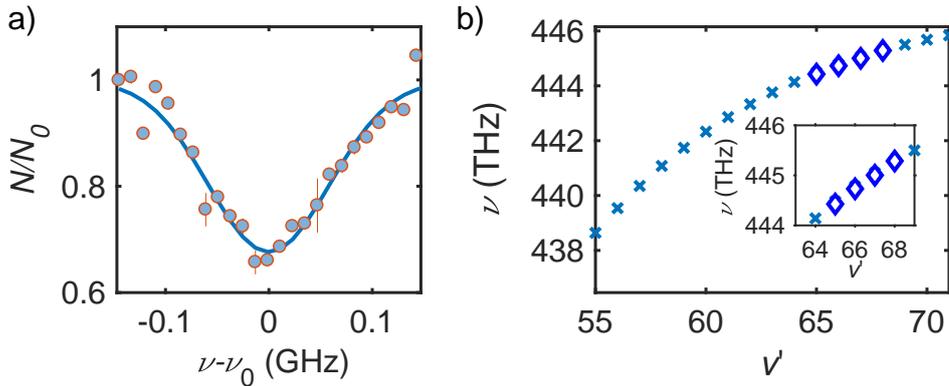
Figure 5.6: Molecule spectroscopy. a) Spectroscopy on a gas with a molecule fraction of about 30% at $B = 650\,\mathrm{G}$. Here, N is the number of atoms in $|1\rangle$. At $\nu_0 = 445.287245\,\mathrm{THz}$ we find the resonance of the $X^1\Sigma_g^+$, $v = 38 \to A^1\Sigma_u^+$, $v' = 68$ transition. The decay of the molecules from the excited to the electronic ground state leads to the observed losses. The natural linewidth of the transition is $\approx 12\,\mathrm{MHz}$. Here, we see power broadening and broadening due to magnetic field fluctuations. b) Measurement results for the $X^1\Sigma_g^+$, $v = 38 \to A^1\Sigma_u^+$, $v' = 65..68$ transitions (diamonds). For comparison, the result of coupled-channel calculations provided by Eberhard Tiemann [161] are shown (crosses).

Removing dimers

As mentioned in the previous passage, in the molecule detection scheme there are two possible mechanisms that lead to dimer losses. The excited dimers can either decay to deeper bound molecules, which are invisible for the detection scheme, or lead to dimer dissociation where the decay products have a large thermal energy and quickly leave the trap. To estimate which process dominates, we have a closer look on the Franck-Condon factors (FCFs) for the decay of the optically excited dimers (taken from ref. [161]). Figure 5.7 shows the corresponding FCFs. The data reveals that a decay to the initial state $X^1\Sigma_g^+$, $v = 38$ with $\mathrm{FCF}(v = 38) = 0.08$ has by far the highest FCF [100, 162] and that the probability for a decay to deeper bound states, where $\Sigma_{R=0}^2\Sigma_{v=0}^{37}\mathrm{FCF}(v, R) = 0.018$, is highly suppressed. The probabilities indicate that a decay to a bound state is comparatively low, making it more likely that molecule losses are mainly driven by a bound-free transition and a subsequent product ejection than a transfer to a deeper bound state.

Besides this, we also looked into the dynamics of the excitation process itself. We find that the dimers decay exponentially as a function of the optical excitation pulse width (see also [99, 105]). In a sample consisting of both, dimers and unbound atoms, this exponential curve is offset by the unbound atoms. In fig. 5.8 a corresponding experiment at $723\,\mathrm{G}$ is shown. The curves show an exponential de-
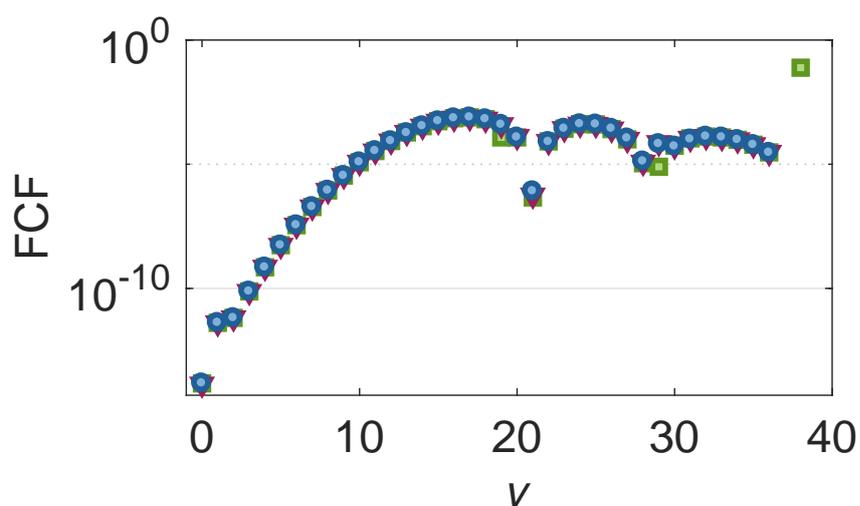
Figure 5.7: Franck-Condon factors (FCFs) for the decay of molecules from $A^1\Sigma_u^+, v' = 68, R' = 1$ to $X^1\Sigma_g^+, v = 0 - 38$ obtained from coupled-channel calculations of Eberhard Tiemann [161]. In the molecule excitation scheme the dimers are transferred to the $A^1\Sigma_u^+, v' = 68, R' = 1$ initially, according to the selection rules. From this state the dimers can decay to $X^1\Sigma_g^+, R = 0, 1, 2, v = 0..38$. The green squares give the FCFs for the decays to states with $R = 0$, the red triangles for the decays to the states with $R = 1$, and the blue circles for the decays to states with $R = 2$, respectively.
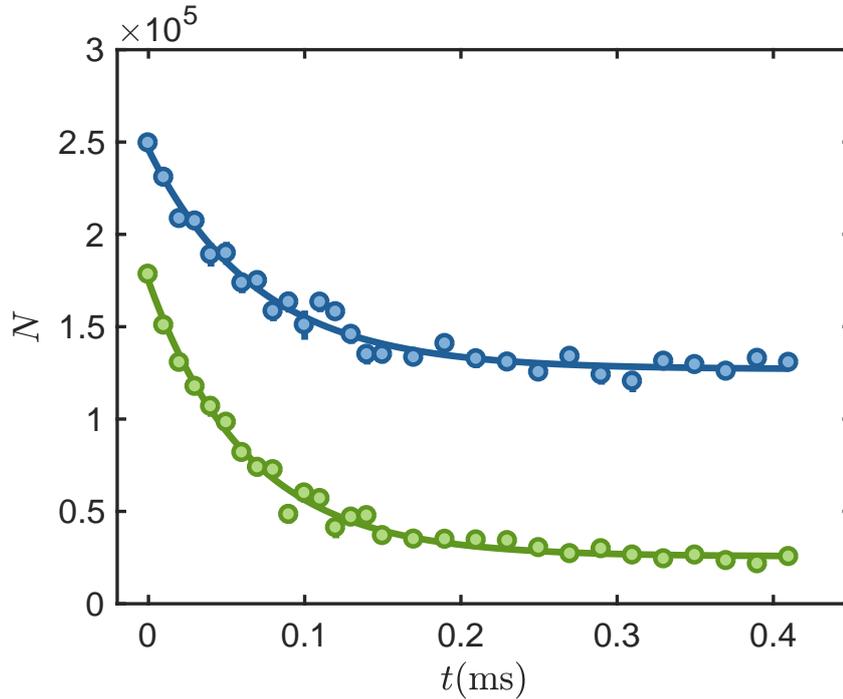
Figure 5.8: Optical excitation of molecules. Number of remaining unbound atoms N in one spin state as a function of the excitation pulse duration t for a temperature of $T = 0.7 T_F$ (green circles) and $T = 1.3 T_F$ (blue circles) at $B = 726$ G. In both cases the number of atoms decays almost exponentially with t. Both curves show an offset which corresponds to the remaining unbound atoms. An exponential fit is applied for both curves (straight lines). The excited molecules mainly decay to unbound atoms that quickly leave the trap leading to the detected losses.

cay and an offset given by the unbound atoms in the gas. Please note that the time constant of the decay is a function of the intensity of the excitation beam which increases with increasing intensity (for more information see refs. [99, 105, 163]). In general, the optical excitation pulse could also lead to photo-association (PA) of two atoms in opposite spin states. The PA rate scales with the atomic density squared. Additionally, in our case the PA rate constant increases for $(k_F a)^{-1} \to 0$ which is due to the fact that the binding energy is small close to resonance. However, for a gas with moderate density (see also appendix A.2) and $(k_F a)^{-1} \gg 1$, which is the case for the experiments presented in this chapter, PA can be neglected. This assumption is supported by the observed dynamics in fig. 5.8 which do not show any onset of a two-body decay.

6 Second sound in the BEC-BCS crossover

Available on arXiv:2003.06847

Daniel Kai Hoffmann[1], Vijay Pal Singh[2], Thomas Paintner[1], Manuel Jäger[1], Wolfgang Limmer[1], Ludwig Mathey[2] and Johannes Hecker Denschlag[1]

[1] *Institut für Quantenmaterie and Center for Integrated Quantum Science and Technology (IQST), Germany*
[2] *Institut für Laserphysik, Zentrum für Optische Quantentechnologien and The Hamburg center for Ultrafast Imaging, Universität Hamburg, Germany*

6.1 Abstract

Second sound is an entropy wave which propagates in the superfluid component of a quantum liquid. Because it is an entropy wave, it probes the thermodynamic properties of the quantum liquid which are determined, e.g., by the interaction strength between the particles of the quantum liquid and their temperature. Here, we study second sound propagation for a large range of interaction strengths within the crossover between a Bose-Einstein condensate (BEC) and the Bardeen-Cooper-Schrieffer (BCS) superfluid. In particular, we investigate the strongly-interacting regime where currently theoretical predictions only exist in terms of an interpolation between the BEC, BCS and unitary regimes. Working with a quantum gas of ultracold fermionic ^{6}Li atoms with tunable interactions, we show that the second sound speed varies only slightly in the crossover regime. We gain deeper insights into sound propagation and excitation of second s ound by varying the excitation procedure which ranges from a sudden force pulse to a gentle heating pulse at the cloud center. These measurements are accompanied by classical-field simulations which help with the interpretation of the experimental data. Furthermore, we determine the spatial extension of the superfluid phase and estimate the superfluid density. In the future, this may be used to construct the so far unknown equation of state throughout the crossover.

6.2 Introduction

Second sound is a transport phenomenon of quantum liquids that emerges below the critical temperature for superfluidity T_C [51, 115, 164]. It was experimentally discovered [52] in 1944 in He II [165] and was described with a hydrodynamic two-fluid model [47, 50, 51, 166] which treats He II as a mixture of a superfluid (SF) and a normal fluid (NF). The SF component has no entropy and flows without dissipation. The NF component carries all the entropy and has non-zero viscosity. In the limit of vanishing temperature $T \rightarrow 0$, the two-fluid model predicts that first sound (i.e. standard sound waves) correspond to a propagating pressure oscillation with constant entropy, while second sound is an entropy oscillation propagating at constant pressure [166].

The properties of a superfluid naturally depend on parameters such as its temperature and the interaction strength between its particles. With the advent of ultracold quantum gases, with tunable interactions, these dependencies can now be studied. In particular, an ultracold fermionic quantum gas with a tunable Feshbach resonance offers a unique opportunity to access various sorts of superfluidity in one system, ranging continuously between a Bose-Einstein condensate (BEC) of bosonic molecules, a resonant superfluid, and a superfluid gas of Cooper pairs (BCS superfluid) [86, 103, 167]. In the experiment this is done by tuning the interaction parameter $(k_F a)^{-1}$, where a is the scattering length, $k_F = \sqrt{2mE_F}/\hbar$ the Fermi wavenumber, E_F is the Fermi energy and m the atomic mass.

A large range of thermodynamical properties of the BEC-BCS crossover has been studied e.g. in refs. [106, 108, 167–172]. Recently, second sound has been measured by Sidorenkov et al. [53] in a unitary Fermi gas and by Ville et al. [56] in a two-dimensional bosonic superfluid.

Here, we experimentally investigate how second sound changes across the BEC – BCS crossover. This is especially important, since full theoretical calculations are not yet available in the strongly interacting regime. Nevertheless, comparing our measurements to existing calculations and interpolations we find reasonable agreement. In particular, c-field simulations in the BEC regime match quite well the corresponding observed wave dynamics of the experiment up to an interaction strength of $1/k_F a = 1$.

Furthermore, we explore how to tune second sound generation by testing experimentally and theoretically various excitation schemes ranging from a gentle local heating of the superfluid to a short local force pulse. As second sound is mainly an entropy wave and first sound is mainly a pressure wave, these different excitation schemes give rise to different responses for first and second sound. This helps for separating the generally weak second sound signals from the first sound ones. We find, that this separation works especially well when both first and second sound are excited as density dip wavepackets. For this case, we were able to quantitatively compare the amplitudes of first and second sound and compare the results to

a prediction.

6.3 Results

6.3.1 Experimental details

Our experiments are carried out with a balanced, two-component ultracold gas of fermionic ^{6}Li atoms in the two lowest hyperfine states $|F,m_F\rangle = |1/2,\pm1/2\rangle$ of the electronic ground state. The gas is confined by a combined magnetic and optical dipole trap with a trap depth of $U_0 \approx 1\,\mu K \times k_B$, for details see ref. [40, 99]. The trap is nearly harmonic and cylindrically symmetric with trapping frequencies $\omega_r = 2\pi \times 305\,\text{Hz}$ and $\omega_x = 2\pi \times 21\,\text{Hz}$. The temperature and the particle density are controlled by evaporative cooling. In the experiments the temperature ranges approximately from $0.12\,T_{\text{F}}$ to $0.28\,T_{\text{F}}$, where $T_{\text{F}} = E_F/k_{\text{B}} = \hbar(3\bar{\omega}^3N)^{1/3}$ is the Fermi temperature, $\bar{\omega} = \left(\omega_x\omega_r^2\right)^{1/3}$ is the geometric mean of the trapping frequencies and N is the total number of atoms. The scattering length a is tunable with an external magnetic field B via a magnetic Feshbach resonance at $832\,\text{G}$ [91].
To excite sound modes in the system, we focus a blue-detuned $532\,\text{nm}$ laser onto the trap center (see ref. [53] and Fig. 6.1a). The laser beam is aligned perpendicularly to the optical dipole trap and produces a repulsive potential barrier of $U_{ex} \approx 0.2\,U_0$. At its focus, the beam has a waist of about $20\,\mu m$, which is comparable to the cloud size in the radial direction. To excite sound waves, the height of this additional potential is modulated. The excited sound modes generally exhibit contributions from both first and second sound [62, 173, 174]. However, it is possible to generate preferentially either one of the two sound modes by adapting the excitation method. To excite primarily first sound, we abruptly switch on the excitation laser beam (see Fig. 6.1b), similarly as for the first experiments on sound propagation in a dilute BEC [175]. This applies pressure on the cold cloud on both sides of the laser beam and creates two density wave packets (see Fig.6.1c) which propagate out in opposite directions along the axial trap axis with the speed u_1. In the experiments we detect these waves with the help of absorption imaging by measuring the density distribution of the atomic cloud as a function of time.
Figure 6.1d shows such density waves for an experiment at $(k_F a)^{-1} \approx (1.91 \pm 0.05)$, $B = 735\,\text{G}$ and a temperature of $T = (140 \pm 30)\,\text{nK} = (0.28 \pm 0.06)\,T_F$, which corresponds to $T = (0.71 \pm 0.15)\,T_C$, where T_C is the critical temperature. For the given interaction strength, we used $T_C = 0.4\,T_F$ (see Supplementary Note 1 in sec. 6.6.1).
Figure 6.1d is a time ordered stack of one-dimensional column density profiles of the atom cloud (see Methods for details). It shows the propagation of the sound waves along the axial direction x as a function of time. The two density wave packets propagate with first sound velocity from the trap center towards the edge
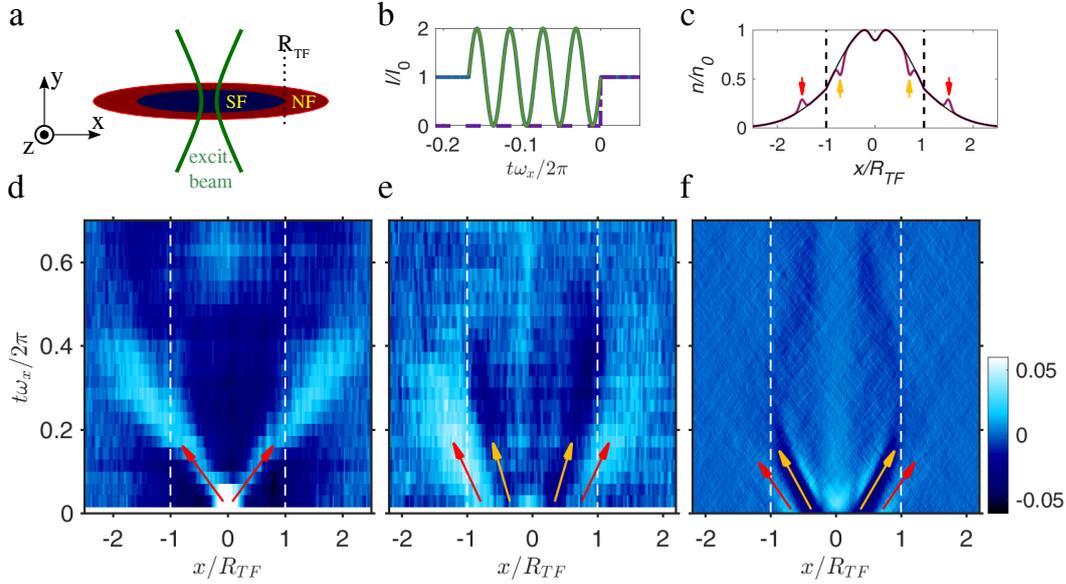
Figure 6.1: **Sound excitation in a trapped superfluid Fermi gas in the vicinity of the BEC-BCS crossover. a,** Set-up: A focussed, intensity-modulated, blue-detuned laser beam excites sound waves in the cigar-shaped atom cloud. **b,** Two different modulation sequences of the laser intensity. Purple dashed line: step excitation. Green solid line: heat pulse. The time t is given in units of the axial trapping period $2\pi/\omega_x$. **c,** Sketch of a bimodal density distribution of a trapped BEC (purple line) at $y = z = 0$. At the center of the trap a blue detuned beam produces a dimple in the potential. Modulating the beam intensity produces first sound waves (red arrows) and second sound (orange arrows) waves. Second sound reduces the local density of the cloud, while for first sound a density peak emerges. The thin black line shows the profile of the unperturbed cloud. **d,** The false color plot shows the measured local change in the density $\Delta\bar{n}(x,t)$ as a function of axial position x and time t. Here, $(k_F a)^{-1} = (1.91 \pm 0.05)$ at $B = 735\,\text{G}$ and $T/T_\text{C} = (0.71 \pm 0.15)$. After excitation, two wave packets (bright traces, marked with red arrows) propagate with first sound velocity u_1 towards the edges of the cloud. The excitation method predominantly excites first sound. Second sound is present as well but is barely discernible here. **e,** Propagation of first sound waves (bright traces, marked with red arrow) and second sound waves (dark traces, marked with orange arrows) after excitation with sinusoidal pulse of b). All other settings are the same as in d). **f,** Simulated sound propagation for the same parameters as in e). The orange arrows mark the propagating second sound and the red arrows the first sound, respectively.

of the cloud (two bright traces, marked with red arrows). To obtain the speed of sound, we examine how the center position of each wave packet changes with time. The center positions are determined via a Gaussian fit. From Fig.6.1d we obtain $u_1 = (17.2 \pm 3)\,\text{mm/s}$ near the trap center. Our analysis shows that the sound propagation slows down as the pulse approaches the edge of the cloud where the particle density decreases. In the following, we focus on the sound speed close to the trap center.

To primarily excite second sound, we sinusoidally modulate the intensity of the excitation beam for 7 ms with a modulation frequency of $\omega_{ex} = 2\pi \times 570\,\text{Hz} \approx 2\omega_r$ and a modulation amplitude of $\Delta U \approx 0.2 U_0$. This parametrically heats the gas in radial direction (see Fig. 6.1b). Subsequent thermalization via collisions occurs within a few milliseconds. This creates a local depletion of the superfluid density, filled with normal gas, forming a region of increased entropy (see Fig.6.1c). This gives rise to two wave packets which propagate outwards along the axial direction with the speed of second sound. Figure 6.1e shows corresponding experimental data where we measure the local density distribution as in Fig. 6.1d. The second sound wave appears here as a density dip (dark traces, marked with orange arrows). A clear indication that the dark trace corresponds to second sound is the fact that it vanishes at the Thomas-Fermi radius $R_{TF} \approx 110\,\mu\text{m}$ where the superfluid fraction vanishes. Second sound only propagates inside the superfluid phase.

Besides a second sound wave the excitation also produces a first sound wave (bright traces, marked with red arrows) which propagates faster than the second sound wave and travels beyond the Thomas-Fermi radius. The first sound wave is broader than in Fig. 6.1d, which can be mainly explained by the longer excitation pulse. To obtain u_2 we measure the time-dependent position of the minimum of each dark trace, which is determined via a Gaussian fit. For Fig. 6.1e we obtain $u_2 = (5.1 \pm 1.1)\,\text{mm/s}$.

Figure 6.1f shows numerical simulations of our experiment applying a dynamical c-field method [176] (see Supplementary Note 2 in sec. 6.6.2 for detailed information on the method). The dimer scattering length [158] is $a_{dd} = 0.6a$ and we assume all fermionic atoms to be paired up in molecules. To compare the simulations with the experimental results we choose the same values of $(k_\text{F}a)^{-1}$ and the same central density of the trapped gas as in the experiment. The theory value for u_2 is $(5.7 \pm 0.05)\,\text{mm/s}$ in agreement with the experimental value $(5.1 \pm 1.1)\,\text{mm/s}$.

6.3.2 Interaction strength dependence of second sound

We now perform measurements of second sound in the range $(-0.26 \pm 0.04) < (k_F a)^{-1} < (1.91 \pm 0.05)$ of the BCS-BEC crossover. These are shown in Fig. 6.2 along with theoretical predictions. The second sound velocity u_2 is given in units of the Fermi velocity $v_F = \hbar k_F^\text{hom}/m$. Here, the Fermi wavenumber k_F^hom is determined
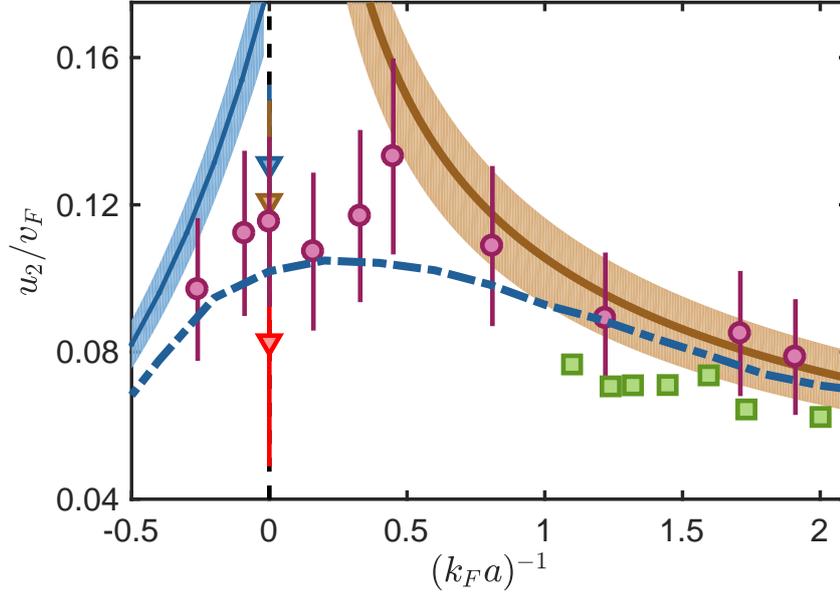
Figure 6.2: **Second sound velocity u_2 as a function of interaction strength.**
The purple circles depict measured data for temperatures in the range
$T = 65 - 145$ nK which corresponds to $T/T_C = 0.69 - 0.81$ (see Sup-
plementary Note 1 in sec. 6.6.1). The error bars are due to statisti-
cal uncertainties. The brown and blue solid line show hydrodynamic
predictions for the BEC and BCS regime at $T = 0.75\,T_C$, respectively
(see Supp. Note 3 in sec. 6.6.3). The shaded areas mark the sec-
ond sound velocity in the temperature range of the experiments. The
blue dash-dotted line shows a theoretical prediction of second sound
in the crossover [62] for a homogeneous gas at $T/T_C = 0.75$. It in-
terpolates between the results from hydrodynamic theory in the BEC
and BCS regime. The green squares are results of our numerical c-field
simulations which are consistent with both, analytic and experimental
results. For comparison we also show the second sound velocity on
the resonance measured in ref. [53] at the temperatures $T/T_C = 0.65$
(blue triangle), $T/T_C = 0.75$ (brown triangle), and $T/T_C = 0.85$ (red
triangle).

from the peak density at the trap center $k_F^{\text{hom}} = \left(3\pi^2 n_0\right)^{1/3}$. The blue dash-dotted line is a calculation from ref. [62], based on a hydrodynamic description in a homogeneous gas for the limiting cases of the BEC and the BCS regime, and unitarity. To connect these regimes, the results are interpolated across the crossover, bridging the range $\left|(k_F a)^{-1}\right| < 1$. The blue solid and the brown solid lines are our analytic hydrodynamic calculations which are valid in the BCS and BEC limit, respectively (see Supplementary Note 3 in sec. 6.6.3). For comparison, we show the results of the numerical c-field simulations (green squares), which agree with both, analytic description and experimental results. Despite the large error bars the measurements indicate an increase of u_2 when approaching unitarity from the BEC side, in agreement with the theoretical results.

a
b
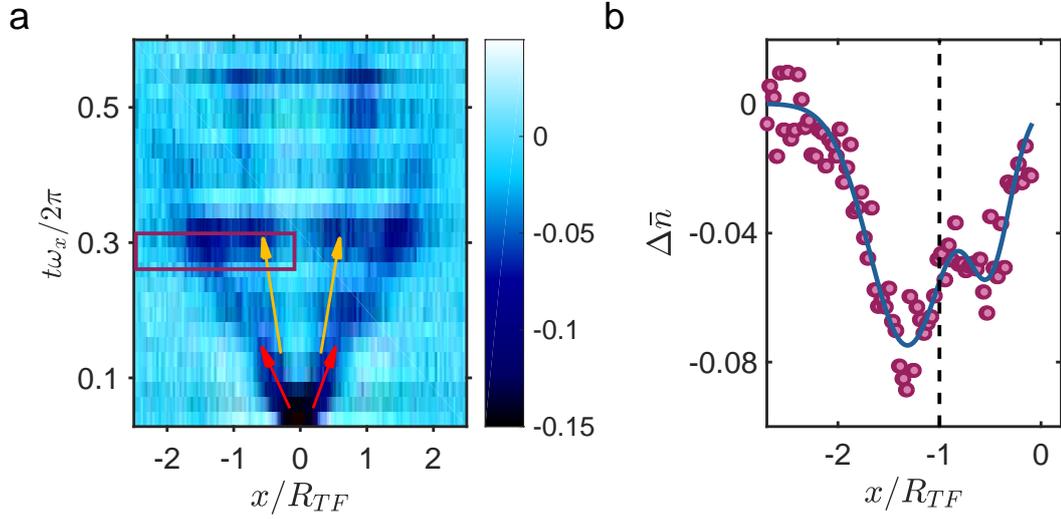
Figure 6.3: **Comparing signal strength of first and second sound. a,** Sound excitation experiment at $(k_F a)^{-1} = (1.91 \pm 0.05)$ and at a temperature of $T/T_{\text{C}} = (0.71 \pm 0.15)$. In contrast to Fig.6.1d, first sound (red arrows) and second sound (orange arrows) are now visible simultaneously. For $t\omega_x/2\pi < 0.15$ first and second sound waves overlap and therefore cannot be distinguished from each other. **b,** shows $\Delta\bar{n}$ for $t = 0.29 v_x$. We fit the center position of each of the two sound waves using a Gaussian function (solid line).

In general, second sound can only propagate in the superfluid phase of the gas. It is therefore natural to ask how the superfluid density n_s and the speed of second sound u_2 are related. This relation could, in principle, be derived from the equation of state. However the equation of state is unknown for the strongly interacting regime. Nevertheless, we can still get a handle on the relationship between n_s and u_2, by estimating the superfluid density for the regime of interme-

diate coupling, $1/k_F a > 1.5$, as follows. We carry out self-consistent mean-field calculations to determine the density distributions of the superfluid and the normal fluid for an interacting BEC in the trap (see Supplementary Note 4 in sec. 6.6.4). As an important input into these calculations we make use of the Thomas-Fermi radius which we have measured in the second sound experiments (the measured Thomas-Fermi radii can be found in Supplementary Note 1 in sec. 6.6.1). As an example, from the measurement at $(k_F a)^{-1} = (1.91 \pm 0.05)$ we determine the peak superfluid fraction to be $n_{s0}/n_0 = 0.98$ close to the trap center at maximum density, where the local $(k_F^{\mathrm{hom}} a)^{-1} = (1.06 \pm 0.05)$ and $T/T_C^{\mathrm{hom}} = (0.40 \pm 0.15)$, with $T_C^{\mathrm{hom}} = 0.21 T_F^{\mathrm{hom}}$ and $T_F^{\mathrm{hom}} = \hbar^2 (k_F^{\mathrm{hom}})^2/2mk_B$. For comparison, for a homogeneous weakly-interacting BEC with a superfluid fraction close to unity the temperature would need to be $T \ll T_C^{\mathrm{hom}}$, according to $n_s/n = 1 - \left(T/T_C^{\mathrm{hom}}\right)^{3/2}$. At unitarity, by contrast, the superfluid fraction reaches unity already at $T/T_C^{\mathrm{hom}} \approx 0.55$, as shown by Sidorenkov et al. [53]. As expected, this comparison shows that for a given T/T_C^{hom} the superfluid fraction grows with interaction strength.

6.3.3 Tuning the sound mode excitation

In the following we investigate how the superfluid gas responds to different excitation protocols [62, 173, 174]. For this, we tune the excitation scheme, the excitation frequency and amplitude to gain additional insight into the nature of first and second sound.

In Fig. 6.3a we show the evolution of the system after a step pulse excitation at $B = 735\,\mathrm{G}$ and $\Delta U = 0.3\,U_0$, in which both, first and second sound are excited. In contrast to the experiment in Fig. 6.1d, the laser beam is abruptly switched off - not on. As a consequence, the wave packets of both first and second sound now correspond to dips in the particle density. In Fig. 6.3b we show the density distribution for the time and position range indicated by the purple rectangle in Fig. 6.3a. From a fit of two Gaussian dips to the two wave packets, we determine an amplitude ratio of $W_2/W_1 \approx 0.7$. This result approximately matches the predictions of ref. [173, 174] (see also Supplementary Note 3 in sec. 6.6.3), where the response of both, a weakly and a strongly interacting molecular Bose gas has been derived. The prediction yields $W_2/W_1 = 0.9$ for an interaction parameter of $(k_F a)^{-1} = 2$, which is of similar magnitude as our result.

Next, we study the response for first and second sound waves after exciting them with short sinusoidal modulation sequences, as shown in Figs. 6.4a-d, where $(k_F a)^{-1} = (1.91 \pm 0.05)$. The modulation frequency is $\omega_{ex} = 0.61 \omega_r$, so that parametric heating is somewhat suppressed and coupling to first sound is enhanced as compared to the experiment shown in Fig. 6.1e. The numerical simulations in Figs. 6.4b-d demonstrate how the excitation pattern produces a corresponding wave train of first sound. Once waves of first sound have propagated beyond the
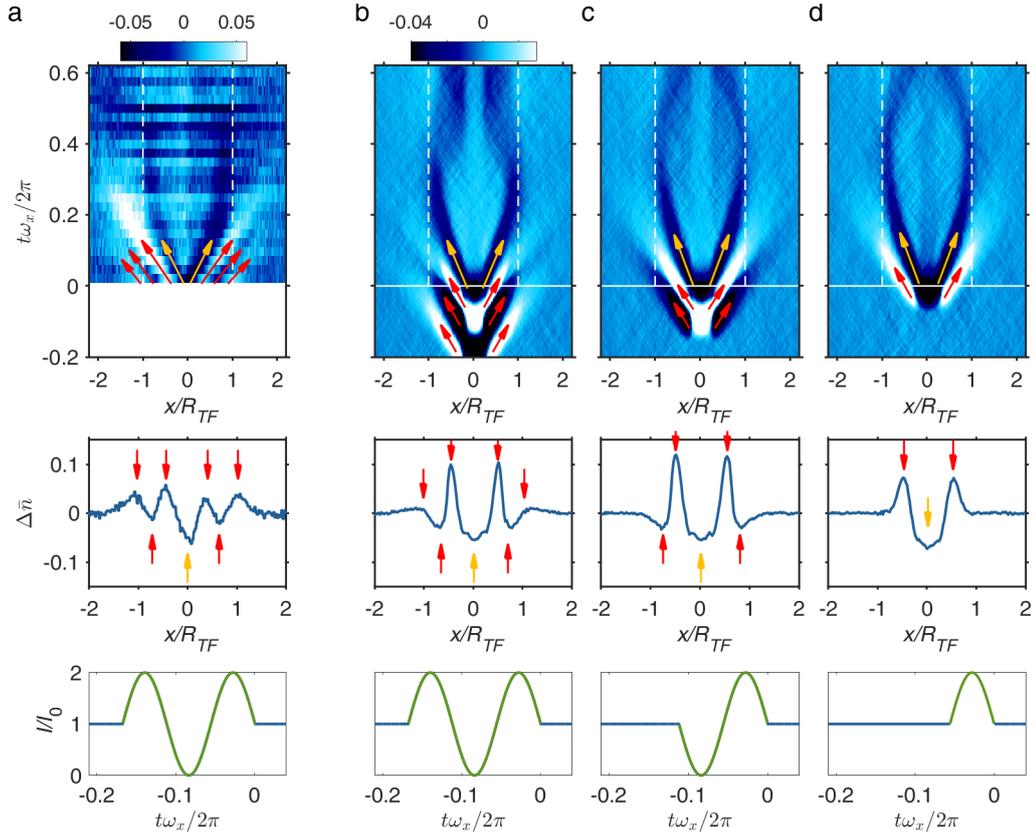
Figure 6.4: **Sound excitation with different modulation sequences. a,** $\Delta\bar{n}(x,t)$
data for $\omega_{ex} = 0.61\omega_r$, $\Delta U = 0.3 U_0$ and at $(k_F a)^{-1} = (1.91 \pm 0.05)$.
The excitation pulse excites both, first and second sound waves (dark
and bright traces). **b-d,** $\Delta\bar{n}(x,t)$ from numerical c-field simulations.
Top row: False color images of $\Delta\bar{n}(x,t)$. First and second sound waves
are marked with red and orange arrows, respectively. Mid row. Shown
is $\Delta\bar{n}$ for $t = 0$. Bottom row: Applied excitation scheme.

Thomas-Fermi radius they diffuse out and lose signal strength. The first sound wave train is always followed by a single dark second sound wave packet. The experimental data in Fig. 6.4a agrees quite well with the simulation in Fig. 6.4b. Notably, the diffusion of the first sound wave train is somewhat less strong than in the simulations. This descrepancy might be explained by the higher longitudinal trap frequencies used in the simulations which lead to a faster dispersion.

6.4 Conclusion

In conclusion, we have studied second sound propagation in an ultracold Fermi gas of ^{6}Li atoms across the BEC-BCS crossover for a range of different superfluidity at $T = 0.7\,T_C$. We find the second sound velocity to vary only slightly across the BCS-BEC crossover, which is in agreement with an interpolation of hydrodynamic theory [62]. In the BEC regime the results match numerical predictions based on c-field simulations.

Additionally, we investigate the response of the superfluid gas on various excitation pulse shapes, ranging from gentle local heating to an abrupt kick which allows for tuning waveform and amplitude of the sound modes. The responses of first and second sound are quite different, which hints at their different nature. We find that a particular useful excitation is a step wise excitation where both first and second sound propagate as density dips. With this scheme we achieve similar amplitudes for second and first sound and the second sound wave can be easily distinguished from the first one. In the future it will be useful to extend our measurements in the strongly interacting regime to a larger range of temperatures below T_C. Since the second sound velocity is related to the local superfluid density, this measurement technique can help to construct the equation of state in the strongly interacting regime.

6.5 Methods

Calculating $\Delta \bar{n}$ from the density profiles

Each of the experimental sound propagation images in Figs. 1d-e, 3a, 4a is a time-ordered stack of one-dimensional column density profiles $\Delta \bar{n}(x,t)$ of the atom cloud. A one-dimensional column density profile $n(x,t)$ is produced as follows: For a given propagation time t after the sound excitation ended we take an absorption image of a cloud to obtain the density distribution $n_{ex}(x,y,t)$. We integrate each absorption image along the y-axis to obtain a one-dimensional column density profile $n_{ex}(x,t)$. To reduce noise, we average 15 density profiles and obtain $\bar{n}_{ex}(x,t)$. We repeat this procedure for an unperturbed cloud to obtain $\bar{n}(x)$. By subtracting the two density profiles from each other we obtain $\Delta \bar{n}(x,t) = (\bar{n}_{ex}(x,t) - \bar{n}(x))/\bar{n}(0)$.

6.6 Supplementary Information

6.6.1 Supplementary Note 1: Temperatures to the measurements in Fig. 6.1 and Fig. 6.2

In this section we present the temperatures to the measurements shown in Fig. 6.1 and Fig. 6.2 (see table 6.1). We determine the temperatures by fitting a second order virial expansion of the density distribution at the wings of the cloud [99]. To compare the absolute temperature with T_C for various interaction strengths we use values for T_C as shown in figure 6.5.

T_C is not precisely known yet in the strongly interacting regime. In the limit of the BEC regime the BEC mean field model should give accurate values for critical temperature. Closer towards the resonance we expect the diagrammatic t-matrix calculation to provide quite good values [177]. For the range in between ($0.5 < (k_F a)^{-1} < 3$) we linearly interpolate between both T_C curves.

For the measurements on the BCS side we have compared our results with temperatures obtained from the approach in reference [178], where the total energy and entropy of a cloud is measured for thermometry. We find reasonable agreement between the temperatures obtained from the two approaches.

6.6.2 Supplementary Note 2: C-field simulation method

Here we present our simulation method that is used to simulate sound mode dynamics in a condensate of ^{6}Li molecules on the BEC side. The system is described

$(k_F a)^{-1}$	T [nK]	T/T_F	T_C/T_F	T/T_C	R_{TF} [μm]
-0.26 ± 0.04	67 ± 23	0.12 ± 0.04	0.171	0.71 ± 0.24	110 ± 5
-0.09 ± 0.03	65 ± 22	0.12 ± 0.04	0.194	0.61 ± 0.21	115 ± 5
0 ± 0.02	114 ± 28	0.17 ± 0.05	0.207	0.81 ± 0.24	124 ± 5
0.16 ± 0.03	90 ± 30	0.17 ± 0.05	0.231	0.74 ± 0.22	139 ± 5
0.33 ± 0.04	90 ± 30	0.18 ± 0.05	0.256	0.69 ± 0.20	153 ± 5
0.45 ± 0.04	120 ± 30	0.22 ± 0.06	0.272	0.79 ± 0.22	156 ± 5
0.81 ± 0.05	120 ± 30	0.22 ± 0.06	0.316	0.69 ± 0.19	121 ± 5
1.22 ± 0.05	130 ± 30	0.24 ± 0.06	0.347	0.70 ± 0.17	108 ± 5
1.71 ± 0.05	150 ± 30	0.28 ± 0.06	0.379	0.73 ± 0.16	107 ± 5
1.91 ± 0.05	140 ± 30	0.28 ± 0.06	0.391	0.71 ± 0.15	96 ± 5

Table 6.1: **Temperatures and Thomas-Fermi radii to the measurements presented in Fig. 6.2.** The temperatures are given in nK as well as units of T_F and T_C. For expressing the temperature in units of T_C we use an interpolated critical temperature curve (see fig. 6.5).

by the Hamiltonian

$$\hat{H}_0 = \int d\mathbf{r} \left[\frac{\hbar^2}{2M} \nabla \hat{\psi}^\dagger(\mathbf{r}) \cdot \nabla \hat{\psi}(\mathbf{r}) + V(\mathbf{r}) \hat{\psi}^\dagger(\mathbf{r}) \hat{\psi}(\mathbf{r}) + \frac{g}{2} \hat{\psi}^\dagger(\mathbf{r}) \hat{\psi}^\dagger(\mathbf{r}) \hat{\psi}(\mathbf{r}) \hat{\psi}(\mathbf{r}) \right]. \tag{6.1}$$

$\hat{\psi}$ and $\hat{\psi}^\dagger$ are the bosonic annihilation and creation operator, respectively. The 3D interaction parameter is given by $g = 4\pi a_{dd} \hbar^2 / M$, where a_{dd} is the dimer-dimer scattering length and M the dimer mass. The external potential $V(\mathbf{r})$ represents the cigar-shaped trap $V_{\text{trap}}(\mathbf{r}) = M(\omega_{ax}^2 x^2 + \omega_r^2 r^2)/2$. ω_{ax} and ω_r are the axial and radial trap frequencies, respectively. $r = (y^2 + z^2)^{1/2}$ is the radial coordinate.

To perform numerical simulations we discretize space with the lattice of $180 \times 35 \times 35$ sites and the discretization length $l = 0.5\,\mu m$, where l is chosen to be smaller than or comparable to the healing length ξ and the de Broglie wavelength λ. In our c-field representation we replace in Eq. 6.1 and in the equations of motion the operators $\hat{\psi}$ by complex numbers ψ, see ref. [176]. We sample the initial states in a grand-canonical ensemble of temperature T and chemical potential μ via a classical Metropolis algorithm. We obtain the time evolution of ψ using the equations of motion. We calculate the observables of interest and average over the thermal ensemble. We use the trap frequencies $(\omega_{ax}, \omega_r) = 2\pi \times (70\,\text{mHz}, 780\,\text{mHz})$, which are higher than those in the experiments. The reason for choosing higher ω_{ax}, ω_r is that we need to keep the effective total lattice size small enough to be able to carry out the numerical calculations. The scattering length a_{dd} and the trap central density n_0 are the same as the experiments. a_{dd} varies in the range $a_{dd} = 720-$
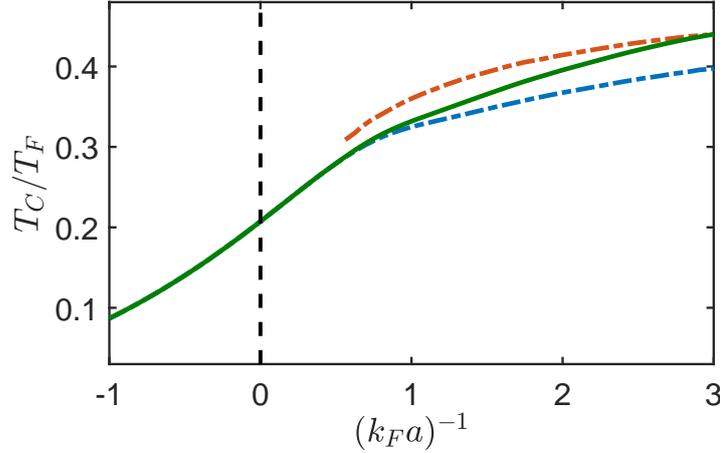
Figure 6.5: **Critical temperature T_C in units of T_F as a function of $(k_F a)^{-1}$ for a harmonically trapped Fermi gas.** The blue dash-dotted line shows a diagrammatic t-matrix calculation and the orange dash-dotted line a calculation based on a BEC mean field model [177]. The green straight line interpolates linearly between the two approaches.

$1650 a_0$, where a_0 is the Bohr radius, and n_0 in the range $n_0 = 8.2 - 11.2\,\mu\text{m}^{-3}$. This results in a cigar-shaped cloud of $N = 4.0 \times 10^4 - 4.5 \times 10^4$ ^{6}Li molecules. The temperature varies in the range $T = 240 - 280\,\text{nK}$ or $T/T_c = 0.4 - 0.6$, where $k_B T_c \approx 0.94\hbar(\omega_{ax}\omega_r^2 N)^{1/3}$ is the critical temperature of a noninteracting gas.

To excite sound modes we add the perturbation $\mathcal{H}_{ex}(t) = \int d\mathbf{r}\, V(\mathbf{r},t)n(\mathbf{r})$, where $n(\mathbf{r})$ is the density at the location $\mathbf{r} = (x,y,z)$. The excitation potential $V(\mathbf{r},t)$ is given by

$$V(\mathbf{r},t) = V_0(t)\exp\left(-\frac{(x-x_0)^2 + (z-z_0)^2}{2\sigma^2}\right), \qquad (6.2)$$

where $V_0(t)$ is the time-dependent strength and σ is the width. The location x_0, z_0 are chosen to be the trap center. We excite sound modes following the scheme used in the experiment, where σ and V_0 are chosen such that the changes in the local density due to the excitation potential are the same as in the experiment. We calculate the density profile $\bar{n}_{ex}(x,t)$, which is integrated in the radial direction. For sound propagation we examine $\Delta\bar{n}(x,t) = \left(\bar{n}_{ex}(x,t) - \bar{n}(x)\right)/\bar{n}(0)$, where $\bar{n}(x)$ is the density profile of the unperturbed cloud integrated in the radial direction and $\bar{n}(0)$ is the maximum density.

The time evolution of $\Delta\bar{n}(x,t)$ shows excitation of second sound identified by a vanishing sound velocity at R_{TF}. We fit the density profile with a Gaussian to determine the second sound velocity u_2 at the trap center. We note that u_2 changes only negligibly compared to the experimental errorbars for the temperatures in the range $T/T_c = 0.5 - 0.7$.

6.6.3 Supplementary Note 3: Analytic description of the sound modes

In the following we present an analytic description of first and second sound based on the two-fluid hydrodynamic model for a uniform gas. The total density n of the gas is a sum of the superfluid n_s and normal fluid density n_n. The first and second sound mode squared velocities are given by [85]

$$u_{1/2}^2 = \frac{1}{2}(c_T^2 + c_2^2 + c_3^2) \pm \left[\frac{1}{4}(c_T^2 + c_2^2 + c_3^2)^2 - c_T^2 c_2^2\right]^{1/2}, \qquad (6.3)$$

where $c_T^2 = 1/M(\partial p/\partial n)_T$ and $c_2^2 = n_s s^2 T/(n_n c_V)$ representing the isothermal and entropic sound velocities, respectively. p is the pressure, s the entropy per unit mass, T the temperature, and $c_V = T(\partial s/\partial T)_n$ the heat capacity per unit mass. The quantity $c_3^2 \equiv c_S^2 - c_T^2 = (\partial s/\partial n)_T^2 (n^2 T/c_V)$ couples the sound velocities c_2 and c_T, where $c_S^2 = 1/M(\partial p/\partial n)_s$ corresponds to the adiabatic sound velocity. The decoupled sound modes in the limit of vanishing T are

$$u_1^2 = c_T^2 = \frac{1}{M}\left(\frac{\partial p}{\partial n}\right)_T \quad \text{and} \quad u_2^2 = c_2^2 = \frac{n_s}{n_n}\frac{s^2 T}{c_V}. \qquad (6.4)$$

Here, first and second sound can be described as a pressure and entropy wave, respectively. To determine the second sound velocity u_2, we calculate the entropy and the normal fluid density defined as

$$S = \sum_{\mathbf{k}}\left(-f_k \log f_k \pm (1 \pm f_k)\log(1 \pm f_k)\right) \qquad (6.5)$$

and

$$n_n = \frac{1}{M}\int \frac{d\mathbf{k}^3}{(2\pi)^3}\frac{\hbar^2 k^2}{3}\left(-\frac{\partial f_k}{\partial E_k}\right), \qquad (6.6)$$

respectively [85]. $f_k = 1/\big(\exp(E_k/k_{\mathrm{B}}T) \mp 1\big)$ is the thermal occupation number, where E_k is the excitation energy and $\mathbf{k}$ the wavevector. The upper and lower sign correspond to a Bose and Fermi gas, respectively.

BEC

We use the Bogoliubov theory, valid in the dilute limit, to analyze the regime $k_{\mathrm{B}}T < gn$, where gn is the mean-field energy. The Bogoliubov spectrum is given by $E_k = \sqrt{\varepsilon_k(\varepsilon_k + 2gn)}$, where $\varepsilon_k = \hbar^2 k^2/(2M)$ is the free-particle spectrum. M is

the molecular mass. To examine the decoupled modes in Eq. 6.4 we approximate E_k by the linear spectrum $E_k \approx \hbar c k$, where $c = \sqrt{gn/M}$ is the Bogoliubov sound velocity. We obtain the entropy and the normal fluid density, respectively,

$$S = V \frac{2\pi^2}{45\hbar^3} (k_B T)^3 \left(\frac{M}{gn}\right)^{3/2} \quad \text{and} \quad n_n = \frac{2\pi^2}{45} \frac{(k_B T)^4}{\hbar^3} \frac{M^{3/2}}{(gn)^{5/2}}. \tag{6.7}$$

The entropy per unit mass is $s = S/(NM) = gn_n/(MT)$ and the heat capacity per unit mass is $c_V = 3s$.

Within upper description we can deduce following sound speeds

$$u_1 = \sqrt{\frac{gn}{M}} \quad \text{and} \quad u_2 = \sqrt{\frac{1}{3}\frac{gn}{M}}. \tag{6.8}$$

Here, u_2 is $u_1/\sqrt{3}$. This result is only valid at zero temperature, see Fig. 6.6a, where we show the full numerical solutions of Eq. 6.3 using the Bogoliubov description.

For $k_B T > gn$ instead we make use of a thermal gas description to determine s, c_V, and n_n, which are given by $s = 2.568 k_B n_n/(2Mn)$, $c_V = 3s/2$, and $n_n = n(T/T_C)^{3/2}$, respectively [85]. In our experiments on the BEC side $k_B T/gn$ ranges from 1.9 to 3.2 which allows us to apply the thermal gas description.

In this regime, solving eq. 6.3 the sound velocities read,

$$u_1 = \sqrt{\frac{gn}{M} + \frac{0.856 k_B T}{M}} \quad \text{and} \quad u_2 = \sqrt{\frac{n_s}{n}\frac{gn}{M}}. \tag{6.9}$$

u_2 is proportional to $\sqrt{n_s/n}$ and can be approximated by $u_2 = \sqrt{\left(1 - (T/T_C)^{3/2}\right)gn/M}$ (see Fig. 6.6a).

Sound amplitudes

Besides the sound velocity, our analytic description can be used to determine the amplitudes of the propagating sound modes, described as [173]

$$\delta n(x,t) = W_1 \delta\tilde{n}(x \pm u_1 t) + W_2 \delta\tilde{n}(x \pm u_2 t). \tag{6.10}$$

where $\delta\tilde{n}(x,t)$ is the density variation created by the excitation potential. $\delta\tilde{n}(x \pm u_{1/2}t)$ represent wave packets of first and second sound with weights $W_{1/2}$. The relative weight is given by

$$\frac{W_2}{W_1} = \frac{c_2^2 - u_2^2}{u_1^2 - c_2^2} \frac{u_1^2}{u_2^2} \qquad\qquad (6.11)$$

We determine W_2/W_1 by numerically solving Eq. 6.3 for the regimes $k_{\mathrm{B}}T < gn$ and $k_{\mathrm{B}}T > gn$ using the Bogoliubov and thermal gas description, respectively. We show these results in Fig. 6.6b. The Bogoliubov description of the weight works only for $k_B T \ll gn$. We note that at higher temperatures terms beyond Bogoliubov are needed to account for the thermal damping of the modes. The Bogoliubov description thus leads to an overestimation of the weight at high temperatures. For temperatures above the mean-field energy the weight is described by the thermal gas description, which we use to estimate the relative weight of the two modes in the main text. Please note that the thermal description gives unphysical solutions for $k_B T/gn \to 1$.
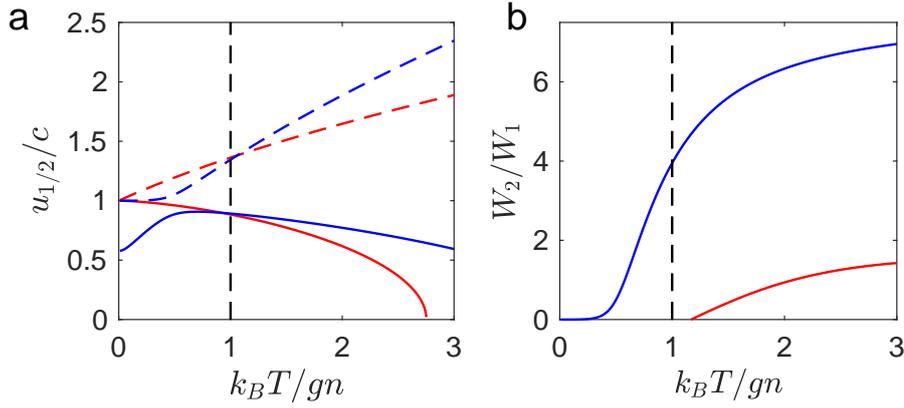
Figure 6.6: **Sound velocities and amplitudes. a,** Sound velocities $u_{1/2}$ are determined from eq. 6.3 and are shown as a function of $k_{\mathrm{B}}T/gn$ using the Bogoliubov (blue lines) and thermal gas description (red lines). Here, c is the Bogoliubov sound speed introduced in the text. **b,** shows the relative weight W_2/W_1 for $k_{\mathrm{B}}T < gn$ (blue line) and $k_{\mathrm{B}}T > gn$ (red line).

BCS

A condensate of an interacting Fermi gas is described by the BCS spectrum $E_k = \sqrt{\xi_k^2 + \Delta^2}$, with $\xi_k = \hbar^2 k^2/(2m) - \mu$, where μ is the chemical potential and $\Delta(T)$ the gap. At low $k_{\mathrm{B}}T \ll \Delta$, we use $\mu \approx E_F$ and expand ξ_k near the Fermi surface, i.e. $\xi_k = \hbar^2 k^2/(2m) - E_F \approx \hbar v_F |k - k_F|$ (see ref. [179]). The entropy in Eq. 6.5

results in

$$S = \frac{3N_{\text{tot}}}{E_F} \int_0^\infty d\xi_k \frac{E_k}{k_B T} \exp\left(-\frac{E_k}{k_B T}\right) = 3N_{\text{tot}} \frac{\Delta_0}{E_F} \sqrt{\frac{\pi \Delta_0}{2k_B T}} \exp\left(-\frac{\Delta_0}{k_B T}\right), \quad (6.12)$$

with

$$\Delta_0 = (2/e)^{7/3} E_F \exp\left(\pi/(2k_F a)\right) \qquad (6.13)$$

which is the gap at zero temperature [180]. With Eq. 6.12 we determine $s = S/(mN_{\text{tot}})$ and c_V. The normal fluid density in Eq. 6.6 gives

$$\frac{n_n}{n_{\text{tot}}} = 2 \int_0^\infty d\xi_k \left(-\frac{\partial f_k}{\partial E_k}\right) = \sqrt{\frac{2\pi \Delta_0}{k_B T}} \exp\left(-\frac{\Delta_0}{k_B T}\right). \qquad (6.14)$$

Using s, c_V, and n_n in Eq. 6.4 we obtain the second sound velocity

$$u_2 = \frac{\sqrt{3}}{2} \frac{k_B T}{E_F} v_F, \qquad (6.15)$$

which is valid for $T < T_C$. The BCS critical temperature is given by $k_B T_C = (\gamma/\pi)\Delta_0 = 0.567\Delta_0$, which depends on the interaction parameter $(k_F a)^{-1}$. We show in the main text the result u_2 at various interactions on the BCS side (see Fig. 2). u_2 vanishes at zero temperature contrary to the BEC superfluids. We note that this result is consistent with ref. [62].

6.6.4 Supplementary Note 4: BEC mean-field model

To estimate the density distribution of a partially Bose condensed cloud in the BEC regime we carry out a self-consistent calculation where the condensate phase is treated within the Thomas-Fermi approximation and for the normal phase we use a standard thermodynamical approach. Specifically, we solve the following set of coupled equations [181]

$$n_s(\mathbf{r}) = \frac{\mu_s - V_{\text{ext}}(\mathbf{r}) - 2g n_n(\mathbf{r})}{g} \Theta\left(\mu_s - V_{\text{ext}}(\mathbf{r}) - 2g n_n(\mathbf{r})\right) \qquad (6.16)$$

$$n_n(\mathbf{r}) = \frac{1}{\lambda_{dB}^3} \text{Li}_{3/2}\left(\exp\left\{\frac{\mu_n - V_{\text{ext}}(\mathbf{r}) - 2g n_s(\mathbf{r}) - 2g n_n(\mathbf{r})}{k_B T}\right\}\right). \qquad (6.17)$$

Here, λ_{dB} is the thermal deBroglie wavelength, $g = 4\pi\hbar^2 a_{dd}/M$ is the coupling constant, T is the temperature and $V_{\text{ext}}(\mathbf{r})$ is the external potential consisting of the harmonic trapping potential and the repulsive potential of the excitation beam, μ_s

and μ_n are the chemical potentials of the superfluid and the normal fluid part, respectively. For the calculation we set $\mu_n = \min[V_{ext}(\mathbf{r}) + 2gn_s(\mathbf{r}) + 2gn_n(\mathbf{r})]$ which ensures that the normal gas reaches the critical density $n_{n,crit} = \mathrm{Li}_{3/2}(1)/\lambda_{dB}^3$ at the Thomas-Fermi radius. This way, the number of normal fluid atoms is fixed. μ_s is chosen such that the total atom number matches the experimental value.
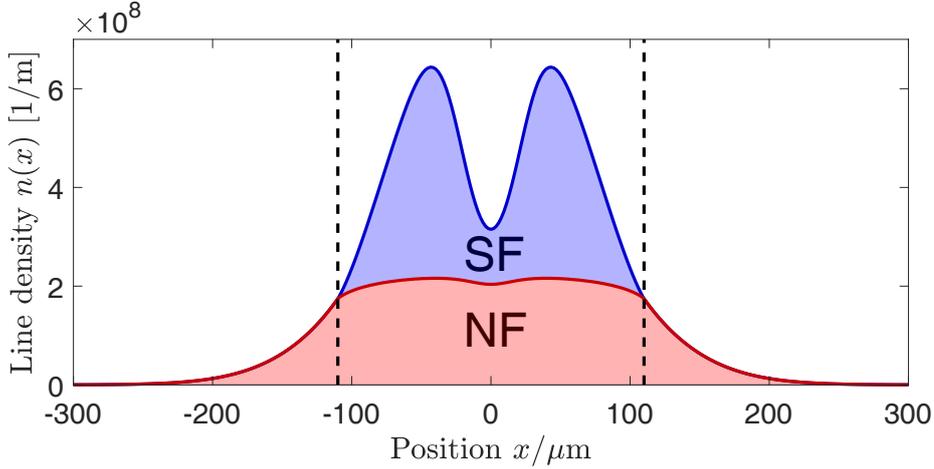
Figure 6.7: **Axial line densities of the superfluid and the normal phase obtained from a self-consistent calculation**. The calculation is performed for a gas at $(k_F a)^{-1} = 1.91$ and a temperature of $T = 145\,\mathrm{nK}$. The repulsive potential of the excitation laser beam at the center locally reduces the density of the cloud. The vertical dotted lines indicate the Thomas-Fermi radius at $x = \pm 110\,\mu\mathrm{m}$.

Equation 6.16 represents the Thomas-Fermi approximation where we take into account the repulsive mean-field potential of the normal fluid part. Equation 6.17 is the density distribution of a thermal bosonic cloud, again including the additional mean field potential produced by the atoms. By self-consistently solving the coupled equations we obtain the density distributions of the superfluid and the normal fluid gas as shown in fig. 6.7.

6.7 Additional information to the sound excitation scheme

In this section I provide additional details to the excitation scheme (not presented in the paper, i.e. sections 6.1 to 6.6.4).

First sound experiments

To investigate the propagation of the two sound modes we choose two different excitation schemes. Depending on the modulation scheme the perturbation excites predominantly first or second sound waves. For first sound excitation, the intensity of the excitation beam is modulated by a step function. The excitation laser is deactivated initially and is abruptly switched on at $t_{ex} = 0$ (starting point of wave propagation). This way the dimple at the trap center is removed (see fig. 6.8 a) and b), red line) such that only the cylinder symmetric trap, produced by the dipole laser, and the magnetic field curvature remains. The system responds upon the modulation with two counter-propagating wave packets [76, 170] (see fig. 6.8 c) red line).

Figure 6.8 e) shows $\Delta\bar{n}$ for an experiment at $808\,\mathrm{G}$ and at a temperature of $T \approx 0.7T_C$. The horizontal-axis is given in units of the Thomas-Fermi radius which marks the position where the superfluid density approaches zero. The vertical axis gives the time after the excitation pulse ended and is scaled by the axial trapping frequency $\omega_x = 2\pi \times \nu_x = 2\pi \times 21\,\mathrm{Hz}$. The axial trapping frequency sets the time scale for the propagating excitation. Due to momentum conservation, the local perturbation leads to two wave packets (bright traces) propagating from the trap center to the edges of the cloud. We observe the two wave packets propagating along the axial direction to the edge of the cloud, where $n \to 0$, $c_1 = \sqrt{gn/2m} \to 0$ and where the signal starts fades out.

Second sound experiments

To investigate second sound, the excitation scheme is changed from a step excitation to a sinusoidal modulation of the excitation potential (see fig. 6.8 a), b), green line). This heats the system locally. The deposited energy is transported via entropy wave packets.

For the excitation the modulation frequency is chosen to be $\omega_{ex} \approx 2\omega_r$, where ω_r is the radial trapping frequency. The excitation couples to the motional states of the particles in the radial direction, which corresponds to a local parametric heating of the gas. Due to the large anisotropy of the trap the motional states in the radial direction are excited selectively.
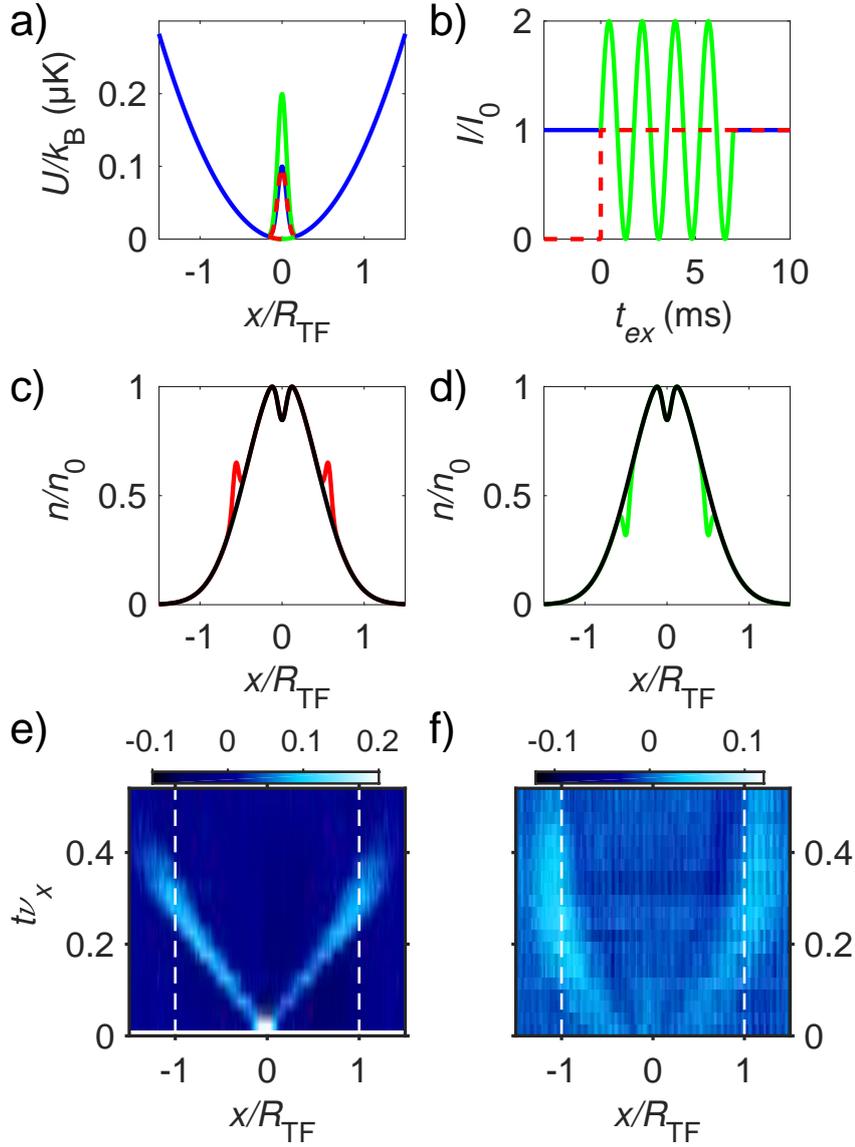
Figure 6.8: Sound excitation. Excitation scheme, system response and measure-
ments. a) Trapping potential (blue line). The height of the dimple
is modulated (see also b)) to produce predominantly first or second
sound waves. The axial position is scaled by the Thomas-Fermi ra-
dius R_{TF}. b) Intensity modulation. For first sound excitation a step
function (red dashed line) and for second sound excitation a sinusoidal
modulation (green solid line) is used. c) Sketch of the response of a
gas on first sound excitation. For simplicity a 1D Gaussian particle
distribution is shown which roughly matches the particle distribution
of a strongly interacting degenerate Fermi gas. The modulated beam
produces two wave packets propagating to the cloud edges (red solid
lines). For comparison the black line shows the density distribution of
the unperturbed system. d) Sketch of the 1D particle distribution in a
second sound experiment (Gaussian particle distribution considered).
The excitation produces two wave packets reducing the local density
(green solid lines). e) and f) show $\Delta\bar{n}(t)$ (see also sec. 6.5) for a first
and a second sound experiment at 808 G at $T \approx 0.7 T_C$, respectively.
The white dashed line marks the SF/NF transition.

The strong confinement in the radial direction $\omega_r \gg \omega_z$ has another consequence. Due to the high radial trapping frequency the time constant for particle motion is much smaller as in the axial direction such that the gas is able to thermalize quickly in the radial direction. Therefore, on the time scale of the experiments the gas is essentially always in thermal equilibrium in this direction (see also [62]).

The local temperature variation manifests itself as a decrease of the local density (see fig. 6.8 d)). Figure 6.8 f) shows $\Delta\bar{n}$ for a measurement at 808 G and at $T \approx 0.7 T_C$. The propagating wave packets (dark lines) propagate from the center to $|x| = R_{\mathrm{TF}}$, where the superfluid density $n_s \to 0$. At this point (SF/NF transition) $c_2 \to 0$ and the propagation stops. The bright traces in Figure 6.8 correspond to first sound excitation which could not be fully suppressed with the excitation scheme. Since the modulation is done over an extended period of time the first sound signal is blurred and broadened.

7 Holographic method for site-resolved detection of a 2D array of ultracold atoms

The content of this chapter has been published in Applied Physics B: Lasers and Optics. The material is taken from:

Please note that the format of the (journal) article was modified in order to fit the style and layout of the thesis. Hence a consecutive numbering of figures and references for the whole thesis was applied as well.

7.1 Abstract

We propose a novel approach to site-resolved detection of a 2D gas of ultracold atoms in an optical lattice. A near resonant laser beam is coherently scattered by the atomic array and after passing a lens its interference pattern is holographically recorded by superimposing it with a reference laser beam on a CCD chip. Fourier transformation of the recorded intensity pattern reconstructs the atomic distribution in the lattice with single-site resolution. The holographic detection method requires only about two hundred scattered photons per atom in order to achieve a high reconstruction fidelity of 99.9%. Therefore, additional cooling during detection might not be necessary even for light atomic elements such as lithium. Furthermore, first investigations suggest that small aberrations of the lens can be post-corrected in imaging processing.

7.2 Introduction

Ultracold atoms in optical lattices allow for investigating many-body physics in a very controlled way (see e.g. [182]). For such experiments site-resolved detection of the exact atomic distribution in the lattice can be very advantageous and it has recently been demonstrated [69–72, 74, 75]. In these experiments, the fluorescence of illuminated atoms is detected using a high-resolution objective. During the imaging process, typically several thousand photons are scattered per atom. This leads to strong heating of the atoms, requiring additional cooling.
Alternative imaging techniques using the diffraction of a laser beam by an atomic ensemble have been demonstrated for the detection of cold atomic clouds [76–79, 183, 184]. However, these techniques have neither been discussed for single-particle resolution nor single-site detection.
Here, we propose to image an atomic array with high resolution by using a variation of the off-axis holography technique of Leith and Upatnieks [77, 80]. Two coherent laser beams are used to record the hologram of an illuminated atomic array. One acts as a probe beam and is coherently scattered by the atoms [185], while the other acts as a reference beam which bypasses the atoms. Both beams are superimposed to interfere and to generate the hologram which is recorded with a charge-coupled device (CCD) camera. An algorithm based on fast Fourier transformation reconstructs an image of the atomic array. The reference beam fulfills two purposes: On the one hand it separates the holographic image from disturbing low spatial frequency signals in the reconstruction. On the other hand it strongly amplifies the atomic signal, as in spatial heterodyne detection [77]. This allows the use of a weak probe beam while keeping the signal high compared to detection noise. We estimate that for our scheme the number of scattered photons per atom can be small enough (≈ 150 photons) such that single site detection could be re-

alized without additional cooling. Moreover, the scheme might open the path for multi-particle detection per lattice site, since the low photon flux reduces photoassociation.

The paper is organized as follows: Section 7.3 sketches the basic scheme of the holographic detection method. Section 7.4 reviews theoretical background on atom light interaction, and on optical signals. In Section 7.5, we present the results of numerical calculations for the concrete example of ^{6}Li atoms in an optical lattice. Furthermore, we discuss the conditions for which a successful reconstruction of an atomic distribution can be achieved, including noise, mechanical vibrations, and lens aberrations. Section 7.6 concludes with a short summary and an outlook.

7.3 Detection scheme

We discuss the proposal in terms of a concrete example. As depicted in Fig. 7.1, we consider an ensemble of $N_A = 50$ atoms distributed over a 2D lattice with 11×11 sites and a lattice constant of $a = 1\,\mu$m. Each site is either empty or occupied by one single atom. We assume the lattice potential to be deep enough such that tunneling between the lattice sites is negligible.

The overall setup for the detection method is shown in Fig. 7.2. A Gaussian laser beam, near resonant to an optical atomic transition, is split into two beams, the probe and the reference beam. The probe beam propagates perpendicularly to the atomic layer and illuminates the atoms in the optical lattice. It has a diameter much larger than the spatial extent of the atomic sample, such that its electric field strength is approximately the same for all atoms.

The atoms are treated as Hertzian dipoles that coherently scatter the probe light. The scattered light is collimated by a diffraction-limited lens with a large numerical aperture and forms nearly perfect plane waves, which propagate towards the CCD detector. Since the spatial extent of the atomic sample is typically about three orders of magnitude smaller than the focal length f (Fig. 7.2 is not to scale!), the wave vectors of the plane waves are nearly parallel to the z-direction (optical axis). The non-scattered part of the probe beam is blocked by a small beam dump in the back focal plane of the lens. The reference beam bypasses the atomic layer and is superimposed with the collimated scattered light in the detection plane at an angle θ. In order to keep θ small (see discussion in Sec. 7.5), the reference beam is transmitted through the same lens as the scattered probe light. For this purpose, it is strongly focussed to a micrometer spot size in the front focal plane (at a sufficiently large distance to the atoms) and then collimated by the lens.

The overall intensity pattern is recorded by a CCD camera with a high dynamic range in order to resolve weak interference fringes on a high background signal. The pattern is subjected to a 2D Fourier transform (FT) [186] which directly yields the atomic distribution in the lattice. This step is analogous to classical hologra-
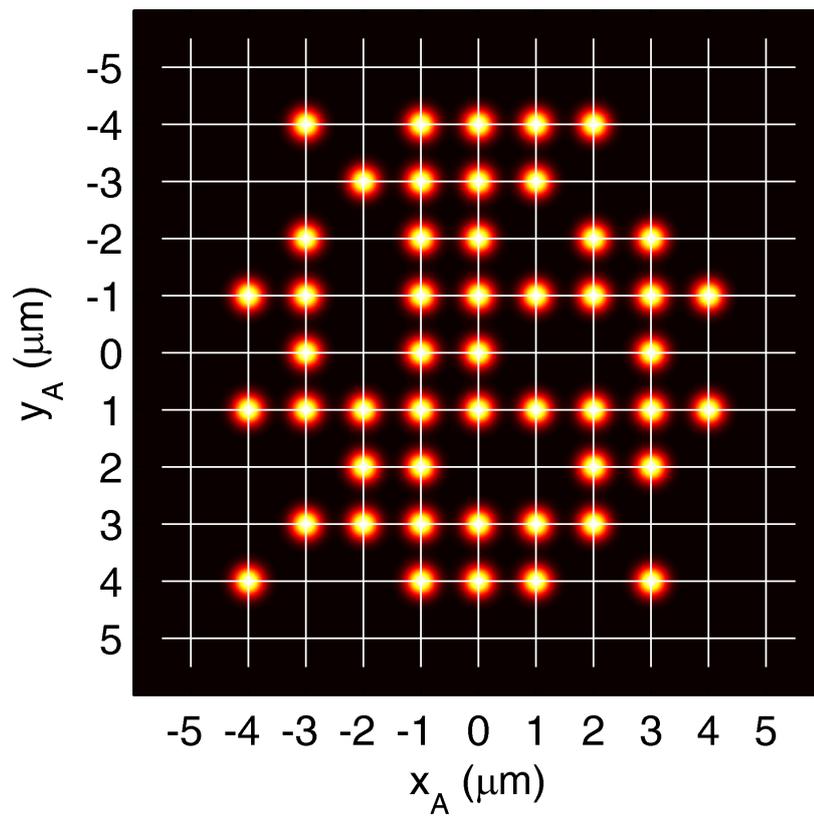
Figure 7.1: Ensemble of $N_A = 50$ atoms, distributed over a 2D square lattice with lattice constant $a = 1\,\mu\mathrm{m}$.
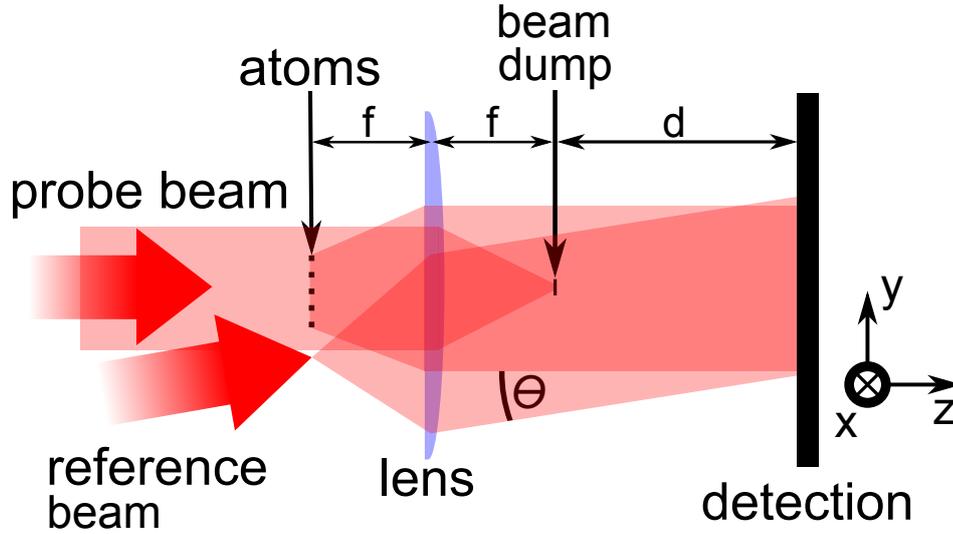
Figure 7.2: Basic scheme of the holographic detection method. A probe beam illuminates the 2D array of atoms and the scattered light is collimated by a lens with focal length f. The scattered light is superimposed with a reference beam on the CCD detector which is placed at a distance d behind the back focal plane. A beam dump blocks the unscattered light.

phy where a readout wave reconstructs the original object, corresponding to the holograms Fourier transform [133].

7.4 Theoretical description

Coherent light scattering

We use a semi-classical model for the interaction of a single atom with a monochromatic coherent light field. Each atom acts as a quantum mechanical two-level system with transition frequency ω_0. The atom is driven by a weak external laser field with frequency ω. This leads to photon scattering with a rate [187]

$$R_S = \frac{\Gamma}{2} \frac{I/I_{sat}}{1 + (2\Delta/\Gamma)^2 + I/I_{sat}} = \frac{N_{ph}}{T_{ac}}, \tag{7.1}$$

where I denotes the incident intensity of the driving field, I_{sat} the saturation intensity of the atomic transition, and $\Delta = \omega - \omega_0$ the detuning between laser and transition frequency. Γ is the linewidth of the atomic transition, and N_{ph} the total number of scattered photons per atom within the acquisition time T_{ac}.

In general, the intensity I_{sc} of the scattered light consists of both coherently and incoherently scattered parts. The coherent fraction of the scattered light I_{coh}/I_{sc} is

given by [187, 188]

$$\frac{I_{\text{coh}}}{I_{\text{sc}}} = \frac{1 + (2\Delta/\Gamma)^2}{1 + (2\Delta/\Gamma)^2 + I/I_{\text{sat}}}. \tag{7.2}$$

A weak incident beam with large detuning will therefore yield mainly coherently scattered light. As a concrete example, choosing $I/I_{\text{sat}} < 1$ and $\Delta = -\Gamma$ yields mostly coherent emission.

The probe beam as well as the reference beam ($\theta \approx 1°, \phi = 45°$ see Eq. (7.9)) are linearly polarized along the y direction. Treating the atoms as Hertzian dipoles, the electric field at position $\mathbf{r} = (x, y, z)$ in the far field, emitted by a single atom n at position $\mathbf{r}_n = (x_n, y_n, 0)$, is given by

$$E_{\text{A}}(\mathbf{r}, \mathbf{r}_n) = E_{\text{A0}} \frac{\sqrt{(x - x_n)^2 + z^2}}{k |\mathbf{r} - \mathbf{r}_n|^2} e^{ik|\mathbf{r} - \mathbf{r}_n|}, \tag{7.3}$$

with the wavenumber $k = 2\pi/\lambda$. Integrating the corresponding intensity over the entire solid angle 4π relates E_{A0} and the total number N_{ph} of scattered photons per atom

$$E_{\text{A0}}^2 = \frac{3k^2\hbar\omega}{4\pi c\varepsilon_0 T_{\text{ac}}} N_{\text{ph}}. \tag{7.4}$$

Here, c denotes the speed of light in vacuum and ε_0 the permittivity of free space.

The wave emitted by the nth atom in the optical lattice is converted by the lens into a nearly perfect plane wave with wave vector

$$\mathbf{k}_n = \begin{pmatrix} k_{n,x} \\ k_{n,y} \\ k_{n,z} \end{pmatrix} = \frac{k}{\sqrt{x_n^2 + y_n^2 + f^2}} \begin{pmatrix} -x_n \\ -y_n \\ f \end{pmatrix}. \tag{7.5}$$

The field distribution of the plane wave in the detector plane $z = z_D$ reads

$$E_{\text{S},n}(x, y) = E_{\text{A0}} g_{\text{A}}(x, y) e^{i(xk_{n,x} + yk_{n,y} + \varphi_n)}, \tag{7.6}$$

where φ_n includes the constant term $z_D k_{n,z}$ and the phase shift acquired by the wave while passing through the lens.

The field envelope $g_{\text{A}}(x, y)$ is a slowly varying function which can be determined from Eq. (7.3). Since $f \gg |x_n|, |y_n|$, the propagation directions of all plane waves behind the lens are almost parallel to the z-axis and $g_{\text{A}}(x, y)$ is essentially independent of z. Therefore, we calculate $g_{\text{A}}(x, y)$ at the position of the lens. Setting $z = f$ in Eq. (7.3) and using the relation $|\mathbf{r}_n| \ll |\mathbf{r}|$ we obtain

$$g_{\text{A}}(x, y) \approx \frac{\sqrt{x^2 + f^2}}{k(x^2 + y^2 + f^2)} \Theta(r_l - \sqrt{x^2 + y^2}). \tag{7.7}$$

The Heaviside function Θ accounts for the finite size of the lens with radius r_l. The electric field of the Gaussian-shaped reference beam at the detector reads

$$E_{\mathrm{R}}(x,y) = E_{\mathrm{R0}}\, g_{\mathrm{R}}(x,y) e^{i(x k_{R,x} + y k_{R,y} + \varphi_R)}, \tag{7.8}$$

with the wave vector

$$\mathbf{k}_R = \begin{pmatrix} k_{R,x} \\ k_{R,y} \\ k_{R,z} \end{pmatrix} = k \begin{pmatrix} \sin\theta\cos\phi \\ \sin\theta\sin\phi \\ \cos\theta \end{pmatrix}. \tag{7.9}$$

For small θ, the Gaussian field envelope $g_R(x,y)$ is given by

$$g_R(x,y) \approx e^{-(x^2+y^2)/w^2}\Theta(r_l - \sqrt{x^2+y^2}), \tag{7.10}$$

with reference beam waist w.

Interference and Fourier transformation

The total electric field in the detector plane is obtained by adding up all individual fields. The corresponding intensity,

$$I_{\mathrm{D}}(x,y) = \frac{1}{2} c\varepsilon_0 \left| E_{\mathrm{R}}(x,y) + \sum_n E_{\mathrm{S},n}(x,y) \right|^2, \tag{7.11}$$

can be written as a sum of three contributions

$$I_{\mathrm{D}} = I_0 + I_{\mathrm{S}} + I_{\mathrm{RS}}. \tag{7.12}$$

The particle distribution is derived from the Fourier transform F_{D} of the intensity profile I_D. F_{D} decomposes into three parts, F_0, F_{S}, and F_{RS}. This is illustrated in the schematic plot in Fig. 7.3, which depicts a 1D cut through a 2D FT along the spatial frequency axis ν_x at $\nu_y = 0$. The illustration is consistent with the atomic distribution in Fig. 7.1 and presumes a wave vector $\mathbf{k}_R$ with $k_{R,y} = 0$.
The first contribution I_0 in Eq. (7.12) is a broad structureless intensity background

$$I_0 \propto E_{\mathrm{R0}}^2\, g_{\mathrm{R}}^2(x,y) + N_{\mathrm{A}} E_{\mathrm{A0}}^2\, g_{\mathrm{A}}^2(x,y) \tag{7.13}$$

whose FT F_0 is represented by the large peak at the origin in Fig. 7.3. The width of the peak is determined by the inverse beam sizes g_R and g_A. The second contribution

$$I_{\mathrm{S}} \propto E_{\mathrm{A0}}^2\, g_{\mathrm{A}}^2(x,y) \sum_{n>m} \cos[2\pi(\nu_{nmx}x + \nu_{nmy}y) + \Delta\varphi_{nm}] \tag{7.14}$$
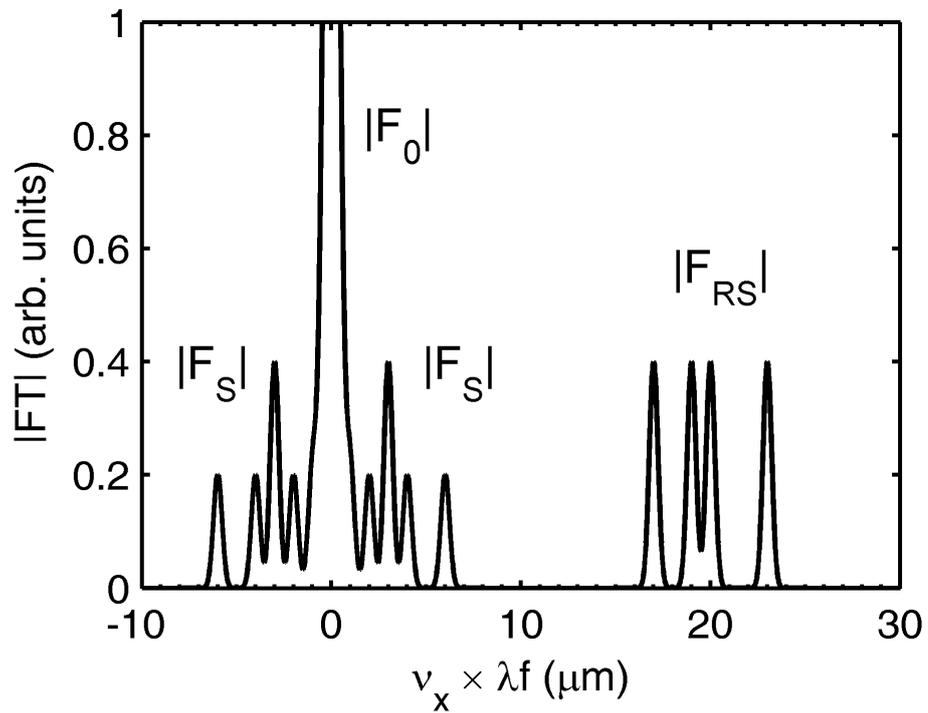
Figure 7.3: 1D cut through a schematic 2D FT along the spatial frequency axis v_x at $v_y = 0$, illustrating the contributions of F_0, F_S, and F_{RS}. The four peaks around $v_x \times \lambda f \approx 20 \ \mu$m reconstruct the positioning of the four atoms in Fig. 7.1 arranged along the x_A axis at $y_A = 0$.

with $\Delta\varphi_{nm} = \varphi_n - \varphi_m$ arises from the interference between the electric fields $E_{S,n}$ emitted by the individual atoms in the optical lattice. Since $f \gg |x_n|, |y_n|$, the spatial frequencies ν_{nmx} and ν_{nmy} are approximately given by

$$\nu_{nmx} = \frac{x_m - x_n}{f\lambda}, \quad \nu_{nmy} = \frac{y_m - y_n}{f\lambda}, \tag{7.15}$$

where (x_n, y_n) are the atomic positions in the optical lattice. Each pair of spatial frequencies ν_{nmx}, ν_{nmy} gives rise to a well-defined peak in the FT close to the origin. The width of the peaks is again determined by the inverse of the collimated beam width g_A. The third term in Eq. (7.12),

$$\begin{aligned} I_{RS} &\propto E_{R0}E_{A0}\, g_R(x,y)\, g_A(x,y) \times \\ &\times \sum_n \cos[2\pi(\nu_{nx}x + \nu_{ny}y) + \Delta\varphi_{Rn}], \end{aligned} \tag{7.16}$$

arises from the interference of the scattered beams with the reference beam. Here, $\Delta\varphi_{Rn} = \varphi_R - \varphi_n$. The FT of I_{RS}, i.e. F_{RS}, can be conveniently used to extract the atomic distribution in the lattice. Apart from an overall constant factor λf, the spatial frequencies ν_{nx} and ν_{ny} directly correspond to the coordinates x_n and y_n of each particle n.

$$\begin{aligned} \nu_{nx} &= \frac{x_n}{\lambda f} + \frac{\sin\theta\cos\phi}{\lambda}, \\ \nu_{ny} &= \frac{y_n}{\lambda f} + \frac{\sin\theta\sin\phi}{\lambda} \end{aligned} \tag{7.17}$$

The offsets, $\sin\theta\cos\phi/\lambda$ and $\sin\theta\sin\phi/\lambda$, can be tuned by adjusting the direction of the incident reference beam (see Eq. (7.9)). As in spatial heterodyne detection, they are used to shift the peaks of the signal F_{RS} away from the origin to separate them from the peaks of F_0 and F_S. Resolving Eq. (7.17) for the atomic coordinates x_n and y_n yields

$$\begin{aligned} x_n &= \lambda f \nu_{nx} - f\sin\theta\cos\phi, \\ y_n &= \lambda f \nu_{ny} - f\sin\theta\sin\phi. \end{aligned} \tag{7.18}$$

7.5 Numerical Calculations

In this section, we present the results of our numerical calculations. First, we specify the used parameters and discuss the case of a noiseless detection. Then, we include detection noise and analyze its influence on the reconstruction fidelity. Finally, we compare our method with direct fluorescence detection and estimate its

sensitivity to mechanical vibrations.

7.5.1 Parameters and details

In the following, we consider an ensemble of $N_A = 50$ ^{6}Li atoms in a 2D lattice (see Fig. 7.1). The wavelength of the coherent probe and reference laser beams is set to $\lambda = 671$ nm, close to the D_2 transition of ^{6}Li. The saturation intensity is $I_{sat} = 2.54$ mW/cm^2 at a natural linewidth of $\Gamma = 2\pi \times 5.87$ MHz. The focal length of the collimation lens is chosen to be $f = 7$ mm and the numerical aperture (NA) is 0.71, which matches typical parameters of a custom long working distance objective (see Fig. 7.2).

In the given case, we set the reference beam waist to $w = 5$ *mm* (see Eq. (7.10)). The illuminated area in the detection plane, which is located 70 mm away from the lens, has a radius of about 7 mm. In our simulations we consider only a part of this area, namely a square section of 10×10 mm^2. The CCD pixel size is assumed to be $A_P = 7 \times 7$ μm^2, the quantum efficiency is set to $Q = 0.8$. We choose an acquisition time T_{ac} of 200 μs. On the considered time scale mechanical vibrations and particle tunneling inside the lattice can be neglected.

Two fundamental parameters are varied: The average number of photons N_{ph} scattered by a single atom into the entire solid angle 4π within T_{ac}, and the total power P_R of the reference beam. In the present study, we consider the ranges $100 \leq N_{ph} \leq 500$ and 10^{-8} W $\leq P_R \leq 10^{-2}$ W. Given an average number of scattered photons N_{ph}, the corresponding electric ld strength E_{A0} is obtained from Eq. (7.4). Using Eqs. (7.1) and (7.2), we verify that with these parameters we stay in the regime of mainly coherent emission.

7.5.2 Intensity pattern

We calculate the image captured by the CCD camera as follows. First, the intensity profile $I_D(x, y)$ in the considered section of the detection plane is calculated using Eq. (7.11). Then, the intensity $I_{CCD}(x_p, y_p)$ collected by a CCD pixel at position (x_p, y_p) is obtained by averaging over all intensity contributions covered by the corresponding pixel area. In contrast to x and y, the coordinates x_p and y_p exhibit only discrete values. I_{CCD} is converted into an integer number N_D of nominally incident photons, ignoring for now photon shot noise,

$$N_D(x_p, y_p) = \text{round}\left(\frac{I_{CCD}(x_p, y_p)T_{ac}A_P}{\hbar\omega}\right). \quad (7.19)$$

The output signal of a CCD camera in counts is

$$N_{\text{counts}}(x_p, y_p) = \text{round}\left(\frac{N_D(x_p, y_p)Q}{\alpha}\right), \qquad (7.20)$$

where α denotes the number of accumulated electrons per pixel that correspond to one count. It predefines the dynamic range of the CCD camera, which decreases with increasing α. In the calculations presented in Sec. 7.5 we use $\alpha = 1$. For the considered parameters, however, values up to $\alpha = 10$ yield almost the same results.

7.5.3 Calculations without noise

Let us start the discussion of our calculations by considering the idealized situation of absent noise. Furthermore, for the purpose of better illustration, we choose an example where the power of the reference laser is comparatively low ($P_R = 10^{-8}$ W). For this choice, interference fringes are clearly visible, since the ratio I_{RS}/I_0 is comparatively high.

Figure 7.4a shows a cut through the corresponding intensity profile $I_D(x, y)$ along the x axis at y = 0 calculated with $N_{\text{ph}} = 500$.

The pronounced oscillations on top and at the tails of a Gaussian profile as well as weak oscillations in between arise from the interference between the scattered probe light and the Gaussian-shaped reference beam. Since the relevant information about the atom positions is stored in these interference fringes, the period length of the oscillations must be large enough to be resolved even after averaging intensity values within a pixel (see explanation above). We achieve this by using a small angle of incidence $\theta \approx 1°$. This results in a sufficiently large period length of about $40\,\mu$m as revealed by the inset of Fig. 7.4a. The angle corresponds to a distance between the focus of the reference beam and the atomic ensemble of about $100\,\mu$m (see Fig. 7.2).

The emergence of the pronounced interference peaks at $0, \pm 4.5$mm in Fig. 7.4a can be understood as follows. To first order, the light scattered by the rectangular array of atoms resembles the diffraction pattern of a perfect 2D square lattice, as depicted in Fig. 7.4b. The quickly-oscillating intensity peaks in the center and at the edges in Fig. 7.4a are the corresponding zeroth and first-order diffraction peaks which interfere with the reference beam. The atomic array, however, is not perfect as a number of lattice sites are unoccupied. As a consequence, the intensity in between the major diffraction peaks is non-zero. This leads to the weak, but still clearly visible interference patterns in Fig. 7.4a between the strong oscillations in the middle and at the edges. The information about occupied lattice sites is contained in these oscillations. In order to resolve them, especially for a higher reference laser power, the CCD camera needs a large dynamic range (12 bit or better).
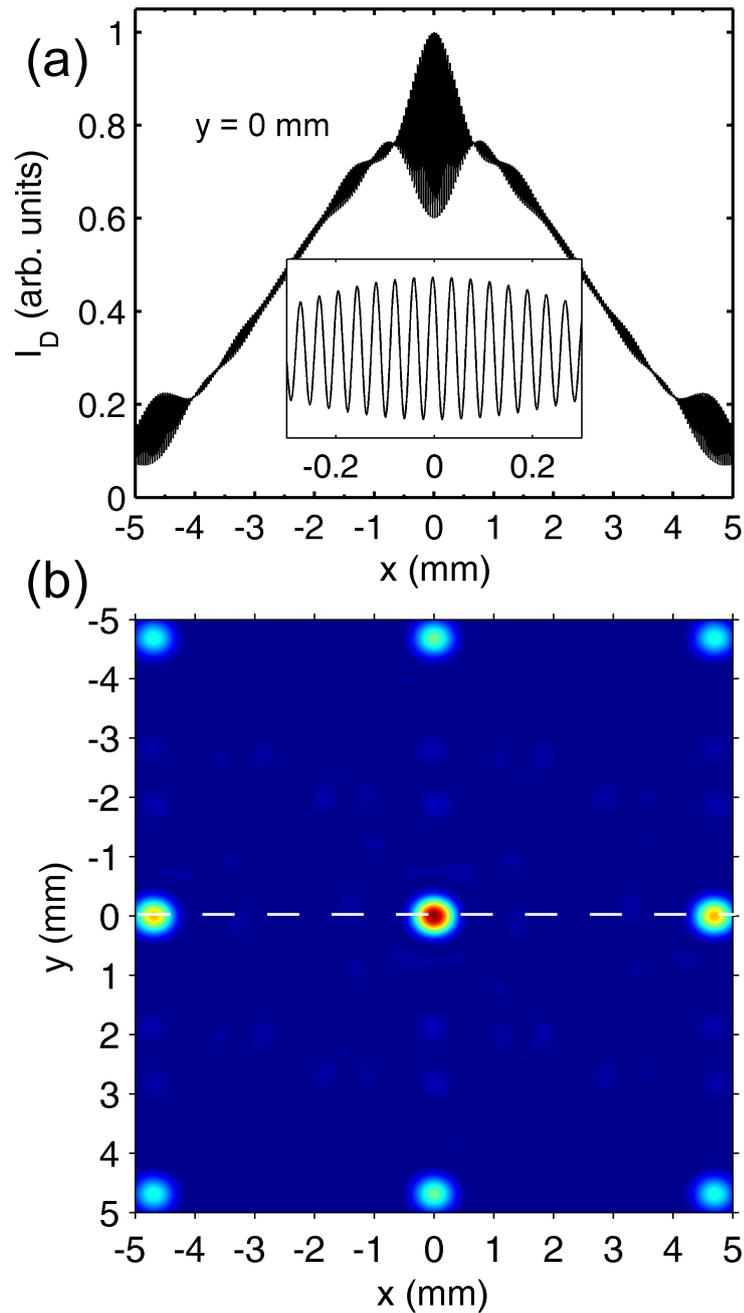
Figure 7.4: (a) 1D cut through the calculated 2D intensity profile $I_D(x,y)$ in the detection plane along the x axis for y = 0. The intensity profile results from a superposition of the scattered probe beam and the broad Gaussian reference beam. An enlargement of the central part (inset) clearly reveals a sinusoidal interference pattern. For illustration purposes, a very low reference signal has been used in this model calculation, such that the interference fringes are clearly visible on the Gaussian background signal. (b) 2D intensity distribution in the detection plane without reference beam (false color image; blue: low, red: high intensity). It strongly resembles the diffraction pattern of a 2D square lattice where the zeroth and first-order peaks are located in the center and at the edges, respectively.
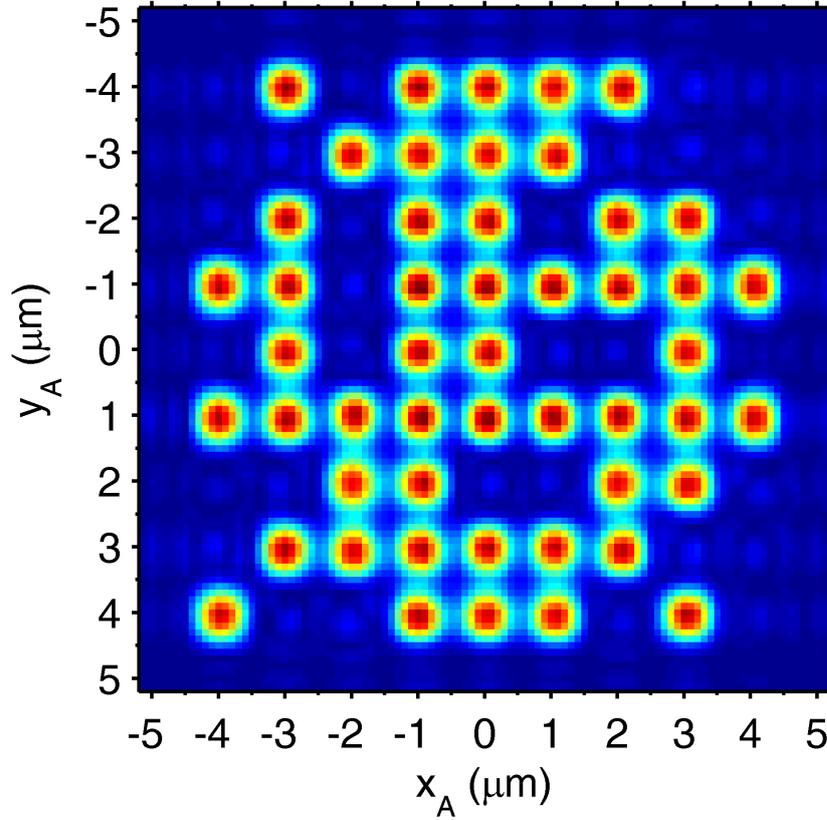
Figure 7.5: Section of the 2D FT yielding a perfectly reconstructed image of the
atomic distribution in Fig. 7.1. The false color plot displays absolute
values of the Fourier coefficients (blue: low, red: high FT amplitude).
The simulation was performed without noise using the parameters N_{ph}
= 150 and $P_R = 10^{-5}$W.

As explained in Sec. 7.4, the atomic positions in the lattice can be directly derived
from a 2D FT of the intensity profile $I_D(x,y)$, or more precisely from a FT of
$N_{\text{counts}}(x_p, y_p)$. An appropriately chosen section of such a FT is shown in Fig. 7.5,
where the absolute values of the Fourier coefficients are displayed as a false color
image.

The coordinates x_A and y_A give the position within the atomic layer and are related
to the spatial frequencies ν_x and ν_y of the FT by (see Eq. (7.18))

$$
\begin{aligned}
x_A &= \lambda f \nu_x - f \sin\theta \cos\phi, \\
y_A &= \lambda f \nu_y - f \sin\theta \sin\phi.
\end{aligned} \tag{7.21}
$$

The maxima in the 2D plot at $y_A = 0$ correspond to the group of peaks labeled by
F_{RS} in the schematic 1D illustration of Fig. 7.3. In contrast to Fig. 7.4a, $N_{\text{counts}}(x_p, y_p)$

is calculated using $N_{\text{ph}} = 150$ and $P_{\text{R}} = 10^{-5}$ W. A comparison with Fig. 7.1 reveals that the atomic distribution is perfectly reconstructed.

7.5.4 Speckle and shot noise

Let us now turn to the realistic situation where the image acquired by the CCD camera is disturbed by different kinds of noise. These need to be taken into account to understand where the limits of the presented holographic detection method lie. In general, in an experiment there are several sources which decrease the fidelity of a detection. For a CCD camera, there are photon shot noise, read-out noise, and dark counts which have to be taken into account. However, for the case of a relatively strong reference beam and thus of a high light intensity, the dominant detection noise is given by shot noise. Shot noise describes fluctuations in the number of detected photons and obeys a Poisson distribution. It is taken into account by replacing N_D, calculated from $I_{\text{CCD}}(x_p, y_p)$ in Eq. (7.19), by a Poisson-distributed variable with expectation value N_D.

Imperfections of the ideally Gaussian intensity profiles of the probe and reference beams will also have an effect on the reconstruction. Such corrugations can be caused by effects such as shortcomings in the quality of optical elements or weak stray reflections of the laser beams. The resulting intensity distribution typically shows high-frequency intensity fluctuations similar to laser speckle [189, 190]. If we assume the fluctuations to occur on a length scale of about $1\,\mu$m in the detection plane, this kind of noise adds the intensity $I_{\text{SP}}(x, y)$ to $I_{\text{D}}(x, y)$. It is known [189, 190] that this added noise has an exponentially decreasing probability as a function of $|I_{\text{SP}}|$

$$P_{\text{SP}}(I_{\text{SP}}) \propto \exp\left(-\frac{|I_{\text{SP}}|}{\alpha I_{\text{D}}}\right). \tag{7.22}$$

From our own laboratory experience we estimate that the typical amplitude of these fluctuations is on the level of about one percent. Therefore, we set $\alpha = 0.01$.

In order to take into account read-out noise, we add an integer number $\Delta N_{\text{counts}}(x_p, y_p)$ to $N_{\text{counts}}(x_p, y_p)$. This noise is obtained from a zero-centered normal distribution with a standard deviation of 3 counts (typical specification of a commercial electron multiplying CCD camera).

The combined effects of intensity averaging, noise, as well as photon counting (see Eq. (7.20)) are illustrated in Fig. 7.6. It depicts a 1D cut through the CCD image $N_{\text{counts}}(x_p, y_p)$ along the x_p axis for $-0.3\,\text{mm} \leq x_p \leq 0.3\,\text{mm}$ and $y_p = 0$, calculated with $N_{\text{ph}} = 150$ and $P_R = 10^{-5}$W. In contrast to the inset of Fig. 7.4a, which displays the same x range, the interference pattern is now barely perceptible.

The corresponding 2D FT is shown in Fig. 7.7.

In contrast to Fig. 7.5, it is very noisy. However, we can still reconstruct the atomic distribution with a sufficiently high fidelity.
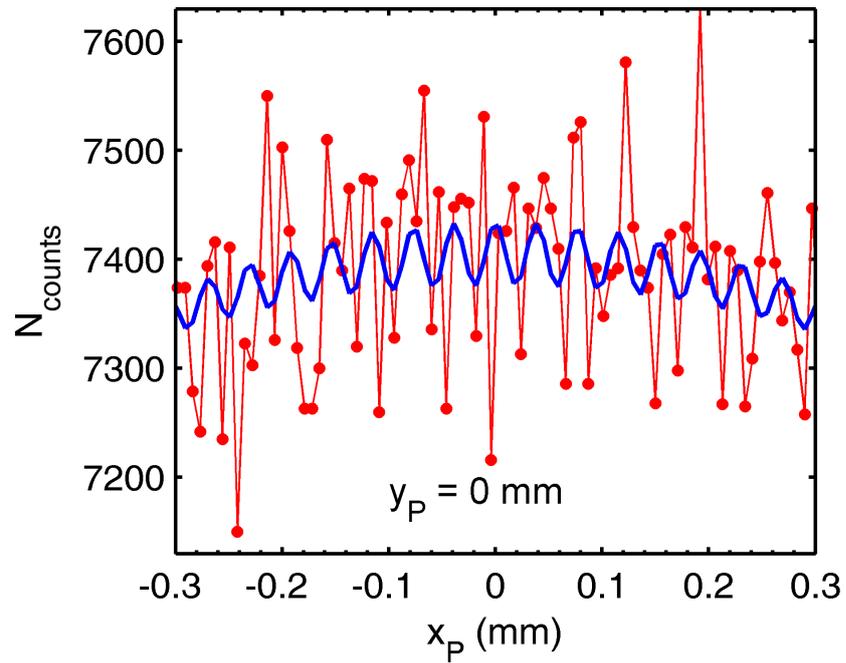
Figure 7.6: 1D cut through the calculated CCD image $N_{counts}(x_p, y_p)$ along the x_p axis at $y_p = 0$ including noise (red line/dots). The parameters used in the calculation are $N_{ph} = 150$ and $P_R = 10^{-5}$W. The blue line depicts the undisturbed interference signal for comparison.
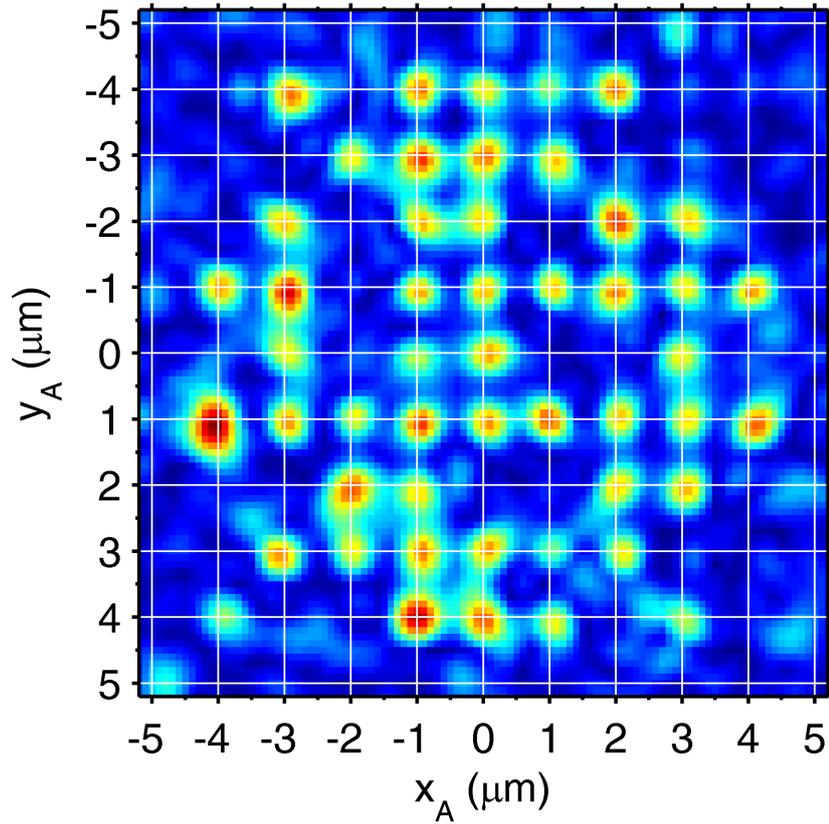
Figure 7.7: Example of a reconstructed image of the atomic distribution (2D FT
of $N_{\mathrm{counts}}(x_p, y_p)$) taking into account speckle, shot, and read-out noise
(blue: low, red: high FT amplitude). The simulation was performed
using the parameters $N_{\mathrm{ph}} = 150$ and $P_R = 10^{-5}$W. For this example our
simple recognition algorithm (see text) yields a fidelity of 99.2% to
identify the occupation of an individual site.
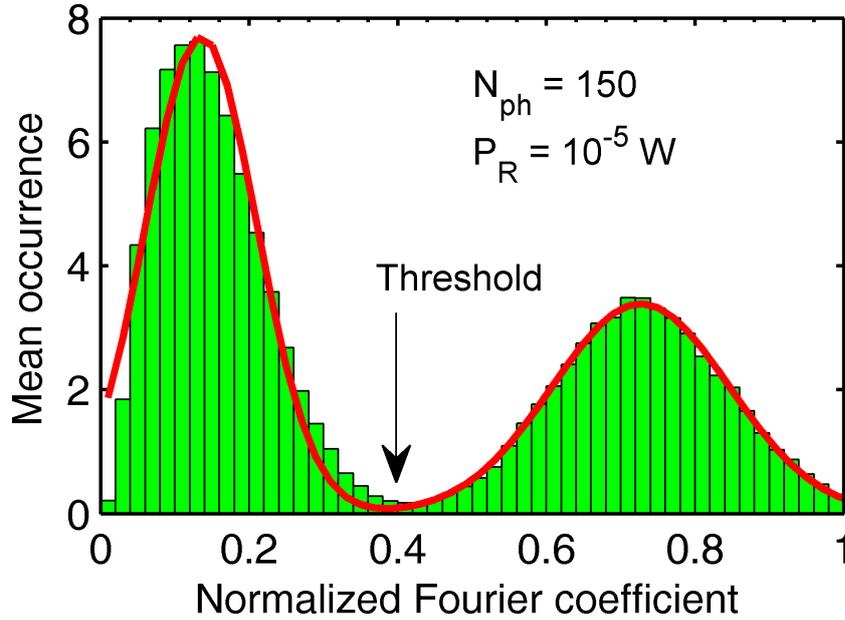
Figure 7.8: Probability distribution of the normalized Fourier coefficients determined at the optical lattice sites (see Fig. 7.7). The histogram represents an average over 1000 probability distributions obtained for N_{ph} = 150, $P_R = 10^{-5}$W, fixed speckle noise, and randomly varying shot noise. The dip at 0.4 coincides with the threshold value with highest reconstruction fidelity. The red solid curve are two partially overlapping Gaussians which are fitted to the histogram.

For this, we use the following simple algorithm. We normalize the reconstruction signal (absolute values of the Fourier coefficients) within the FT section depicted in Fig. 7.5 and Fig. 7.7. Next, we place the lattice grid on top as shown in Fig. 7.7. The normalized value at each grid point is compared to a threshold value. If the value lies (below) above the threshold, the lattice site is identified as (un)occupied. We define a fidelity as the percentage of correctly identified sites. An analysis of a variety of atomic arrays with different filling factors shows that for the investigated range of parameters N_{ph} and P_R a threshold value of 0.4 yields the highest fidelity. The histogram in Fig. 7.8 displays the probability distribution of the normalized Fourier coefficients for N_{ph} = 150, $P_R = 10^{-5}$W. It is obtained by averaging over the probability distributions of 1000 reconstructed images of the particle distribution of Fig. 7.1. The calculation includes a fixed speckle noise and randomly varying shot and read-out noise. As shown by the red line in Fig. 7.9, the distribution resembles two overlapping Gaussians with a pronounced minimum at 0.4.

In Fig. 7.9, the fidelity is plotted as a function of P_R for different values of N_{ph}. Each data point is again obtained by averaging over the fidelities of 1000 reconstructed

images, calculated with randomly varying shot and read-out noise. For $N_{\text{ph}} \geq 150$ the fidelity reaches maximum values clearly exceeding 99.5%, for $N_{\text{ph}} = 100$ (not shown) it is still nearly 98.5%.

Depending on the range of P_{R}, the fidelity is limited by different kinds of noise. At low and high reference power, read-out noise and speckle noise prevail, respectively. In both cases, the noise leads to a strong decline of the fidelity. In between, shot noise is dominant. The dependence of the fidelity on P_{R} and N_{ph} can be understood by the signal-to-noise ratio (SNR) of the interference fringes on the CCD camera. Neglecting atomic contributions to I_0 in Eq. (7.13), a rough estimate yields

$$\text{SNR} \approx \frac{I_{\text{RS}}}{\sqrt{I_0}} \propto E_{\text{A0}} \propto \sqrt{N_{\text{ph}}}. \tag{7.23}$$

In the fraction $I_{\text{RS}}/\sqrt{I_0}$, the field amplitude E_{R0} of the reference beam drops out and the SNR is independent of P_{R}. As a consequence, the fidelity features a plateau. The width of the plateau as well as the maximum fidelity decreases with decreasing N_{ph}. This can be explained by the proportionality of SNR to the atomic field amplitude $E_{\text{A0}} \propto \sqrt{N_{\text{ph}}}$. Above a critical value of P_{R}, marked by the dashed line in Fig. 7.9, the pixels near the center of the CCD camera saturate (assuming a dynamic range of 16 bit). Therefore, in practice the speckle-induced drop should be irrelevant.

Moreover, all effects leading to global laser intensity fluctuations do not disturb the interference signal, since they do not change the relative phase between atomic and reference signal.

7.5.5 Comparison with fluorescence detection

As demonstrated in Fig. 7.9, the proposed detection scheme should yield fidelities higher than 99.5% even for moderate numbers of scattered photons. This is achieved by means of the reference beam which amplifies the atomic diffraction signal. In contrast, the direct fluorescence detection method, e.g. used in [70–72, 74, 75], does not involve such a reference beam. During detection several thousands of photons are scattered by a single atom. As a disadvantageous consequence, the atoms are strongly heated and may hop between lattice sites even in the case of deep optical lattices (see e.g. [75]). Therefore, complex cooling techniques have to be applied.

To compare our scheme with the fluorescence detection, we estimate the particle heating. We assume that the particles are initially in the vibrational ground state $|v = 0\rangle$ of a deep optical lattice with a depth of 2.5 mK and a Lamb-Dicke parameter of $\eta = 0.23$ (see [73]). During detection, the particles scatter 150 photons per atom. The transition probability from $|v = n\rangle$ to $|v = n \pm 1\rangle$ for a single scattering event is given by $\eta^2 (n+1)$ and $\eta^2 n$, respectively. An estimate based on random
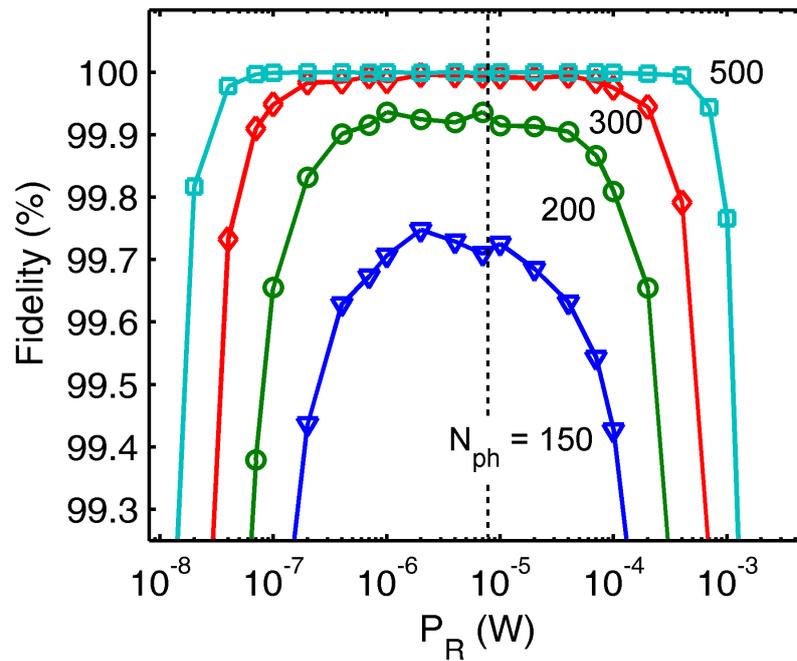
Figure 7.9: Fidelity as a function of P_R for different average total numbers of scat-
tered photons per atom N_{ph}. Each data point is obtained by averaging
over the fidelities of 1000 reconstructed images (with fixed particle dis-
tribution), calculated with randomly varying shot and read-out noise.
Above a critical value of P_R, marked by the dashed line, the pixels near
the center of a CCD camera with a dynamic range of 16 bit start to
saturate.

walk yields that 99% of the atoms end up at a vibrational state $|v_{Final} \leq 24\rangle$. The excitation to higher vibrational states reduces the tunneling time of a particle inside the lattice. However, since the tunneling time of a particle in state $|v_{Final} = 24\rangle$ is on the order of 1 ms, i.e. long compared to the acquisition time $T_{ac} = 200\,\mu s$, tunneling can be neglected. This means that the heating due to light scattering should hardly influence the reconstruction fidelity. Therefore, our scheme might open the path to circumvent additional cooling during detection.

7.5.6 Mechanical vibrations

In terms of a technical issue of the proposed scheme, we need to take into account the sensitivity of the setup to mechanical vibrations. For this, we consider Eq. (7.16) and Eq. (7.21). During the acquisition time, the relative phases $\Delta\varphi_{nR}$ between reference and scattered laser fields may vary, leading to a blurring of the contrast of the interference fringes. A jitter $\delta\theta$ in the reference angle θ leads to a similar effect. In order to estimate the influence of the jitter, we rewrite x_A in Eq. (7.21) for angles close to $\theta \approx 1°$ (as used in our simulations) with $\phi = 45°$ fixed:

$$x_A = \lambda f v_x - \frac{f}{\sqrt{2}}\theta. \tag{7.24}$$

A jitter $\delta\theta$ thus causes a blurring $\delta x = f\delta\theta/\sqrt{2}$ of the coordinates in the reconstruction. If we demand $\delta x \ll a$, the jitter has to be much smaller than $\sqrt{2} \times 1\,\mu m/f \approx 200\,\mu rad$. This should not pose a problem since pointing stabilities of $10\,\mu rad$ or better are typical in an optical lab environment. Furthermore, achieving fluctuations in the relative phase $\Delta\varphi_{nR} \ll \pi$ is standard on an optical table.

7.5.7 Lens aberrations

Another technical issue of the holographic detection scheme is lens aberrations. In our scheme a large NA lens collimates the emitted light of the atoms and the reference beam. Even for a high-quality lens the transmitted wavefront can be distorted by lens imperfections and aberrations. To estimate such shortcomings, we perform a 1D calculation in the presence of small spherical aberration which results in a position-dependent tilt of the wave vectors $\mathbf{k}_n$ and $\mathbf{k}_R$ (see Eqs. (7.5), (7.9)). We simulate the tilt in the detection plane by

$$\mathbf{k}_{n,R} \propto \begin{pmatrix} -x_{n,R} - \beta(x + 10\,x_{n,R})^3 \\ f \end{pmatrix}, \tag{7.25}$$

where the empirical parameter β sets the influence of the spherical aberration and x_R denotes the position of the reference beam in the front focal plane of the lens.
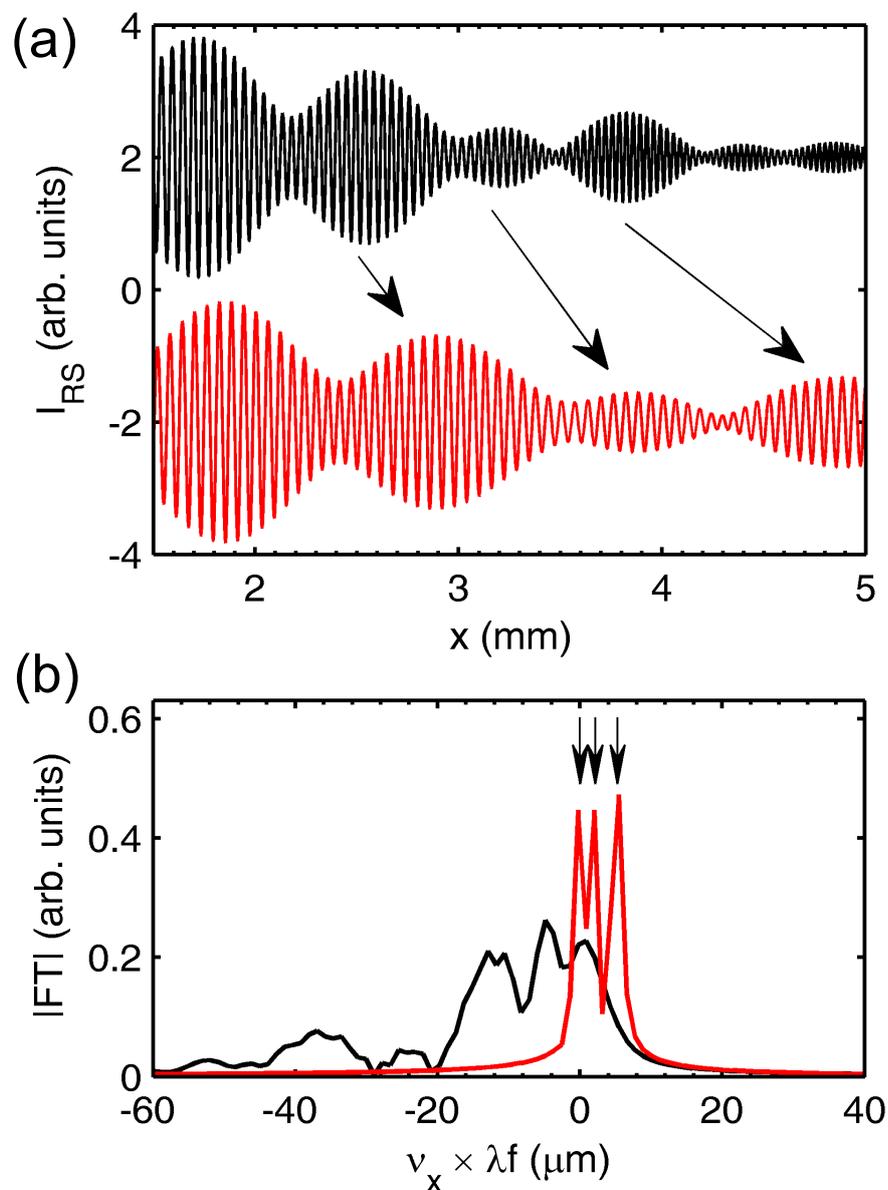
Figure 7.10: Distortion of the interference pattern due to spherical aberration and its correction. (a) Shown is a distorted 1D holographic interference pattern in the presence of spherical aberration (black curve). The atomic emitters are located 0, 2, 5 μm away from the optical axis. Using an appropriate mapping the interference pattern can be corrected (red curve). (b) Reconstruction of the particle distribution with (red) and without (black) correction. The positions of the atomic emitters are marked with arrows.

The black curves in Fig. 7.10a and 10b show the interference fringes and the corresponding reconstruction, respectively, for a reference beam and three atoms at positions $x_n = 0, 2, 5 \, \mu$m. The aberration leads to an increase of the spatial frequency $\nu_{SF}(x)$ in the interference pattern with increasing distance x to the optical axis. As a result, the Fourier transform no longer yields a high-fidelity reconstruction (Fig. 7.10b). However, the effect of the aberration can be compensated with the help of an empirical non-linear mapping which locally stretches the interference pattern such that it exhibits a constant ν_{SF} (red curve in Fig. 7.10a). The sharp peaks at $x_n = 0, 2, 5 \, \mu$m in Fig. 7.10b demonstrate that the atomic distribution can be successfully reconstructed in this way.

In order to derive an appropriate non-linear mapping, we calculated the interference between the reference beam and a single point emitter at $x_n = 0 \, \mu$m in the presence of aberration and determined the dependence of $\nu_{SF}(x)$ on the position x. The mapping results from a comparison between $\nu_{SF}(x)$ and the known spatial frequency in the case of absent aberration. Although the correction is obtained only for a single point emitter it successfully works even for a larger number of atoms. We thus demonstrate a preliminary way to correct distorted interference patterns. Clearly, more general and sophisticated compensation algorithms can be developed which will turn the holographic detection scheme robust against aberrations of the lens. This might prove to be very useful in the future as it relaxes the required lens specifications for high-resolution imaging.

7.6 Conclusion

In conclusion, we propose a holographic scheme for site-resolved detection of a 2D gas of ultracold atoms in an optical lattice. We have discussed the method for the example of 50 lithium atoms in a square optical lattice, but it will also work for larger sample sizes, other atomic elements, or other lattice geometries. The method features a high detection fidelity ($> 99.5\%$) even for a low number of scattered photons per atom (≈ 150) in the presence of detection noise and small lens aberration.

The low number of scattered photons might open the path for single site detection without additional cooling. Moreover it might allow for imaging multiple occupancy of a single lattice site.

8 Concluding remarks and outlook

In my thesis, I have set up an experimental apparatus with ultracold ^{6}Li atoms in a small team including Thomas Paintner and me. I have described in detail the technical implementations and experimental sequences required to prepare and work with an ultracold gas. Subsequently, I have described two experimental studies and one theoretical proposal.

In the first experimental study, reactive collisions between ultracold Feshbach dimers have been investigated. The main focus in the study lies on the dynamics of the dissociation process. Especially its dependence on the interaction strength and on the collision energy has been studied.

In the second experimental work, the properties of a superfluid Fermi gas in the close vicinity of a magnetic Feshbach resonance has been targeted. We used a local perturbation to excite entropy wave packets in order to determine the speed of second sound in the gas. We measured the speed of second sound across the BEC-BCS crossover and verified a theoretical prediction based on hydrodynamic theory and compared our results to numerical c-field calculations. Additionally, we investigated the coupling of first and second sound modes to the pertubation.

In the theoretical proposal, a holographic detection approach for ultracold atoms in optical lattices has been introduced. The scheme is based on off-axis holography and requires only a small number of photons from the detected atoms to determine the lattice occupancy.

Extension of previous work

In the next few paragraphs I will present a few prospects for future work.

Second sound in two dimensions

One way to extend our work on second sound could be to switch to a lower dimensional quantum gas. Especially, the study on a quasi two-dimensional gas is of interest, since second sound has never been detected in liquid Helium in the two-dimensional case [115]. In previous experiments on Helium films on a substrate second sound has not been observed. This is due to the fact that the movement of the normal phase was prevented in the experimental configuration [54, 55, 115]. Recently, for the first time a measurement of second-sound in a two-dimensional system has been reported in an experiment with an ultracold Bose gas [56]. However, the experiment was limited to weak interactions. Using our setup the mea-

surements can be extended to an interacting Bose gas and can be performed for a quasi two-dimensional Fermi gas, which has not been reported yet [191].

Second sound in lower dimensions, especially for tunable interactions, offer rich physics as predicted theoretically [55, 115]. For an ultracold gas in two dimensions the behavior of second sound changes drastically when the particle interaction is tuned [55]. For weak interaction, second sound is a density wave, while for strong coupling second sound is an entropy wave as in the 3D case. In this context, it would be interesting to study second sound in the crossover between three and two dimensions.

Additionally, second sound experiments in a quasi two-dimensional gas could be used as an alternative way to prove a Berezinskii-Kosterlitz-Thouless (BKT) transition, which has recently been reported for an ultracold gas of ^{6}Li atoms [192, 193]. This detection of the BKT transition has been debated in ref. [194], such that an independent measurement using second sound can be beneficial.

Alternative excitation protocols

In addition to the work on a lower-dimensional configuration, alternative excitation protocols might be investigated in three-dimensional gases. Due to the underlying wave nature of the second sound, the interference between multiple separately excited entropy waves could be studied. This could include measurements with barriers in the propagation direction in order to investigate the diffraction of entropy waves.

Molecule dissociation dynamics in lower dimensions

In another extension of ongoing work molecule-dissociation dynamics in lower dimensional systems might be investigated. As described in appendix A1, the trapping geometry highly influences the character of pairs inside the trap. For weakly-bound pairs and high transversal trapping frequencies (2D confinement), the confinement dominates the degrees of freedom of the individual atoms of a dimer such that pairs are two-dimensional objects (see e.g. [141, 192, 195, 196]). In this configuration the paths for two approaching pairs are geometrically limited. Therefore, the scheme described in sec. 5 might enable studies on stereochemistry with a focus on the reaction kinetics on a state-to-state level.

Furthermore, an additional confinement can be used to go to an one-dimensional system. There, the collision paths are even more restricted such that reactive collisions for very specific trajectories can be investigated (see also [38]).

Combination of sound excitation and molecule dissociation measurements

Finally, a combination of a molecule-dissociation measurement and second-sound excitation can be used in future studies. After an initial second-sound excitation the molecule fraction of the system could be determined for various sound propagation times. The transported thermal energy changes the thermodynamical state of the gas locally, which should trigger local dissociation processes.

In combination with an additional molecule detection we could investigate the dissociation process as a function of the interaction strength. If we tune to a weak particle interaction we can adjust the dissociation to be slow compared to the second sound speed close to the trap center. As long as the entropy wave packet propagates faster than the time scale of the dissociation process, there will be a delay in the state change of the system. Reaching the Thomas-Fermi radius the second sound speed reduces, such that the dissociation process can follow. Although the second sound signal vanishes approaching the Thomas-Fermi radius, changes in the molecule number should be visible in the molecule detection.

A Appendix

A.1 Two-dimensional systems

In almost all physical systems dimensionality has a significant impact on the behavior of the system. In recent years tremendous effort has been made to extend the studies on ultracold Fermi gases from three- to two-dimensional systems [141, 182, 197]. So far, in this work I have focused on three-dimensional gases. However, the experimental setup established in this thesis (see sec. 3) is constructed to enable studies on two-dimensional Fermi gases. Therefore, I will introduce a few peculiarities of such a gas. The focus lies on fundamental aspects of particle statistics as well as the particle interaction. The description starts with a non-interacting Fermi gas in a highly anisotropic confinement and will be extended to the case of strong interactions.

A.1.1 Condition for two-dimensional Fermi gases

In this subsection I will summarize conditions for two-dimensional/quasi two-dimensional ultracold Fermi gases. To do so, I consider a confined non-interacting two-component Fermi gas at temperatures where quantum statistics has to be taken into account (for fermions: $T \ll T_F$). For a highly anisotropic harmonic confinement (see Fig. A.1) with $\omega_x, \omega_y \ll \omega_z$ the motion of the trapped particles is limited to the x-y-plane as long as

$$\hbar\omega_z \gg E_F, k_B T \tag{A.1}$$

is fulfilled. A gas obeying eq. (A.1) is called two-dimensional (please note that I follow the description of ref. [141] in this passage).
To illustrate and explain the two conditions in eq. (A.1) the probability distribution of a single component Fermi gas in a harmonic trap is sketched in fig. A.2 a).
The first condition in eq. (A.1) reflects that the energy of the last occupied state[1] has to be much smaller than the trap state separation $\hbar\omega_z$. According to Fermi-Dirac statistics even at temperatures close to zero the trap can be filled to energies with $n_z > 0$. If higher transversal states are occupied at non-zero temperature, kinematics are no longer limited to in-plane movement and the gas cannot be considered

---

[1]Here, the occupied state with the largest energy at $T = 0$.
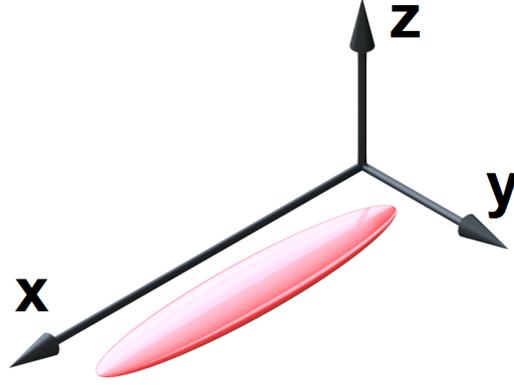
Figure A.1: Sketch of a gas in a highly anisotropic trap. The strong confinement
            freezes out the motion in z-direction.

2D anymore. The second condition demands that the probability distribution for
a transversal excitation vanishes. For instance, a gas with a temperature that is
comparable with $\hbar \omega_z / k_B$ the probability for the occupation of states with $n_z > 0$ is
non-negligible even for weak particle interaction due to the large tail of the energy
distribution function. Therefore, in this case the occupied motional states are not
restricted to the transversal ground state solely.

For an ensemble fulfilling upper criteria, we can calculate the critical particle num-
ber N_{crit} which is the maximum number of particles in the ground state $n_z = 0$. To
do so, we count all in-plane states of the harmonic confinement for $n_z = 0$, which
yields

$$N_{crit} = \frac{\omega_z^2}{2\omega_x \omega_y}. \tag{A.2}$$

Besides the strict definition of eq. (A.1), a gas occupying $n_z > 0$ at temperatures
of $T \ll \frac{\hbar}{k_B} \omega_z$ can essentially be considered as a two-dimensional gas as well. This
is due to the fact that for a gas fulfilling the second condition of eq. (A.1) the
probability for a collisional excitation to a higher transversal state is small (see fig.
A.2 b)). Therefore such a system is called quasi 2D Fermi gas [141].

In the group of Chris Vale measurements were performed that showed the transi-
tion of a Fermi gas from the transversal ground state to higher states [141]. To
determine the critical particle number experimentally, time-of-flight (TOF) experi-
ments on a Fermi gas loaded into a 2D trap have been carried out at temperatures
of $T \ll T_F$. It was found that tuning the particle number inside the trap, the cloud
size σ_z showed a plateau for $N < N_{crit}$ at fixed time of flight. For larger particle
numbers σ_z increased almost linearly (see fig. A.3). This can be understood as
follows. For $N < N_{crit}$ all atoms are in the motional ground state $n_z = 0$ with the
ground state wave function. Releasing the gas from the trap, particles with the
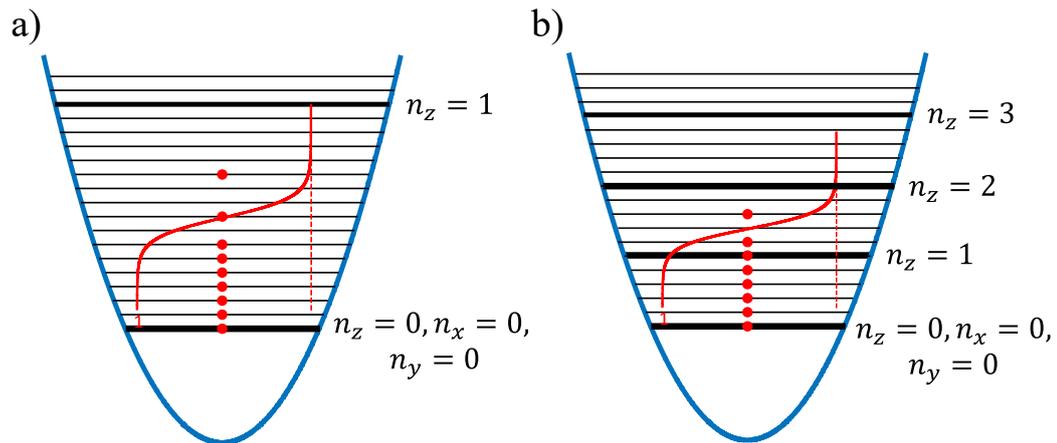
Figure A.2: Sketch of the trap-state occupancy of a Fermi gas in a highly anisotropic trap. The ladder shows the trap-state energies (n_x, n_y, and n_z denote the corresponding quantum numbers). The red dots indicate the occupied states and the red lines shows a Fermi-Dirac distribution of a Fermi gas with $T \neq 0$, respectively. a) 2D Fermi gas. The temperature and particle number of the gas are low enough, such that states with $n_z = 0$ are occupied, exclusively (kinematically 2D). b) Quasi 2D gas. The particle number is larger than N_{crit} such that higher transversal states are occupied. Since $n_z = 1$ is the only partly occupied state, the gas can be treated as a 2D system in the presence of a filled Fermi sea.

same wave function propagate the same way such that the transversal cloud size $\sigma_z(N < N_{crit}, t_{TOF})$ is constant. Or vice versa, for $N > N_{crit}$ higher transversal trap states with larger potential energy are occupied and the cloud size after TOF (reflecting the momentum distribution of the gas) is larger with respect to a gas in the ground state.

A.1.2 2D Fermi gas, statistics, and density distribution

In this subsection I summarize a few basic aspects of a 2D Fermi gas inside a harmonic trap. The density-of-states (DOS) of a two-dimensional quantum gas inside a harmonic potential is given by $g(\varepsilon) = \varepsilon/(\omega_x \omega_y \hbar^2)$, where ε is the energy. Integrating over the product of the DOS and the Fermi-Dirac distribution (at $T = 0$) with given particle number per spin state $N_\uparrow$, we get the Fermi energy

$$E_{F,2D} = \hbar\sqrt{\omega_x \omega_y}\sqrt{2N_\uparrow}. \tag{A.3}$$

Another important quantity is the absolute temperature of the gas. One way to determine it, is to measure the density distribution at the cloud wings after TOF or in situ. For a not fully superfluid gas, we consider the wing of the cloud to follow the Boltzmann distribution [192].

$$\tilde{n}(x) \propto \exp\left(-\frac{M\omega_x^2 x^2}{2k_B T}\right) \tag{A.4}$$

Here $\tilde{n}$ is a doubly integrated density profile, M is the mass of the particles, ω_x is the trapping frequency in x-direction, and T is the absolute temperature.

For in situ measurements we can fit the corresponding function to the thermal tail or use the full density distribution of a doubly integrated density profile

$$n_{1D}(x) = n_{1D,0}\frac{\mathrm{Li}_{5/2}\left(-\exp\left(\mu\beta - \frac{x^2}{R_x^2}f\left(e^{\beta\mu}\right)\right)\right)}{\mathrm{Li}_{5/2}\left(-e^{\beta\mu}\right)}, \tag{A.5}$$

to determine T (see [86]). Here, $n_{1D,0}$ is the peak density, $\beta = 1/(k_B T)$, $R_x = \sqrt{\frac{2E_F}{m\omega_x^2}}$ is the Thomas-Fermi radius, $\mathrm{Li}_{5/2}$ is the polylogarithm of order 5/2, and the function f is given by $f(x) = \frac{1+x}{x}\ln(1+x)$.
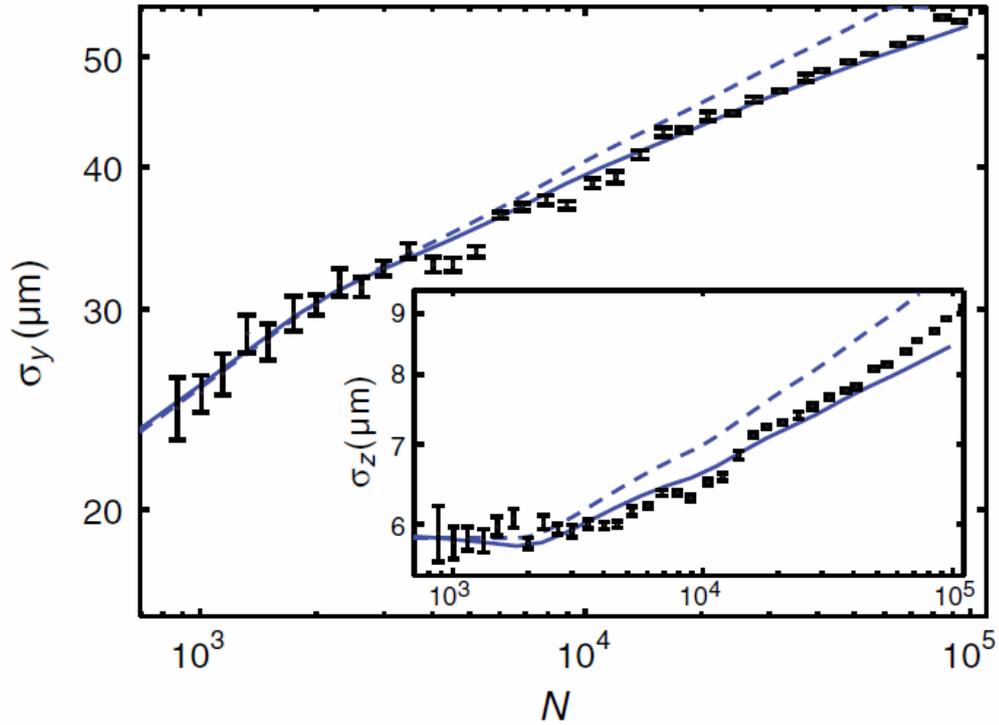
Figure A.3: Transition from three to two dimensions taken from ref. [141]. A de-
generate Fermi gas of ^{6}Li is loaded into a 2D trap at 992 G. After a
TOF of $t = 500\mu s$ the transversal and in-plane cloud widths σ_z and σ_y,
respectively, are measured as a function of the particle number N. The
solid and dashed lines show theoretical predictions for a weakly inter-
acting and an ideal Fermi gas, respectively. Inset: For $N < N_{crit}$ all
particles are in the transversal ground state and the expansion is inde-
pendent of the particle number. For $N > N_{crit}$ higher transversal states
are occupied and the cloud width depends on the particle number.

A.1.3 Interacting Fermi gas in 2D

In the previous section we have discussed 2D Fermi gases where no or only weak particle interaction was considered. In the following, I will give a brief introduction to the main aspects of elastic scattering in a 2D quantum gas and its influence on the thermodynamical state of the system.

A.1.4 Scattering theory in 2D

Analog to scattering theory in 3D the discussion in 2D starts with the wave function of colliding atoms [195],

$$\psi(\mathbf{r}) \approx e^{i\mathbf{r}\mathbf{q}} - f(q,\Phi)\sqrt{\frac{i}{8\pi qr}}e^{iqr}, \tag{A.6}$$

with the scattering amplitude f (characterizing the interaction strength), the relative momentum q, the inter-particle distance r (here: $r \to \infty$) and the scattering angle Φ. In the case of $qR_e \ll 1$ (R_e is the characteristic interaction radius) the scattering amplitude is dominated by the s-wave contribution [195]. Inserting the wave function in the Schrödinger equation gives the s-wave scattering amplitude for $rq \ll 1$

$$f(q) = \frac{2\pi}{\ln(1/qd_*) + i\pi/2}, \tag{A.7}$$

with $d_* = (d/2)C$, where C is the Euler constant. Here, $d > 0$ is computed from the time-independent Schrödinger equation for $q = 0$ and is depending on the details of the interaction potential [195].

However, the discussion so far is only valid for an ideal 2D system. This means that no spatial extension of the gas in the transversal direction is considered so far. A real gas has a finite size in the transversal direction which is included in the following. To do so, we follow the description in [195] to get the scattering amplitude in the s-wave regime

$$f(q) = \frac{4\pi}{\sqrt{2\pi}l_z/a_{3D} - \ln(\pi q^2 l_z^2/A) + i\pi}, \tag{A.8}$$

with $A = 0.905$, and $l_z = \sqrt{\hbar/(m\omega_z)}$ being the harmonic oscillator length of the strong confinement, and $a_{3D} = a$ representing the scattering length in 3D. In equation (A.8), the definition of the 2D scattering length
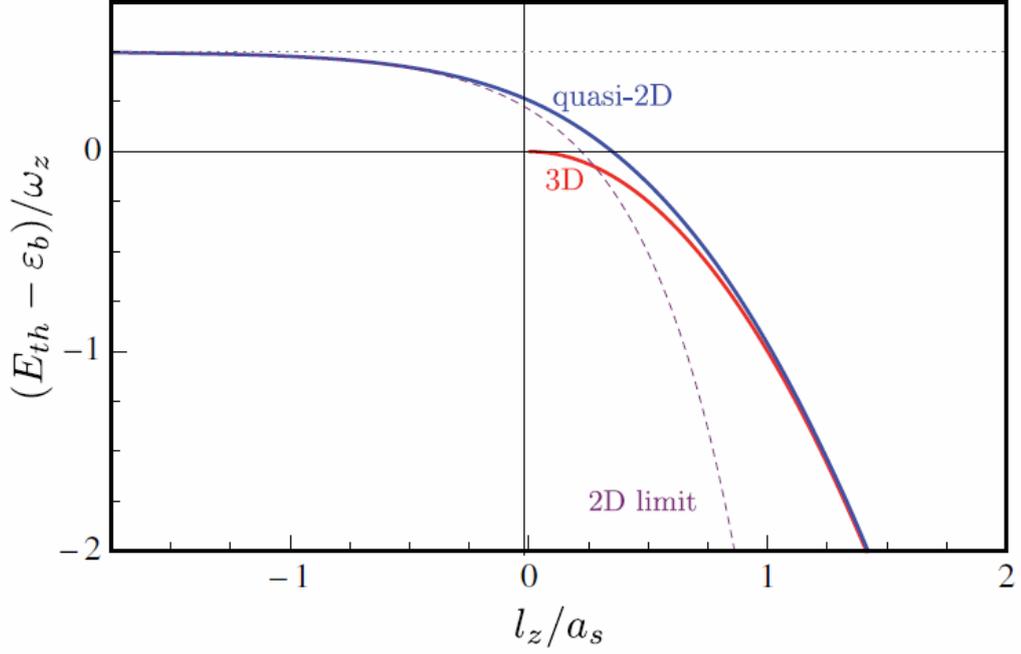
Figure A.4: Binding energy of dimers in a 2D potential (finite size) as a function of l_z/a_{3D} ($a_{3D} = a_s$) taken from ref. [196]. Here, E_{th} is the thermal energy, and ε_b is the binding energy. In the 2D scattering case the continuum is shifted by $\hbar\omega_z/2$ (here: $\hbar$ is set to 1). In the limiting cases $|l_z/a_{3D}| \gg 1$ the binding energy can be obtained from eq. (A.11) and eq. (2.31), respectively.

$$a_{2D} = l_z\sqrt{\frac{\pi}{A}}\exp\left(-\sqrt{\frac{\pi}{2}}\frac{l_z}{a_{3D}}\right) \tag{A.9}$$

has been used. Contrary to the 3D case, we find a two-body bound state for all interaction strengths (see e.g. supplementary to [192]) in the 2D system. The strong confinement induces bound states even for negative 3D scattering lengths. The binding energy of the pairs E_B can be obtained from the following transcendental equation [196] (see fig. A.4):

$$\frac{l_z}{a_{3D}} = \int_0^\infty \frac{\mathrm{d}u}{\sqrt{4\pi u^3}}\left(1 - \frac{e^{-E_B u/(\hbar\omega_z)}}{\sqrt{(1 - e^{-2u}/2u)}}\right). \tag{A.10}$$

The quantity l_z/a_{3D} plays a crucial role in the analysis of the two-body character of these pairs. Using eq. (A.10) we can define three regimes:

2D limit - 2D dimers

For $l_z/a_{3D} \ll -1$ the binding energy of the confinement induced dimers is small and the dimer size is large compared to the harmonic oscillator length in the strongly confined direction. Therefore, the degrees of freedom of the pairs are limited. The dimers can be treated as two-dimensional objects with binding energy

$$E_B = \frac{\hbar^2}{ma_{2D}^2} \approx \hbar\omega_z \frac{A}{\pi}\exp\left(\sqrt{2\pi}l_z/a_{3D}\right). \qquad (A.11)$$

Intermediate regime

For $l_z/a_{3D} \sim 0$ (close to the position of the three-dimensional FB resonance) the dimer state is highly influenced by the confinement. The binding energy can be extracted from eq. (A.10) and takes the universal value $E_B = 0.244\hbar\omega_z$ [196].

3D dimers in 2D confinement

For $l_z/a_{3D} \gg 1$ the dimer binding energy matches the 3D dimer binding energy given in equation (2.31). In this regime the binding energy is large and the dimer size small compared to l_z. Therefore, the dimer state is only weakly influenced by the confinement. The internal structure of the dimer can be considered to be 3D. For deeply bound molecules and low enough temperature, the gas can be considered as a weakly interacting Bose gas occupying the lowest transversal state (see supplementary to [192]) as in any other two-dimensional Bose gas.

A.1.5 Two dimensional kinematics in the presence of interaction

Adding interaction to a kinematically 2D degenerate quantum gas has another crucial consequence. For strong particle interaction transversal excitations can occur and shift the system out of the regime of 2D kinematics. Measurements performed in the group of Chris Vale [143] reveal the dependency of the critical particle number on the interaction strength. The results show that the interaction energy can be converted to the excitation of motional/external states such that N_{crit} is reduced with increasing interaction strength. In other words, the larger the scattering length a_{3D} the smaller the critical particle number.
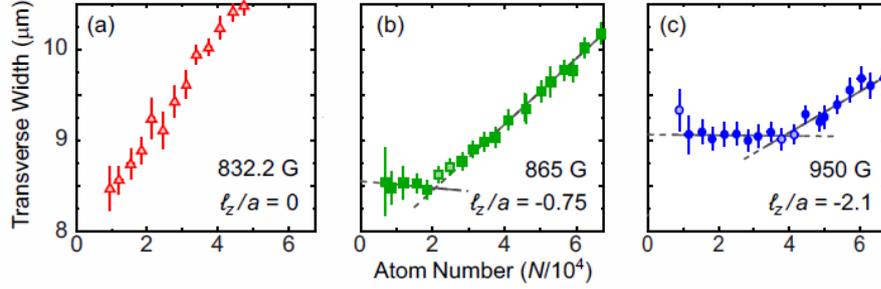
Figure A.5: Crossover of a trapped Fermi gas from the kinematically 2D to the 3D regime in the presence of particle interaction obtained using TOF experiments (Pictures taken from ref. [143]). The interaction strength increases from c) to a). With increasing interaction strength the critical particle number decreases. N_{crit} is obtained from the kink in the cloud width.

In the measurement shown in fig. A.5 N_{crit} is determined using the technique introduced in sec. A.1.1. The results of [143] can be used to impose a second condition for a gas to be motional 2D:

$$E_B \ll E_F. \tag{A.12}$$

A.1.6 Achievements on two-dimensional gases and future steps

In the course of this thesis the basic steps towards experiments with two-dimensional gases have been made. In future experiments the recent technical achievements might be combined with experimental sequences on second sound excitation to provide extended studies on the thermodynamical properties of lower dimensional Fermi gases. A first step towards such studies is the production of a superfluid gas in lower dimensions.

Fortunately, in recent years tremendous progress in the production and in the understanding of such two-dimensional Fermi gases has been made. Among others, this includes studies on superfluidity in two-component Fermi gases [192, 193], as well as the equation-of-state [198, 199] of such systems. Especially, the production of pair condensates in two dimensions [193] and the observation of the Berezinsky-Kosterlitz-Thouless (BKT) transition [192] are the basis for future studies on second sound in two-dimensional Fermi gases. The natural next step in our experiment would be to prepare a superfluid gas in lower dimensions. To prove the phase transition it is planned to use the matter wave focusing technique introduced in [192, 200], which allows for measuring the momentum distribution of the gas. A phase
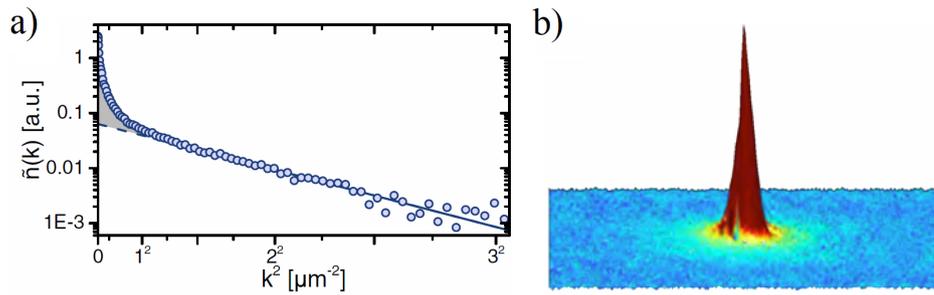
Figure A.6: Momentum distribution of a superfluid two-dimensional interacting
            Fermi gas taken from ref. [192]. a) The momentum distribution is
            obtained using the matter wave focusing technique [200] for $l_z/a_{3D} =$
            1.55. The data points are obtained by averaging over 30 measurements.
            b) False colour image of the momentum distribution extracted from the
            TOF measurements of the gas. The image shows the data displayed in
            a).

transition manifests in a steep increase in the momentum distribution (see fig. A.6
a)).
An obvious further step would be to produce a superfluid gas and perform second
sound experiments. This can be the starting point for an extended study of second
sound in the BEC-BCS crossover in a lower dimensional system. With this our
recent work on second sound might be extended to two dimensions which has been
shown recently for a bosonic gas [56].

A.2 Pair fraction in a finite-temperature Fermi gas on the BEC side of the BCS-BEC crossover

The content of this chapter has been published in Physical Review A. The material is taken from:

Pair fraction in a finite-temperature Fermi gas on the BEC side of the BCS-BEC crossover

Thomas Paintner,[1] Daniel K. Hoffmann,[1] Manuel Jäger,[1] Wolfgang Limmer,[1] Wladimir Schoch,[1] Benjamin Deissler,[1]
Michele Pini,[2] Pierbiagio Pieri,[2,3] Giancarlo Calvanese Strinati,[2,3,4] Cheng Chin,[5] and Johannes Hecker Denschlag[1,*]

[1]*Institut für Quantenmaterie and Center for Integrated Quantum Science and Technology (IQST), Universität Ulm, D-89069 Ulm, Germany*
[2]*School of Science and Technology, Physics Division, Università di Camerino, I-62032 Camerino (MC), Italy*
[3]*INFN, Sezione di Perugia, I-06123 Perugia (PG), Italy*
[4]*CNR-INO, Istituto Nazionale di Ottica, Sede di Firenze, I-50125 Firenze (FI), Italy*
[5]*James Franck Institute, Enrico Fermi Institute, and Department of Physics, The University of Chicago, Chicago, Illinois, USA*

We investigate pairing in a strongly interacting two-component Fermi gas with positive scattering length. In this regime, pairing occurs at temperatures above the superfluid critical temperature; unbound fermions and pairs coexist in thermal equilibrium. Measuring the total number of these fermion pairs in the gas we systematically investigate the phases in the sectors of pseudogap and preformed pair. Our measurements quantitatively test predictions from two theoretical models. Interestingly, we find that already a model based on classical atom-molecule equilibrium describes our data quite well.

I. INTRODUCTION

A unique feature of fermionic superfluids is the pairing. For a weakly interacting Bardeen-Cooper-Schrieffer (BCS) superfluid pairing occurs directly at the critical temperature for superfluidity T_c [1]. This pairing is accompanied with the emergence of an excitation gap Δ_{sc} which is identified with the superfluid order parameter and Δ_{sc}^2 is proportional to the density of condensed pairs [2]. For fermions with strong coupling, an excitation gap already emerges at a temperature above T_c. This is referred to as the pseudogap regime [3]. The existence of the pseudogap has been observed early on, e.g., in underdoped high-T_c superconductors [4,5]. While its nature has been intensely studied, it is still not fully understood. Understanding the pseudogap is expected to be the key for revealing the mechanism behind high-T_c superconductivity [6,7]. One interpretation of the pseudogap is based on the presence of noncondensed pairs with nonvanishing momentum [8].

Ultracold Fermi gases are an excellent system for investigating the gap and pseudogap physics from the BCS to Bose-Einstein condensate (BEC) regimes [9]. Using radio-frequency (RF) spectroscopy in various forms, e.g., [10–13], the excitation gap has been studied in the way similar to angle-resolved photoemission spectroscopy (ARPES) of solid-state systems [14]. Evidence for pairing above T_c was found in the RF experiments, as well as in other physical quantities, such as viscosity [15], heat capacity [16], and Tan's contact [17,18].

In this article, we investigate pairing of fermions for various temperatures and interaction strengths on the BEC side of the BEC-BCS crossover. For this, we measure the total number of bound fermion pairs N_p in our sample for $T > T_c$. Such counting of fermion pairs is in general not

possible for solid-state systems and therefore complements existing methods. We determine the fermion pair number by converting all atom pairs to tightly bound diatomic molecules, either by photoexcitation [19] or by a fast magnetic-field ramp [20,21] and measuring the decrease in atom number of the cloud. When we compare the measured and calculated pair numbers we find quite good agreement with two models: an *ab initio* t-matrix approach and a classical statistical model of atom-molecule equilibrium [22]. We provide an explanation why the classical model achieves good results, despite the fact that strong interactions and quantum statistics play an important role in our system.

In the following, we consider an ultracold, spin-balanced, strongly interacting two-component Fermi gas in a harmonic trap. Collisions lead to pairing of atoms with opposite spins, $|\uparrow\rangle$, $|\downarrow\rangle$. For a given temperature and interaction strength well-defined fractions of pairs and atoms are established at thermal equilibrium, as long as collisional losses are negligible. Figure 1 shows the phase diagram of such a system in the vicinity of a Feshbach resonance at $(k_F a)^{-1} = 0$. Here, a is the s-wave scattering length, $k_F = \sqrt{2mE_F}/\hbar$ denotes the norm of the Fermi wave vector, m is the atomic mass, and $E_F = k_B T_F$ is the Fermi energy in the trap center with k_B the Boltzmann constant. The dash-dotted and solid lines are contours of constant molecular fractions N_p/N_σ for two different approaches. Here, $N_\sigma = N_p + N_a$ is the number of all atoms per spin state regardless of whether they are bound in pairs (N_p) or free (N_a). The dotted lines are calculations based on a self-consistent t-matrix approach [23], while the solid lines correspond to a statistical mechanics approach treating the particles as a canonical ensemble of noninteracting molecules and atoms in chemical equilibrium (see [22] and Appendix A). Here, the molecules have a binding energy of $E_b = -\hbar^2/(ma^2)$. Also shown is a calculation (cyan dash-dotted line) by Perali *et al.* [24] of the BCS mean-field critical temperature which provides an approximate estimate of the pair breaking temperature. It partially coincides
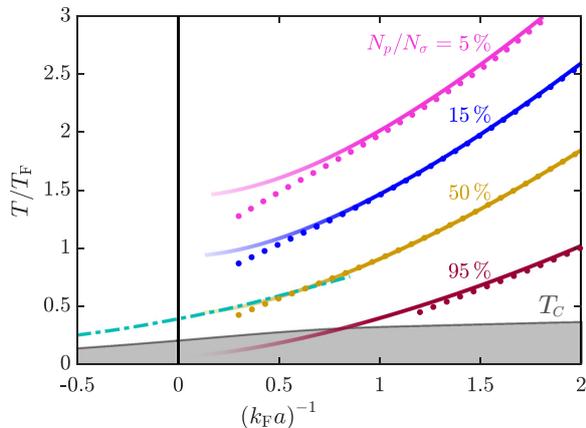
FIG. 1. Theoretical phase diagram for a balanced two-component harmonically trapped ultracold Fermi gas in the vicinity of a Feshbach resonance (vertical line) where k_F and T_F are determined in the trap center. Shown are calculated contours for various pair fractions. Dotted lines are based on a self-consistent t-matrix approach [23], while solid lines are based on a classical model of noninteracting atoms and molecules (see text) [22]. Close to the Feshbach resonance the solid lines are blurred because the classical model is expected to lose its validity. The cyan dash-dotted line marks a pair breaking temperature, as calculated by [24] with a BCS mean-field model that was extended to the near-BEC regime. The gray shaded area marks the superfluid phase below the critical temperature T_c which was calculated within the self-consistent t-matrix approach [25].

with the 50 % pair fraction line of the statistical mechanics approach.

We carry out our experiments with a spin-balanced two-component Fermi gas of ^{6}Li atoms which is initially prepared at a magnetic field of 780 G. The atoms have magnetic quantum numbers $m_F = +1/2$ ($|\uparrow\rangle$) and $m_F = -1/2$ ($|\downarrow\rangle$) and correlate to the $F = 1/2$ hyperfine level of the ground state at 0 G. They are confined in a harmonic three-dimensional cigar-shaped trapping potential which is generated in radial direction mainly by a focused 1070-nm dipole trap laser beam and along the axial direction mainly by a magnetic field gradient. The temperature T is set via evaporative cooling and is measured by fitting a distribution obtained from the second-order quantum virial expansion to the outer wings of the density profile [26]. The particle number N_σ per spin state ranges from 3×10^4 for the lowest temperature of about $0.3 T_F$ to 3×10^5 for the highest temperature of about $3 T_F$. The population balance of the two spin states is assured by means of a 100-ms-long resonant RF pulse that mixes the two Zeeman states $|\uparrow\rangle$ and $|\downarrow\rangle$. For a spin-balanced system the Fermi energy is given by $E_F = \hbar(6N_\sigma \omega_r^2 \omega_a)^{1/3}$, where ω_r and ω_a denote the radial and axial trapping frequency, respectively. In our experiment ω_r ranges from about $2\pi \times 300$ Hz to $2\pi \times 1.6$ kHz while $\omega_a = 2\pi \times 21$ Hz is almost constant as it is dominated by the magnetic confinement. The interaction parameter $(k_F a)^{-1}$ can be tuned by changing either the scattering length a via the broad magnetic Feshbach resonance located at 832 G [27,28], or by adjusting the Fermi energy E_F.

II. MEASURING THE PAIR FRACTION

In order to determine the pair fraction N_p/N_σ we measure the particle numbers N_p and N_σ separately. N_σ is obtained by means of spin-selective absorption imaging of the $|\uparrow\rangle$ component using a σ^--polarized 671-nm laser beam resonant with the D_2 transition of ^{6}Li [29]. This transition is essentially closed due to a decoupling of the nuclear spin and the total electronic angular momentum in the Paschen-Back regime of the hyperfine structure [30]. All $|\uparrow\rangle$ atoms will be counted regardless of whether they are free or bound in the weakly bound pairs. Since the binding energy E_b of these pairs is always less than $h \times 1$ MHz in our experiments, the imaging laser is resonant with both free atoms and bound pairs. In order to determine the number of bound pairs N_p, we transfer all pairs to states that are invisible in our detection scheme and measure again the remaining $|\uparrow\rangle$ state atom number via absorption imaging. We use two different bound-state transfer methods which produce consistent results. They are briefly described in the following.

A. Optical transfer (OT) method

This transfer method is based on resonant excitation of fermion pairs to a more strongly bound molecular state ($A^1\Sigma_u^+$, $v' = 68$) with a laser ($\lambda = 673$ nm) which is detuned by 2 nm from the atomic transition; see also [19]. Subsequently, the excited molecules quickly decay to undetected atomic or molecular states; see Fig. 2(a). This optical excitation of the fermion pairs occurs via an admixture of the molecular bound state $X^1\Sigma_g^+$, $v = 38$ to the fermion pair wave function [19].

If, for now, we ignore other loss processes, the number of fermion pairs decays exponentially as a function of the laser pulse length Δt such that the measured total number $N_\sigma(\Delta t)$ of $m_F = +1/2$ atoms as a function of time is given by

$$N_\sigma(\Delta t) = N_\sigma(0) - N_p(1 - e^{-k_1 \Delta t}), \tag{1}$$

where $1/k_1$ is the time constant for the optical excitation. Figure 2(b) shows this decay for five different initial temperatures T/T_F at a magnetic field of 726 G. By fitting Eq. (1) to the measured data (see fit curves) we are able to extract the pair number N_p. Besides the photoexcitation of pairs a loss in N_σ could in principle also be induced by photoassociation of two free atoms. However, we made sure that within our field range its rate is negligible. The photoassociation rate constants range between 1×10^{-9} and 3×10^{-9} cm^5(W s)$^{-1}$ for magnetic fields between 726 and 820 G. We work with low particle densities of at most 10^{11} cm^{-3} and a maximum laser intensity of about 1.9 W/cm^2.

For the data shown in Fig. 2(b) the laser intensity is 0.22 W/cm^2 and the peak density for the lowest temperature of $T/T_F = 0.64$ is 1.4×10^{11} cm^{-3} which corresponds to an initial photoassociation time constant of about 33 ms. This is much longer than the loss dynamics observed in Fig. 2(b). Indeed, the fact that the curves in Fig. 2(b) approach constant values for pulse times $t \gtrsim 0.3$ ms already suggests that the photoassociation of free atoms is negligible.

However, closer to resonance the time constants for photoassociation and pair excitation become more comparable.
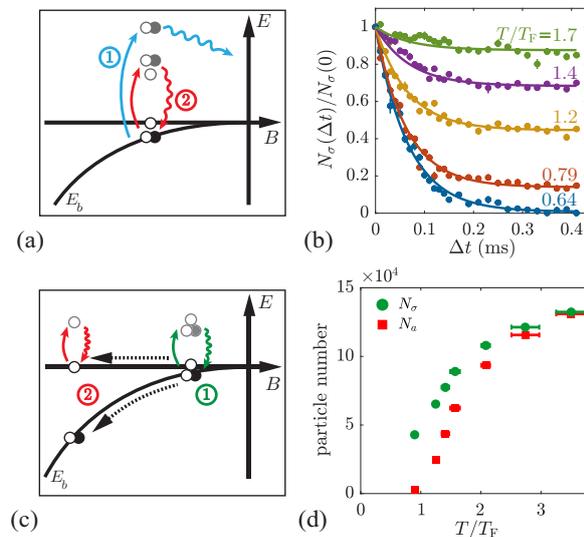
FIG. 2. Measurement of the number of fermion pairs. (a) and (b) Optical transfer method. A resonant laser pulse transfers pairs to states which are invisible to our detection scheme [blue arrows (1)]. The total number $N_\sigma(\Delta t)$ of remaining fermion pairs and single atoms is measured by absorption imaging [red arrows (2)]. (b) $N_\sigma(\Delta t)/N_\sigma(0)$ as a function of the pulse width Δt at a magnetic field of 726 G for various temperatures $T/T_F = \{0.64, 0.79, 1.2, 1.4, 1.7\}$. The solid lines are fit curves using Eq. (1). (c) and (d) Magnetic transfer method. Using absorption imaging, the particle number $N_\sigma = N_a + N_p$ is measured at the magnetic field (1) and the number of unbound atoms N_a is measured after a fast ramp to (2). (d) The measured particle numbers at (1) ($B = 726$ G, green solid circles) and at (2) ($B = 550$ G, red solid squares) for various temperatures T/T_F.

Therefore, we generally release the particles from the trap 0.3 ms before applying the laser pulse. The subsequent expansion lowers the cloud density by about a factor of 4 and assures additionally that photoassociation is negligible. Furthermore, lowering the density also strongly suppresses regeneration of depleted Fermi pairs during the laser pulse, since pair regeneration mainly occurs via three-body recombination. We have checked that during the expansion the fermion pairs do not break up. For this, we carried out measurements at a magnetic field of 780 G, working at the lowest temperatures of about 0.3 T_F, where only about 10%−15% of the atoms are unbound and thus photoassociation does not play a significant role. We measured the same pair numbers with and without expansion.

In general the OT method works very well up to magnetic fields of about $B = 820$ G, close to the Feshbach resonance. There, we observe marked deviations from the exponential decay in Eq. (1), a behavior that also had been reported earlier by the Rice group [19]. An analysis of these signals would require a better understanding of the nature of strongly interacting pairs. For this reason, we decide to stay below magnetic fields of 820 G for the present investigations where the analysis is unequivocal.
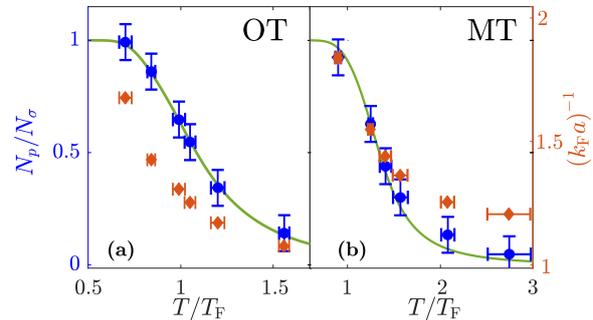
FIG. 3. Measured pair fractions N_p/N_σ (blue circles) at 726 G for various temperatures T/T_F. (a) Optical transfer (OT) method; (b) magnetic transfer (MT) method (see Fig. 2). We note that due to evaporative cooling $(k_F a)^{-1}$ also changes with T/T_F (orange diamonds). The green curves are calculations based on the classical model.

B. Magnetic transfer (MT) method

Here, we increase the binding energy of the pairs to $h \times$ 80.6 MHz by quickly ramping the magnetic field at 20 G/ms down to 550 G; see Fig. 2(c). This works very efficiently without breaking up the molecules as previously shown in [20,21]. At 550 G the fermion pairs cannot be resonantly excited anymore by the imaging laser and become invisible to our detection scheme; see [31]. N_p is determined as the difference of the numbers for atoms and pairs (N_σ) measured before the ramp and unbound atoms (N_a) obtained after the ramp. Figure 2(d) shows these particle numbers for different temperatures at a magnetic field of 726 G.

We did not perform measurements with the MT method for magnetic fields higher than 750 G because of technical limitations for the ramping speed. If the field ramp duration ($\approx$10 ms for the case of 750 G) becomes comparable to the equilibration time for the atom-molecule mixture (a few milliseconds at 750 G) the measurement does not yield the correct molecule number anymore. This restriction of the magnetic field ramp implies that we cannot use the MT method in the strong interaction crossover regime, but only in the far BEC regime. There, however, the MT method is quite useful to check for consistency with the OT method. This consistency is shown in Fig. 3 where we plot the pair fractions N_p/N_σ obtained at 726 G from both methods as a function of the temperature (blue circles). Since the temperature was adjusted by varying the evaporative cooling, different temperatures correspond to different particle numbers N_σ and thus to different interaction parameters $(k_F a)^{-1}$ (orange diamonds). The green lines are calculated pair fractions using the classical model. In general, we find good agreement between the experimental data and the theoretical prediction, which also indicates consistency between the OT and MT methods.

III. RESULTS

We now apply the OT and MT methods to map out the fraction of pairs on the BEC side. For this, we perform measurements for a variety of magnetic fields and temperatures. The pair fractions N_p/N_σ obtained from both experimental
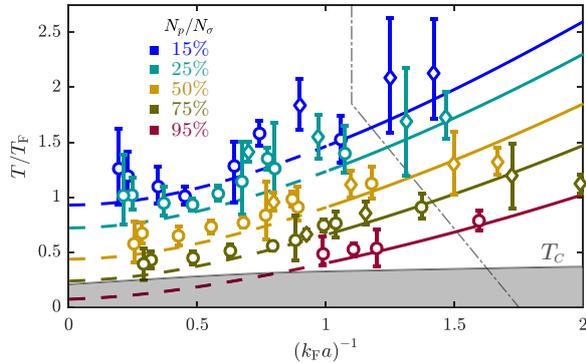
FIG. 4. Map of the pair fraction N_p/N_σ as a function of temperature and interaction strength on the BEC side of the Feshbach resonance. The circles (diamonds) are measurements obtained with the OT (MT) method. The thick solid and dashed lines are classical model calculations (cf. Fig. 1). They are dashed in the strong-interaction regime where the classical model is expected to be no longer valid. The error bars include both a statistical and a systematic part, i.e., the standard deviation of the mean of 10 temperature measurements and the uncertainty in determining the molecule fraction from the fit, respectively. The upper-right area bounded by the gray dash-dotted line exhibits $>5\%$ particle loss due to inelastic collisions on the time scale of a measurement. The gray shaded area indicates the superfluid phase below T_c, as in Fig. 1.

methods are shown in Fig. 4 (circles, OT method; diamonds, MT method). The area on the right-hand side of Fig. 4, as bounded by the thin dash-dotted line, marks a region where we observe non-negligible loss of particles ($>5\%$) during our measurements due to inelastic collisions of bound pairs. This loss increases with $(k_F a)^{-1}$; see, e.g., [32,33]. In order to simplify our discussion we only consider data points outside this area.

The solid and dashed lines in Fig. 4 represent the statistical mechanics model without any adjustable parameters. For higher temperatures we generally observe larger fluctuations and thus larger error bars, because of the larger atom cloud within a limited field of view. Overall, we find that the agreement between measurement and model remains quite good even in the crossover regime where this model of classical particles with no interaction energy should be expected to break down. In fact, the model could be expected to work to the extent that the internal degrees of freedom of the fermion pairs are frozen and only the degrees of freedom associated with the center of mass of the pair remain active. This approximately occurs when the fermionic chemical potential changes sign which, using a t-matrix approach, we estimate to occur at a coupling value of about $(k_F a)^{-1} = 0.5$ at T_c. This might explain the good agreement found between the model and the experimental data when $(k_F a)^{-1} \gtrsim 0.5$ as well as with the theoretical calculation based on a self-consistent t-matrix approach.

IV. CONCLUSION

To conclude, we have systematically mapped out the fermion pair fraction in a strongly interacting Fermi gas

as a function of both temperature and coupling strength. Our measurements show how pairing of ultracold fermions changes as we move from the BEC regime into the strong interaction regime. We demonstrate a novel method to measure the pair fractions from the near-BEC limit to the pseudogap regime, which is based on a number measurement of fermion pairs. This method is complementary to existing excitation-gap measurements and has no counterpart in conventional condensed matter systems. We find that a statistical mechanics model treating the fermions and pairs as classical particles describes the measured data quite well in the investigated range, as we have also confirmed through an advanced many-body calculation based on a t-matrix approach. In the future, we plan to extend our measurements and investigate more in detail the coupling region $[0.1 \lesssim (k_F a)^{-1} \lesssim 0.5]$ where the preformed-pair and the pseudogap regimes overlap with each other.

APPENDIX A: MODEL OF A CANONICAL ENSEMBLE OF NONINTERACTING ATOMS AND MOLECULES

In our simple statistical mechanics model we treat the cold gas of fermions and fermion pairs as a classical canonical ensemble of atoms and molecules, respectively, with negligible interaction energy among each other. In collisions a pair of $|\uparrow\rangle$ and $|\downarrow\rangle$ atoms can combine to form a molecule, and vice versa a molecule can break up into an unbound pair of $|\uparrow\rangle$, $|\downarrow\rangle$ atoms. At a given temperature the atom and molecule numbers are in chemical equilibrium. Following [22], the equilibrium condition is derived by minimizing the Helmholtz free energy $F = k_B T \ln Z$, subject to the constraint of particle number conservation. Here

$$ Z = \frac{Z_s^{2N_a} Z_s^{N_p} e^{N_p E_b/k_B T}}{N_a! N_a! N_p!} $$

is the partition function of the system and Z_s and $Z_s e^{-E_b/k_B T}$ are the single-particle partition functions for atoms and molecules, respectively. $\overline{\omega} = \sqrt[3]{\omega_r^2 \omega_a}$ is the geometric mean of the trapping frequencies ω_a, ω_r in axial and in radial direction, respectively. Using Stirling's formula to approximate the factorials a minimum in the free energy is found at a molecule (pair) number,

$$ N_p = \frac{1}{Z_s} N_a^2 \, e^{-E_b/k_B T}, $$

for a given temperature T and binding energy $E_b = -\hbar^2/(ma^2)$. Using the partition function $Z_s = (k_B T/\hbar \overline{\omega})^3$,
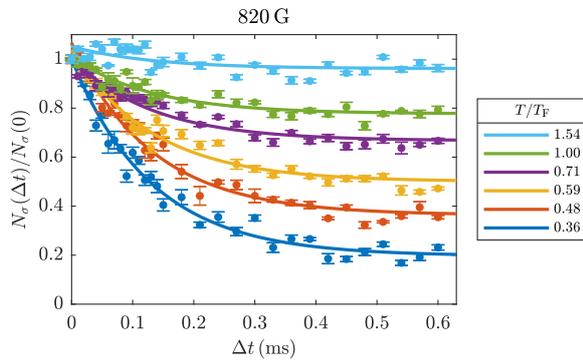
820 G

FIG. 5. Ratio $N_\sigma(\Delta t)/N_\sigma(0)$ after an optical transfer pulse of length Δt at a magnetic field of 820 G for various temperatures (see legend). The solid lines are fits of an exponential decay towards a constant offset.

the Fermi energy $E_F = k_B T_F = \hbar\overline{\omega}\sqrt[3]{6N_\sigma}$, and the total pair fraction per spin state $N_\sigma = N_a + N_p$ we obtain the following

implicit expression for the pair fraction N_p/N_σ in thermal equilibrium:

$$\frac{(1 - N_p/N_\sigma)^2}{N_p/N_\sigma} = 6\left(\frac{T}{T_F}\right)^3 \exp\left[\frac{E_b}{k_B T}\right].$$

APPENDIX B: MEASUREMENTS CLOSE TO UNITARITY

As pointed out in the main text we only carry out measurements at magnetic fields of up to 820 G because for higher magnetic fields we observe deviations from an exponential decay during the optical excitation of the pairs towards deeply bound molecules. Such deviations are indeed expected close to resonance as a result of many-body effects [34]. In addition, as the optical excitation cross section decreases towards the resonance its rate becomes increasingly comparable to the one of photoassociation. In order to clarify that an exponential fit towards a constant value is still a good description at 820 G, we show corresponding decay curves in Fig. 5. A slight nonexponential behavior of the measured decay will increase the uncertainty in the measured equilibrium pair fraction.

[1] J. Bardeen, L. N. Cooper, and J. R. Schrieffer, Phys. Rev. **108**, 1175 (1957).
[2] J. Bardeen, L. N. Cooper, and J. R. Schrieffer, Phys. Rev. **106**, 162 (1957).
[3] Q. Chen, J. Stajic, S. Tan, and K. Levin, Phys. Rep. **412**, 1 (2005).
[4] H. Ding, T. Yokoya, J. C. Campuzano, T. Takahashi, M. Randeria, M. R. Norman, T. Mochiku, K. Kadowaki, and J. Giapintzakis, Nature (London) **382**, 51 (1996).
[5] A. G. Loeser, Z.-X. Shen, D. S. Dessau, D. S. Marshall, C. H. Park, P. Fournier, and A. Kapitulnik, Science **273**, 325 (1996).
[6] J. Stajic, Science **357**, 561 (2017).
[7] E. J. Mueller, Rep. Prog. Phys. **80**, 104401 (2017).
[8] Q. Chen and K. Levin, Phys. Rev. Lett. **95**, 260406 (2005).
[9] J. Stajic, J. N. Milstein, Q. Chen, M. L. Chiofalo, M. J. Holland, and K. Levin, Phys. Rev. A **69**, 063610 (2004).
[10] C. Chin, M. Bartenstein, A. Altmeyer, S. Riedl, S. Jochim, J. Hecker Denschlag, and R. Grimm, Science **305**, 1128 (2004).
[11] A. Schirotzek, Y.-i. Shin, C. H. Schunck, and W. Ketterle, Phys. Rev. Lett. **101**, 140403 (2008).
[12] J. P. Gaebler, J. T. Stewart, T. E. Drake, D. S. Jin, A. Perali, P. Pieri, and G. C. Strinati, Nat. Phys. **6**, 569 (2010).
[13] Y. Sagi, T. E. Drake, R. Paudel, R. Chapurin, and D. S. Jin, Phys. Rev. Lett. **114**, 075301 (2015).
[14] M. Hashimoto, I. M. Vishik, R.-H. He, T. P. Devereaux, and Z.-X. Shen, Nat. Phys. **10**, 483 (2014).
[15] E. Elliott, J. A. Joseph, and J. E. Thomas, Phys. Rev. Lett. **113**, 020406 (2014).
[16] J. Kinast, A. Turlapov, J. E. Thomas, Q. Chen, J. Stajic, and K. Levin, Science **307**, 1296 (2005).
[17] F. Palestini, A. Perali, P. Pieri, and G. C. Strinati, Phys. Rev. A **82**, 021605(R) (2010).
[18] E. D. Kuhnle, S. Hoinka, P. Dyke, H. Hu, P. Hannaford, and C. J. Vale, Phys. Rev. Lett. **106**, 170402 (2011).

[19] G. B. Partridge, K. E. Strecker, R. I. Kamar, M. W. Jack, and R. G. Hulet, Phys. Rev. Lett. **95**, 020404 (2005).
[20] C. A. Regal, M. Greiner, and D. S. Jin, Phys. Rev. Lett. **92**, 040403 (2004).
[21] M. W. Zwierlein, C. A. Stan, C. H. Schunck, S. M. F. Raupach, A. J. Kerman, and W. Ketterle, Phys. Rev. Lett. **92**, 120403 (2004).
[22] C. Chin and R. Grimm, Phys. Rev. A **69**, 033612 (2004).
[23] M. Pini, P. Pieri, and G. C. Strinati, Phys. Rev. B **99**, 094502 (2019).
[24] A. Perali, P. Pieri, L. Pisani, and G. C. Strinati, Phys. Rev. Lett. **92**, 220404 (2004).
[25] M. Pini *et al.* (unpublished).
[26] X.-J. Liu, Phys. Rep. **524**, 37 (2013).
[27] G. Zürn, T. Lompe, A. N. Wenz, S. Jochim, P. S. Julienne, and J. M. Hutson, Phys. Rev. Lett. **110**, 135301 (2013).
[28] M. Bartenstein, A. Altmeyer, S. Riedl, R. Geursen, S. Jochim, C. Chin, J. H. Denschlag, R. Grimm, A. Simoni, E. Tiesinga, C. J. Williams, and P. S. Julienne, Phys. Rev. Lett. **94**, 103201 (2005).
[29] W. Ketterle and M. Zwierlein, in *Ultra-Cold Fermi Gases*, International School of Physics Enrico Fermi, Vol. Course CLXIV, edited by M. Inguscio, W. Ketterle, and C. Salomon (IOS Press, Amsterdam, 2008).
[30] S. Jochim, *Bose Einstein Condensation of Molecules* (Fraunhofer-IRB-Verlag, Stuttgart, 2005).
[31] S. Jochim, M. Bartenstein, A. Altmeyer, G. Hendl, C. Chin, J. H. Denschlag, and R. Grimm, Phys. Rev. Lett. **91**, 240402 (2003).
[32] T. Bourdel, L. Khaykovich, J. Cubizolles, J. Zhang, F. Chevy, M. Teichmann, L. Tarruell, S. J. J. M. F. Kokkelmans, and C. Salomon, Phys. Rev. Lett. **93**, 050401 (2004).
[33] D. S. Petrov, C. Salomon, and G. V. Shlyapnikov, Phys. Rev. Lett. **93**, 090404 (2004).
[34] F. Werner, L. Tarruell, and Y. Castin, Eur. Phys. J. B **68**, 401 (2009).

List of Figures

List of Tables

Bibliography

1. Yang, X. State-to-State Dynamics of Elementary Bimolecular Reactions. *Annual Review of Physical Chemistry* **58.** PMID: 17105413, 433–459. https://doi.org/10.1146/annurev.physchem.58.032806.104632 (2007).

2. Jankunas, J. & Osterwalder, A. Cold and Controlled Molecular Beams: Production and Applications. *Annual Review of Physical Chemistry* **66,** 241–262. https://doi.org/10.1146/annurev-physchem-040214-12130 (2015).

3. Krems, R. V. Cold controlled chemistry. *Phys. Chem. Chem. Phys.* **10,** 4079–4092. http://pubs.rsc.org/en/content/articlelanding/2008/cp/b802322k#!divAbstract (2008).

4. Quéméner, G. & Julienne, P. S. Ultracold Molecules under Control! *Chemical Reviews* **112,** 4949–5011. https://pubs.acs.org/doi/abs/10.1021/cr300092g (2012).

5. Chin, C., Grimm, R., Julienne, P. & Tiesinga, E. Feshbach resonances in ultracold gases. *Rev. Mod. Phys.* **82,** 1225–1286. https://link.aps.org/doi/10.1103/RevModPhys.82.1225 (2 Apr. 2010).

6. Inouye, S. *et al.* Observation of Feshbach resonances in a Bose–Einstein condensate. *Nature* **392,** 151–154. https://doi.org/10.1038/32354 (1998).

7. Donley, E. A., Claussen, N. R., Thompson, S. T. & Wieman, C. E. Atom–molecule coherence in a Bose–Einstein condensate. *Nature* **417,** 529–533. https://doi.org/10.1038/417529a (2002).

8. Jochim, S. *et al.* Pure Gas of Optically Trapped Molecules Created from Fermionic Atoms. *Phys. Rev. Lett.* **91,** 240402. https://link.aps.org/doi/10.1103/PhysRevLett.91.240402 (24 Dec. 2003).

9. Greiner, M., Regal, C. A. & Jin, D. S. Emergence of a molecular Bose-Einstein condensate from a Fermi gas. *Nature* **426,** 537–540. https://www.nature.com/articles/nature02199 (2003).

10. Xu, K. *et al.* Formation of Quantum-Degenerate Sodium Molecules. *Phys. Rev. Lett.* **91,** 210402. https://link.aps.org/doi/10.1103/PhysRevLett.91.210402 (21 Nov. 2003).

11. Herbig, J. *et al.* Preparation of a Pure Molecular Quantum Gas. *Science* **301,** 1510–1513. eprint: https://science.sciencemag.org/content/301/5639/1510.full.pdf. https://science.sciencemag.org/content/301/5639/1510 (2003).

12. Regal, C. A., Ticknor, C., L., B. J. & Jin, D. S. Creation of ultracold molecules from a Fermi gas of atoms. *Nature* **424,** 47–50. https://www.nature.com/articles/nature01738 (2003).

13. Strecker, K. E., Partridge, G. B. & Hulet, R. G. Conversion of an Atomic Fermi Gas to a Long-Lived Molecular Bose Gas. *Phys. Rev. Lett.* **91,** 080406. https://link.aps.org/doi/10.1103/PhysRevLett.91.080406 (8 Aug. 2003).

14. Cubizolles, J., Bourdel, T., Kokkelmans, S. J. J. M. F., Shlyapnikov, G. V. & Salomon, C. Production of Long-Lived Ultracold Li_2 Molecules from a Fermi Gas. *Phys. Rev. Lett.* **91,** 240401. https://link.aps.org/doi/10.1103/PhysRevLett.91.240401 (24 Dec. 2003).

15. Dürr, S., Volz, T., Marte, A. & Rempe, G. Observation of Molecules Produced from a Bose-Einstein Condensate. *Phys. Rev. Lett.* **92,** 020406. https://link.aps.org/doi/10.1103/PhysRevLett.92.020406 (2 Jan. 2004).

16. Fioretti, A. *et al.* Formation of Cold Cs_2 Molecules through Photoassociation. *Phys. Rev. Lett.* **80,** 4402–4405. https://link.aps.org/doi/10.1103/PhysRevLett.80.4402 (20 May 1998).

17. Carr, L. D., DeMille, D., Krems, R. V. & Ye, J. Cold and ultracold molecules: science, technology and applications. *New Journal of Physics* **11,** 055049. http://iopscience.iop.org/article/10.1088/1367-2630/11/5/055049/meta (2009).

18. Dulieu, O. & Gabbanini, C. The formation and interactions of cold and ultracold molecules: new challenges for interdisciplinary physics. *Reports on Progress in Physics* **72,** 086401. https://doi.org/10.1088%2F0034-4885%2F72%2F8%2F086401 (July 2009).

19. Marte, A. *et al.* Feshbach Resonances in Rubidium 87: Precision Measurement and Analysis. *Phys. Rev. Lett.* **89,** 283202. https://link.aps.org/doi/10.1103/PhysRevLett.89.283202 (28 Dec. 2002).

20. Weber, T., Herbig, J., Mark, M., Nägerl, H.-C. & Grimm, R. Three-Body Recombination at Large Scattering Lengths in an Ultracold Atomic Gas. *Phys. Rev. Lett.* **91,** 123201. https://link.aps.org/doi/10.1103/PhysRevLett.91.123201 (12 Sept. 2003).

21. Härter, A. *et al.* Population distribution of product states following three-body recombination in an ultracold atomic gas. *Nature Physics* **9,** 512. `https://doi.org/10.1038/nphys2661%20http://10.0.4.14/nphys2661%20https://www.nature.com/articles/nphys2661%7B%5C#%7Dsupplementary-information` (June 2013).

22. Efimov, V. N. Weakly-bound states of three resonantly-interacting particles. *Sov. J. Nucl. Phys.* **12,** 589–595 (5 1971).

23. Evidence for Efimov quantum states in an ultracold gas of caesium atoms. *Nature* **440,** 315–318. `https://doi.org/10.1038/nature04626` (2006).

24. Braaten, E. & Hammer, H.-W. Universality in few-body systems with large scattering length. *Physics Reports* **428,** 259–390. `http://www.sciencedirect.com/science/article/pii/S0370157306000822` (2006).

25. Ferlaino, F. *et al.* Efimov Resonances in Ultracold Quantum Gases. *Few-Body Systems* **51,** 113. `https://doi.org/10.1007/s00601-011-0260-7` (2011).

26. Pires, R. *et al.* Observation of Efimov Resonances in a Mixture with Extreme Mass Imbalance. *Phys. Rev. Lett.* **112,** 250404. `https://link.aps.org/doi/10.1103/PhysRevLett.112.250404` (25 June 2014).

27. Tung, S.-K., Jimenez-Garcia, K., Johansen, J., Parker, C. V. & Chin, C. Geometric Scaling of Efimov States in a ^{6}Li$-^{133}$Cs Mixture. *Phys. Rev. Lett.* **113,** 240402. `https://link.aps.org/doi/10.1103/PhysRevLett.113.240402` (24 Dec. 2014).

28. Naidon, P. & Endo, S. Efimov physics: a review. *Reports on Progress in Physics* **80,** 056001. `http://stacks.iop.org/0034-4885/80/i=5/a=056001` (2017).

29. Bethlem, H. L., Berden, G. & Meijer, G. Decelerating Neutral Dipolar Molecules. *Phys. Rev. Lett.* **83,** 1558–1561. `https://link.aps.org/doi/10.1103/PhysRevLett.83.1558` (8 Aug. 1999).

30. Van de Meerakker, S. Y. T., Bethlem, H. L., Vanhaecke, N. & Meijer, G. Manipulation and Control of Molecular Beams. *Chemical Reviews* **112,** 4828–4878. `https://doi.org/10.1021/cr200349r` (Sept. 2012).

31. Chin, C. *et al.* Observation of Feshbach-Like Resonances in Collisions between Ultracold Molecules. *Phys. Rev. Lett.* **94,** 123201. `https://link.aps.org/doi/10.1103/PhysRevLett.94.123201` (12 Apr. 2005).

32. Ferlaino, F. *et al.* Collisions between Tunable Halo Dimers: Exploring an Elementary Four-Body Process with Identical Bosons. *Phys. Rev. Lett.* **101,** 023201. `https://link.aps.org/doi/10.1103/PhysRevLett.101.023201` (2 July 2008).

33. Zirbel, J. J. *et al.* Collisional Stability of Fermionic Feshbach Molecules. *Phys. Rev. Lett.* **100,** 143201. https://link.aps.org/doi/10.1103/PhysRevLett.100.143201 (14 Apr. 2008).

34. Regal, C. A., Greiner, M. & Jin, D. S. Lifetime of Molecule-Atom Mixtures near a Feshbach Resonance in ^{40}K. *Phys. Rev. Lett.* **92,** 083201. https://link.aps.org/doi/10.1103/PhysRevLett.92.083201 (8 Feb. 2004).

35. Mukaiyama, T., Abo-Shaeer, J. R., Xu, K., Chin, J. K. & Ketterle, W. Dissociation and Decay of Ultracold Sodium Molecules. *Phys. Rev. Lett.* **92,** 180402. https://link.aps.org/doi/10.1103/PhysRevLett.92.180402 (18 May 2004).

36. Staanum, P., Kraft, S. D., Lange, J., Wester, R. & Weidemüller, M. Experimental Investigation of Ultracold Atom-Molecule Collisions. *Phys. Rev. Lett.* **96,** 023201. https://link.aps.org/doi/10.1103/PhysRevLett.96.023201 (2 Jan. 2006).

37. Zhang, S. & Ho, T.-L. Atom loss maximum in ultra-cold Fermi gases. *New Journal of Physics* **13,** 055003. https://doi.org/10.1088%2F1367-2630%2F13%2F5%2F055003 (May 2011).

38. Drews, B., Deiß, M., Jachymski, K., Idziaszek, Z. & Hecker Denschlag, J. Inelastic collisions of ultracold triplet Rb2 molecules in the rovibrational ground state. *Nat. Commun.* **8,** 14854. https://www.nature.com/articles/ncomms14854 (2017).

39. Wolf, J. *et al.* State-to-state chemistry for three-body recombination in an ultracold rubidium gas. *Science* **358,** 921–924. eprint: http://science.sciencemag.org/content/358/6365/921.full.pdf. http://science.sciencemag.org/content/358/6365/921 (2017).

40. Hoffmann, D. K., Paintner, T., Limmer, W., S., P. D. & Hecker Denschlag, J. Reaction kinetics of ultracold molecule-molecule collisions. *Nature Communications* **9,** 5244. https://doi.org/10.1038/s41467-018-07576-1 (2018).

41. Pauli, W. Über den Zusammenhang des Abschlusses der Elektronengruppen im Atom mit der Komplexstruktur der Spektren. *Zeitschrift für Physik* **31,** 765–783. https://link.springer.com/article/10.1007%2FBF02980631 (1925).

42. Petrov, D. S., Salomon, C. & Shlyapnikov, G. V. Weakly Bound Dimers of Fermionic Atoms. *Phys. Rev. Lett.* **93,** 090404. https://link.aps.org/doi/10.1103/PhysRevLett.93.090404 (9 Aug. 2004).

43. Petrov, D. S., Salomon, C. & Shlyapnikov, G. V. Scattering properties of weakly bound dimers of fermionic atoms. *Phys. Rev. A* **71,** 012708. https://link.aps.org/doi/10.1103/PhysRevA.71.012708 (1 Jan. 2005).

44. D'Incao, J. P., Rittenhouse, S. T., Mehta, N. P. & Greene, C. H. Dimer-dimer collisions at finite energies in two-component Fermi gases. *Phys. Rev. A* **79,** 030501. https://link.aps.org/doi/10.1103/PhysRevA.79.030501 (3 Mar. 2009).

45. Allen, J. F. & Misener, A. D. Flow of Liquid Helium II. *Nature* **141,** 75. https://doi.org/10.1038/141075a0 (1938).

46. Kapitza, P. Viscosity of Liquid Helium below the λ-Point. *Nature* **141,** 74. https://doi.org/10.1038/141074a0 (1938).

47. Tisza, L. Sur la supraconductibilité thermique de l'Helium II liquide et al statistique de Bose-Einstein. *C. R. Acad. Sci.* **207** (1938).

48. Tisza, L. Transport Phenomena in Helium II. *Nature* **141,** 913. https://doi.org/10.1038/141913a0 (1938).

49. London, F. The λ-Phenomenon of Liquid Helium and the Bose-Einstein Degeneracy. *Nature* **141,** 643–644. https://doi.org/10.1038/141643a0 (1938).

50. Landau, L. D. Theory of the Superfluidity of Helium II. *J. Phys. (USSR)* **5,** 71 (1941).

51. Donnelly, R. J. The two-fluid theory and second sound in liquid helium. *Physics Today* **62,** 34. https://physicstoday.scitation.org/doi/10.1063/1.3248499 (10 2009).

52. Peshkov, V. P. Determination of the velocity of propagation of the second sound in helium II. *J. Phys. USSR* **10** (1946).

53. Sidorenkov, L. A. *et al.* Second sound and the superfluid fraction in a Fermi gas with resonant interactions. *Nature* **498,** 78–81. https://www.nature.com/articles/nature12136 (2013).

54. Bishop, D. J. & Reppy, J. D. Study of the Superfluid Transition in Two-Dimensional ^{4}He Films. *Phys. Rev. Lett.* **40,** 1727–1730. https://link.aps.org/doi/10.1103/PhysRevLett.40.1727 (26 June 1978).

55. Ota, M. & Stringari, S. Second sound in a two-dimensional Bose gas: From the weakly to the strongly interacting regime. *Phys. Rev. A* **97,** 033604. https://link.aps.org/doi/10.1103/PhysRevA.97.033604 (3 Mar. 2018).

56. Ville, J. L. *et al.* Sound Propagation in a Uniform Superfluid Two- Dimensional Bose Gas. *Phys. Rev. Lett.* **121,** 145301. https://link.aps.org/doi/10.1103/PhysRevLett.121.145301 (14 Oct. 2018).

57.   Jochim, S. *et al.* Bose-Einstein Condensation of Molecules. *Science* **302,** 2101–2103. eprint: http://science.sciencemag.org/content/302/5653/2101.full.pdf. http://science.sciencemag.org/content/302/5653/2101 (2003).

58.   Zwierlein, M. W. *et al.* Observation of Bose-Einstein Condensation of Molecules. *Phys. Rev. Lett.* **91,** 250401. https://link.aps.org/doi/10.1103/PhysRevLett.91.250401 (25 Dec. 2003).

59.   DeMarco, B. & Jin, D. S. Onset of Fermi Degeneracy in a Trapped Atomic Gas. *Science* **285,** 1703–1706. eprint: http://science.sciencemag.org/content/285/5434/1703.full.pdf. http://science.sciencemag.org/content/285/5434/1703 (1999).

60.   Zwierlein, M. W., Abo-Shaeer, J. R., Schirotzek, A., Schunck, C. H. & Ketterle, W. Vortices and superfluidity in a strongly interacting Fermi gas. *Nature* **435,** 1047. http://dx.doi.org/10.1038/nature03858%20http://10.0.4.14/nature03858 (June 2005).

61.   Hoffmann, D. K. *et al.* Second sound in the BEC-BCS crossover, arXiv: 2003.06847. https://arxiv.org/abs/2003.06847 (2020).

62.   Heiselberg, H. Sound modes at the BCS-BEC crossover. *Phys. Rev. A* **73,** 013607. https://link.aps.org/doi/10.1103/PhysRevA.73.013607 (1 Jan. 2006).

63.   Bloch, I. Ultracold quantum gases in optical lattices. *Nature Physics* **1,** 23–30. https://doi.org/10.1038/nphys138 (2005).

64.   Georgescu, I. M., Ashhab, S. & Nori, F. Quantum simulation. *Rev. Mod. Phys.* **86,** 153–185. https://link.aps.org/doi/10.1103/RevModPhys.86.153 (1 Mar. 2014).

65.   Bloch, I. Quantum simulations come of age. *Nature Physics* **14,** 1159–1161. https://doi.org/10.1038/s41567-018-0371-x (2018).

66.   Greiner, M., Mandel, O., Esslinger, T., Hänsch, T. W. & Bloch, I. Quantum phase transition from a superfluid to a Mott insulator in a gas of ultracold atoms. *Nature* **415,** 39–44. https://doi.org/10.1038/415039a (2002).

67.   Schneider, U. *et al.* Metallic and Insulating Phases of Repulsively Interacting Fermions in a 3D Optical Lattice. *Science* **322,** 1520–1525. eprint: http://science.sciencemag.org/content/322/5907/1520.full.pdf. http://science.sciencemag.org/content/322/5907/1520 (2008).

68. Jördens, R., Strohmaier, N., Günter, K., Moritz, H. & Esslinger, T. A Mott insulator of fermionic atoms in an optical lattice. *Nature* **455,** 204. https://doi.org/10.1038/nature07244%20http://10.0.4.14/nature07244 (Sept. 2008).

69. Nelson, K. D., Li, X. & Weiss, D. S. Imaging single atoms in a three-dimensional array. *Nature Physics* **3,** 556. http://dx.doi.org/10.1038/nphys645%20http://10.0.4.14/nphys645%20https://www.nature.com/articles/nphys645%7B%5C#%7Dsupplementary-information (June 2007).

70. Bakr, W. S., Gillen, J. I., Peng, A., Folling, S. & Greiner, M. A quantum gas microscope for detecting single atoms in a Hubbard-regime optical lattice. *Nature* **462,** 74–77. http://dx.doi.org/10.1038/nature08482 (Nov. 5, 2009).

71. Sherson, J. F. *et al.* Single-atom-resolved fluorescence imaging of an atomic Mott insulator. *Nature* **467.** 00907, 68–72. http://dx.doi.org/10.1038/nature09378 (Sept. 2, 2010).

72. Haller, E. *et al.* Single-atom imaging of fermions in a quantum-gas microscope. *Nature Physics* **11,** 738. http://dx.doi.org/10.1038/nphys3403%20http://10.0.4.14/nphys3403%20https://www.nature.com/articles/nphys3403%7B%5C#%7Dsupplementary-information (July 2015).

73. Omran, A. *et al.* Microscopic Observation of Pauli Blocking in Degenerate Fermionic Lattice Gases. *Phys. Rev. Lett.* **115,** 263001. https://link.aps.org/doi/10.1103/PhysRevLett.115.263001 (26 Dec. 2015).

74. Cheuk, L. W. *et al.* Quantum-Gas Microscope for Fermionic Atoms. *Phys. Rev. Lett.* **114,** 193001. https://link.aps.org/doi/10.1103/PhysRevLett.114.193001 (19 May 2015).

75. Parsons, M. F. *et al.* Site-Resolved Imaging of Fermionic ^{6}Li in an Optical Lattice. *Phys. Rev. Lett.* **114,** 213002. https://link.aps.org/doi/10.1103/PhysRevLett.114.213002 (21 May 2015).

76. Andrews, M. R. *et al.* Direct, Nondestructive Observation of a Bose Condensate. *Science* **273,** 84–87. eprint: http://science.sciencemag.org/content/273/5271/84.full.pdf. http://science.sciencemag.org/content/273/5271/84 (1996).

77. Kadlecek, S., Sebby, J., Newell, R. & Walker, T. Nondestructive spatial heterodyne imaging of cold atoms. *Optics letters* **26,** 137–139. https://www.osapublishing.org/ol/abstract.cfm?uri=ol-26-3-137 (2001).

78. Turner, L. D., Weber, K. P., Paganin, D. & Scholten, R. E. Off-resonant defocus-contrast imaging of cold atoms. *Opt. Lett.* **29,** 232–234. http://ol.osa.org/abstract.cfm?URI=ol-29-3-232 (Feb. 2004).

79. Sobol, J. P. & Wu, S. Imaging cold atoms with shot-noise and diffraction limited holography. *New Journal of Physics* **16,** 093064. http://iopscience.iop.org/article/10.1088/1367-2630/16/9/093064/pdf (2014).

80. Leith, E. N. & Upatnieks, J. Reconstructed wavefronts and communication theory. *JOSA* **52,** 1123–1130 (1962).

81. Hoffmann, D. K., Deissler, B., Limmer, W. & Hecker Denschlag, J. Holographic method for site-resolved detection of a 2D array of ultracold atoms. *Applied Physics B* **122,** 227. https://link.springer.com/article/10.1007/s00340-016-6501-1 (2016).

82. Singh, V. P. Privat communication. Jan. 2018.

83. De Broglie, L. Waves and Quanta. *Nature* **112.** http://dx.doi.org/10.1038/112540a0 (1923).

84. Foot, C. J. *Atomic Physics* (Oxford University Press, 2005).

85. Pethick, C. & Smith, H. *Bose-Einstein Condensation in dilute gases.* (Cambridge University Press, 2008).

86. Ketterle, W. & Zwierlein, M. Making, probing and understanding ultracold Fermi gases. **31,** 247. https://www.sif.it/riviste/sif/ncr/econtents/2008/031/05-06/article/0 (2008).

87. Landau, L. & Lifschitz, E. M. *Quantum Mechanics* §131 (Pergamon Press, Oxford, 1977).

88. Lompe, T. *Efimov Physics in a three-component Fermi gas* PhD thesis (Ruperto-Carola University of Heidelberg, 2011).

89. Köhler, T., Góral, K. & Julienne, P. S. Production of cold molecules via magnetically tunable Feshbach resonances. *Rev. Mod. Phys.* **78,** 1311–1361. https://link.aps.org/doi/10.1103/RevModPhys.78.1311 (4 Dec. 2006).

90. Moerdijk, A. J., Verhaar, B. J. & Axelsson, A. Resonances in ultracold collisions of ^{6}Li, ^{7}Li, and ^{23}Na. *Phys. Rev. A* **51,** 4852–4861. https://link.aps.org/doi/10.1103/PhysRevA.51.4852 (6 June 1995).

91. Zürn, G. *et al.* Precise Characterization of ^{6}Li Feshbach Resonances Using Trap-Sideband-Resolved RF Spectroscopy of Weakly Bound Molecules. *Phys. Rev. Lett.* **110,** 135301. https://link.aps.org/doi/10.1103/PhysRevLett.110.135301 (13 Mar. 2013).

92. Gao, B. Binding energy and scattering length for diatomic systems. *Journal of Physics B: Atomic, Molecular and Optical Physics* **37,** 4273. `http://stacks.iop.org/0953-4075/37/i=21/a=004` (2004).

93. Julienne, P. S. & Hutson, J. M. Contrasting the wide Feshbach resonances in ^{6}Li and ^{7}Li. *Phys. Rev. A* **89,** 052715. `https://link.aps.org/doi/10.1103/PhysRevA.89.052715` (5 May 2014).

94. Chin, C. *et al.* Observation of the Pairing Gap in a Strongly Interacting Fermi Gas. *Science* **305,** 1128–1130. `http://science.sciencemag.org/content/305/5687/1128` (2004).

95. Gehm, M. *Preparation of an optically-trapped degenerate Fermi gas of ^{6}Li: Finding the route to degeneracy* PhD thesis (Duke University, 2003).

96. Mayer-Kuckuck, T. *Atomphysik* (Teubner Studienbücher, 1985).

97. Wing, W. H. On neutral particle trapping in quasistatic electromagnetic fields. *Prog. Quant. Electr* **8.** `https://www.sciencedirect.com/science/article/pii/0079672784900120` (1984).

98. Chin, C. & Grimm, R. Thermal equilibrium and efficient evaporation of an ultracold atom-molecule mixture. *Phys. Rev. A* **69,** 033612. `https://link.aps.org/doi/10.1103/PhysRevA.69.033612` (3 Mar. 2004).

99. Paintner, T. *et al.* Pair fraction in a finite-temperature Fermi gas on the BEC side of the BCS-BEC crossover. *Phys. Rev. A* **99.** `https://journals.aps.org/pra/abstract/10.1103/PhysRevA.99.053617` (2019).

100. McAlexander, W. I. *Collisional Interactions in an Ultracold Lithium Gas* PhD thesis (Rice University, 2000).

101. Grimm, R. in *Ultracold Fermi Gases, Proceedings of the International School of Physics "Enrico Fermi". Ultracold Fermi gases in the BEC-BCS crossover: a review from the Innsbruck perspective* (eds M. Inguscio, W. K. & Salomon, C.) (2007).

102. Petrov, D. S. Three-body problem in Fermi gases with short-range interparticle interaction. *Phys. Rev. A* **67,** 010703. `https://link.aps.org/doi/10.1103/PhysRevA.67.010703` (1 Jan. 2003).

103. Giorgini, S., Pitaevskii, L. P. & Stringari, S. Theory of ultracold atomic Fermi gases. *Rev. Mod. Phys.* **80,** 1215–1274. `https://link.aps.org/doi/10.1103/RevModPhys.80.1215` (4 Oct. 2008).

104. Bourdel, T. *et al.* Experimental Study of the BEC-BCS Crossover Region in Lithium 6. *Phys. Rev. Lett.* **93,** 050401. `https://link.aps.org/doi/10.1103/PhysRevLett.93.050401` (5 July 2004).

105. Partridge, G. B., Strecker, K. E., Kamar, R. I., Jack, M. W. & Hulet, R. G. Molecular Probe of Pairing in the BEC-BCS Crossover. *Phys. Rev. Lett.* **95,** 020404. https://link.aps.org/doi/10.1103/PhysRevLett.95.020404 (2 July 2005).

106. Sagi, Y., Drake, T. E., Paudel, R., Chapurin, R. & Jin, D. S. Breakdown of the Fermi Liquid Description for Strongly Interacting Fermions. *Phys. Rev. Lett.* **114,** 075301. https://link.aps.org/doi/10.1103/PhysRevLett.114.075301 (7 Feb. 2015).

107. Navon, N., Nascimbène, S., Chevy, F. & Salomon, C. The Equation of State of a Low-Temperature Fermi Gas with Tunable Interactions. *Science* **328,** 729–732. http://science.sciencemag.org/content/328/5979/729 (2010).

108. Ku, M. J. H., Sommer, A. T., Cheuk, L. W. & Zwierlein, M. W. Revealing the Superfluid Lambda Transition in the Universal Thermodynamics of a Unitary Fermi Gas. *Science* **335,** 563–567. http://science.sciencemag.org/content/335/6068/563 (2012).

109. Semczuk, M., Gunton, W., Bowden, W. & Madison, K. W. Anomalous Behavior of Dark States in Quantum Gases of ^{6}Li. *Phys. Rev. Lett.* **113,** 055302. https://link.aps.org/doi/10.1103/PhysRevLett.113.055302 (5 July 2014).

110. Weimer, W. *et al.* Critical Velocity in the BEC-BCS Crossover. *Phys. Rev. Lett.* **114,** 095301. https://link.aps.org/doi/10.1103/PhysRevLett.114.095301 (9 Mar. 2015).

111. Stenger, J. *et al.* Bragg Spectroscopy of a Bose-Einstein Condensate. *Phys. Rev. Lett.* **82,** 4569–4573. https://link.aps.org/doi/10.1103/PhysRevLett.82.4569 (23 June 1999).

112. Steinhauer, J., Ozeri, R., Katz, N. & Davidson, N. Excitation Spectrum of a Bose-Einstein Condensate. *Phys. Rev. Lett.* **88,** 120407. https://link.aps.org/doi/10.1103/PhysRevLett.88.120407 (12 Mar. 2002).

113. Veeravalli, G., Kuhnle, E., Dyke, P. & Vale, C. J. Bragg Spectroscopy of a Strongly Interacting Fermi Gas. *Phys. Rev. Lett.* **101,** 250403. https://link.aps.org/doi/10.1103/PhysRevLett.101.250403 (25 Dec. 2008).

114. Hoinka, S. *et al.* Goldstone mode and pair-breaking excitations in atomic Fermi superfluids. *Nature Physics* **13,** 943–946. http://dx.doi.org/10.1038/nphys4187 (June 2017).

115. Pitaevskii, L. & Stringari, S. Second Sound in Ultracold Atomic Gases, arXiv:1510.01306. https://arxiv.org/abs/1510.01306 (2015).

116. Jochim, S. *Bose-Einstein Condensation of Molecules* PhD thesis (Leopold-Franzens-Universität Innsbruck, 2004).

117. Ottenstein, T. *Few-body physics in ultracold Fermi gases* PhD thesis (Ruperto-Carola University of Heidelberg, 2010).

118. Bartenstein, M. *et al.* Precise Determination of ^{6}Li Cold Collision Parameters by Radio-Frequency Spectroscopy on Weakly Bound Molecules. *Phys. Rev. Lett.* **94,** 103201. https://link.aps.org/doi/10.1103/PhysRevLett.94.103201 (10 Mar. 2005).

119. Truscott, A. G., Strecker, K. E., McAlexander, W. I., Partridge, G. B. & Hulet, R. G. Observation of Fermi Pressure in a Gas of Trapped Atoms. *Science* **291,** 2570–2572. eprint: http://science.sciencemag.org/content/291/5513/2570.full.pdf. http://science.sciencemag.org/content/291/5513/2570 (2001).

120. Bartenstein, M. *et al.* Crossover from a Molecular Bose-Einstein Condensate to a Degenerate Fermi Gas. *Phys. Rev. Lett.* **92,** 120401. https://link.aps.org/doi/10.1103/PhysRevLett.92.120401 (12 Mar. 2004).

121. Bartenstein, M. *et al.* Collective Excitations of a Degenerate Gas at the BEC-BCS Crossover. *Phys. Rev. Lett.* **92,** 203201. https://link.aps.org/doi/10.1103/PhysRevLett.92.203201 (20 May 2004).

122. Paintner, T. *Aufbau eines Lasersystems zur Kühlung von ^{6}Li* (not published). MA thesis (Universität Ulm, 2012).

123. Vogler, B. *Design und Aufbau einer Vakuumapparatur zur Laserkühlung von Lithium* (not published). MA thesis (Universität Ulm, 2012).

124. Hoffmann, D. K. *Abbildung ultrakalter Lithiumatome* (not published). MA thesis (Universität Ulm, 2013).

125. Lupfer, T. *Aufbau einer Dipolfalle zur Erzeugung eines quantenentarteten Fermigases aus Lithiumatomen* (not published). MA thesis (Universität Ulm, 2013).

126. Griener, M. *Optical transport and evaporation to a degenerate Fermi gas* (not published). MA thesis (Universität Ulm, 2014).

127. Sansonetti, C. J. *et al.* Absolute Transition Frequencies and Quantum Interference in a Frequency Comb Based Measurement of the ^{6,7}Li *D* Lines. *Phys. Rev. Lett.* **107,** 023001. https://link.aps.org/doi/10.1103/PhysRevLett.107.023001 (2 July 2011).

128. S. Chu, C. C.-T. & Phillips, W. D. Nobel lecture: The manipulation of neutral particles; Manipulating atoms with photons; Laser cooling and trapping of neutral atoms. *Rev. Mod. Phys.* **70,** 685–741. https://journals.aps.org/rmp/issues/70/3 (1998).

129. Grimm, R., Weidemüller, M. & Y, O. Optical dipole Traps for Neutral Atoms. *Adv. Atom. Mol. Opt. Phy.* **42,** 95–170. https://www.sciencedirect.com/science/article/pii/S1049250X0860186X (2000).

130. Ketterle, W. & Druten, N. J. V. in (eds Bederson, B. & Walther, H.) 181–236 (Academic Press, 1996). http://www.sciencedirect.com/science/article/pii/S1049250X08601019.

131. Pieri, P. *et al.* Pairing-gap, pseudogap, and no-gap phases in the radio-frequency spectra of a trapped unitary ^{6}Li gas. *Phys. Rev. A* **84,** 011608. https://link.aps.org/doi/10.1103/PhysRevA.84.011608 (1 July 2011).

132. Butler, J. S. & Authors, W. N. *Wireless Networking in the Developing World: Black and White Version* (CreateSpace Independent Publishing Platform, 2013).

133. Goodman, J. W. *Introduction to Fourier optics* (Roberts and Company Publishers, 2005).

134. Hecht, E. *Optik* (Oldenbourg Wissenschaftsverlag, 2009).

135. Haferkorn, H. *Optik: Physikalisch-technische Grundlagen und Anwendungen* (Wiley-VCH Verlag GmbH und Co. KGaA, 2002).

136. Meyrath, T. P., Schreck, F., Hanssen, J. L., Chuu, C. .-.-S. & Raizen, M. G. A high frequency optical trap for atoms using Hermite-Gaussian beams. *Opt. Express* **13,** 2843–2851. http://www.opticsexpress.org/abstract.cfm?URI=oe-13-8-2843 (Apr. 2005).

137. Gleiter, J. *Aufbau eines Lasersystems für eine 2D-Atomfalle* (not published). MA thesis (Universität Ulm, 2015).

138. Bergamini, S. *et al.* Holographic generation of microtrap arrays for single atoms by use of a programmable phase modulator. *J. Opt. Soc. Am. B* **21,** 1889–1894. http://josab.osa.org/abstract.cfm?URI=josab-21-11-1889 (Nov. 2004).

139. Holland, M. J., DeMarco, B. & Jin, D. S. Evaporative cooling of a two-component degenerate Fermi gas. *Phys. Rev. A* **61,** 053610. https://link.aps.org/doi/10.1103/PhysRevA.61.053610 (5 Apr. 2000).

140. Granade, S. R., Gehm, M. E., O'Hara, K. M. & Thomas, J. E. All-Optical Production of a Degenerate Fermi Gas. *Phys. Rev. Lett.* **88,** 120405. https://link.aps.org/doi/10.1103/PhysRevLett.88.120405 (12 Mar. 2002).

141. Dyke, P. *et al.* Crossover from 2D to 3D in a Weakly Interacting Fermi Gas. *Phys. Rev. Lett.* **106,** 105304. https://link.aps.org/doi/10.1103/PhysRevLett.106.105304 (10 Mar. 2011).

142. Serwane, F. *et al.* Deterministic Preparation of a Tunable Few-Fermion System. *Science* **332,** 336–338. eprint: http://science.sciencemag.org/content/332/6027/336.full.pdf. http://science.sciencemag.org/content/332/6027/336 (2011).

143. Dyke, P. *et al.* Criteria for two-dimensional kinematics in an interacting Fermi gas. *Phys. Rev. A* **93,** 011603. https://link.aps.org/doi/10.1103/PhysRevA.93.011603 (1 Jan. 2016).

144. Haller, E. *et al.* Single-atom imaging of fermions in a quantum-gas microscope. *Nat. Phys.* **11,** 738–742. https://www.nature.com/articles/nphys3403 (2015).

145. Häußler, S. *Raman Seitenbandkühlen von ^6Li Atomen in einem optischen Gitter* (not published). MA thesis (Universität Ulm, 2015).

146. Richter, F. *et al.* Ultracold chemistry and its reaction kinetics. *New Journal of Physics* **17,** 055005. http://iopscience.iop.org/article/10.1088/1367-2630/17/5/055005 (2015).

147. Zahzam, N., Vogt, T., Mudrich, M., Comparat, D. & Pillet, P. Atom-Molecule Collisions in an Optically Trapped Gas. *Phys. Rev. Lett.* **96,** 023202. https://link.aps.org/doi/10.1103/PhysRevLett.96.023202 (2 Jan. 2006).

148. Syassen, N., Volz, T., Teichmann, S., Dürr, S. & Rempe, G. Collisional decay of ^{87}Rb Feshbach molecules at 1005.8 G. *Phys. Rev. A* **74,** 062706. https://link.aps.org/doi/10.1103/PhysRevA.74.062706 (6 Dec. 2006).

149. Ospelkaus, S. *et al.* Quantum-State Controlled Chemical Reactions of Ultracold Potassium-Rubidium Molecules. *Science* **327,** 853–857. eprint: https://science.sciencemag.org/content/327/5967/853.full.pdf. https://science.sciencemag.org/content/327/5967/853 (2010).

150. Ni, K.-K. e. a. Observation of pseudogap behaviour in a strongly interacting Fermi gas. *Nature* **464,** 1324–1328. https://www.nature.com/articles/nature08953 (2010).

151. De Miranda, M. H. G. e. a. Controlling the quantum stereodynamics of ultracold bimolecular reactions. *Nat. Phys.* **7,** 502–507. https://www.nature.com/articles/nphys1939 (2011).

152. Wang, T. T., Heo, M.-S., Rvachov, T. M., Cotta, D. A. & Ketterle, W. Deviation from Universality in Collisions of Ultracold ^{6}Li$_2$ Molecules. *Phys. Rev. Lett.* **110,** 173203. https://link.aps.org/doi/10.1103/PhysRevLett.110.173203 (17 Apr. 2013).

153. Knoop, S. *et al.* Magnetically Controlled Exchange Process in an Ultracold Atom-Dimer Mixture. *Phys. Rev. Lett.* **104,** 053201. https://link.aps.org/doi/10.1103/PhysRevLett.104.053201 (5 Feb. 2010).

154. Rui, J. *et al.* Controlled state-to-state atom-exchange reaction in an ultracold atom–dimer mixture. *Nature Physics* **13,** 699. http://dx.doi.org/10.1038/nphys4095%20http://10.0.4.14/nphys4095%20https://www.nature.com/articles/nphys4095%7B%5C#%7Dsupplementary-information (Apr. 2017).

155. Fedichev, P. O., Reynolds, M. W. & Shlyapnikov, G. V. Three-Body Recombination of Ultracold Atoms to a Weakly Bound *s* Level. *Phys. Rev. Lett.* **77,** 2921–2924. https://link.aps.org/doi/10.1103/PhysRevLett.77.2921 (14 Sept. 1996).

156. Jo, G.-B. *et al.* Itinerant Ferromagnetism in a Fermi Gas of Ultracold Atoms. *Science* **325,** 1521–1524. eprint: http://science.sciencemag.org/content/325/5947/1521.full.pdf. http://science.sciencemag.org/content/325/5947/1521 (2009).

157. Sanner, C. *et al.* Correlations and Pair Formation in a Repulsively Interacting Fermi Gas. *Phys. Rev. Lett.* **108,** 240404. https://link.aps.org/doi/10.1103/PhysRevLett.108.240404 (24 June 2012).

158. Petrov, D. S., Baranov, M. A. & Shlyapnikov, G. V. Superfluid transition in quasi-two-dimensional Fermi gases. *Phys. Rev. A* **67,** 031601. https://link.aps.org/doi/10.1103/PhysRevA.67.031601 (3 Mar. 2003).

159. D'Incao, J. P. & Esry, B. D. Scattering Length Scaling Laws for Ultracold Three-Body Collisions. *Phys. Rev. Lett.* **94,** 213201. https://link.aps.org/doi/10.1103/PhysRevLett.94.213201 (21 June 2005).

160. Jag, M. *et al.* Observation of a Strong Atom-Dimer Attraction in a Mass-Imbalanced Fermi-Fermi Mixture. *Phys. Rev. Lett.* **112,** 075302. https://link.aps.org/doi/10.1103/PhysRevLett.112.075302 (7 Feb. 2014).

161. Tiemann, E. privat communication. 2017.

162. Partridge, G. B. *Pairing of Fermionic ^{6}Li Throughout the BEC-BCS crossover* PhD thesis (Rice University, 2007).

163. Prodan, I. D., Pichler, M., Junker, M., Hulet, R. G. & Bohn, J. L. Intensity Dependence of Photoassociation in a Quantum Degenerate Atomic Gas. *Phys. Rev. Lett.* **91,** 080402. https://link.aps.org/doi/10.1103/PhysRevLett.91.080402 (8 Aug. 2003).

164. Halperin, W. P. Eighty years of superfluidity. *Nature* **553,** 413–414. https://www.nature.com/articles/d41586-018-00417-7/ (2018).

165. Griffin, A. New light on the intriguing history of superfluidity in liquid ^{4}He. *Journal of Physics: Condensed Matter* **21,** 164220. https://doi.org/ 10.1088%2F0953-8984%2F21%2F16%2F164220 (Mar. 2009).

166. Putterman, S. J. *Superfluid Hydrodynamics* (North Holland, Amsterdam, 1974).

167. Zwerger, W. *Lecture Notes in Physics: The BCS-BEC Crossover and the Unitary Fermi Gas* (Springer-Verlag Berlin Heidelberg, 2012).

168. Nascimbène, S., Navon, N., Jiang, K. J., Chevy, F. & Salomon, C. Exploring the thermodynamics of a universal Fermi gas. *Nature* **463,** 1057. http: //dx.doi.org/10.1038/nature08814%20http://10.0.4.14/ nature08814%20https://www.nature.com/articles/nature08814% 7B%5C#%7Dsupplementary-information (Feb. 2010).

169. Shin, Y.-i., Schunck, C. H., Schirotzek, A. & Ketterle, W. Phase diagram of a two-component Fermi gas with resonant interactions. *Nature* **451,** 689. http://dx.doi.org/10.1038/nature06473%20http://10.0.4.14/ nature06473%20https://www.nature.com/articles/nature06473% 7B%5C#%7Dsupplementary-information (Feb. 2008).

170. Joseph, J. *et al.* Measurement of Sound Velocity in a Fermi Gas near a Feshbach Resonance. *Phys. Rev. Lett.* **98,** 170401. https://link.aps.org/ doi/10.1103/PhysRevLett.98.170401 (17 Apr. 2007).

171. Taylor, E. *et al.* First and second sound in a strongly interacting Fermi gas. *Phys. Rev. A* **80,** 053601. https://link.aps.org/doi/10.1103/ PhysRevA.80.053601 (5 Nov. 2009).

172. Perali, A., Pieri, P., Pisani, L. & Strinati, G. C. BCS-BEC Crossover at Finite Temperature for Superfluid Trapped Fermi Atoms. *Phys. Rev. Lett.* **92,** 220404. https://link.aps.org/doi/10.1103/PhysRevLett.92. 220404 (22 June 2004).

173. Arahata, E. & Nikuni, T. Propagation of second sound in a superfluid Fermi gas in the unitary limit. *Phys. Rev. A* **80,** 043613. https://link.aps. org/doi/10.1103/PhysRevA.80.043613 (4 Oct. 2009).

174. Hu, H., Taylor, E., Liu, X.-J., Stringari, S. & Griffin, A. Second sound and the density response function in uniform superfluid atomic gases. *New Journal of Physics* **12,** 043040. http://stacks.iop.org/1367-2630/12/i= 4/a=043040 (2010).

175. Andrews, M. R. *et al.* Propagation of Sound in a Bose-Einstein Condensate. *Phys. Rev. Lett.* **79,** 553–556. https://link.aps.org/doi/10.1103/ PhysRevLett.79.553 (4 July 1997).

176. Singh, V. P. *et al.* Probing superfluidity of Bose-Einstein condensates via laser stirring. *Phys. Rev. A* **93,** 023634. https://link.aps.org/doi/10.1103/PhysRevA.93.023634 (2 Feb. 2016).

177. Pini, M., Pieri, P., Jäger, M., Hecker Denschlag, J. & Calvanese Strinati, G. Pair correlations in the normal phase of an attractive Fermi gas, arXiv: 1912.04802. https://arxiv.org/abs/1912.04802 (2019).

178. Luo, L. & Thomas, J. E. Thermodynamic Measurements in a Strongly Interacting Fermi Gas. *J Low Temp Phys* **154,** 1–29. https://link.springer.com/article/10.1007/s10909-008-9850-2 (2009).

179. Lifschitz, E. M. & Pitaevskii, L. *Statistical Physics, Part 2, Theory of the Condensed State* (Butterworth-Heinemann, 1980).

180. Gorkov, L. P. & Melik-Barkhudarov, T. K. Contribution to the Theory of Superfluidity in an Imperfect Fermi Gas. *Sov. Phys. JETP* **13,** 1018. http://www.jetp.ac.ru/cgi-bin/e/index/e/13/5/p1018?a=list (1961).

181. Pitaevskii, L. & Stringari, S. *Bose-Einstein Condensation* (Oxford University Press, 2003).

182. Bloch, I., Dalibard, J. & Zwerger, W. Many-body physics with ultracold gases. *Rev. Mod. Phys.* **80,** 885–964. https://link.aps.org/doi/10.1103/RevModPhys.80.885 (3 July 2008).

183. Turner, L. D., Domen, K. F. E. M. & Scholten, R. E. Diffraction-contrast imaging of cold atoms. *Phys. Rev. A* **72,** 031403. https://link.aps.org/doi/10.1103/PhysRevA.72.031403 (3 Sept. 2005).

184. Light, P. S., Perrella, C. & Luiten, A. Phase-sensitive imaging of cold atoms at the shot-noise limit. *Applied Physics Letters* **102,** 171108. https://aip.scitation.org/doi/full/10.1063/1.4803703 (2013).

185. Weitenberg, C. *et al.* Coherent Light Scattering from a Two-Dimensional Mott Insulator. *Phys. Rev. Lett.* **106,** 215301. https://link.aps.org/doi/10.1103/PhysRevLett.106.215301 (21 May 2011).

186. Schnars, U. & Jüptner, W. P. Digital recording and numerical reconstruction of holograms. *Meas. Sci. and Technol.* **13,** R85. http://iopscience.iop.org/article/10.1088/0957-0233/13/9/201/meta (2002).

187. Loudon, R. *The quantum theory of light* (Oxford University Press, 2009).

188. Mollow, B. R. Power Spectrum of Light Scattered by Two-Level Systems. *Phys. Rev.* **188,** 1969–1975. https://link.aps.org/doi/10.1103/PhysRev.188.1969 (5 Dec. 1969).

189. Dainty, J. C. *Laser Speckle and Related Phenomena* (Springer, 1984).

190. Goodman, J. W. Some fundamental properties of speckle∗. *J. Opt. Soc. Am.* **66,** 1145–1150. http://www.osapublishing.org/abstract.cfm?URI=josa-66-11-1145 (Nov. 1976).

191. Bighin, G. & Salasnich, L. Finite-temperature quantum fluctuations in two-dimensional Fermi superfluids. *Phys. Rev. B* **93,** 014519. https://link.aps.org/doi/10.1103/PhysRevB.93.014519 (1 Jan. 2016).

192. Ries, M. G. *et al.* Observation of Pair Condensation in the Quasi-2D BEC-BCS Crossover. *Phys. Rev. Lett.* **114,** 230401. https://link.aps.org/doi/10.1103/PhysRevLett.114.230401 (23 June 2015).

193. Murthy, P. A. *et al.* Observation of the Berezinskii-Kosterlitz-Thouless Phase Transition in an Ultracold Fermi Gas. *Phys. Rev. Lett.* **115,** 010401. https://link.aps.org/doi/10.1103/PhysRevLett.115.010401 (1 June 2015).

194. Matsumoto, M., Inotani, D. & Ohashi, Y. Cooper pairs with zero center-of-mass momentum and their first-order correlation function in a two- dimensional ultracold Fermi gas near a Berezinskii-Kosterlitz-Thouless transition. *Phys. Rev. A* **93,** 013619. https://link.aps.org/doi/10.1103/PhysRevA.93.013619 (1 Jan. 2016).

195. Petrov, D. S. & Shlyapnikov, G. V. Interatomic collisions in a tightly confined Bose gas. *Phys. Rev. A* **64,** 012706. https://link.aps.org/doi/10.1103/PhysRevA.64.012706 (1 June 2001).

196. Levinsen, J. & Parish, M. *Annual Review of Cold Atoms and Molecules: Volume 3, Chapter 1* (eds Cohen-Tannoudji, C. *et al.*) https://www.worldscientific.com/worldscibooks/10.1142/9561 (World Scientific, 2015).

197. Martiyanov, K., Makhalov, V. & Turlapov, A. Observation of a Two- Dimensional Fermi Gas of Atoms. *Phys. Rev. Lett.* **105,** 030404. https://link.aps.org/doi/10.1103/PhysRevLett.105.030404 (3 July 2010).

198. Fenech, K. *et al.* Thermodynamics of an Attractive 2D Fermi Gas. *Phys. Rev. Lett.* **116,** 045302. https://link.aps.org/doi/10.1103/PhysRevLett.116.045302 (4 Jan. 2016).

199. Boettcher, I. *et al.* Equation of State of Ultracold Fermions in the 2D BEC-BCS Crossover Region. *Phys. Rev. Lett.* **116,** 045303. https://link.aps.org/doi/10.1103/PhysRevLett.116.045303 (4 Jan. 2016).

200. Murthy, P. A. *et al.* Matter-wave Fourier optics with a strongly interacting two-dimensional Fermi gas. *Phys. Rev. A* **90,** 043611. https://link.aps.org/doi/10.1103/PhysRevA.90.043611 (4 Oct. 2014).

Vermerk zu bereits publizierten Artikeln

Teile dieser Dissertation wurden bereits in folgenden Fachartikeln bzw. als preprint veröffentlicht:

- **Chapter 5: Reaction kinetics in ultracold molecule-molecule collisions**

  D. K. Hoffmann et al., *Reaction kinetics of ultracold molecule-molecule collisions*, Nature Communications, **9**, 5244 (2018),
  https://doi.org/10.1038/s41467-018-07576-1

  Dieser Artikel wurde unter Verwendung folgender Lizenz publiziert: CC-BY 4.0. Lizenzinformation unter: https://creativecommons.org/licenses/by/4.0/

- **Chapter 7: Holographic method for site-resolved detection of a 2D array of ultracold atoms**

  D. K. Hoffmann et al., *Holographic method for site-resolved detection of a 2D array of ultracold atoms*, Applied Physics B, **122**, 227 (2016),
  https://link.springer.com/article/10.1007/s00340-016-6501-1

- **Chapter 6: Second sound in the BEC-BCS crossover**

  D. K. Hoffmann et al., *2nd sound in the BEC-BCS crossover*, arXiv:2003.06847,
  https://arxiv.org/abs/2003.06847

- **Appendix A.2: Pair fraction in a finite-temperature Fermi gas on the BEC side of the BCS-BEC crossover**

  T. Paintner et al., *Pair fraction in a finite-temperature Fermi gas on the BEC side of the BCS-BEC crossover*, Phys. Rev. A, **99**, 053617 (2019),
  https://journals.aps.org/pra/abstract/10.1103/PhysRevA.99.053617

  Die Richtlinien der American Physical Society erlauben das Abdrucken eigener Publikationen in der Abschlussarbeit, siehe hierzu https://journals.aps.org/copyrightFAQ.html.

Danksagung

An dieser Stelle möchte ich mich ganz herzliche bei allen Personen die das gelingen dieser Arbeit ermöglicht haben bedanken. In erster Linie gilt mein Dank meinem Doktorvater Johannes Hecker Denschlag, welcher mir diese Arbeit in seinem Institut ermöglichte und mir stets mit Rat und Tat zur Seite stand.

Einen sehr großen Dank möchte ich auch an meinen Kollegen und Mitstreiter Thomas Paintner richten. Die langjährige freundschafltiche Zusammenarbeit ermöglichte nicht nur die Umsetzung aller technischen Verrichtungen an unserer Anlage, sondern war auch immer Grundpfeiler für das positive Arbeitsklima.

Ein weiterer Dank geht auch an die anderen Kollegen der Arbeitsgruppe. Hierbei sind Markus Deiss, Björn Drews, Tobias Kampschulte und Simon Rupp aus dem Rubidium Experiment, sowie Arne Härter, Artjom Krükow, Amir Mohammadi, Amir Mahdian und Joschka Wolf aus dem BaRbI Experiment zu nennen. Neben den vielen wissenschaftlichen und technischen Diskussionen standen sie jederzeit auch für gesellschaftliche Unternehmungen zur Verfügung.

Neben den Kollegen im Labor möchte ich meinen Dank auch an Wolfgang Limmer, der eine wichtige Stütze bei der theoretischen Aufarbeitung der Projekte war, richten. Darüber hinaus möchte ich mich bei Benjamin Deissler, Wladimir Schoch, Holger Schieferdecker und Moritz Bieber für die Unterstützung bei der Realisierung der neuen Anlage bedanken.

Für die Unterstützung bei administrativen Vorgängen möchte ich mich bei Martina Schweizer und Astrid Sproll bedanken. Des Weiteren danke ich den Kollegen aus der AG von Klaus Thonke für den stets kollegialen und positiven Umgang im Institut.

Zuletzt möchte ich noch meiner Familie danken. Meinen Eltern Irena, Kurt und meiner Schwester Lena. Ohne euch wäre der lange Weg bis zu diesem Punkt nicht denkbar gewesen. Abschließend gilt mein Dank noch meiner Frau Daniela. Sie stand stets bei allen Rückschlägen und Erfolgen an meiner Seite.

Erklärung

Ich versichere hiermit, dass ich die Arbeit selbständig angefertigt habe und keine anderen als die angegebenen Quellen und Hilfsmittel benutzt, sowie die wörtlich oder inhaltlich übernommenen Stellen als solche kenntlich gemacht habe.

Ulm, den 16.04.2020

 Daniel Kai Hoffmann